Optical microscopy-based mechanical phenotyping of heterogeneous cellular migration and contractility.

Adithan Kandasamy

A dissertation
submitted in partial fulfillment of the
requirements for the degree of

Doctor of Philosophy

University of Washington

2024

Reading Committee:

Juan Carlos del Álamo, Chair

Nathan Sniadecki

Susanne Rafelski

Michael Regnier

Program Authorized to Offer Degree:
Mechanical Engineering

University of Washington

Abstract

Optical microscopy-based mechanical phenotyping of heterogeneous cellular migration and contractility.

Adithan Kandasamy

Chair of the Supervisory Committee:
Juan Carlos del Álamo
Department of Mechanical Engineering

All forms of matter, including biological entities, are bound to the law of physics. While mechanical forces have been implicated in the development of organisms almost a century ago, the recent ability to quantitatively measure forces has revealed that physical principles drive fundamental cellular processes. For specialized cells such as leukocytes or cardiomyocytes, the biological function is tightly linked to the cell's mechanical state, misregulation of which is implicated in numerous diseases. Optical microscopy empowered with fluorescence tagging of biomolecules enables kinetic visualization of the cytoplasm and the surrounding substrate. By combining physical modeling, statistical methods and experimental microscopy data at the cellular level, the heterogeneous mechanical behavior of single cells and their collectives can be quantified. This thesis describes methodological advancements in the field of cell migration profiling, cell-exerted traction force measurements and the estimation of cardiomyocyte material properties.

First, the stochastic motility of leukocytes in three-dimensional interstitial environment is studied by measuring the matrix deformation measurements, random walk models and single-cell trajectory analysis. Neutrophils migrating through extravascular spaces must negotiate narrow matrix pores without losing directional tendencies to reach their target. Neutrophils in low collagen concentration matrices were observed to exert large deformation and followed relatively straight trajectories. However, as the collagen concentration increased, matrix deformation decreased and neutrophils turned often to circumvent rather than remodel matrix pores. Inhibiting protrusive or contractile forces shifted this transition to lower collagen concentration, implying that mechanics play a crucial role in defining migratory strategies. Leukocytes exhibit considerable cell-cell variability in their migration response, and thus their effector function. Hence, there is a need to identify leukocyte population

heterogeneity to properly characterize the migratory behavior. A pipeline to autonomously identify clusters of cells exhibiting different random walk characteristics identified two naturally occurring migratory phenotypes: a high motility cluster with faster, persistent cells undergoing fewer turns and a low motility cluster with lower speed and increased incidence of large turns. This cluster proportion was modified by the process of transendothelial migration with an enrichment of the low-motility population. As transendothelial migration is a necessary step in the inflammation response, these observations provide insights into the biophysical importance of differential priming of neutrophil sub-populations to conduct sentinel functions. Such migratory heterogeneity was also demonstrated in mouse primary T-cells showing that proteins of the same Formin family (Formin-like 1 and mammalian diaphanous-related formin 1), despite modulating linear actin polymerization, differentially regulate T-cell motility based on the collagen density.

Secondly, many biophysical measurements (such as leukocyte matrix deformation quantification) rely on image-based motion estimation and further computational modeling to estimate forces. Traction Force Microscopy (TFM) is a widely adapted method to measure cell-exerted forces by tracking fiduciary markers embedded in the substrate. TFM calculations are numerically ill-conditioned and smoothing/regularization is routinely employed to avoid overfitting input noise. While it is known that such image-derived deformation measurements are sensitive to local image features and the choice of the regularization parameter, the existing force reconstruction algorithms do not account for variations in image quality. This hinders objective comparison between experiments, requiring ad-hoc manual smoothing parameter selection and masking the variability of force readouts. TFM-UQ, a TFM uncertainty quantification pipeline is developed to estimate the local, image-dependent deformation uncertainty and propagate it to obtain traction stress error bars using a Bayesian framework. This approach enables spatially adaptive, automated regularization and provides traction stress error bars which was previously not possible. Force readout uncertainty allows decoupling biological heterogeneity from measurement variability, as well as providing a roadmap to enable automating analysis of large datasets by parameter-free input data-based regularization. The Bayesian modeling in TFM-UQ was extended to sub-cellular platelet force resolution using a reference-free TFM procedure.

Finally, the TFM biomechanical model is augmented to estimate the effective stiffness of *in vitro* multi-cellular colonies such as human induced Pluripotent Stem Cells derived cardiomyocytes (hiPSC-CM) monolayers. While physiological assays with hiPSC-CMs are powerful tools for the development of new drugs, high throughput methods to quantify cardiomyocyte contractile force are not prevalent. Furthermore, there are no optical high-

throughput methods to quantify cardiomyocyte stiffness in a multiplexed experimental format. To this end, a computational pipeline that can measure kinematic and dynamic contraction metrics including the stiffness of the monolayer in a non-invasive manner was developed. This pipeline is applied to spontaneously beating monolayers of hiPSC-CMs treated with different doses of benchmark compounds affecting contractility, diastolic tension, and stiffness, demonstrating mechanical phenotyping of hiPSC-CMs in a comprehensive and computational efficiency manner.

The methods developed in this thesis advance image-based mechanical characterization and biophysical measurements in 3D cell migration, cardiomyocyte mechanics and more generally enable precision in mechanobiology applications. The use of statistical modeling is essential to model inherent uncertainties due to biological activity and allows quantitative testing of new hypotheses. Improvements to the precision of biophysical measurements with microscopy images have significant implications in personalized medicine and enable more rigorous comparison between experiments.

DEDICATION

To my grandparents, through whom I have known unconditional love.

TABLE OF CONTENTS

LIST OF FIGURES

LIST OF TABLES

ACKNOWLEDGMENTS

Pursuing a PhD in mechanobiology could not have been further away from the realm of possibilities when I started college. However, through numerous opportunities and the guidance of several incredible individuals that became a reality - for which I am immensely grateful.

First and foremost, I owe a great deal to Juan Carlos del Álamo for almost all aspects of my graduate journey. Witnessing his creative and scientific process firsthand for tackling a diverse range of problems has been truly inspiring. I deeply appreciate his unwavering support throughout my PhD when the state of affairs was seldom in order. He provided me with intellectual freedom, resources, and encouragement, all of which were indispensable to completing my thesis. I value all the many interactions over lunch, coffee, in the classroom or on the trail that continue to inspire me beyond the lab.

I extend my gratitude to Juan Lasheras for his wisdom and guidance during my time at UC San Diego. His mentorship and the far-reaching impact it has had on generations of scientists and engineers never cease to inspire me.

I extend my deepest appreciation to my reading committee members - Nathan Sniadecki, Susanne Rafelski and Mike Regnier. I very much appreciate the consideration and patience afforded to me during a period of turmoil and for the constructive feedback time after time. Their insights during the defense exam and while reviewing the draft helped me appreciate the broader significance of my work. I am especially thankful for their interactions beyond the committee meetings, which fostered a connection to the wider scientific community.

I sincerely thank David Santillan and William Young for serving on my qualifying committee at UCSD and for some of the best lectures I've had the privilege to learn from, particularly the PDE course, which continues to influence me daily. I also extend my gratitude to Alberto Aliseda for serving on my qualifying committee and for guidance and approachability as the chair at UW.

I am fortunate to have had the opportunity to work with Julie Theriot, whose

scientific pursuits and passion have left a profound impact on every interaction. It had been very rewarding working with Mugdha and Chris, and to the entire Theriot lab for always making me feel welcome and included. I have had the opportunity to participate in exciting research through exceptional collaborators: Molly Mollica, Kevin Beussman, Jordan Jacobelli, Ashton Sigler and Mark Mercola. In particular, I am indebted to Ricardo Serrano, whose patience, attention to detail, and guidance were instrumental in the cardiomyocyte work and in shaping my career.

I still remember my disbelief when I first spoke to Benoit Ladoux, who graciously decided to hire me as an intern after I reached out to him via email. My initial steps into this field, wet laboratory and microscopy skills are thanks to Benoit and Shreyansh. My foray into research would not have been possible without the exceptional guidance of Sujatha Srinivasan and Madhu Ganesh, whose generosity and infectious passion set a standard I strive to uphold.

I would also like to thank past and present lab members for their contributions to my projects, as well as for the countless lunches, conversations, and support over the years. Thanks to Yi-Ting, Cathleen, Alejandro, Clarissa, Tu, Amy, Josh, Ernesto, Lorenzo, Stephen, Shun, Stephanie, Manuel, and Christian. Your kind words, listening ears, and camaraderie have been invaluable, especially during challenging times. I am grateful to all my friends - Jen, Mepuka, Swetha, Nicole, Jesse and so many others - with whom I was able to cultivate a sense of community, an abundance of love and originality that allowed me to thrive. I cannot imagine navigating the coursework in my first year without Cathleen, Hossein, Jennifer and Jack. Thank you for the support and the memorable moments.

I am profoundly thankful to my family for their unwavering support of my graduate school decisions and for allowing me to pursue my interests while encouraging excellence. My grandparents hold a special place in my heart for raising me and for the surplus of love. I know they would have been very proud to see me finish my PhD.

Finally, I want to express my heartfelt gratitude to Vaishali. Your unwavering empathy, kindness, and strength have been an anchor throughout these years. Your presence has brought peace, safety, and emotional support during turbulent moments, and I will always be grateful for having you by my side.

I would also like to acknowledge the contribution of various authors to the dissertation chapters as follows.

Chapter 2, in part, has been published as it may appear the following venues

: *Science Advances* [1] (Joshua François, Adithan Kandasamy, Yi-Ting Yeh, Amy Schwartz, Cindy Ayala, Ruedi Meili, Shu Chien, Juan C Lasheras, Juan C del Álamo), *biorxiv* [2] (Amy Schwartz, Adithan Kandasamy, Juan C del Álamo, Yi-Ting Yeh) and *Frontiers in Immunology* [3] (Ashton L Sigler, Scott B Thompson, Logan Ellwood-Digel, Adithan Kandasamy, Mary J Michaels, Dean Thumkeo, Shuh Narumiya, Juan C del Álamo, Jordan Jacobelli). The dissertation author is a co-author in these publications.

Chapter 3, in part, is under revision at PLoS Computational Biology and is available as a pre-print in *biorxiv* [4] (Adithan Kandasamy, Yi-Ting Yeh, Ricardo Serrano, Mark Mercola, Juan C del Álamo). The dissertation author is the primary author of this paper.

Chapter 4, in part, has been published as it may appear in *Biophysical Journal* [5] (Molly Y Mollica, Kevin M Beussman, Adithan Kandasamy, Lesley Martínez Rodríguez, Francisco R Morales, Junmei Chen, Krithika Manohar, Juan C del Álamo, José A López, Wendy E Thomas, Nathan J Sniadecki). The dissertation author is a co-author of this publication.

Chapter 5, in part, is in preparation for submission of the material (Ricardo Serrano, Adithan Kandasamy, Mark Mercola, Juan C del Álamo). The dissertation author is the co-primary author of this paper.

VITA

2024	Ph.D. in Mechanical Engineering University of Washington, Seattle
2019	M.S. in Engineering Sciences (Mechanical Engineering) Univeristy of California, San Diego
2018	B.E. in Mechanical Engineering PSG College of Technology, Coimbatore
2017 - 2018	Research Intern Dr. Benoit Ladoux, Mechanobiology Institute, Singapore
2017	Research Intern Dr. Sujatha Srinivasa, Indian Institute of Technology - Madras, Chennai

PUBLICATIONS

Kandasamy, A., Yeh, Y.-T., Serrano, R., Mercola, M. and del Álamo, J.C. Uncertainty-Aware Traction Force Microscopy. *bioRxiv* (2024)

Serrano, R*., Kandasamy, A*., Staudt, D.W., Mercola, M. and del Álamo, J.C. Multimodality high-throughput contractility and stiffness measurement of hiPSC-derived cardiomyocytes. *In preparation.* * Co-first authors.

François, J., Kandasamy, A., Yeh, Y.-T., Schwartz, A., Ayala, C., Meili, R., Chien, S., Lasheras, J.C. and del Álamo, J. C. The interplay between matrix deformation and the coordination of turning events governs directed neutrophil migration in 3D matrices. *Science Advances* (2021)

Schwartz, A. B., Kandasamy, A., del Álamo, J. C. and Yeh, Y.-T. Neutrophils exhibit distinct migration phenotypes that are modulated by transendothelial migration. *bioRxiv* (2024)

Mollica, M. Y., Beussman, K.M., Kandasamy, A., Rodríguez, L.M., Morales, F.R., Chen, J., Manohar, K., del Álamo, J.C., López, J.A., Thomas, W.E. and Sniadecki, N.J. Distinct platelet F-actin patterns and traction forces on von Willebrand factor versus fibrinogen. *Biophysical Journal* (2023)

Sathe, M., Prinz, C., Kandasamy, A., Belliveau, N., Footer, M., Kennard, A., del Álamo, J.C. and Theriot, J. Epidermal T-cells migrate towards anode under applied electric fields. *In preparation*

Sigler, A. L., Scott T.B., Ellwood-Digel, L., Kandasamy, A., Michaels-Foster, M.J., Thumkeo D., Narumiya, S., del Álamo, J.C. and Jacobelli, J. FMNL1 and mDia1 promote efficient T cell migration through complex environments via distinct mechanisms. *Frontiers in Immunology* (2024)

Garcia-Herreros, A., Yeh, Y.-T., Tu, Y., Kandasamy, A., del Álamo, J.C. and Criado-Hidalgo, E. Tunable photoinitiated hydrogel microspheres for direct quantification of cell-generated forces in complex three-dimensional environment. *biorxiv* (2023)

Nguyen, C.M., Martinez-Legazpi, P., Maidu, B., Kandasamy, A., Gonzalo, A., Kahn, A.M., Bermejo, J. and del Álamo, J. C. Bayesian vector flow mapping with uncertainty quantificaiton. *In preparation.*

Yeh, Y.-T., Skinner, D. E., Criado-Hidalgo, E., Chen, N. S., Garcia-De Herreros, A., El-Sakkary, N., Liu, L., Zhang, S., Kandasamy, A., Chien, S., Lasheras, J.C. and del Álamo, J.C. Biomechanical interactions of schistosoma mansoni eggs with vascular endothelial cells facilitate egg extravasation. *PLoS Pathogens* (20222)

Chapter 1

INTRODUCTION

Eukaryotic cells possess the remarkable ability to mechanically remodel the cytoskeleton and apply mechanical forces on neighboring cells and the surrounding environment. The dynamic regulation facilitates complex and coordinated physical cellular response such as immune surveillance [6], collective cell migration and homeostasis [7, 8], cell division [9–11], stem cell fate determination [12], pumping blood [13], etc. Over the last few decades, it has been clear that the physical interaction between cells and the environment by application and sensing of forces is important for development [14, 15] as well as throughout an organism's lifetime [16, 17].

1.1 Cellular mechanical phenotyping

Phenotype broadly refers to the characteristics (appearance, behavior and function) of an organism as a result of the history of the interaction of the genetic information (genotype) with external environmental cues [13]. Measurement of gene expression and protein activity provides a direct quantification of the genome activity. Since cells are the fundamental unit of life, single-cell sequencing provides an understanding of the biological diversity, rare populations and patterning over space and time that can be lost with bulk approaches [18, 19]. Indeed, cell-cell asymmetries are observed in embryonic development as early as the four-cell stage [20]. In a similar vein, mechanical phenotyping refers to quantification of physical characteristics of a cell such as contractile state, tension, migratory behavior, material properties, etc. [21]

Specialized cells such as leukocytes and cardiomyocytes rely on physical interactions and active physical force generation for their corresponding biological functions [6]. Measurement of mechanical state (phenotype) is therefore necessary for measuring the functional capabilities (e.g. ability to reach the point of infection and cardiac output respectively). Combining optical microscopy of fluorescently tagged membranes and embedded markers, computational analysis and biophysical modeling allows inference of mechanical variables that are otherwise inaccessible (Fig 1.1 A). Therefore, the measurement of functional output in addition to sequencing, especially in high content screening, holds the potential for a mechanistic understanding of genotype-to-function link [21] and pre-clinical drug development [22, 23]. This thesis describes improvements to mechanical phenotyping to allow

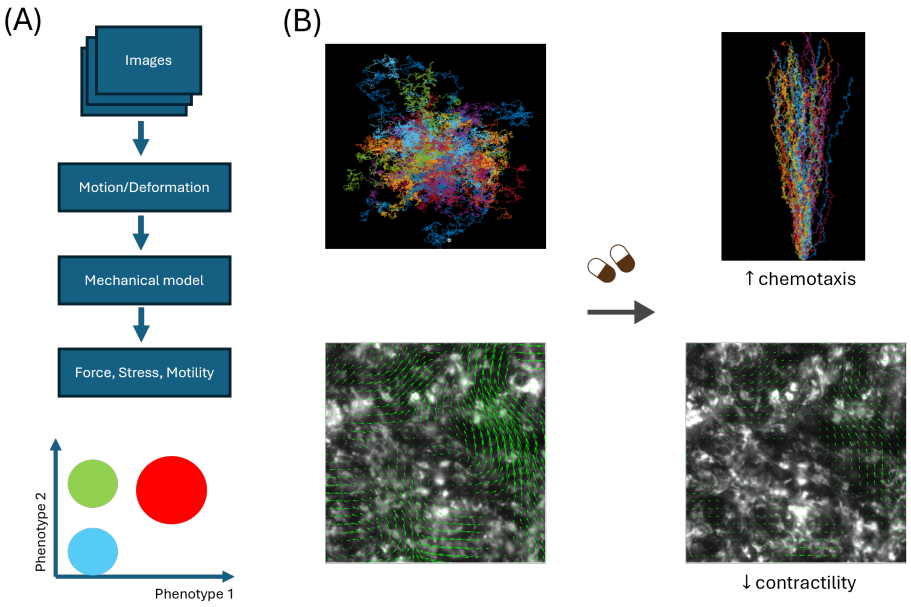

Fig 1.1. Microscopy-based cellular mechanical phenotyping. (A) First, images are processed to obtain quantitative information such as deformation (observable). The measured quantity is related to parameters of interest (such as forces, typically not observed) using a biophysical model. High throughput methods allow quantification of large number of cells to identify populations with significant phenotypic differences. (B) Examples showing practical utility of biomechanical phenotyping (Top) Simulated random walk trajectories showing before (left) and after (right) introduction of a chemotactic gradient. *In silico* cells display a switch in migratory phenotype towards directed motion. (Bottom) Spontaneously contracting human cardiomyocytes before (left) and after (right) treatment with a candidate pharmacological compound (leading to decreased contraction magnitude as evidenced by the displacement field vectors).

heterogeneous profiling of cell migration, traction forces and material properties, with immediate applications to study inflammation and heart failure (Fig 1.1 B). The physical models used in various chapters to model the quantity of interest are first reviewed in §1.2. Computational methods that relate microscopy-based measurements to model parameters are reviewed in §1.3. Finally, existing biophysical measurement methods in the literature are reviewed in §1.4.

1.2 Physical models of cellular motility and contractility

Application of mathematical concepts and physical laws to understand the shape of organisms and relation to function of biological organisms has been explored since a century ago, pioneered by D'Arcy Thompson [24]. Ever since, the growth of physical biology investigations saw the utility of physics-based models adopted from the different fields of physics.

Quantitative models rely on quantitative data which is increasingly the case with experimental methods [25]. The following paragraphs describe the various such models used for analyzing the mechanical behaviour of the cells and tissue in this dissertation.

1.2.1 Random walk model of single cell motility

Motile cells in the timescales greater than few motility cycles can be considered as noisy automatic control devices [26]. In this sense, directed (chemotaxis, Galvanotaxis, etc.) and undirected (chemokinesis) motion of cells can be considered as the response of a stochastic device with or without feedback respectively. Since the cellular behavior is stochastic in nature, the behavior of individual cells cannot be predicted deterministically. Stochastic differential equations (SDE), particularly *Langevin* equations, are powerful tools to model the equations of motion of an active agent (migrating cell) under noisy signal transduction/noise. Langevin SDE originates in the study of Brownian dynamics of colloidal particles (1908) where a random Markovian force was used to introduce random collision with the surrounding water molecules [27],

$$\dot{v} = -\gamma v + \Gamma(t), \tag{1.1}$$

where γ is the frictional force normalized by mass, v the velocity of the particle and $\Gamma(t)$ the random Langevin force normalized by mass (units of velocity). The characteristic time scale, τ (inverse of γ) is denoted the persistence time to change directions. Further assumptions can be made to the stochastic velocity change $\Gamma(t)$ by assuming it to be white noise process with a strength q :

$$\begin{aligned} \langle \Gamma(t) \rangle &= 0, \\ \langle \Gamma(t)\Gamma(t') \rangle &= q\delta(t-t'). \end{aligned}$$

First constraint specifies no bias to the random noise and the second constraint assumes delta-correlated noise or a Markovian process. For a SDE, only the probability of an ensemble of particles following eqn(1.1) can be calculated. This is obtained from the corresponding Fokker-Planck equation for the speed of the agents $W(v,t)$:

$$\frac{\partial W(v,t)}{\partial t} = \left(\gamma \frac{\partial}{\partial v} v + \frac{1}{2} q \frac{\partial^2}{\partial v^2} \right) W(v,t). \tag{1.2}$$

Without the persistence term in eqn (1.1), eqn (1.2) corresponds to a simple diffusion equation. At stationary, eqn (1.2) tends to a Gaussian distribution centered at zero (as-

suming no bias),

$$W_{st} \propto \exp\left(-\frac{q}{\gamma}v^2\right). \tag{1.3}$$

Eqn (1.1) is referred to as the Ornstein-Uhlenbeck (OU) process with the following general solution :

$$v(t) = v_0 e^{-\gamma t} + \int_0^t e^{-\gamma(t-t')\Gamma(t')\mathrm{d}t'}.$$

If $\Gamma(t) = 0$, then $v(t)$ is an exponential decay to 0 from the initial condition v_0. At the stationary state (i.e. timescales larger than τ, $\gamma t \gg 1$), the velocity correlations are given by,

$$\begin{aligned} \langle v(t)\rangle &= v_0 e^{-\gamma t}, \\ \langle v(t)v(t')\rangle &\to \frac{q}{2\gamma} e^{-\gamma|t-t'|}. \end{aligned} \tag{1.4}$$

Velocity Auto-correlation Function (VAF) (Eqn (1.4)) is an important prediction that can be tested experimentally to gauge the applicability of the model. Another quantity of practical importance is the mean squared displacement (MSD), at stationary is given by,

$$\langle (x - x_0)^2\rangle = \frac{q}{\gamma^3}(\gamma t - 1 + e^{-\gamma t}). \tag{1.5}$$

generalizing to all timescales. For $t \gg \tau$, $\langle (x - x_0)^2\rangle \to \frac{q}{\gamma^2} t = 2Dt$, where D is the diffusion co-efficient defined by Einstein [28] solving eqn (1.2). Eqn (1.5) shows a ballistic (super-linear) MSD initially and tend to the linear regime at large timescales.

Persistent Random Walk (PRW) or correlated random walk are important class of models that are extensively used in cell migration studies [26, 29–32] (Chapter 2). In the continuum limit, they are equivalent to the OU process (1.1). An important distinction from colloidal studies is that the source of variability in cells that arises due to the inherent activity of the cellular cytoskeleton and sensing mechanisms as opposed to external collisions in suspensions. VAF (1.4) and MSD (1.5) are predictions from the model that can be used to test if an ensemble of *homogenously* migrating cells can be described by a persistent random walk model.

1.2.2 Continuum mechanical model of cells and tissues

Traction Force Microscopy (TFM) based assays [33–40] provide mechanically controlled elastic substrates in the physiological and pathological range of stiffness (§1.4.1). In TFM experiments, cells are cultured on flat, linearly elastic substrates and are mechanically connected to the substrates via focal adhesion complexes and transmit traction forces onto the substrate [13]. The same forces also control the focal adhesion dynamics creating a feedback loop between the substrate deformation and the applied force, which enables mechanotransduction and adaptation of the cell intrinsic stiffness to that of the substrate.

Hence, it is important to understand the coupling between the environment (substrate) and the individual cells or a monolayer to parse the experimental observations. This helps investigate the emergent mechanical composition of the cells such as the elasticity and the internal stresses withstood by the cells, which is important in physiological contexts [41].

An contractile monolayer exerting inhomogeneous traction stress on soft elastic substrate can be modeled in the continuum limit as a multimer of contractile elements connected by springs. The cell monolayer is taken to have an uniform thickness $h_c \ll L$, the lateral size of the monolayer. In this case, the force balance at the cell-substrate interface is given by,

$$Y\mathbf{u}(\mathbf{x},t) = h_c \nabla \cdot \boldsymbol{\sigma}(\mathbf{x},t), \tag{1.6}$$

where Y is the effective stiffness of the substrate (and focal adhesion), $\mathbf{u}(\mathbf{x})$ the displacement field of the cells at the interface $z = h$ and $\boldsymbol{\sigma}$ is the z - averaged Cauchy stress tensor, $\boldsymbol{\sigma}(\mathbf{x}) = 1/h_c \int_{z=h}^{z=h+h_c} \boldsymbol{\sigma}_{3D}(\mathbf{x})$. When the monolayer behaves in the elastic limit, the following constitutive relation can be prescribed :

$$\boldsymbol{\sigma}(\mathbf{x}) = f(\theta_{mat}, \mathbf{u}(\mathbf{x})) + \boldsymbol{\sigma}_a. \tag{1.7}$$

$\boldsymbol{\sigma}_a$ is the active stress arising from actomyosin or sarcomeric (cardiomyocytes) contractility. $\boldsymbol{\sigma}_a$ is modeled to excite the bulk deformation and therefore, it is a diagonal tensor. The substrate deformation $\mathbf{u}_s$ is given by eqn (1.8) with $\boldsymbol{t}(\mathbf{x}') = \nabla \cdot \boldsymbol{\sigma}(\mathbf{x}')$ is the traction stresses at the substrate exerted by the cell's activity. From elastostatics, the response of an isotropic elastic substrate due to traction stresses at $z = h$ is given by,

$$\boldsymbol{u}_{\mathrm{h}}(\mathbf{x}) = \int \mathbf{G}(\mathbf{x} - \mathbf{x}')\boldsymbol{t}(\mathbf{x}')\mathrm{d}\mathbf{x}', \tag{1.8}$$

$\mathbf{G}(\mathbf{x})$ is the 2D/3D elastostatic Green's function that relates the traction stresses $\boldsymbol{t}$ to the substrate displacement field $\boldsymbol{u}_{\mathrm{h}}$.

Linear constitutive relation for cells

The simplest constitutive equation (in 3D) that can be prescribed is that of a linearly elastic material :

$$\boldsymbol{\sigma}(\mathbf{x}) = K\,\mathrm{tr}(\mathbf{u})\epsilon + 2\mu\left(\epsilon - \frac{1}{3}\,\mathrm{tr}(\epsilon)\boldsymbol{I}\right), \tag{1.9}$$

$$\boldsymbol{\sigma}(\mathbf{x}) = \frac{E}{2(1+\nu)}\left(\epsilon + \frac{\nu}{1-2\nu}\,\mathrm{tr}(\epsilon)\boldsymbol{I}\right). \tag{1.10}$$

$\epsilon = (\nabla\mathbf{u} + \nabla\mathbf{u}^T)/2$ is the linear strain tensor. (K, μ) represent the bulk and shear modulus (3D modulus) while (E, ν) is the Young's modulus and Poisson's ratio respectively. By applying the deviatoric transformation on the stress tensor $\boldsymbol{\sigma}(\mathbf{x}) = 1/3\,\mathrm{tr}(\boldsymbol{\sigma})\boldsymbol{I} + (\boldsymbol{\sigma} - 1/3\,\mathrm{tr}(\boldsymbol{\sigma})\boldsymbol{I})$ and relating to eqn (1.9), it can be seen that $\mathrm{tr}(\mathbf{u}) = \mathrm{tr}(\boldsymbol{\sigma})/3K$ represents the hydrostatic compression. Likewise, the second term represents a pure shear since it is trace-free (e.g. $\sigma_{12} = 2\mu\epsilon_{12}$).

For large timescales, migrating cells are known to be viscoelastic in nature [42]. Viscoelastic models allows including stress relaxation and introduces a timescale to the model. A Kelvin-Voigt model represents elastic and viscous elements arranged in parallel, leading to the following constitutive relation :

$$\boldsymbol{\sigma}(\mathbf{X}, t) = (1 + \tau\partial_t)\left(K\,\mathrm{tr}(\epsilon)\boldsymbol{I} + 2\mu\left(\epsilon - \frac{1}{3}\,\mathrm{tr}(\epsilon)\boldsymbol{I}\right)\right). \tag{1.11}$$

The linearly elastic and viscous contributions (relaxation time τ) are additive and decoupled, representing a viscoelastic solid. For a viscoelastic fluid, an appropriate model is Maxwell model [43].

Non-linear elastic constitutive relation for cells

More realistically for biological cells, the elastic behavior (neglecting dissipation for shorter timescales) is non-linear with different behavior for compression and extension. The non-linearity arises from large deformations (geometric non-linearity) as well as material non-linearities (hyper elasticity). Under large deformations, the infinitesimal strain tensor ϵ is inadequate to map a material point(position vector) in a *reference* (initial) configuration ($\mathbf{X}$) to the *current* (stressed) configuration ($\mathbf{x}$) including rigid body motion. The motion of the material point is described by the displacement vector, $\mathbf{x} = \mathbf{u}(\mathbf{X}) + \mathbf{X}$. Suppose, a material line element of length $\mathrm{d}\mathbf{X}$ positioned at $\mathbf{X}$ in the reference configuration is mapped into another line element of length $\mathrm{d}\mathbf{x}$ at $\mathbf{x}$ according to the *deformation gradient* tensor,

$$\mathbf{F} = \frac{\partial \mathbf{x}}{\partial \mathbf{X}} = \frac{\partial \mathbf{u}(\mathbf{X}) + \mathbf{X}}{\partial \mathbf{X}} = \boldsymbol{I} + \nabla_{\mathbf{X}} \mathbf{u}. \tag{1.12}$$

$\mathbf{F} = F_{ij}\mathbf{e}_i \otimes \mathbf{E}_j$ is a two-point tensor with one leg in the reference configuration (reference unit vector denoted by $\mathbf{E}_j$) and other in the current configuration ($\mathbf{e}_i$). The suffices denote the Einstein notation. The deformation can be decomposed into a stretching and rotation. The stretch between the line elements $\mathrm{d}\mathbf{X}$ and $\mathrm{d}\mathbf{x}$ of lengths $\mathrm{d}S$ and $\mathrm{d}s$ is given by

$$\mathrm{d}s^2 - \mathrm{d}S^2 = d\mathbf{X} 2\mathbf{E} d\mathbf{X}.$$

$\mathbf{E} = \frac{1}{2}(\mathbf{F}^T\mathbf{F} - \boldsymbol{I})$ is the Lagrangian (finite) strain tensor, defined with respect to the basis in the reference configuration only. In terms of the displacement gradient,

$$\mathbf{E}_{ij} = \frac{1}{2}\left(\frac{\partial u_i}{\partial X_j} + \frac{\partial u_j}{\partial X_i} + \frac{\partial u_k}{\partial X_i}\frac{\partial u_k}{\partial X_j}\right). \tag{1.13}$$

It can be seen that eqn (1.13) simplifies to the infinitesimal strain tensor ϵ when ignoring higher order terms. Depending on the bases of the tensor, different stress tensors can be admitted. Cauchy stress tensor $\mathbf{T}$ at any point $\mathbf{x}$ relates the stress vector $\boldsymbol{t}_n$ to the unit normal $\mathbf{n}$ of the plane on which it acts ($\boldsymbol{t}_n = \mathbf{T}\mathbf{n}$). $\mathbf{T}$ is a symmetric tensor. To measure the internal stresses developed in the current configuration per unit area of the reference configuration, the stress vector $\boldsymbol{t}_n$ needs to be resolved on the geometry of the reference configuration. This is given by the *first Piola-Kirchhoff* stress tensor $\mathbf{P}$, which is unsymmetric as it is two-sided. Cauchy stress tensor and first Piola-Kirchhoff tensor can be related by,

$$\mathbf{T} = \frac{1}{J}\mathbf{P}\mathbf{F}^T,$$

where $J = \det(\mathbf{F})$ is the Jacobian of the deformation gradient tensor. In the reference configuration, the symmetric *Second Piola-Kirchhoff* tensor is defined as $\mathbf{S} = \mathbf{F}^{-1}\mathbf{P} = J\mathbf{F}^{-1}\mathbf{T}\mathbf{F}^{-T}$. A commonly used constitutive equation for hyperelastic material is an extension of eqn (1.9) called the generalized Hookean law,

$$\mathbf{S} = 2\mu\mathbf{E} + \lambda(\operatorname{tr}\mathbf{E})\boldsymbol{I}.$$

A more successful non-linear elastic model is *Neo-Hookean* model that was initially developed to model cross-linked polymer and rubber [44]. Under stretch, the polymers chains realign until maximum stretch causing an increase in the elastic modulus. The first Piola-Kirchhoff stress tensor for a New-Hookean solid is given by

$$\mathbf{P} = 2\mu(\mathbf{F} - \mathbf{F}^{-T}) + 2KJ(J-1)\mathbf{F}^{-T}. \tag{1.14}$$

Active stresses

The active contraction due to actin flow or sarcomeric activity can be modeled as volumetric contraction (i.e.) exciting the bulk modulus. In terms of isometeric contraction, Edwards *et al* [40] modeled the active force F_A of contracting monolayer as

$$\boldsymbol{\sigma} = -\frac{E}{2(1-\nu)} F_A \boldsymbol{I}. \tag{1.15}$$

The negative sign indicates contraction. In this formalation, the active term doesnot contribute to the deviatoric or shear stresses. Since contraction occurs in polarized axis (e.g. F-actin fiber orientation or sarcomere axis), Anderson *et al* [43] models the active contraction along an angle ϕ as,

$$\boldsymbol{\sigma}_a = \begin{pmatrix} \cos\phi & -\sin\phi \\ \sin\phi & \cos\phi \end{pmatrix} \begin{pmatrix} -F_A & 0 \\ 0 & 0 \end{pmatrix} \begin{pmatrix} \cos\phi & \sin\phi \\ -\sin\phi & \cos\phi \end{pmatrix}$$

Linear model of underlying substrate is used in Chapter 3 and Chapter 4 for measurement of traction forces. Along with a non-linear hyperelastic model to model cardiomyocyte monolayer is adapted for non-invasive stiffness measurement in Chapter 5.

1.3 Inference of mechanical quantities using noisy imaging data and physical models

Modern force measurement methods rely on microscopy based information in experimentally controlled environments. Such image analysis tend to be noisy as the actual image generation process is usually not known in addition to camera noise. An example is the imaging of fluorescent tracers in the substrate for TFM measurements, where the substrate heterogeneities in manufacturing affects the measurement but is not typically modeled in the measurement. In addition, inherent biological noise and variability is ubiquitous and a feature enabling cells' function. Fluctuations actively drive force production, cell migration, wound closure and so on. Therefore, it is important to be able to model inherent uncertainties and distinguish them from the measurement noise.

1.3.1 Classical regularization

Regularization is a technique to enforce constraints on the allowable solution space during inversion of an ill-conditioned matrices [45, 46], promoting well-behaved solutions and avoid

overfitting of data noise. This section uses TFM as an example but the regularization methods are applicable to inversion of any linear system of equations. Discretization of a typical forward problem such as the elastostatic response integral (1.8) leads to the matrix equation :

$$\boldsymbol{u}_{\mathrm{h}} = \mathbf{M}\boldsymbol{t}.$$

Depending on the solution method (e.g.Fourier [37] vs. Boundary element [36]) and the geometry (e.g. finite h [33, 38] vs infinite h [36, 37]) the condition number of $\mathbf{M}$, $\kappa(\mathbf{M}) = \left\|\mathbf{M}^{-1}\right\| \|\mathbf{M}\|$ is typically high enough to be susceptible to high frequency noise. $\kappa(\mathbf{M})$ is also given by the ratio of the maximum to the minimum singular value and quantifies how sensitive is the operator $\mathbf{M}$ to changes or error in the input values. Such problems are inverted by regularization by making the matrices well-conditioned by adding a diagonally-dominant matrix $\mathbf{L}$ and minimizing the combined quantity:

$$\|\boldsymbol{u}_{\mathrm{h}} - \mathbf{M}\boldsymbol{t}\|^2 + \lambda \|\mathbf{L}\boldsymbol{t}\|^p, \tag{1.16}$$

where $\|\cdots\|^p$ indicates a $p-$norm and $\lambda > 0$ is the regularization parameter that behaves as a Lagrange multiplier. Various types of regularization has been used in the TFM literature : Tikhonov regularization with $L2$ [47–49] and $L1$ [50] norm, smoothness $\mathbf{L}$ [51], elastic-net [49] and so on. Compared to pre-smoothing input data before inversion, regularization provides more granular control on the form of smoothness employed that can depend on the data and the matrix system employed. The issue with optimizing (1.16) with a user-defined parameter λ is that the results are very sensitive to the value of λ (Chapter 3). Higher the value of λ, the larger is the regularization of smoothing [35]. Several heuritsic methods have been employed to choose the optimal value of λ for a given $\mathbf{M}$ and the input data $\boldsymbol{u}_{\mathrm{h}}$ such as L-curve, Generalized Cross Correlation (GCV) and the discrepancy principle.

In these analyses, the input $\boldsymbol{u}_{\mathrm{h}}$ is considered to be perturbed by an additive noise $\|\epsilon\|$ such that

$$\boldsymbol{u}_{\mathrm{h}} = \mathbf{M}\boldsymbol{t} + \epsilon. \tag{1.17}$$

L-curve criterion determines the optimal $\hat{\lambda}$ as the λ corresponding to the characteristic corner a log-log plot of the residual norm $\left\|\boldsymbol{u}_{\mathrm{h}} - \mathbf{M}\hat{\boldsymbol{t}}\right\|$ and the regularizer norm $\|\mathbf{L}\boldsymbol{t}\|$. It was developed by P.C.Hansen [45, 46] who also published the MATLAB software to find L-curve and other optimal regularization parameter methods using singular value decomposition that is widely in use now. L-curve may not always contain the proper corner [45, 49, 52] and maynot be applicable depending on the input data quality. A class of methods named $\|e\|^2$-

based methods work by choosing the the minimum value of λ such that $\|\mathbf{M}\boldsymbol{t}_\lambda - \boldsymbol{u}_\mathrm{h}\|^2 \geq \|e\|^2$. According to the Morozov discrepancy principle [48, 53], if the model is exact (i.e. the residual is zero when the input is noise-free), then the expected value of $\|e\|^2$ is equal to the $\mathrm{Std}(\epsilon)\sqrt(m)$, where m is the number of datapoints in $\boldsymbol{u}_\mathrm{h}$. However, the estimate for $\mathrm{Std}(\epsilon)$ (i.e. the level of noise in the input) is usually unknown hampering the use of this principle. Discrepancy principle has been shown to oversmooth solutions [53], the reason for which is theorized to be theat a particular realization of $\boldsymbol{u}_\mathrm{h}$ might not satisfy the discrepancy equation. The compensated discrepancy principle minimizes,

$$\|\mathbf{M}\boldsymbol{t}_\lambda - \boldsymbol{u}_\mathrm{h}\|^2 = \mathrm{Std}(\epsilon)\mathcal{T}(\lambda)^{1/2},$$

where $\mathcal{T}(\lambda) = \mathrm{tr}(\boldsymbol{I} - \mathbf{M}\mathbf{M}^{\#})$, the effective degrees of freedom and $\mathbf{M}^{\#}$ is such that $\boldsymbol{t}_\lambda = \mathbf{M}^{\#}\boldsymbol{u}_\mathrm{h}$. In cases where $\mathrm{Std}(\epsilon)$ is unknown, the regularization parameter is found as the minimizer of

$$GCV \equiv \frac{\|\mathbf{M}\boldsymbol{t}_\lambda - \boldsymbol{u}_\mathrm{h}\|^2}{(\mathrm{tr}(\boldsymbol{I} - \mathbf{M}\mathbf{M}^{\#}))^2},$$

the Generalized Cross Validation (GCV) function that is based on leave-one out cross validation and is related to the L-curve [53].

1.3.2 Bayesian inference

The method of statistical inference is concerned with estimation of quantities that are not observed using collected data [54]. Bayesian inference in particular is attractive to biological physics because of the ability to model the uncertainties of the measured quantities that corresponds to both biological and measurement uncertainties. The quantities of interest in biomechanical analysis such as forces, motility states and stiffness cannot be observed and therefore, rely on a prescribed first-principle or phenomenological model that relates the observed quantity (named *data*, x) to model quantities (named *parameters*, θ). This functional relationship is called the model or the *joint distribution* ($p(x, \theta)$) in the framework of statistical inference. In particular, Bayesian statistics is a formal framework for making conclusions about the parameter θ in terms of probabilities relating the likelihood (of data given the model) and the prior knowledge about the parameter. An important distinction with Bayesian statistics compared to a frequentist approach is the use of conditional probabilities (i.e. variables conditioned on observed data, $p(\theta|x)$) and therefore, the inferences are made as updates to the prior knowledge of θ through Bayes' rule :

$$p(\theta|x) = \frac{p(\theta, x)}{p(x)} = \frac{p(\theta)p(x|\theta)}{p(y)}. \tag{1.18}$$

It is assumed that the random variables are continuous and therefore, a probability distribution is associated with them. The model or the joint probability distribution is written as the product of prior distribution, $p(\theta)$, and the likelihood of the data given the model parameters (quantities of interest), $p(x|\theta)$. Bayes' rule in particular refers to the conditioning on the value of the data x. The denominator in eqn (1.18) called the *evidence* is the evidence of the data under a given model considering all possible parameters θ by marginalization, $p(x) = \int p(\theta)p(x|\theta)\mathrm{d}\theta$. It is useful for model selection (comparing two different models $p(\theta, x|M)$, where M denotes a functional model). For a given model, the evidence serves as the normalizing factor that ensures that the *posterior* is a probability distribution (i.e. $\int p(\theta|x)\mathrm{d}\theta = 1$). Note that the likelihood doesnot need to be a probability distribution. Inference on the parameter given some data is performed with the posterior distribution, $p(\theta|x)$ conditioned on the data.

Uncertainties

In Bayesian statistics, a probability distribution serves as the measure of uncertainty associated with the variable. While a frequentist method works with a hypothetical 'true' value of the parameter using a data distribution, Bayesian methods naturally allows (and encodes) the randomness or the uncertainty (lack of information) of the parameter by assigning a probability distribution to the parameters. This information is reflected in the posterior (eqn (1.18))) that updates the prior information $p(\theta)$ with the information contained in the data $p(x|\theta)$.

Bayesian inference for large samples guarantees asymptotic normality of the posterior distribution [54]. In addition, the analysis is consistent in the sense that the mode of the posterior distribution converges to the true parameter value θ_0 as the number of samples $n \to \infty$, if the true data distribution is $p(x|\theta_0)$. Importantly, the distribution increasingly becomes concentrated to smaller and smaller neighborhoods in the large n limit. This illustrates the consistency with other statistical inferences such as frequentist interpretation, but also provides an understanding of the meaning of posterior uncertainty. The prior information is dominated by the large sample, however prior distribution is a critical part of model specification for small sample sizes. In cases where the likelihood model is not uniquely defined, a non-informative prior is not applicable and therefore, careful consideration to the prior specification is required, as is the common case for biophysical measurements.

Bayesian framework is used in this thesis to infer the random walk parameters of leukocyte trajectories using discrete time OU process (§1.2.1) and for modeling uncertainties in Chapter 2 and automatic data-based regularization traction force microscopy (§3.2.4) by extending the classical framework (§1.3.1) in Chapter 3.

1.3.3 Bootstrapping

In cases where the data generating model is not known or too complex to model, bootstrapping (introduced by Efron [55]) is a general computational method to obtain measures of statistical accuracy (i.e. approximate posterior distribution moments). The basic tenet is to randomly sample data with replacement from the dataset assuming independence of the elements. When done B times, a different dataset is obtained (with repetitions). The parameter is estimated for each of the B bootstrap iterations ($\{\theta_B\}$) and any statistical quantity of interest is obtained. This pertains to a Monte-Carlo estimate of the statistical properties (e.g. Variance) under sampling from the empirical distribution for the limited dataset. Compared to the Bayesian methods, the bootstrap distribution approximates the posterior distribution with non-informative priors and Gaussian likelihood [56]. Bootstrap method approximates by perturbing the data instead of perturbing the parameters in a Bayesian framework without the knowledge of the data generating model. Bootstrapping of image pixels PIV uncertainty quantification is adapted in Chapter 3.

1.4 Measurement of micro and nano-scale mechanics

The ability to study mechanics of biological entities in a myriad of mechanically distinct environments require tools that can reproduce the physiologically relevant mechanical and bio-chemical complexities exhibited in vivo [6]. Pioneering studies relied on specialized equipments such as Atomic Force Microscopy (AFM) [57], micropipette aspirations [58], cell stretches [59] and optical/magnetic tweezers [60] that locally probe cells as well as measuring local rheology. These methods have excellent spatio-temporal resolution, probe specific surface receptors or proteins but are usually low-throughput, requires highly specialized equipment and is typically limited to samples on 2D cultures.

Recently, optical imaging-based mechanical assays has been increasingly adapted in laboratories because of the accessibility and compatibility with a wide range of experimental conditions. Broadly, these methods fall into one of the following categories : 1) Traction Force microscopy measuring cell-applied traction stresses on the micro-environment (External forces), 2) Molecular tension probes measuring tension within a specific protein complex (Internal or external forces), 3) Intercellular tension inference to quantify tissue-level stress and mechanical properties (Internal forces).

1.4.1 Traction force microscopy

Traction Force Microscopy (TFM) describes methods that measure forces exerted by the cells on their surrounding substrates. Pioneering work by Harris and colleagues confirmed

the exertion of forces on thin silicon sheets [61], whose wrinkling qualitatively visualized the deformations. Since then, various strategies have been employed to quantify these traction stresses [33, 35–37, 62]. More generally, TFM refers to the use of continuous gel substrates typically made of polyacrylamide (PAA) or polydimethylsiloxane (PDMS). The most common application measures the in-plane and out-of-plane traction stresses on a continuous, planar elastic substrate by imaging gel embedded fluorescent beads with and without the application of the cell-exerted stresses. The displacement of the fluorescent beads are measured using image registration based methods such as Particle Image Velocimetry (PIV, see §1.4.2,3.2.2), optical flow [63], etc. Next, the traction stress calculations rely on inverting a mathematically ill-conditioned equilibrium equation (§3.2.3) that is of the form (restated here from eqn (1.8)) :

$$\boldsymbol{u}_{\mathrm{h}}(\mathbf{x}) = \int \mathbf{G}(\mathbf{x}-\mathbf{x}')\boldsymbol{t}(\mathbf{x}')\mathrm{d}\mathbf{x}', \tag{1.19}$$

where $\mathbf{G}$ is the Green's function of the elastostatic equation for isotropic elastic substrates. The linear system of equations $\boldsymbol{u}_{\mathrm{h}} = \mathbf{M}\boldsymbol{t}$ (§1.3.1) where the linear transformation $\mathbf{M}$ is the elastic response operator. $\boldsymbol{u}_{\mathrm{h}}$ and $\boldsymbol{t}$ can be two- or three- dimensional vector fields and h can be finite or infinite [33, 36, 37, 47, 64–66]. As a starter, TFM methods require only an epifluorescence microscope and methods utilizing Fast Fourier Transform (FFT) [33, 37, 47] perform calculations almost instantaneously. TFM methods are compatible with high-throughput genetic screens [22], extended live imaging and can measure sub-cellular force resolution [67]. The major limitations of TFM are the susceptibility to noise in deformation measurements, which is tackled with ad-hoc regularization or data filtering ([47, 52, 68], §3.4). The lack of a posteriori confidence estimates due to input and model uncertainties across different implementations make the interpretation and validation not trivial for the wider scientific community [35]. Recent efforts utilizing Bayesian models with neural network approximations [69] or linear Gaussian models [49] show promise for principled regularization and uncertainty quantification.

Traditional TFM methods require imaging stress-free state by cell lysing or detachment. Reference-free TFM methods avoid such terminal perturbations by inferring the relaxed state using microfabricated micropillar arrays [70] or printing lattice optical markers ([71–73],§1.3.1). Micropillars were favored initially as they are independent of each other and so the stresses can be directly calculated based on elastic cantilever bending. Reference-free methods can output live reading of tractions as well as allow correlative measurement with other techniques. However, they generally require specialized fabrication processes or can induce artificial adhesion topologies (in case of micropillars). This concept has been applied to measure traction stresses in vivo by photobleaching optical markers [74], though this

implementation requires validation of rheology assumptions.

An extension of TFM to finite volume substrates is the use of deformable hydrogel-based force sensors [75–77] to study local stresses *in vivo*, phagocytosis and immune cell extravasation [78]. By tracking embedded fluorescent beads [76], diffusion of tracers [77] or membrane shape changes [75], the internal stress tensor within the microsphere can be recovered with Finite Element Method (FEM) analysis. The above methods requiring 3D deformation measurements necessitate finer z-resolution imaging, usually with a confocal microscope.

1.4.2 Quantitative measurement of bulk motion - Particle Image Velocimetry

The deformations of the cytoplasmic markers and/or the substrate (embedded markers, $\boldsymbol{u}_{\mathrm{h}}$) (Fig 1.2 A) are measured using Particle Image Velocimetry (PIV), a quantitative imaging technique based on image correlation [79, 80] between the image of interest (Session image) with a reference image. Most common implementation of digital PIV dissects an image into overlapping rectangular sub-domains centered at (i, j), $\mathbf{W}_{ij}$ (interrogation windows) and compares with the corresponding sub-window in a reference image. Digital PIV performs template matching of each of the sub-windows by translating the reference sub-window and finding the most likely displacement vector. This procedure relies on sufficient information (markers that capture motion) in each sub-window of an image, hence parameters such as sub-window size and spacing between sub-windows affect the effective resolution of the motion captured (Fig 1.2 B).

Typically, PIV uses square interrogation window of size W_L separated by a constant distance of W_S across the entire analyzed image. As a general rule, the window size is chosen to be a power of two, since FFT algorithms show an increased performance at those array sizes. Choosing the right number of multi-pass steps and interrogation windows depends on several factors such as the signal-to-noise ratio of the image, the autocorrelation length of the optical tracers, the magnitude and gradients of the displacement field to be resolved, and on the spatial resolution of the imaging system [80]. It is customary to set the window spacing as a fraction of window size, with $W_S = W_L/2$ providing the optimal trade-off between computational cost and the effective spatial resolution based on the Nyquist principle. Decreasing the window length W_L improves displacement field resolution, however, this mostly likely is accompanied by increase in noise and discontinuities if the window doesnot contain any tracers in them (Fig 1.2 B). This is particularly evident for sparse fluorescent tagging with cytoplasmic or membrane markers, while substrate fluorescent beads are more amenable to higher resolution analysis. Note that the measured displacement field is tightly linked to the signal-to-noise ratio and the contrast of the tracers in the acquired images.

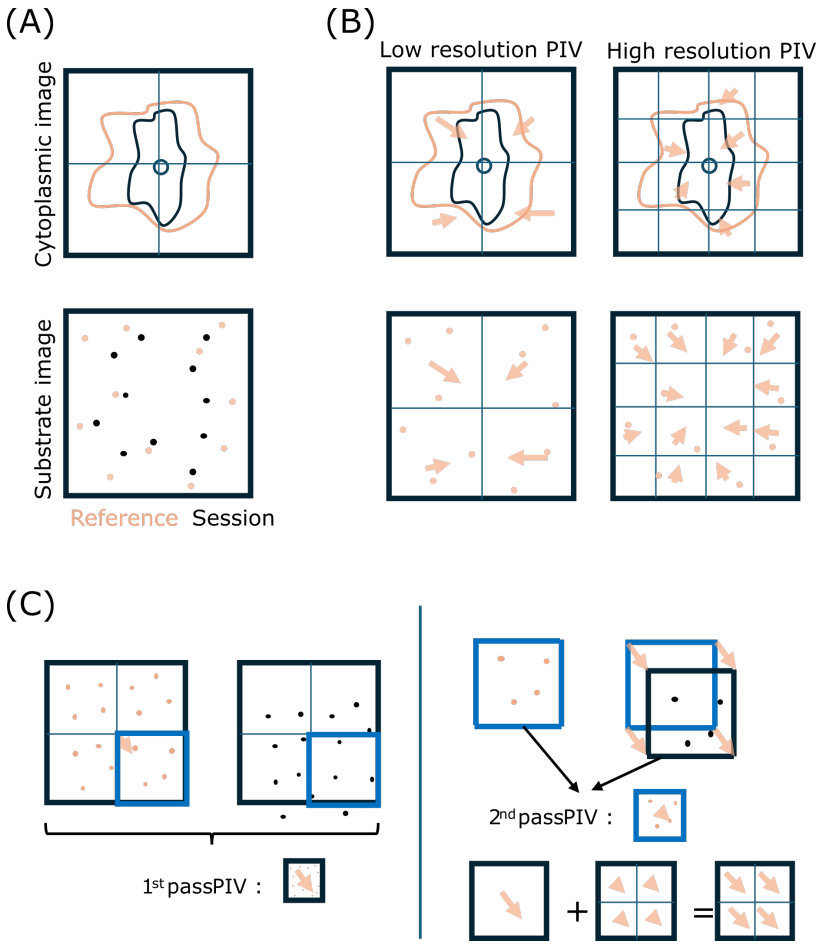

Fig 1.2. Schematic of Particle Image Velocimetry principle and multi-pass capabilities. (A) Illustration of reference and session image overlaid to show motion. PIV can be applied to cytoplasmic images such as cell membrane staining by WGA and mitochondria by MitoTracker, or compliant substrate images embedded with fluorescent beads. (B) PIV analysis at two resolutions by choosing a larger or smaller sub-window. In the low resolution analysis for cell membrane motion, all windows have a displacement estimate, but some windows either donot have any markers or markers move out of the window. Densely seeded fluorescent beads surpass this issue and are amenable to higher resolution analysis. Note that displacement field of simultaneously acquired cytoplasmic and substrate images donot have to be the same since the actual motion can be different. (C) Illustration of Multi-Pass methodology. In the left panel, an example of finite beads undergoing large displacement leading to loss of tracer information in higher resolution. A first pass is performed with lower resolution and the displacement estimate is used to translate the higher resolution session windows to compensate for tracer loss. Non-overlapping windows shown for clarity.

For the same displacement field, different image modalities such as bright field, fluorescent cell tags or substrate embedded beads are not expected to produce equal results (e.g. a saturated image region with maximum intensity will not show any movement).

The result of the cross-correlation presents a maximum at the most likely displacement vector of the image markers for each interrogation window - either the fluorescent beads embedded in the gel, fluorescently labelled membrane or organelles such as mitochondria, or textures from bright field image. If the displacements in the video are large, a significant amount of the tracers within a certain interrogation window can move out of that region, causing a loss of cross-correlation and yielding spurious measurements. Multi-pass PIV algorithm [81] overcomes this limitation in resolution by employing progressively smaller windows, whose in-frame location is shifted by an amount determined in the previous step (Fig 1.2 C). In the first pass, standard PIV analysis is executed, with a window size at least twice in size of the expected magnitude of displacements. Next, a second pass of PIV is executed with a smaller window size, but this time the smaller interrogation windows are offset by the amount that the first PIV displacement yielded. In essence, that offset roughly removes the effect of tracers going out of frame, hence avoiding a loss of cross-correlation.

1.4.3 Molecular force sensors

The use of molecular force sensors utilizing a donor-receptor fluorophores attached on either side of a short peptide sequence allows molecular scale force quantification [6, 82]. The fluorescence intensity reports the elongation by Forster Resonance Energy Transfer (FRET) principle and can be converted to tension readout after careful calibration. FRET sensor pairs are calibrated such that the donor-acceptor pair is quenched under relaxed state. Under tension, the fluorescence is increased inversely proportional to the distance between the FRET pair. In addition, the sensors can be expressed genetically [83], synthetically functionalized to a substrate [84] or on microsphere droplets [85]. FRET sensors can also be expressed in vivo [83], is non-invasive and can measure tension in a specific protein complex such as focal adhesions (cell-substrate forces [84]) and cadherin junctions (cell-cell forces [83]). FRET sensors measure tension magnitude only, require technical calibration, are prone to photobleaching and susceptible to chemical interactions in cytoplasm [86, 87]. An alternative is the use of well-calibrated synthetic DNA duplexes with a discrete on-off behaviour that can be tethered to a substrate [6, 86]. DNA hairpin based sensors have also been manufactured with FRET sensors so that the tension can be visualized in a continuous manner. Such sensors provide real-time tension measurements, but the sensors need to calibrated and work only in the designated range. Combining molecular sensor readouts with other methods opens the door to enhance the force measurements which is

otherwise not possible [88].

1.4.4 Internal stress measurement and rheology of tissues

At the scale of few cells and tissues, continuum mechanical models have been successfuly applied to infer the internal stresses sustained by the tissues (§1.2.2). Such monolayer tension inference, by enforcing continuity of forces across the cell-substrate interface with the measured traction stresses, provides a readout of internal stress tensor within the tissue [41, 82]. Monolayer Stress Microscopy (MSM) pioneered this calculation assuming an elastic thin-plate [65, 89], while recent efforts using either Bayesian methods [51] or particle simulations [90] dispense with the rheology assumption. With an improved 3D MSM method, it has been observed that the z-directed forces impart significant bending contribution to the monolayer tension [91]. Intercellular stress recovery methods incorporate several modeling assumptions, restricted to in vitro cultures and the propagation of noise in the traction stress can be significant [89]. Experimental alternatives include laser ablation of cytoskletal or junctional proteins providing relative tension estimates.

The use of continuum models to describe the interaction between the cells and the substrate allows specifying closed set of equations that relates the cell motion to the substrate deformation (§1.2.2 ,[39]). On short timescales, it has been observed that tissues behave elastically dominated by cortical tension and elasticity of the cytoskeletal components such as actin and intermediate filaments [92]. On longer time scales such as migration, tissues have been observed to behave viscous due to cell-cell rearrangement and cytoskeletal relaxation [93]. More generally, tissues are considered as viscoelastic in nature [92]. Specialized cells such as cardiomyocytes that can produce about 100 nN [94] in short interval of time show viscous relaxation in the contractile cycle that has shown to be microtubule dependent [95].

1.5 Overview of the dissertation

The remainder of the dissertation is organized in the following four chapters:

Chapter 2 presents the studies of stochastic leukocyte migration in 3D interstitial space. The interplay between matrix deformation by traction forces and the turning behavior of neutrophils in efficient chemotaxis is investigated using experimental measurements and a turning model based on a simplified OU process. Then, a computational pipeline to determine heterogeneity in random walk characteristics based on single cell trajectories is described. This method enables the identification of naturally occurring heterogeneity in model cell line and primary leukocytes. The enrichment of a sub-population or shift in

the migratory landscape is observed after physiological processes such as transendothelial migration or pharmacological manipulation of actin nucleators.

Chapter 3 describes the Traction Force Microscopy Uncertainty Quantification (TFM-UQ) methodology that models the uncertainties in the TFM framework. This method estimates the measurement uncertainty associated with the image quality and cell-generated forces, incorporating the variability in the regularization of the recovered traction stresses. The displacement error is first estimated using a new bootstrap method and is propagated to the traction stresses by using a Bayesian framework. The error bounds for the magnitude and direction of traction stresses in space and time of an experiment are investigated showing the dependence on the prior distribution form in the regularization framework. TFM-UQ utility in selecting optimal parameters in regularization, but also in deformation estimation is demonstrated with fibroblast data. TFM-UQ quantitatively identifies the trade-off between the measurement resolution and the noise. Application to endothelial monolayer data shows the capacity of TFM-UQ to identify image artifact-based errors. Chapter 4 applies the Bayesian framework to reference-free TFM estimate to resolve traction forces with sub-cellular resolution.

Chapter 5 describes a high-throughput, non-invasive contractility and elasticity inference method based on timelapse videos of cardiomyocyte contractility. A closed biomechanical model that relates the cellular strain to the substrate deformation based on the Traction Force Microscopy experimental setup is developed. Using timelapse videos, a strong correlation between substrate motion and cellular motion is observed which leads to additional constraints on the model. The passive elasticity parameters are fitted using he deformation field assuming pure elastic response between diastolic and peak systolic state. Benchmark compounds including Omecamtiv Mecarbil and Mavacamten are used to test the computational framework.

Finally, chapter 6 summarizes the contributions of this dissertation and provides future directions.

Chapter 2

INVESTIGATION OF LEUKOCYTE MOTILITY CHARACTERISTICS IN 3D INTERSTITIAL SPACE

2.1 Introduction

Leukocyte migration from the bloodstream to sites of injury or infection is a primary component of innate immunity and inflammatory responses. The circulating leukocytes mount a rapid response to pro-inflammatory stimuli by adapting a very motile yet flexible migration modes to navigate efficiently through a range of complex environments such as endothelial monolayers, basement membranes and interstitial spaces (Fig 2.1). This response requires tightly regulated morphological transformations that include tethering and migrating on the endothelium lining the vasculature, traversing across the endothelium and basement membranes, as well as translocating the cell body embedded within the ECM (Fig 2.1 A).

Among these mechanically distinct environments that the leukocytes encounter, the process of transendothelial migration (TEM) penetrating through the vascular endothelium cells (VEC) is one of the key rate-limiting steps. Mechanical forces are shown to be crucial in determining the site of leukocyte transmigration [78, 96]. Leukocytes probe the underlying VECs by extending protrusions to identify the path of least resistance [97] and translocate through the tight junctional gaps by exerting active forces (Fig 2.1 B). TEM is facilitated by leukocyte-VEC interaction via cadherin, platelet/endothelial-cell adhesion molecule (PECAM1), ICAM, and other surface receptors (Fig 2.1 B, [98]). While the surface receptor expression is well characterized during TEM, the effect of TEM on downstream interstitial migration is poorly understood [82].

Once in the interstitial space, the importance of leukocyte ability to correct their migration path following chemotactic, Galvanotaxis and other cues within the complex 3D environment has been the subject of many investigations both experimental [99–102] and theoretical [26, 103]. Of note, spatially varying ECM complexity requires a diverse migratory strategies by altering contractility, directionality and migration speed [29] to overcome varying level of deformable obstacles. Unlike cancer cells, neutrophils *in vivo* do not exclusively rely on matrix metalloproteases for penetration in collagen matrices, but have been observed to slow down and push around obstacles [104]. This relationship between external gradient sensing and physical deformation of the matrix is not well understood in the context of interstitial leukocyte migration.

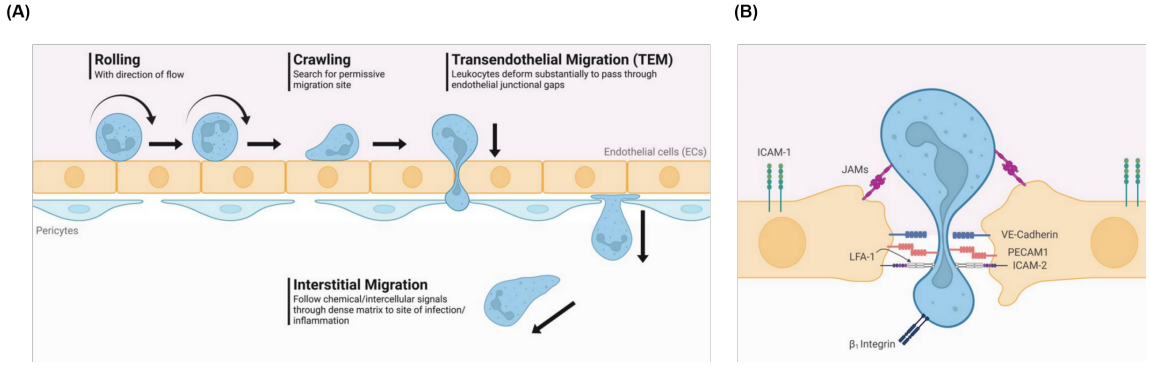

Fig 2.1. Leukocyte migration to the point of inflammation. (A) Circulating leukocytes undergo rapid arrest to the bed of vascular endothelial cell (VEC) by tethering followed by rolling in the direction of the flow. It is followed by rapid arrest and activation of leukocyte accompanied by changes in morphology to a migratory state in search of permissive states for extravasation through the VECs. Once past the basement membrane, leukocytes find their path following an external signal gradient (e.g. chemotaxis). (B) Molecular players and surface receptors during TEM process.

Efficient extravasation and interstitial migration are also important for adaptive immune function such as the ability of T-cells to patrol for antigen-presenting cells in peripheral and lymphoid tissues [105, 106]. Both neutrophil and T-cell infiltration into interstitial space is required for infection clearance, dysfunction of which can lead to autoimmune diseases such as Type 1 diabetes and multiple sclerosis [107]. Mammalian immune cells utilize several migratory modes which includes blebbing, mesenchymal crawling and amoeboid migration [108, 109]. Two main mechanisms are identified for efficient manuevers : front protrusions and rear contractions [105, 110]. Such an highly dynamic actin cytoskeleton in neutrophils are regulated by several actin effector proteins such as Arp2/3 complex [111], non muslce myosin-II [112]. It is not clear how either of these family of proteins affect efficient directed migration in different collagen matrix densities. Similarly in T-cells, formins are a family of linear actin growth mediators, highly expressing formin-like 1 (FMNL1) [113] and mammalian diaphanois-related formin 1 (mDia1) [114]. FMNL1 and mDia1 individually have been shown to be important for T-cell migratory function. While the individual actin effectors are studied in detail, the coordination between different actin nucleators to navigate restrictive spaces is not well understood.

Furthermore, leukocytes show appreciable cell-cell variability in migratory characteristics [82]. This is evident by the failure of random walk models to predict experimentally observed features such as double exponential decay of Velocity Autocorrelation Function (VAF) at the population level [29]. The incidence of sub-populations with different motility states can cause averaging across sub-populations (e.g. actin polymerization factors preferentially

affecting a sub-population of cells). With the availability of extensive spatial-temporal data of both single cell trajectories and deformation of ECM from large number of cells, computational analysis can be used to compare and fit theoretical models (§1.2.1), and are powerful in understanding the heterogeneous migratory modes without bias using statistical methods (§1.3.2).

In this chapter, the mechanical behavior of leukocytes in restrictive interstitial collagen space is discussed for neutrophils and T-cells. First, the coordination of mechanical forces and turning behavior in neutrophils necessary for efficient chemotaxis is studied using numerical simulations, cell trajectory and matrix deformation analysis (§2.4). Next, a statistical framework is developed to quantify phenotypically distinct migratory sub-populations from trajectory data in an unbiased manner(§2.5). This tool is employed to identify naturally occurring sub-populations of neutrophils migrating in 3D collagen matrices. The changes in these identified neutrophil migratory population landscape due to transendothelial migration (TEM) is studied next. Finally, the role of FMNL1 and mDia1 in modulating T-cell migratory sub-populations is presented (§2.6). These studies highlight the utility of the developed statistical and computational framework to identify population-level heterogeneity and quantification of migratory phenotype of individual cells.

2.2 Methods

This section describes the theoretical and computational models utilized to study leukocyte migration and contractility. First, a leukocyte chemotaxis model is described that is based on a biased random walk (§2.2.1). Leukocyte contractile moments of matrix deformation (measured with Particle Image Velocimetry, §1.4.2) are employed to determine the ability of cells to physically overcome obstacles (§2.2.2). Finally, an unbiased random walk clustering framework to identify multi-modality in migratory phenotypes is described (§2.2.3).

2.2.1 Leukocyte turning model

To investigate the dynamics of turning of the chemotaxing leukocytes, we constructed a biased random walk model [26]. The theoretical cell migration model describes cells with velocity magnitude V, moving in a chemotactic field with source at $y \to \infty$. The angle made by the velocity vector with the y axis (chemotactic direction) is denoted as θ. This model is a simplification of Eqn (1.1) with constant velocity and an additive bias term proportional to deviation from chemotactic alignment ($\sin\theta$) as given by the following stochastic differential equation :

$$\mathrm{d}\theta(t) = -\gamma_T \sin\theta(t)\mathrm{d}t + \Gamma(t)\mathrm{d}t, \tag{2.1}$$

where γ_T represents the response frequency (i.e., inerse timescale) to correct the misalignemnt in a chemotactic field. The stochastic function $\Gamma(t)$ denotes the fluctuations in the turning response to model turning events to circumvent obstacles in the 3-D matrix, imperfections in the chemotactic signal transduction, and the inherent stochastic activity of the cell. We assume white noise for fluctuations, i.e.,$\Gamma(t)\mathrm{d}t = \sqrt{\gamma_p}\mathrm{d}\tilde{W}_t(t)$, where $\tilde{W}_t$ is the standard Wiener process with Normal distribution, $\mathrm{d}\tilde{W}_t = \sqrt{\mathrm{d}t}\mathcal{N}(0,1)$. The migratory persistence of the cells is quantified by γ_p, which is a frequency that characterizes the width of the chemotactic angle (θ) distribution. The evolution of such distribution, $p(\theta,t)$ is governed by the associated Fokker-Planck equation:

$$\frac{\partial p(\theta,t)}{\partial t} = \frac{\partial}{\partial \theta}\left[\gamma_T \sin\theta(t) p(\theta,t)\right] + \frac{\gamma_p}{2}\frac{\partial^2}{\partial \theta^2} p(\theta,t). \tag{2.2}$$

Scaling the timescale of the evolution equations with the persistence parameter, $\tau = t\gamma_p/2$, we obtain the following non-dimensional system:

$$\mathrm{d}\theta(\tau) = \lambda\theta(\tau)\mathrm{d}\tau + \sqrt{2\mathrm{d}\tau}\mathcal{N}(0,1), \tag{2.3}$$

$$\frac{\partial p(\theta,\tau)}{\partial \tau} = \frac{\partial}{\partial \theta}\left[\lambda \sin\theta(\tau)\right] + \frac{\partial^2}{\partial \theta^2}(\theta,\tau), \tag{2.4}$$

where the non-dimensional parameter $\lambda = 2\gamma_T/\gamma_p$ is a key non-dimensional parameter that quantifies the ratio between the frequencies of biased and random turning. Following [26] for a similar system, the stationary solution to the Fokker-Planck equation is written as,

$$p_{st}(\theta) = \frac{e^{\lambda\cos\theta}}{\int_0^{2\pi} e^{\lambda\cos\theta}\mathrm{d}\theta}. \tag{2.5}$$

Using Schienbein *et al*'s defintion of order parameter, we characterize the turning response curve of leukocytes with chemotactic order parameter defined as,

$$< \cos\theta >= \int_0^{2\pi} p_{st}(\theta)\cos\theta \mathrm{d}\theta = \frac{I_1(\lambda)}{I_0(\lambda)}, \tag{2.6}$$

where I_0 and I_1 are modified Bessel's functions. For the case of constant velocity magnitude V, temporal and spatial scales cane be trivially interchanged given that $\Delta s = V\Delta t$, and the dimensionless parmeter λ can be experesed as $2\frac{\gamma_T}{\gamma_p} = 2\frac{S_p}{S_T}$, where S_p is the persistence length of the cell's trajectories and S_T is the lengthscale of biased turning, which is closely related to our experimentally determined S_θ.

2.2.2 Three-dimensional matrix incremental deformation fields and matrix deformation moments

We computed the incremental changes in 3-D deformation fields inside our collagen matrix gels, $\mathbf{v}_m = (u, v, w)_m$, by using a multi-grid Particle Image Velocity (PIV) (§1.4.2, [115]) that was an amended version of a previous in-house 3-D PIV algorithm [34]. Briefly, a first PIV pass was performed on each confocal stack of fluorescently labeled beads using the stack from the immediately preceding time point as a reference. An interrogation volume of $56 \times 56 \times 24$ pixels with a spacing of 28, 28, and 22 pixels respectively, was chosen during this pass. PIV was ran again using interrogation volumes of $28 \times 28 \times 22$ pixels with a spacing of 14, 14, and 11 pixels, respectively. During the second pass, the smaller interrogation windows of the reference stack were shifted by the displacements calculated in the first pass. This resulted in a 3-D deformation field that captured large deformations with the relatively large interrogation volumes in the first pass, while also achieving higher spatial resolution from the smaller interrogation volumes used during the second pass [91]. Visualizations of the 3-D cell shapes was constructed and incremental deformation fields by creating Visualization Toolkit (VTK) files, which we imported into the open source software Paraview [116] for 3-D visualization.

To quantify a cell's ability to deform the matrix, we expanded Butler *et al.*'s concept of contractile moment to three dimensions and determined the first-order moments of $\mathbf{v}_m$ [37]. Using the 3-D cell shape data from confocal stacks of fluorescently labeled cells, the cell centroids ($\mathbf{x}_C$) were calculated and a region of interest was defined around each cell, $R : (10\,\mu\text{m} < |\mathbf{x} - \mathbf{x}_C| < 200\,\mu\text{m})$, to calculate the matrix deformation first-order moment tensor,

$$\mathbf{M} = \int_R \mathbf{x} \cdot \mathbf{v}_m^T \mathrm{d}\mathbf{x}. \tag{2.7}$$

The diagonal elements of $\mathbf{M}$ provided the total contraction or extension of the collagen gel around individual cells, in each ordinate direction between two consecutive timepoints ($\Delta t = 0.5\,\text{min}$). The net 3-D matrix deformation moment displacing the collagen gel was given by $\text{tr}(\mathbf{M})$. Note that $\text{tr}(\mathbf{M}) > 0$ indicates that the matrix is being deformed away from the cell, whereas $\text{tr}(\mathbf{M}) < 0$ indicates that the matrix is being deformed towards the cell. The matrix deformation moment tensor was projected along the directions parallel and perpendicular to the chemoattractant gradient, and the mean absolute values of these projections, $|\mathbf{M}_{\parallel}|$ and $|\mathbf{M}_{\perp}|$, were quantified. Finally, the time-averaged absolute quantity $\langle \text{tr}(\mathbf{M}) \rangle$ represented a concise metric for gauging cells' ability to incrementally deform surrounding extracellular matrix fibers.

2.2.3 Unsupervised identification of heterogeneous sub-population from the random walk characteristics

To facilitate a nuanced analysis of the population-level changes in migratory state (i.e. the random walk parameters), an unsupervised, two-step clustering algorithm that identifies heterogeneous motility modes within a cell and across all experimental conditions is employed.

Time-dependent Bayesian sequential inference of heterogeneous random walk

A 2D first-order, auto-regressive process was used to model the persistent random walk of individual cells with time-varying motility parameters. The time series of the velocity vector of an individual cell, $\{\mathbf{v}_1, \ldots, \mathbf{v}_{t-1}, \mathbf{v}_t, \mathbf{v}_{t+1}, \ldots, \mathbf{v}_{N_t-2}\}$, was numerically differentiated with 2^{nd} order finite differences, where N_t is the number of images in the timelapses (equivalently the number of spots in a trajectory). Adapting the methodology of [30], the stochastic change in the velocity of a cell given the previous time step is described by the time-discrete stochastic process,

$$\mathbf{v}_t = q_t \mathbf{v}_{t-1} + a_t \mathbf{n}_t. \tag{2.8}$$

Here $q_t \in [-1, 1]$corresponds to the local persistence of the random walk, $a_t \in [0, \infty)$ represents the local activity (stochastic amplitude) that sets the spatial scale of the random walk and $\mathbf{n}_t$ represents an uncorrelated normally distributed noise with unit variance. The persistence q_t is a measure of the directional correlation between the successive time steps, not necessarily in the direction of the chemotactic gradient. $q_t = 1$ corresponds to a straight line and $q_t = 0$ to a non-persistence Brownian diffusion. Higher values of a_t correlate with increase in metrics such as cell speed, total displacement and track length. Together, the activity and persistence parameters determine the variance of displacement steps within a cell track according to $\mathrm{Var}(\mathbf{v}) = a^2/((1 - q^2))$ independently in each coordinate. Bayesian sequential inference (adapted from [30]) was performed in MATLAB to estimate the time-varying heterogeneous migration parameters of an individual cell.

Semi-unsupervised identification of heterogeneous sub-populations in migrating T-cells with K-means clustering

This method of classification with K - means clustering is suitable for smaller dataset with more circular desnities. Each migrating cell (tracked for at least 240 s) is characterized by the average random walk parameters (q, a) of persistence and activity obtained from sequential Bayesian inference [30]. These parameters represent the average motility state

of the migrating T-cell in relation to a persistent random walk model. The density-based clustering `DBSCAN` algorithm [117] was used to detect outliers. K - means clustering was employed to detect clusters in the (q, a) parameter space of all cells. Using silhouette width [118] as a reference guide and bootstrapping as a measure of stability [119], $k = 4$ was selected for k-means clustering in §2.6. The mean silhouette scores for $k = 2, 3, 4$ were comparable, indicating that similar clustering accuracies would be obtained by allocations containing 2, 3 or 4 clusters. However, inspecting the probability distributions of (q, a) (Fig 2.10 B-G) indicated that $k = 4$ clusters reflected these distributions optimally across different conditions by identifying a $(\uparrow a \uparrow q)$ sub-population, a $(\downarrow a \uparrow q)$ sub-population, and two $(\downarrow a \downarrow q)$ sub-populations, one of which consisted of essentially non-motile cells. Therefore, each cell was assigned to one of the 4 clusters that minimized the Euclidean distance to the cluster centroid, cells belonging to either one of the two $(\downarrow a \downarrow q)$ sub-populations were merged into a single $(\downarrow a \downarrow q)$ sub-population, and the proportions of the three sub-populations: $(\uparrow a \uparrow q)$, $(\downarrow a \uparrow q)$, and $(\downarrow a \downarrow q)$, were reported. Bootstrap analysis was performed to assess the stability of the clustering solution [119], providing confidence intervals (t-statistic) for the proportion of cells belonging to each cluster. The bootstrap analysis resamples the data points (i.e. (q, a) average of a cell) with replacement and performs the clustering procedure described above. This bootstrap procedure was repeated 100 times.

Autonomous identification of heterogeneous sub-populations in neutrophil random walk parameters from large content imaging with GMM model

Each individual cell was analyzed for changes in the migratory state during the duration of imaging to avoid averaging over different motility modes. A density based spatial clustering (DBSCAN) algorithm [117] in MATLAB was employed to identify outliers and clusters in the inferred random walk parameters (q_t, a_t) within a single cell trajectory data. The parameter a_t for each cell was normalized to the range $[0, 1]$ for subsequent analyses. The parameters $\epsilon = 0.1$ and `minPts` $= 10$ was used for the DBSCAN algorithm. This procedure is termed *local clustering*. If more than one cluster was detected, they were treated as individual cells for further analysis. Each migrating cell's trajectory was characterized by the average random walk parameters $(\bar{q}, \bar{a})$ of persistence and activity after local clustering.

To automatically identify sub-populations and shifts in the sub-populations across all experimental conditions (e.g. control, pharmacological treatments, etc.), cell-averaged random walk parameters $(\bar{q}, \bar{a})$ were pooled together. A Variational Bayesian Gaussian Mixture Model (VB-GMM) was used to cluster in the parameter space of $(\bar{q}, \bar{a})$. A Gaussian mixture model has the advantage of identifying elliptical clusters with anisotropic variances and the

Bayesian formulation allows automatic inference of the number of clusters from the data. This step, termed *global clustering*, was performed to autonomously identify heterogeneous sub-populations based on the trajectory data alone.

VB-GMM clustering algorithm fits the datapoints in cell-averaged random motility parameter space with K Gaussian distributions delineating the densely populated regions ([120], Code adapted from `mixGaussVb.m`, MATLAB File Exchange. Note that there is an error in the posterior covariance matrix in the code). Briefly, GMM model assumes a mixture of K Gaussian clusters, each with a mean μ_k and precision matrix $\mathbf{\Lambda}_k$, such that the distribution of the cell-averaged random walk parameters $x_n = (\bar{q}, \bar{a})_n$ follows,

$$p(\mathbf{x}) = \sum_{k=1}^{K} \pi_k \mathcal{N}(\mathbf{x}|\mu_k, \mathbf{\Lambda}_k^{-1}). \tag{2.9}$$

π_k is the mixing coefficient, such that $\sum_{k=1}^{K} \pi_k = 1$ and $0 \leq \pi_k \geq 1$, controlling the proportion of each cluster. A symmetric Dirichlet distribution is chosen as the conjugate prior for π_k with the density,

$$p(\pi) = \mathrm{Dir}(\pi|\alpha_0) \propto \Pi_{k=1}^{K} \pi_k^{\alpha_0 - 1}. \tag{2.10}$$

The concentration hyper-prior α_0 controls the sparsity of cluster numbers and the influence of data on the inference of the number of components K. α_0 values closer to 0 impart a priori belief that prefers fewer clusters that is influenced by data and as $\alpha_0 \to \infty$, the posterior of $\pi_k \to 1/K$ (no sparsity). For this manuscript, $\alpha_0 = 1$ was used which produces a flat Dirichlet distribution letting the parameter K be determined only from the data. Such a flat distribution is advantageous when working with a large number of data points. For the parameters μ_k and $\mathbf{\Lambda}_k$, a conjugate Gaussian-Wishart prior is prescribed with zero mean. The variational inference of the GMM mean μ_k and precision matrix $\mathbf{\Lambda}_k$ as well as the number of clusters K is based on factorized approximation to the posterior distribution through a latent variable representation. The specific details of the inference method are omitted here, and the reader is referred to Bishop *et al* ([120] Section 10.2).

2.2.4 2D contour plot generation

The 3D persistent random walk parameter space is discretized in the domain $a \in [0, \infty)$ and $q \in [0, 1]$ encompassing the results of sequential Bayesian inference of heterogenous random walk. Each parameter (a_t, q_t) represents the random walk behavior describing two successive velocity vectors from a cell trajectory. All such pairs of parameters (a_t, q_t) within an experimental condition and collagen concentration is used as input to `histcounts2`

function in MATLAB to produce bivariate histograms. The resulting 2D histogram is plotted as 2D contour plots with three levels that contains 50%, 80% and 95% of the joint probability mass. 1D histogram projections of the corresponding variables are plotted to the top and the right.

2.3 Experimental methods

2.3.1 In-vitro 3D directed migration assay and collagen gel fabrication

A version of a previously published custom-built chemotaxis device was adapted to study 3-D neutrophil chemotaxis (Fig 2.2 A) [108, 121]. First, 25 mm glass coverslips (Fisher Scientific) were treated on one side with 250 μL of 0.1 M NaOH for 5 minutes. NaOH was removed and the coverslips were rinsed with distilled H_2O. The coverslips were dries and added with (3-aminopropyl) triethoxysilane (APTES, Sigma) to their treated sides afterwards. After 30 minutes, the coverslips were rinsed again with distilled H_2O and placed on Kimwipes^{TM} for air-drying, with the treated surfaces facing up. Next, a 12 mm diameter hole was punched in the center of 50×9 mm Falcon petri dishes (BD Falcon). The treated glass coverslips were attached to the bottom of the petri dishes with their treated sides face up using vacuum grease (Beckman Vacuum Grease Silicone). Separate treated glass coverslips were attached to the tops of the holes with their treated sides face down and covering most of the holes' diameters. This sandwiching of coverslips created a pocket that was used later to place collagen gel solutions. Before fabricating collagen gels, the devices were rested on top of a metal block that sat in a container filled with ice.

Collagen gels were fabricated by neutralizing solutions of rat-tail type-I collagen dissolved in 0.2 N acetic acid (Corning) with 1 N NaOH in proportions recommended by the manufacturer. A suspension of supplemented RPMI 1640 medium, instead of the recommended 10X PBS and water, containing 4.7×10^3 dHL-60 cells were added to the device. A 1.2% solution of fluorescent microspheres (Molecular Probes) was mixed with the collagen solution. While mixing the different constituents of the collagen gel, all solutions were placed in a small container filled with ice. After the collagen gel solution was made, 113 μL of the solution was pipetted into the pocket of each device and the devices were placed in an incubator at 37 °C and 5% CO_2 for 30 minutes. The devices were placead in an incubator vertically to allow the gel solution to settle to the lower half of the pocket. 113 μL of supplemented RPMI medium was added into the remnant volume of the pocket and the device was placed in the incubator for another 30 minutes. Finally, before imaging, the supplemented RPMI medium was replaced with either fresh supplemented RPMI medium or a 50 nM solution of N-formyl-L-methionyl-L-leucyl-L-phenylalanine (fMLP, Sigma-Aldrich). For experiments involving reflection microscopy imaging, collagen gels were fabricated in

the same manner as described above, leaving out the cells and fluorescent microspheres in the supplemented RPMI 1640 medium. 100 μL of the gel solution was placed on top of glass coverslips attached to the bottoms of petri dishes with 12 mm diameter holes. A second coverslip was not added on top of the holes. Eacg petri dish were placed in an incubator at 37 °C and 5% CO_2 for 30 minutes. Afterwards, these dishes were filled with 2 ml of supplemented RPMI 1640.

The collagen fibers were fluorescently labelled with 5-Carboxytetramethylrhodamine (TAMRA, ThermoFisher) by following a previously published protocol [122]. We first added 25 mg of TAMRA to a 2.5 mL solution of DMSO and stored at −20 °C in an Eppendorf tube. The Eppendorf tube was covered with aluminum foil to protect the solution from light. Next,a labeling buffer was made with 0.25 M $NaHCO_3$ and 0.4 M NaCl, and subsequently adjusted the pH to 9.5 by using a 10 M solution of NaOH. A 1 mL syringe was filled with an 8.46 mg/mL solution of rat-tail type I collagen in a 0.2 N acetic acid solution (Corning) and injected the solution into a 3 mL dialysis cassette. The cassette used had a 10 kDa molecular weight cutoff. Before retracting the hypodermic needle, air was removed from the cassette by pulling the syringe plunger up. An overnight dialysis was performed in a beaker containing a 1 L solution of the labeling buffer at 4 °C. 100 μL of the 10 mg/mL TAMRA solution was mixed with 900 μL of the labeling buffer, with both solutions at room temperature. After mixing, the TAMRA solution was placed in a 4 °C fridge. The collagen was removed from the cassette using a 2 mL syringe and 1 mL of the solution was mixed with 1 mL of diluted TAMRA using a pipette. The resulting solution was placed in a micro-centrifuge tube and incubated with rotation overnight at 4 °C. At this point, the collagen was labeled with the TAMRA dye and this mix was placed in a dialysis cassette and dialyzed it overnight at 4 °C against a 1 L solution of the labeling buffer. Finally, the TAMRA-labeled collagen was dialyzed overnight at 4 °C against a 0.2% acetic acid solution with a pH of 4. The final volume was useed to calculate the concentration of the TAMRA-labeled collagen.

2.3.2 Cell culture, differentiation and labelling

For neutrophil experiments, the model cells from the human promyelocytic leukemia cell line (HL-60, ATCC) were cultured and differentiated into neutrophil-like cells (dHL-60) as previously described [1, 123].Experiments were performed with dHL-60 cells 4 days after being cultured in the presence of DMSO (between 5 and 7 days). For experiments involving fluorescently labeled cells, day 4 differentiated dHL-60 cells were labelled with CellTracker Deep Red (Thermo Fisher Scientific) prior to mixing them with collagen solutions. Cells were incubated in a 10 nM solution of CellTracker in RPMI-1640 without FBS for 30 minutes at

37 °C and 5% CO_2. Afterwards, the cells were centrifuged and re-suspended in RPMI-1640 containing 10% FBS. Primary human vascular umbilical vein endothelial cells (HUVECs, Cell Applications) were grown at 37 °C and 5% CO_2 in Medium 199 with L-glutamine, 2.2 g/L sodium bicarbonate, and Earle's salts (M199, Gibco Thermo Fisher Scientific) supplemented with 10% v/v FBS, 10% v/v Endothelial Cell Growth Medium (ECGM, Cell Applications), and 1% v/v pen strep until they formed a confluent monolayer. HUVEC were passaged following standard protocols for adherent mammalian cells: spent culture medium was aspirated and cells were washed using Dulbecco's phosphate buffered saline without calcium chloride or magnesium chloride (DPBS, Gibco Thermo Fisher Scientific); wash solution was aspirated and replaced with the pre-warmed 0.25% trypsin-EDTA (Gibco Thermo Fisher Scientific); the plate was incubated at 37 °C and 5% CO_2 until at least 90% detachment was observed on an inverted microscope, at which point a volume of pre-warmed supplemented M199 equal to at least two times the volume of trypsin used was added to the plate and circulated by repeated pipetting to dislodge tenuously adherent cells; cells were collected via centrifugation, resuspended at the desired concentration in fresh supplemented M199, seeded in a situationally appropriate vessel, and incubated at 37 °C and 5% CO_2 at least twenty-four hours prior to next use. Experiments were performed using cells between 4 and 7 passages. For mouse primary T-cell experiments, FMNL1 KO mice and mDia1 KO mice were generated as described in [113] and [124] respectively. All mice were bred and housed at the University of Colorado Anschutz Medical Campus Vivarium. Formin KO mice were paired with C57BL/6 mice that were age and sex matched. Polyclonal T cells were harvested from C57BL/6 mouse superficial and mesenteric lymph nodes and activated using plate-bound anti-CD3 (2C11, BioXCell), soluble anti-CD28 (PV-1, BioXCell), and autologous splenocytes for two days. Cells were then removed from the stimulating antibodies and further cultured in RPMI (Corning) with 10% FCS, glutamine and antibiotics supplemented with 10 U/mL recombinant human IL-2 (NCI), refreshed every two days post-activation. On day four post-activation, dead cells were removed using a Histopaque-1110 (Sigma) gradient. Activated T cells were typically used for experiments on day 5 post-activation.

2.3.3 Transwell-based leukocyte treatment assay

Prior to loading, Transwell (TW) inserts with 3 μm pore polycarbonate membrane (12 mm insert, Corning) were incubated with 200 μL of 50 ng/mL] fibronectin (Millipore Sigma Aldrich) at 4 °C for at least twenty-four hours. The inserts were then washed twice with DPBS and equilibrated per manufacturer recommendation by incubating them at 37 °C and 5% CO_2 for twenty-four to forty-eight hours with 1 mL of fresh supplemented M199 in the

lower chamber and 500 μL in the upper chamber. Following equilibration, the medium in the lower chamber was replaced with 1 mL fresh supplemented M199 and the medium in the upper chamber was replaced with 500 μL HUVEC suspended at a concentration of 4.5×10^5 cells/mL in supplemented M199. Inserts were incubated at 37 °C and 5% CO_2 for thirty minutes, then washed with supplemented M199 to remove HUVEC that were not adhered to the polycarbonate membrane and incubated for twenty-four hours to form a confluent monolayer. The medium was then aspirated from the upper chamber and replaced with fresh M199 with 20 ng/mL tumor necrosis factor alpha (TNF-α) for at least eight hours to activate the HUVEC monolayer. Following TNF-α activation, medium in the lower chamber was refreshed, day 5 dHL-60 cells were resuspended in supplemented M199 and loaded into the upper chamber at a density of approximately 8×10^6 cells, and the inserts were incubated at 37 °C and 5% CO_2. After thirty-six to forty-eight hours, dHL-60 cells that had migrated through the HUVEC monolayer and the polycarbonate membrane of the *TW* support, termed *TW* treated cells, were collected from the lower chamber of the *TW* insert and resuspended in fresh supplemented RPMI-1640 at an appropriate concentration for further pre-treatment or use in experiments.

2.3.4 Imaging and trajectory capture

Bright-field images were obtained for neutrophil (dHL60) population migration experiments using an enclosed Leica DMI6000 B microscope with a 5X air lens at 37 °C and 5% CO_2. The microscope's magnifier was retracted to produce images that made automated cell tracking easier. In each experiment, four planes were acquired at 200 μm spacing in each collagen gel every $\Delta t = 30$ s for 1 hour.These four planes were imaged in order to follow a larger a number of cells with a z-spacing of 200 μm spacing to avoid imaging the same cells in more than one plane.

Automated cell tracking for standard time resolution experiments was performed using the Fiji plugin Trackmate [125, 126], discarding the first 50 frames of the time course for each experiment to eliminate migration artifacts caused by rapid gel drift. Cells were identified using a Laplacian of Gaussian (LoG) edge detection filter with median filtering enabled and frame linking was performed using a linear assignment problem (LAP) tracker. Final cell tracks were filtered based on quality and duration, then exported to MATLAB for bulk drift correction and further analysis. Drift velocity was calculated based on the bulk motion of non-motile cells within each experiment. Briefly, the first and second moments of inertia were calculated for each cell track, then used as the basis for selecting the 15% of the experimental population with the lowest overall motility. Visual inspection confirmed that these cells were non-motile, and the one-minute smoothed median velocities of the

non-motile population in each Cartesian direction were taken as the bulk drift velocity for the experiment. The drift velocity was then subtracted from each cell track within the experimental population to correct for bulk gel deformations during the experiment.

For neutrophil high-resolution single cell and matrix deformation, imaging was performed on an enclosed Zeiss LSM 880 Laser Scanning Microscope in the fast Airyscan mode, with a 40x water lens and 1.3x zoom. Two 80 μm imaging stacks were acquired with 0.7 μm spacing between planes every 30 seconds. The duration of time-lapse experiments varied depending on the time for the cell to exit the imaging volume. Given that dHL-60 cells are relatively fast-moving cells, imaging channels were switched for the labeled cells and microspheres per line scan during acquisition. This was to minimize significant differences in cell positions with respect to matrix deformations during the acquisition of the two stacks for a single time point. The raw Carl Zeiss Image (CZI) Airyscan output files from the Zeiss LSM 880 microscope underwent Airyscan processing using Zeiss's imaging software Zen Black. After Airyscan preprocessing, these files were loaded into FIJI [127] and then exported as uncompressed .TIFF files. The .TIFF files were loaded into MATLAB for further quantitative analysis.

For primary mouse T-cell *in vitro* confocal imaging experiments,a Zeiss LSM 800 Confocal Laser Scanning Microscope. For live cell imaging, samples were kept at 37 °C using a stage heater. Bulk motility experiments were captured using a 10X objective and high resolution single-cell analysis experiments were captured using a 40X water objective. Images were processed using ImageJ (NIH) and motility parameters were analyzed using Imaris software (Bitplane) to automatically track cells, followed by manual correction of tracking errors that resulted in broken tracks. Immobile cells with no cytoplasmic motion were assumed dead and removed from the analysis. The parameters quantified were mean track speed, arrest coefficient (% of timepoints a cell's instantaneous speed was less than 2 μm/min), and mean squared displacement. Data were filtered to include only cells tracked for at least 4 min. Mean track speed was also filtered to include cells with a minimum displacement of 15 μm. For experiments using para-nitroblebbistatin, tracks were filtered only by a minimum duration of 4 min.

2.4 The interplay between matrix deformation and the coordination of turning events govern directed motion in 3D matrices

We assembled a 3-D migration chamber using a well-established design (See §2.3.1 and Fig 2.2 A) [108]. We used type I collagen in our chamber because collagen is the extracellular matrix protein most commonly found in mammals and, specifically, type I collagen is the most common type of collagen [128, 129]. We used neutrophil-like dHL-60 cells differentiated

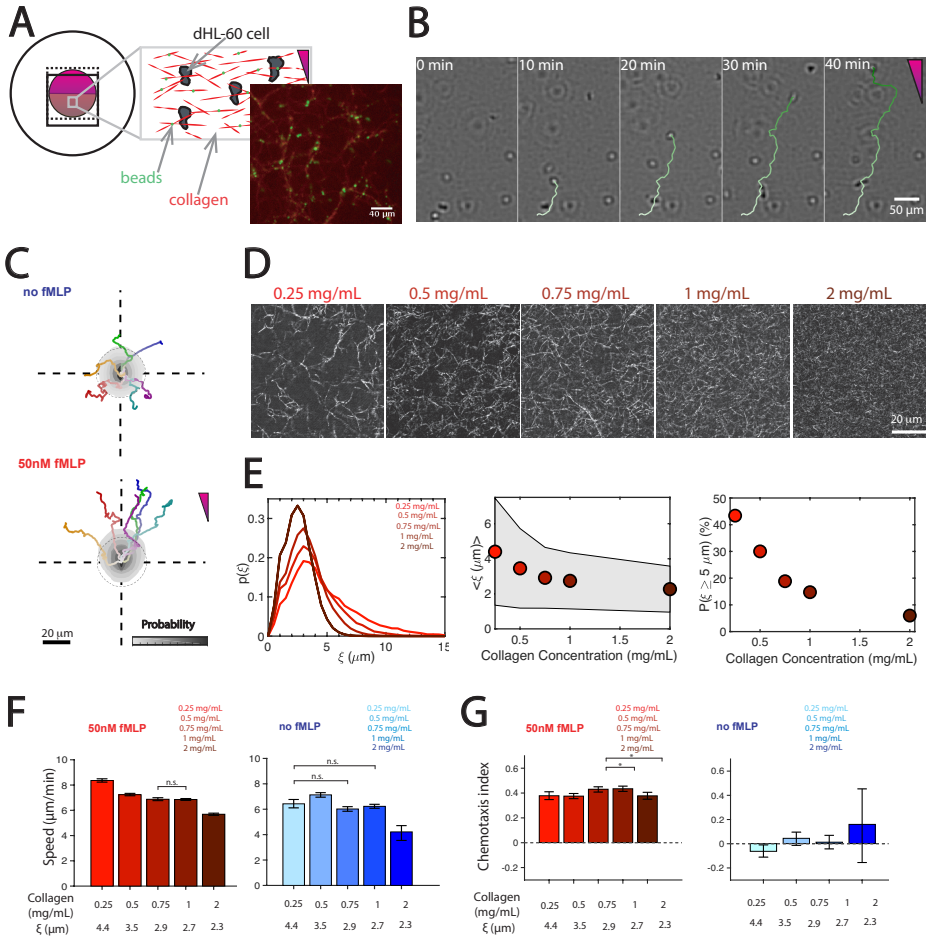

Fig 2.2. Neutrophil experimental setup and migratory statistics (A) 3-D migration chamber schematic with dHL-60 cells (gray) and fluorescent micro-beads (green) embedded in a collagen gel (red). Imaging fluorescently labeled collagen showed micro-beads localize to collagen fibers. (B) Image sequence of chemotaxing cell and tracked trajectory (green). (C) Probability density maps of cell coordinates (gray) and representative cell trajectories in the absence (top) and presence (bottom) of fMLP gradient (0.75 mg/mL collagen). Dashed circles represent unbiased random motion. In B-C, time progression along each trajectory is represented by increasing color saturation, and the fMLP gradient's direction is indicated by purple triangle. (D) Confocal reflection images of matrices with collagen concentrations [col] ranging 0.25 - 2 mg/ml. (E) Left: Probability distributions of matrix pore radii ξ from bubble analysis. Center: Mean pore size $\langle\xi\rangle$ vs. [col]. Right: Fraction of available pores with $\xi \geq 5\,\mu$m vs. [col]. (F) Mean cell speeds vs. matrix density (expressed as [col] or $\langle\xi\rangle$) in the presence (left) and absence (right) of fMLP gradient. (G) Chemotactic index vs. matrix density. Error bars represent 95% confidence interval. All pair-wise conditions showed statistically significant differences besides those labeled n.s. in (F). $*$ indicates $p < 0.05$ from Mann-Whitney U test.

from the human promyelocytic leukemia cell line (HL-60, ATCC). We used fluorescent microbeads attached to the collagen fibers to track matrix deformation (Fig 2.2 A, inset). We chose N-Formyl-L-methionyl-L-leucyl-L-phenylalanine (fMLP) – a small peptide secreted by bacteria after infection [130] – as a chemoattractant.

To study the kinematics of directed 3-D neutrophil migration with high throughput, we developed a fully automated algorithm to track cell trajectories from brightfield microscopy time-lapse sequences (Fig 2.2 B). Overall, we tracked 21,150 cell trajectories under different conditions. We confirmed that our system enabled directed neutrophil migration by performing experiments with and without the addition of fMLP. In both conditions, we mapped the probability density $p(x, y)$ of the cell coordinates in the directions parallel (y) and perpendicular (x) to the chemoattractant gradient (Fig 2.2 C). For illustrative purposes, we plotted the 6 longest trajectories, which were long enough to be representative of the qualitative features of cell paths in our experiments. In the absence of fMLP, the distribution of cell trajectories was symmetric, leading to circular contours in $p(x, y)$, as expected for random migration. In contrast, the chemoattractant gradient created by adding fMLP resulted in cell trajectories preferentially directed towards the chemoattractant source, with a $p(x, y)$ being markedly asymmetric and shifted towards the positive y-direction. These data confirm that our system recapitulated 3-D neutrophil chemotaxis, and that our cell-tracking algorithm was able to capture this process from brightfield microscopy, without the need for fluorescent labeling.

2.4.1 Collagen density affects the cell speed but not the chemotaxis of 3-D neutrophils

In physiological contexts, neutrophils must travel across diverse microenvironments. To study the effect of collagen density ([col]) on the ability of neutrophils to undergo directed migration, we fabricated gels with $0.25\,\mathrm{mg/mL} \leq [\mathrm{col}] \leq 2.0\,\mathrm{mg/mL}$. Varying collagen concentration has been previously shown to affect the matrix microenvironment, most notably its pore size[131–133]. Thus, we visualized the structure of our collagen gels (Fig 2.2 D) and quantified their distribution of pore radii (ξ) (Fig 2.2 E). This distribution became narrower and shifted to lower values of ξ with increasing [col] (Fig 2.2 E, left panel). In particular, $\langle\xi\rangle$ decreased monotonically from 4.4 to 2.3 μm when [col] was increased from 0.25 to 2.0 mg/mL (Fig 2.2 E, center panel). We took $\xi \sim 5\,\mu\mathrm{m}$ as an approximate value for the radius of dHL-60 cell nuclei [134] and calculated $p(\xi \geq 5\,\mu\mathrm{m})$ to assess the availability of pores through which cells could easily squeeze through without significant nuclear deformation. This calculation showed that the fraction of pores larger than $5\,\mu$m was over 40% in $0.25\,\mathrm{mg/mL}$ matrices, but it decreased to under 10% as the [col] increased to $2\,\mathrm{mg/mL}$ (Fig 2.2 E, right panel). Overall, these data highlight that the different collagen concen-

trations considered in our experiments allowed us to study 3-D neutrophil-like migration through microenvironments that ranged from non-restrictive to highly restrictive. Next, we were interested in how these different matrix microenvironments affected directed 3-D neutrophil migration. We found that cells migrated with mean speeds that decreased from $\langle v \rangle = 8.4\,\mu$min to $\langle v \rangle = 5.7\,\mu$/min as [col] was increased and $\langle \xi \rangle$ decreased (Fig 2.2 F, left panel). A similar dependence of $\langle v \rangle$ on $\langle \xi \rangle$ was observed for randomly migrating cells in chemotaxis devices without fMLP (Fig 2.2 F, right panel). In spite of migrating more slowly as [col] was increased, cells were still able to undergo directed migration towards an added fMLP source in all matrices investigated (Fig 2.2 G, left panel). This is in contrast to migration in chambers without fMLP (Fig 2.2 G, right panel). Overall, these results indicate that decreasing matrix pore size and availability has a marked effect on the migration speed of wild-type neutrophil-like cells, but not on their ability to perform chemotaxis.

2.4.2 3-D neutrophil migration requires turning but not mechanical forces to negotiate restrictive matrices

In addition to reducing pore size, increasing [col] from 0.25 to 2 mg/mL is known to cause significant matrix stiffening (i.e., bulk Young's modulus raised from 440 to 5200 Pa, [131]). Thus, we were interested in finding whether changes in [col] affected the mechanical interactions between neutrophils and their environment. To this end, we imaged fluorescently labeled, chemotaxing cells in our custom-made devices along with fluorescent micro-beads that were attached to matrix fibers. We used Airyscan confocal microscopy to image both the cells and micro-beads in 0.25 and 2 mg/mL collagen gels (Fig 2.3 A, left panel). Matrix deformations were evident in 0.25 mg/mL gels by comparing the location of beads at any given time-point (green) with that at the previous time-point (orange). The 3-D incremental matrix deformations $\mathbf{u} = (u, v, w)$ were quantified using PIV (Fig 2.3 A). Our measurements showed clear deformations in the 0.25 mg/ml matrices, with a magnitude ($\sim 3\,\mu$m) comparable to the cell nucleus size. These data suggest that, in addition to navigating the matrix searching for large pores, cells in low-[col] matrices are able to significantly deform and enlarge matrix pores (Fig 2.3 B). In contrast, cells in high-[col] matrices did not exert forces large enough to cause appreciable matrix deformations (Fig 2.3 C). These observations were confirmed by our statistical analysis of 3-D matrix deformation moments generated by neutrophils for [col] = 0.25, 0.75 and 2 mg/mL. By extension of Butler et al.'s two-dimensional definition [37], the matrix deformation moments were defined as $\mathrm{tr}(\mathbf{M})$, where the elements of the M tensor are the first-order moments of vector $\mathbf{u}$ in a sphere of 200 microns surrounding the cell (see eqn (2.7) in §2.2.2). The statistics of the absolute value $|\,\mathrm{tr}(\mathbf{M})|$ indicated a 2.5-fold decrease in matrix deformations between [col] = 0.25

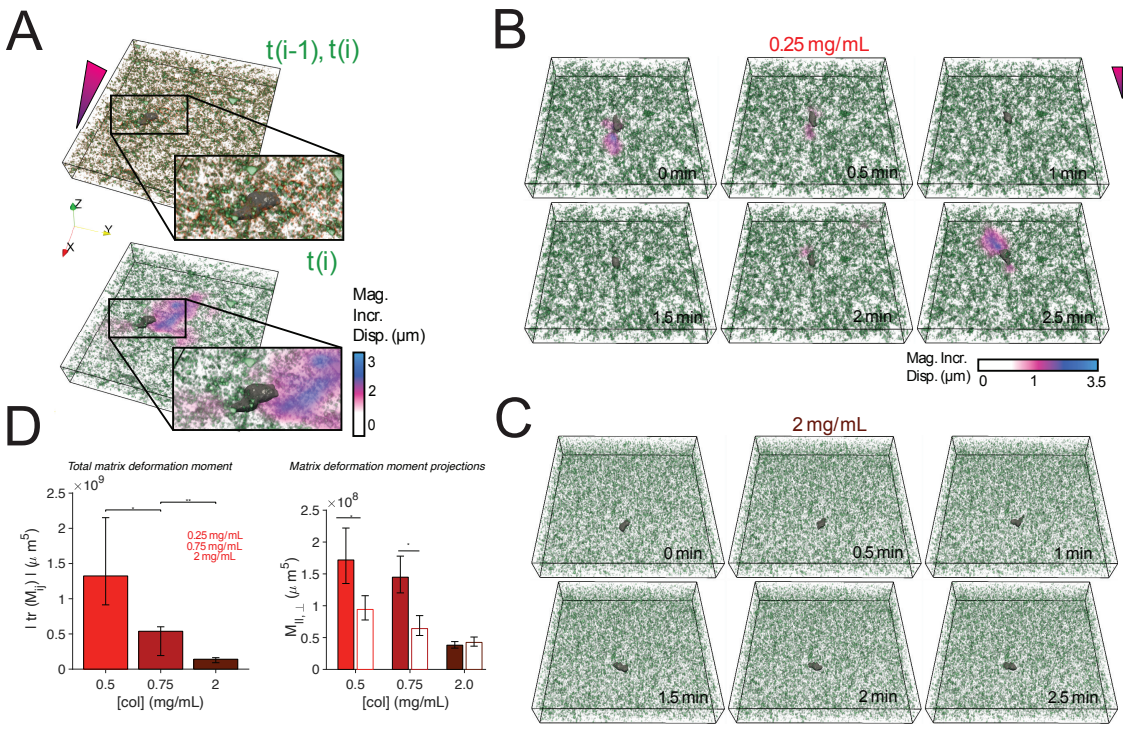

Fig 2.3. Mechanical remodeling of surrounding matrix in low and high-density collagen matrices. (A) Top: Reconstruction of a fluorescently labeled cell (grey), and fluorescent micro-beads at $t = (i-1)\Delta t$ (orange) and $t = i\Delta t$ (green) during chemotactic migration in 0.75 mg/mL collagen gel; $\Delta t = 30$ s. Bottom: Absolute magnitude of incremental deformations computed by 3-D Particle Image Velocimetry. (B) Representative time-lapse reconstructions of cells (grey), beads (green), and incremental 3-D matrix deformation (magenta – blue colormap) during migration in a low collagen concentration matrix (0.25 mg/mL). (C) Same as panel B for high collagen concentration matrix (2 mg/mL). (D) Left: Mean magnitude of 3-D total matrix deformation moment, $|\mathrm{tr}(\mathbf{M})|$, vs. collagen density. Right: Projections of the deformation moment in the directions parallel ($|\mathbf{M}_{\parallel}|$, colored bars) and perpendicular ($|\mathbf{M}_{\perp}|$, hollow bars) to the fMLP gradient.

and 0.75 mg/mL, and a 10-fold decrease between [col] = 0.25 and 2 mg/mL (Fig 2.3D, left panel). Furthermore, we found the sign of tr($\mathbf{M}$) to be preferentially negative regardless of [col], indicating that cells preferentially pulled the matrix towards them (Fig 2.4 A). Projecting the $\mathbf{M}$ tensor in the directions parallel ($\parallel$) and perpendicular ($\perp$) to the fMLP gradient (Fig 2.3 D, right panel) revealed that cell contractions were significantly larger in $\parallel$ the direction than in the $\perp$ direction for [col] = 0.25 and 0.75 mg/mL; however, these contractions became isotropic in the more restrictive [col] = 2 mg/mL matrices.

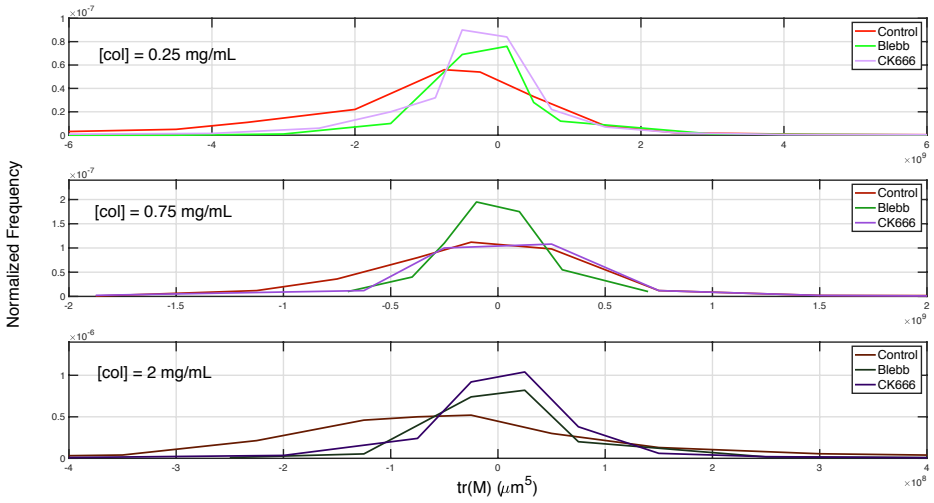

Fig 2.4. Matrix deformation moments. Probability distributions of signed matrix deformation moments, tr(**M**). Note that tr(**M**) > 0 indicates that the matrix is being deformed away from the cell, whereas tr(**M**) < 0 indicates that the matrix is being deformed towards the cell. The top, middle and bottom rows correspond to [col] = 0.25, 0.75, and 2.0 mg/mL, respectively. The asymmetric probability distributions for untreated cells (red lines) indicate that cells preferentially deform the matrix towards the cells regardless of [col]. Conversely, the symmetry of the probability distributions for ck666-treated (purple) and blebbistatin treated (green) cells indicates that the ability of the cells to pull the matrix towards them is reduced when Arp2/3-mediated actin polymerization or myosin II contraction are inhibited.

Of note, the representative cell in the 2.0 mg/mL collagen matrix initially moved towards the chemoattractant source, but seemed unable to continue moving in that direction at t = 1 min (Fig 2.3 C). Subsequently, it performed a sharp, $\sim \pi/2$ radian turn and continued to migrate in the direction perpendicular to the fMLP gradient for the next minute. In comparison, the representative cell in the 0.25 mg/mL matrix was able to sustain directed motion towards the fMLP source for t = 2.5 minutes. These observations support the idea that as [col] increases, these cells must adapt their migration strategy to circumvent the more frequent impassable, non-deformable sections of the matrix.

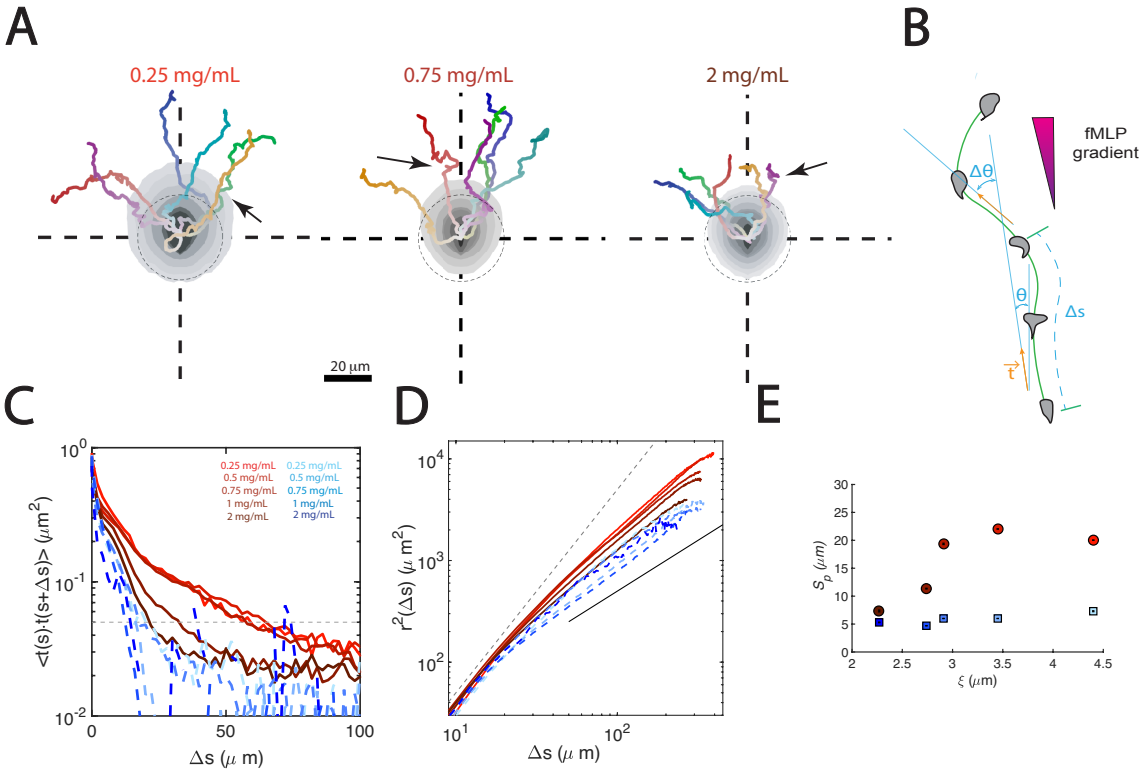

Fig 2.5. Persistence in cell trajectories for varying collagen densities. (A) Probability density maps of cell coordinates (gray contours) and representative cell trajectories for non-restrictive ([col] = 0.25 mg/mL), intermediate ([col] = 0.75 mg/mL), and restrictive ([col] = 2 mg/mL) matrices. Arrows indicate representative turns. Time progression along each trajectory is represented by increasing color saturation. Dashed circles represent unbiased random motion. (B) Schematic of a cell trajectory, indicating a segment of length Δs, along which the tangent vector changes its orientation θ with respect to the gradient by $\Delta\theta$ (C) Tangent vector autocorrelations vs. distance traveled, $C_{tt}(\Delta s)$, for no fMLP (dashed blue) and fMLP (red solid) conditions, in matrices of varying density. Dashed line marks the cutoff $C_{tt} = 0.05$ used to determine the trajectories persistence (S_p). (D) Mean squared displacements vs. distance separation along cell trajectories, $r^2(\Delta s)$. Dashed and solid lines represent $r^2 \sim (\Delta s)^2$ and $r^2 \sim \Delta s$ respectively. (E) S_p of cell trajectories vs. matrix mean pore size, $\langle \xi \rangle$, for no fMLP (blue squares) and fMLP (red circles) conditions. Error bars Sp are superimposed on top of data points and represent 95% confidence intervals of the mean. $*$ and $**$ respectively indicate $p < 0.05$ and $p < 0.01$ according to the Mann-Whitney U test.

2.4.3 Neutrophils migrating in 3-D matrices retain overall chemotactic migration despite turning more frequently as matrix pore size decreases

The results presented thus far led us to hypothesize that turning events are a major factor that enabled the directed migration of neutrophils in restrictive 3-D matrices at the expense of decreasing speed. To examine this hypothesis, we aimed to statistically characterize the cell trajectories in matrices with different collagen concentrations. We first examined the probability distribution $p(x, y)$ of cell coordinates along their trajectories for different collagen concentrations (Fig 2.5 A). In all the matrices investigated, the trajectories were biased towards the chemoattractant source, and the maps of $p(x, y)$ had eccentric, elongated contours in the y direction. However, the trajectories were shorter and the $p(x, y)$ contours extended less into the $y > 0$ plane as [col] increased, in agreement with the decreasing cell speed (Fig 2.2 F). Qualitative inspection of cell trajectories suggested that cells perform sharper turns with increasing [col]. Visually, this trend was most evident at several points along the longest trajectories (see arrows in Fig 2.5 A). To characterize turning events statistically, we computed the autocorrelation function of the vector tangent to the trajectory in intrinsic coordinates, $C_{tt} = \langle \boldsymbol{t}(s) \cdot \boldsymbol{t}(s + \Delta s) \rangle$ (see diagram in Fig 2.5 B). This function was plotted in Fig 2.5C for chemotaxing and randomly moving cells in different matrices, showing that C_{tt} decayed with increasing Δs from its value of $C_{tt}(0) = 1$ at the origin as the cells added turns to their trajectories. For chemotaxing cells, this decrease was more pronounced in high-[col] matrices than in low-[col] ones. By contrast, randomly moving cells showed a weak dependence of C_{tt} with [col].

Next, we determined the mean squared displacements (MSDs) of the cells' trajectories. The MSD versus time, i.e., $r(\Delta t) = \langle (\mathbf{x}(t + \Delta t) - \mathbf{x}(t))^2 \rangle$, have been widely used to quantify 2-D and 3-D cell migration by exploiting the analogy between these processes and a random walk [29, 135, 136]. In particular, the logarithmic slope of the MSD plot is often used to assess whether migration is random or directed. This time-domain analysis has proven useful to study rate-limiting processes governing cell migration. However, considering this study's focus was analyzing the shape of cells trajectories affected by physical confinement in 3-D matrices, we considered the MSDs as a function of distance traveled, i.e., in intrinsic coordinates$r(\Delta s) = \langle (\mathbf{x}(s+\Delta s) - \mathbf{x}(s))^2 \rangle$. Intrinsic coordinates are widely used in differential geometry and allow for studying the geometry of cell trajectories independent of cell speed. This consideration is relevant because cell speed can depend on [col] and varies significantly along each cell's trajectory as the cell turns to avoid impassable sections of the matrix (shown below). The rate of increase of the MSDs with Δs depends on whether cells maintain directed translocation over a distance equal to Δs. Note that since the MSDs can be expressed as

$$r(\Delta s) = \int_0^{\Delta s} \int_0^{\Delta s} C_{tt}(\Delta s) \mathrm{d}\Delta s \mathrm{d}\Delta s. \tag{2.11}$$

the MSDs are tightly linked to the autocorrelation of the direction of cell migration. The MSDs of chemotaxing and randomly moving cells were plotted in Figure 3D for various collagen concentrations. For short travel distances, $r(\Delta s) \sim \Delta s^2$ in all conditions tested, a hallmark of directed motion that is consistent with the $C_{tt} \approx 1$ values that are shown in Fig 2.5 C. Subsequently, the MSDs tapered towards $r(\Delta s) \sim \Delta s$ as Δs increased and the cells began to add changes of direction (turning events) along their paths as C_{tt} progressively dropped. The MSD and C_{tt} plots in the time domain are represented in Fig 2.6 A-B for reference.

The rate of decay of C_{tt} governs the transition between the linear and quadratic regimes of the MSDs according to eqn (2.11), and is related to the persistence length of the trajectories, S_p [137]. Thus, we estimated S_p using an exponential decay model for C_{tt} ($S_p \approx -\Delta s_0 / \log C_{tt,0}$, with $C_{tt}(\Delta s_0) = 0.05$) and plotted the results in Fig 2.5E. These data show that the persistence of the paths of neutrophils undergoing directed migration through 3-D matrices plateaued at $S_p \approx 20\,\mu$m for matrices with $\langle \xi \rangle \geq 3\,\mu$m, and then fell sharply to reach $S_p \approx 7\,\mu$m for $\langle \xi \rangle \leq 3\,\mu$m . In contrast, randomly moving neutrophils had trajectories with $S_p \approx 5\,\mu$m regardless of $\langle \xi \rangle$. The persistence times obtained from C_{tt} in the time domain follow a similar trend with $\langle \xi \rangle$ (Fig 2.6 C). Together with the matrix deformation measurements presented in Fig 2.3, these results suggest that neutrophils undergoing chemotaxis perform more frequent turns in restrictive matrices with narrower pores that cannot be easily deformed. In our most restrictive matrices, these turns became almost as frequent as those performed by randomly moving cells.

2.4.4 Directional bias depends on Arp2/3 and requires on average three consecutive turning events, regardless of matrix density and myosin-II contractility

Neutrophils chemotaxing on 2-D surfaces have been shown to immediately correct their misalignments with respect to a chemotactic gradient in one turn [138]. However, our data suggests that in 3-D matrices, these cells need a longer distance to achieve the same objective (Fig 2.5). We denoted this distance S_θ (see diagram in Fig 2.7 A) and estimated it in two steps. First, we obtained $p(\Delta\theta, v|\Delta s)$ as described above and calculated the difference between the most likely turning angle in this distribution, $\Delta\theta_m(\theta, \Delta s)$, and a full directional correction (i.e., $\Delta\theta_m(\theta, \Delta s) = \theta$) for each value of Δs,

$$d_{\Delta\theta_m}(\Delta s) = \pi^{-2} \int_0^{\pi} |\Delta\theta_m(\theta, \Delta s) - \theta| \mathrm{d}\theta. \tag{2.12}$$

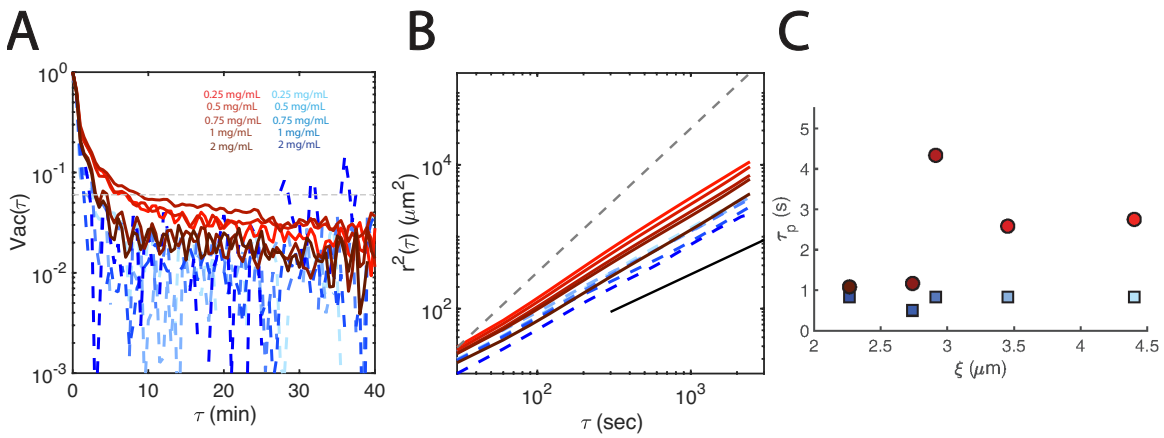

Fig 2.6. Statistical analysis of time-dependent persistence in cell trajectories for varying collagen densities. (A) Velocity vector autocorrelations as a function of time lags, Vac(τ), for no fMLP (dashed blue lines) and fMLP (red solid lines) conditions, in matrices of varying density. Dashed line represents the cutoff Vac = 0.05 used to determine the persistence time of the trajectories (τ_p). (B) Mean squared displacements vs. time lags, $r^2(\tau)$. Dashed and solid lines represent $r^2 \sim tau^2$ and $r^2 \sim \tau$ respectively. (C) Persistence time of cell trajectories, τ_p, as a function of matrix mean pore size, $\langle\xi\rangle$, for no fMLP (blue squares) and fMLP (red circles) conditions.

It is straightforward to show that this definition yields $d_{\Delta\theta_m} = 1/2$ for a narrow (e.g., Dirac delta) distribution with $\Delta\theta_m = 0$. Consistently, we found that $d_{\Delta\theta_m}(\Delta s)$ decreases with Δs from its value $d_{\Delta\theta_m}(0) \approx 1/2$ at the origin (Fig 2.7 A, bottom panel). The second step to determine S_θ was to use the intersection between the $d_{\Delta\theta_m}(\Delta s)$ curve and the threshold value 1/4 to estimate S_θ for each collagen concentration, both for untreated and pharmacologically manipulated cells. We chose the 1/4 threshold because $d_{\Delta\theta_m}(\Delta s) = 1/4$ for a uniform distribution with $\Delta\theta_m = \pi/2$.

The results of this analysis (Fig 2.7 B, left panel) indicated that untreated cells and blebbistatin-treated cells were able to correct misalignments with respect to the gradient over a distance $S_\theta = 50\mu m$ in non-restrictive, low-[col] matrices with $\langle\epsilon\rangle > 3\mu m$. However, this distance decreased to $S_\theta \approx 30\mu m$ in restrictive, high-[col] matrices with $\langle\epsilon\rangle < 3\mu m$. To investigate this seemingly counter-intuitive result that cells can restore their chemotactic compass over a shorter distance in more restrictive matrices, we plotted S_θ vs. the persistence distance S_p (Fig 2.7 B, center panel). Interestingly, we found that S_θ spanned a relatively narrow range when scaled with S_p [$S_\theta \approx (2-4)S_p$]. This result implies that

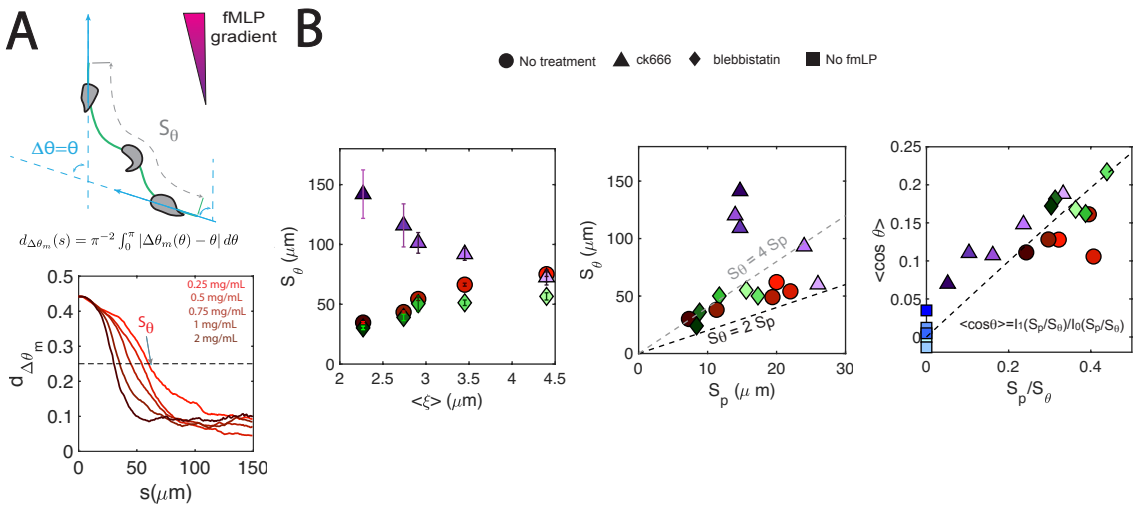

Fig 2.7. Cell realignment with the chemoattractant gradient (A) Top: Schematic indicating the bias length scale, S_θ, defined as the distance that cells need to correct an angular misalignment θ with respect to the chemoattractant gradient. Bottom: Metric $d_{\Delta\theta_m}$ (eqn in figure) that quantifies how close cells are to a total alignment correction $\Delta\theta = \theta$ as a function of distance separation Δs. The data comes from untreated chemotaxing cells in matrices of different densities. The grey dashed line indicates the threshold used to determine S_θ. (B) Left: S_θ vs. $\langle\xi\rangle$ for different treatments and matrix densities. Error bars for bias length scale calculations are superimposed on top of data points and represent 95% confidence intervals of the mean. Right: S_θ vs. S_p for different treatments and matrix densities. The dashed dark and light lines represent $S_\theta = 2S_p$ and $S_\theta = 4S_p$ respectively. Untreated cells, ck666-treated cells and blebbistatin-treated cells are represented by red circles, purple triangles, and green diamonds respectively, and their color indicates collagen density (0.25, 0.5, 0.75, 1 and 2 mg/mL from light to dark).

it takes neutrophils between two and four turns on average to realign their motion with the chemoattractant gradient in 3D collagen matrices. Furthermore, since cells turn more often in more restrictive matrices, they need a shorter physical distance to realign. Our data suggest that collagen concentration or myosin-II contractility did not seem to affect this result, but ck666-inhibition of the Arp2/3 complex drastically increased S_θ (Fig 2.7 B, center panel). Thus, ck666-treated cells that performed turns to avoid obstacles in their restrictive microenvironments had a reduced ability to control the direction of turning to remain aligned with the chemotaxis gradient.

Given that S_p and S_θ can be loosely interpreted as the frequencies per unit distance of random and biased turns along a cell's trajectory, we hypothesized that the chemotactic efficiency of the cells would depend on the ratio S_p/S_θ. To test this hypothesis, we plotted the average of $\cos\theta$ vs. S_p/S_θ for all our experimental conditions (Fig 2.7 B, right panel). These

data confirm that cell motion remained more aligned with the chemoattractant gradient for larger values of S_p/S_θ. In addition, we built mathematical models of biased random walks with persistence distance S_p and bias lengthscale S_θ arising from an angular controller,

$$\dot{\theta}(s) = -\frac{1}{S_\theta}\sin\theta(s) + \Gamma(s), \tag{2.13}$$

where $\Gamma(s)$ is a white noise source with $\langle\Gamma(s)\Gamma(s')\rangle = \frac{2}{S_p}\delta(s-s')$ (§2.2.1, [26]). The simplest version of these models, which assumes constant cell speed independent of θ, is particularly interesting because it has an exact analytical solution for the average of $\cos\theta$ that does not have any adjustable parameter, i.e., $\langle\cos\theta\rangle = \frac{I_1(S_p/S_\theta)}{I_0(S_p/S_\theta)}$, where I_1 and I_0 are modified Bessel functions of the first kind. This model prediction agrees well with our experimental data (Fig 2.7 B, right panel).

2.4.5 Cell-generated mechanical forces affect the rate of turning and speed of neutrophils migrating in 3D, but not their chemotactic efficiency

We examined to what extent neutrophils relied on mechanical forces to migrate in 3-D environments by quantifying the matrix deformations caused by untreated, ck666-treated and blebbistatin-treated cells. In our 0.25 mg/mL matrices, both treatments caused a notable decrease in 3-D matrix deformations (Fig 2.8 A-C) that was statistically significant in the case of blebbistatin treatment as measured by the 3-D matrix deformation moment ($|\operatorname{tr}(\mathbf{M})|$ defined in Eqn (2.7) , Fig 2.8 D); however, the treated cells were still able to appreciably deform their microenvironment. We measured the matrix deformation moments created by blebbistatin-treated cells in these matrices (Fig 2.8 E), and found that $|\operatorname{tr}(\mathbf{M})|$ was significantly reduced after treatment. The matrix deformation moments in our most restrictive matrices were about 10 times lower than in non-restrictive matrices, and also decreased after ck666 or blebbistatin treatment (Figure 2.8 F). Of note, these treatments also caused the distribution of the signs of $\operatorname{sgn}(\operatorname{tr}(\mathbf{M}))$ to be symmetric, implying that they reduced matrix contraction towards the cell (Fig 2.4).

Since blebbistatin- and ck666-treated cells had lower migration speeds than untreated cells, we examined the relationship between $|\operatorname{tr}(\mathbf{M})|$ and $\langle v\rangle$ (Fig 2.8 G). This analysis revealed that $|\operatorname{tr}(\mathbf{M})|$ and $\langle v\rangle$ collapsed on a single curve regardless of treatment and [col], suggesting that the ability of 3-D migrating neutrophils to mechanically remodel their environment is a key factor governing their speed. We plotted S_p vs. $|\operatorname{tr}(\mathbf{M})|$ (Fig 2.8 H) and found that, for both treatments and control conditions, S_p decreased when $|\operatorname{tr}(\mathbf{M})|$ fell below $\sim 5\times10^3\mu m^2$ regardless of [col]. Thus, neutrophils may transition to a migratory strategy with an increased rate of turning when they become unable to sufficiently deform

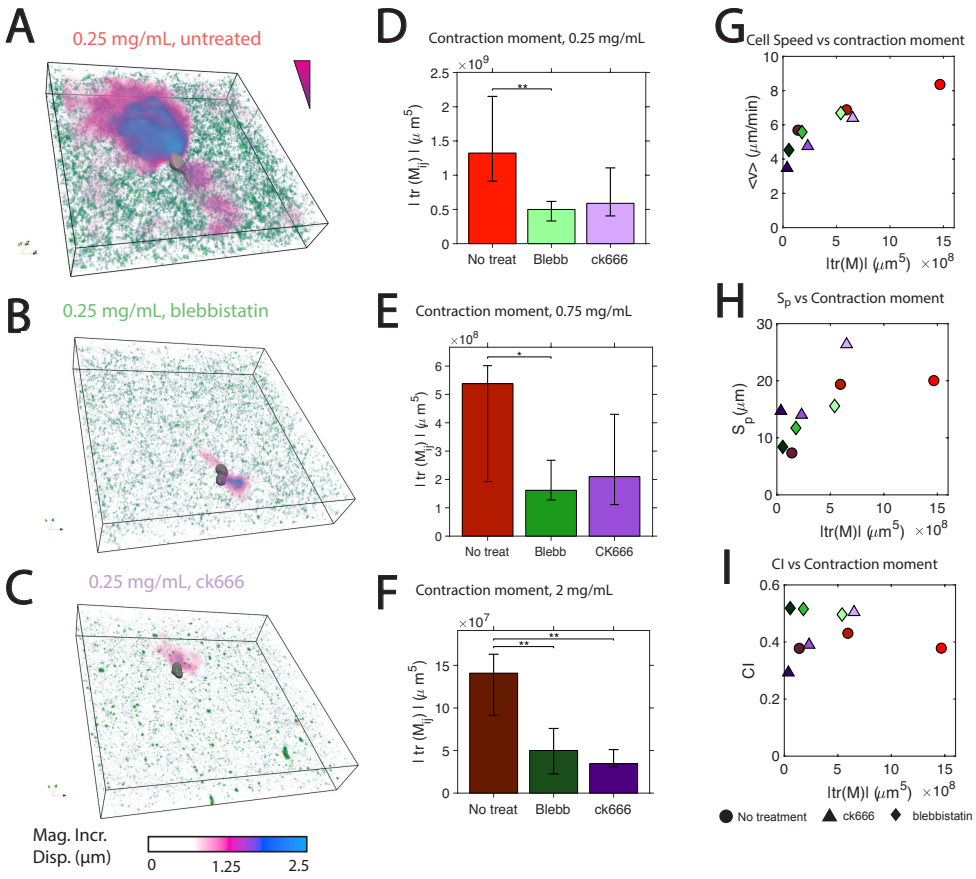

Fig 2.8. Relationship between cell-generated matrix deformations and cell migration parameters (A-C) Representative reconstruction of cells (grey), beads (green), and incremental 3-D matrix deformation (magenta – blue colormap) during migration in a sparse (0.25 mg/mL) collagen matrix for no treatment (A), blebbistatin treatment (B), and ck666 treatment (C). (D-F) Mean magnitude of 3-D contractile moment, $|\mathrm{tr}(\mathbf{M})|$, for different treatments in sparse (0.25 mg/mL, panel D), intermediate (0.75 mg/mL, panel (E), and dense (2 mg/mL, panel (F) matrices. Error bars represent 95% confidence intervals of the mean. $*$ and $**$ respectively indicate $p < 0.05$ and $p < 0.01$ according to the Mann-Whitney U test. (G) Mean cell speed $\langle v \rangle$ vs. $|\mathrm{tr}(\mathbf{M})|$ for different treatments and matrix densities. (H) Persistence length of cell trajectories, S_p, vs. $|\mathrm{tr}(\mathbf{M})|$ for different treatments and matrix densities. (I) Chemotaxis index CI vs. $|\mathrm{tr}(\mathbf{M})|$ for different treatments and matrix densities. * and ** respectively indicate $p < 0.05$ and $p < 0.01$ according to the Mann-Whitney U test.

their surrounding matrix. Finally, we plotted the chemotactic index vs. $|\mathrm{tr}(\mathbf{M})|$ (Fig 2.8 I) and found that this index did not depend on $|\mathrm{tr}(\mathbf{M})|$ except when Arp2/3 was inhibited.

2.5 Neutrophils exhibit distinct migration phenotypes modulated by transendothelial migration

Polymorphonuclear leukocytes (PMN) extravasation, a critical component of the innate immune response, comprises two sequential processes: transendothelial migration (TEM) and interstitial migration. TEM requires intimate physical contact between leukocytes and vascular endothelial cells, triggering a cascade of biochemical and biomechanical interactions whose effect on leukocyte interstitial migration is currently unclear. To address this question, we culture human vascular endothelial cells on a fibronectin-treated transwell insert, mimicking the endothelium and basement membrane *in vitro* (Fig 2.8 A). PMN-like differentiated HL60 (dHL-60) cells are loaded in the upper chamber of the insert, and cells that cross the membrane-supported monolayer are collected from the lower chamber (TW condition). These cells are then seeded in a custom-built chemotaxis device containing a collagen gel matrix to study their 3D migration in the presence or absence of an fMLP gradient. dHL-60 cells from culture are used as control.

2.5.1 TEM process alters PMN phenotype associating with the loss of directional motility

To observe the impact of TEM on subsequent PMN migration in 3D matrices, we performed in vitro 3D migration experiments as described by Francois *et al* [1]. Briefly, dHL-60 cells were pre-treated in accordance with their experimental condition, then seeded a 1 mg/mL collagen gel embedded in a custom pocket device (Fig 2.2 A) and imaged at 10 second intervals while they chemotaxed in response to a stable linear gradient of the bacterial chemoattractant N-formylmethionine-leucyl-phenylalanine (fMLP). At the conclusion of the 70-minute time course, cell tracks were generated using TrackMate, an opensource Fiji plugin [126], then exported to MATLAB for bulk drift correction and further analysis with custom software.

Fig 2.8 B show representative trajectories for chemotaxing dHL-60 cells in each treatment condition superimposed onto a probability density map of aggregated endpoint coordinates for every cell included in that condition. A red dashed circle representing unbiased random motion is included for reference. As expected, untreated control cells exhibit highly directional motion in response to the gradient of fMLP, migrating preferentially in the direction of increasing chemoattractant concentration in a manner consistent with previously published results [1]. By contrast, TW-treated cells exhibited a marked reduction in spatial exploration and chemotactic preference. This data qualitatively suggest that TEM negatively impacts neutrophils' chemotactic efficiency while their ability to spatially explore the microenvironment. This is reflected in the population-level statistics of means speed and chemotaxis index (Fig 2.8 C).

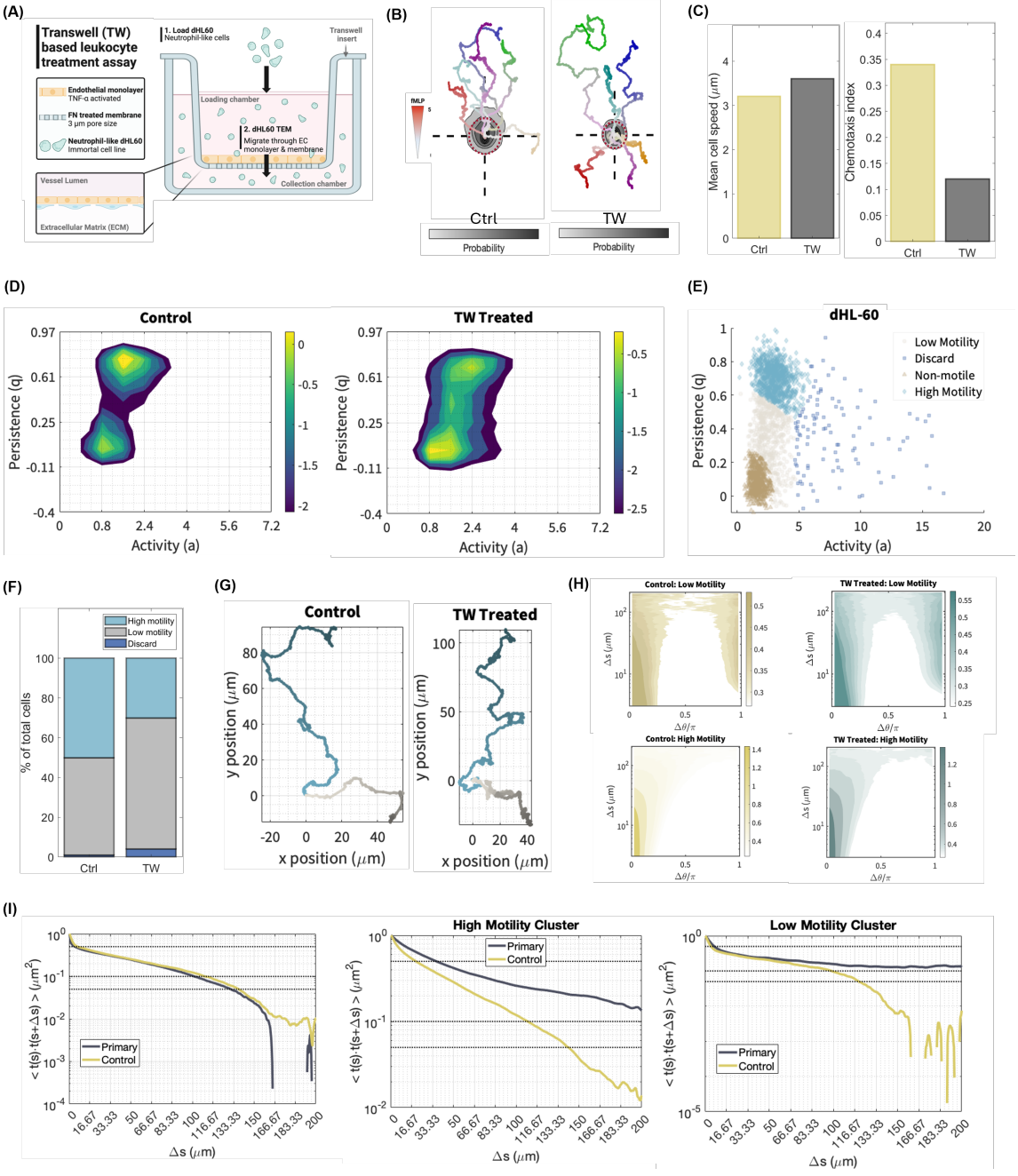
(A)
Transwell (TW) based leukocyte treatment assay
Endothelial monolayer
TNF-α activated
FN treated membrane
3 μm pore size
Neutrophil-like dHL60
Immortal cell line
1. Load dHL60
Neutrophil-like cells
Transwell insert
Loading chamber
2. dHL60 TEM
Migrate through EC monolayer & membrane
Collection chamber
Vessel Lumen
Extracellular Matrix (ECM)
(B)
fMLP
Ctrl
TW
Probability
Probability
(C)
Mean cell speed (μm)
Chemotaxis index
Ctrl
TW
Ctrl
TW
(D)
Control
TW Treated
Persistence (q)
Activity (a)
(E)
dHL-60
Low Motility
Discard
Non-motile
High Motility
Persistence (q)
Activity (a)
(F)
High motility
Low motility
Discard
% of total cells
Ctrl
TW
(G)
Control
TW Treated
y position (μm)
x position (μm)
(H)
Control: Low Motility
TW Treated: Low Motility
Control: High Motility
TW Treated: High Motility
Δs (μm)
Δθ/π
(I)
< t(s)·t(s+Δs) > (μm²)
Primary
Control
High Motility Cluster
Low Motility Cluster
Δs (μm)

Fig 2.8. Neutrophils exhibit distinct migration phenotypes modulated by transendothelial migration. (A) Schematic of transwell-based assay with HUVEC endothelial cell layer to replicate the physiological effects of TEM on neutrophils. (B) Probability density maps of aggregated trajectory endpoints are shown for dHL-60 cells with representative sample tracks overlaid. Sample track color saturation increases with time. The dashed red reference circle superimposed on each inset figure represents unbiased random motion. fMLP concentration increases linearly in the positive y direction. (C) Population level statistics of cell speed and chemotaxis index defined as the projection of the start-end vector on the chemotactic axis. (D) Probability density contour plots for motility modes, comprised of paired activity and persistence values. Contours are plotted for 5, 10, 20, 40, 60, 80, and 90% of total population density for each condition. (E) Global clustering of cell-averaged persistence and activity across all experimental conditions using VB-GMM. (F) Proportion of each cluster in E for control and TW condition showing shift in population composition after extravasation. (G) Representative trajectories from high (blue colormap) and low motility cluster (red colormap) for control and TW treated, with origin at (0,0). (H) 2D histogram of conditional probabilities of turning distance Δs conditioned on the turning angle $\Delta\theta$. (I) Velocity Autocorrelation Function (VAF) at the population level (left), only for high motility cluster (middle) and low motility cluster (right). High motility VAF doesnot show the strong elbow (double exponential decay) at low distance lags compared to population VAF graph.

2.5.2 Mapping individual cell tracks to a heterogeneous persistent random walk reveals the existence of naturally occurring migratory sub-populations

To facilitate a more nuanced analysis of the effect of TEM on the individual cell changes in migration speed and directionality, we next apply an unsupervised, two-step clustering algorithm that identifies heterogeneous motility modes within a cell and across all experimental conditions (§2.2.3).

The first step (local clustering) quantifies the motility mode of an individual cell as described below (§2.2.3). Each cell's trajectory is described by discrete-time random walk model with time-varying random walk parameters, persistence q_t and activity a_t [30]. q_t represent the directional correlation in successive steps, with $q_t = 1$ denoting a perfect straight line and $q_t = 0$ an uncorrelated Brownian diffusion. The lengthscale of the trajectory steps is set by a_t, higher values correlating with metrics such as cell speed, total displacement and track length. Bayesian sequential inference implemented in MATLAB to obtain a time-series of (q_t, a_t) for a single cell trajectory. A density-based clustering algorithm (`DBSCAN`) is then employed to determine heterogeneity within a single cell's trajectory. Bayesian inference method of sequential inference to those measured migration trajectories, describing the local migration time series for each individual cell in terms of a heterogeneous random walk [30]. Representative activity (a) and persistence (q) parameters were then assigned to collectively describe the motion of each individual cell.

Probability density contour plots of the representative activity and persistence parameter

pairs, termed *motility modes*, are shown for control and TW conditions in Fig 2.8 D. Two distinct clusters of motility modes, each characterized by a unique migration phenotype, are immediately intuitive in the control condition. One cluster of cells is both more active and substantially more persistent and was therefore referred to as the *high motility cluster* while the other, which is less active and less persistent, was referred to as the *low motility cluster*. Taken together, these results strongly support the idea that extravasation plays a vital role in determining interstitial migration phenotype for dHL-60 cells. Not only do these interactions generate a population level increase in the variation of dHL-60 cell activity, but they appear to induce a preferential shift toward a low motility migration phenotype.

2.5.3 Autonomous classification of migratory subpopulations by variational Bayesian inference

To further explore quantitative differences between the motility subpopulations identified visually in Fig 2.8 D, we leveraged an algorithm employing variational Bayesian inference for a Gaussian Mixture Model (VB-GMM). VB-GMM autonomously assign cells to representative global motility clusters (across experimental conditions) based on the shape and density of the overall motility mode distribution of cell-averaged random walk parameters without hands-on categorization or pre-determined thresholds for activity and persistence biasing the end result (§2.2.3).

The VB-GMM algorithm identified several distinct motility mode clusters from within the pooled distribution of migrating dHL-60 cells (Fig 2.8 E). Manual inspection of each track within the least populous cluster (of high activity levels), comprising less than 10% of the total population, confirmed that all trajectories contained therein included obvious tracking errors. As such, the subgroup was labeled "Discard", and its tracks were excluded from further analysis. The remaining subpopulations identified by the VB-GMM algorithm were neatly aligned with those distinguishable by eye in Fig 2.8 D and were therefore similarly referred to as high and low motility clusters. The observed changes in relative prevalence of each motility cluster across treatment conditions (Fig 2.8 F) explain the differences in population level migration phenotype. In a reflection of the changes observed in Fig 2.8 D, the even split between motility clusters in the control cells (48.90% high, 50.20% low) exhibits a significant shift in favor of the low motility cluster after TW treatment (30.65% high, 65.50% low). These well-defined 3D migration phenotypes that are conserved across treatment conditions, a finding qualitatively supported by representative sample tracks from each cluster shown in Fig 2.8 3G.

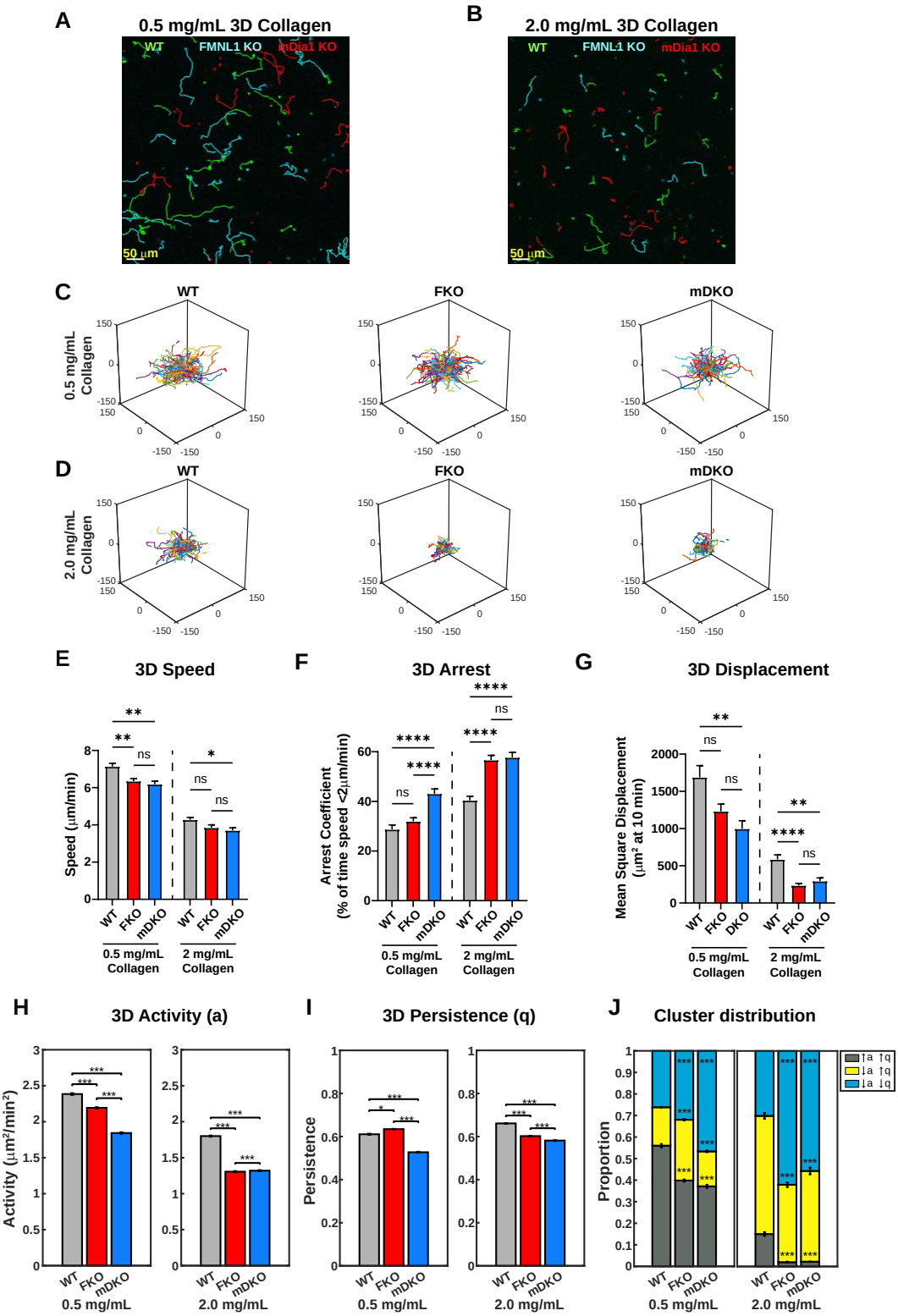
A
0.5 mg/mL 3D Collagen
WT
FMNL1 KO
mDia1 KO
50 μm
B
2.0 mg/mL 3D Collagen
WT
FMNL1 KO
mDia1 KO
50 μm
C
WT
FKO
mDKO
0.5 mg/mL Collagen
D
WT
FKO
mDKO
2.0 mg/mL Collagen
E
3D Speed
Speed (μm/min)
0.5 mg/mL Collagen
2 mg/mL Collagen
F
3D Arrest
Arrest Coefficient (% of time speed <2μm/min)
G
3D Displacement
Mean Square Displacement (μm² at 10 min)
H
3D Activity (a)
Activity (μm²/min²)
I
3D Persistence (q)
Persistence
J
Cluster distribution
Proportion
↑a ↑q
↓a ↑q
↓a ↓q

Fig 2.8. The roles of FMNL1 and mDia1 in T cell migration are dependent on environmental context. WT, FMNL1 KO, and mDia1 KO T cells were isolated from donor mice, ex vivo activated, and differentially labeled using CFSE, CTV, or CTFR. The cells were embedded in collagen matrices and allowed to migrate freely at 37^oC for 1-2 hours before imaging. (A-B) Representative maximum Z-projection showing migration of WT (green), FMNL1 KO (cyan), and mDia1 KO (red) T cells in 0.5 mg/mL (A) or 2.0 mg/mL (B) collagen matrices. Track lines show the T cell path over 30 minutes. (C-D) Trajectory plots of WT, mDKO, and FKO T cells migrating in 0.5 mg/mL (C) or 2.0 mg/mL (D) collagen matrices. (E-G) 3D quantifications of average track speed (E), average arrest coefficient (F), and mean squared displacement of cells tracked continuously for 10 min (G). (H-I) Average activity (H) and persistence (I) calculated from persistent random walk analysis. (J) Stacked bar plots representing the proportion of cells clustering to three motility modes in 0.5 and 2.0 mg/mL collagen matrices. Data in (E-G) represents the mean +/- SEM of at least 70 cells per condition pooled from 4 independent experiments. Data in H-I) represent the mean +/- SEM of all instantaneous velocity vectors of at least 70 cells per condition pooled from 4 independent experiments. Data in (J) represents the mean +/- SEM of $n = 100$ bootstrap resampling repetitions. Significance in (E-G) was determined by Brown-Forsythe and Welch ANOVA tests with Games-Howell's multiple comparisons test. Significance in (H-J) was determined by Mann-Whitney U test. ns = not significant, $* = p < 0.05$, $** = p < 0.01$, $* * ** = p < 0.0001$.

2.5.4 Autonomously identified sub-populations display distinct migratory phenotypes

Previous studies have uncovered key features of 3D random cancer cell migration [29] and 3D directed neutrophil migration [1] by characterizing the probability distribution of turning angles in cell tracks. We next determined the probability distribution of turning angles ($\Delta\theta$) conditional to separation distance (Δs),$p(\Delta\theta|\Delta s)$, for control dHL-60 trajectories classified in both the high and low motility sub-populations separately. Control cells assigned to the high motility cluster (Fig 2.8 H, bottom left) exhibit similar behavior of dHL-60 cells navigating a complex 3D matrix in response to an externally imposed gradient of fMLP [1]. The narrow distribution of $\Delta\theta$ for small values of Δs suggests the neutrophils follow a fairly direct path for small spatial separations. The distribution of $\Delta\theta$ broadens for increasing values of $\Delta\theta$ as the cells encounter environmental obstacles that require them to turn, deviating from their original path and progressively losing their directional persistence with increasing spatial separation in the process.

PMNs assigned to the low motility cluster (Fig 2.8 H, top left), however, exhibit a markedly different migration phenotype. Although the distribution of $\Delta\theta$ is marginally broader than the high motility cluster, the low motility cells exhibit a similarly directed path for small spatial separations. Beginning at displacements on the order of $10\,\mu$m, however, a second peak appeared centered around $\Delta\theta/\pi = 1$, indicating an increase in near 180^o turns. The low motility distribution of $\Delta\theta$ remains bimodal for displacements up to the order of $100\,\mu$m, approximately the same spatial separation for which the distribution of $\Delta\theta$ in the

high motility cluster becomes uniform. Probability distribution maps of $p(\Delta\theta|\Delta s)$ for high and low motility clusters of TW treated cells shown in Fig 2.8 (H, right panel) exhibit the same migration phenotype, confirming that the autonomously identified motility clusters characterized in Fig 2.8 E represent distinct and well-defined migration phenotypes that are conserved across dHL-60 treatment conditions.

Furthermore, plotting the Velocity Autocorrelation Function (VAF) for the trajectories in the instrinsic coordinates for the population of control dHL-60 and primary neutrophils show two exponential distributions, a faster decay for small distance lags and a slow decay at large distance intervals (Fig 2.8 I, left panel). As noticed by others [29], this is in contrast with the predictions of persistent random walk (PRW) model (§1.2.1, (1.4)). The VAF curves for control and primary also suggest to lie on top of each other. Applying the autonomous classification algorithm (§2.2.3) for both control dHL-60 and primary neutrophils, classifying into high motility and low motility clusters, the VAF curves are plotted for each sub-population (Fig 2.8 I, middle and right panel). Immediately, for VAF for high motility cluster (middle panel) doesnot show the 'elbow' present in the population VAF graphs and is close to a single exponential decay. It is also clear that within the high motility clusters, primary neutrophils show larger persistance distances. In the low motiltiy clusters (right panel), primary and control dHL-60 cells are much closer except at larger distance lags. The 'elbow',however, remains indicating heterogeneous sub-population in terms of the parameters a and q of the random walk. This is likely because of the lower density of cells in the transitional region between high motiltiy and non-motile cluster (Fig 2.8 E).

These results suggest that the low motility subpopulation is phenotypically distinct from the high motility cluster. The low motility subpopulation is characterized on a single-cell level by an increased frequency of large angle turns without concomitant loss of directional persistence, suggesting these cells can retain the memory of their prior movements despite tortuous, meandering trajectories.

2.6 FMNL1 and mDia1 differentially modulates T-cell motility in 3D matrices

Lymphocyte trafficking and migration through tissues is critical for adaptive immune function and, to perform their roles, T cells must be able to navigate through diverse tissue environments that present a range of mechanical challenges. T-cells predominantly express two members of the formin family of actin effectors, Formin-like 1 (FMNL1) and mammalian diaphanous-related formin 1 (mDia1). While both FMNL1 and mDia1 have been studied individually, they have not been directly compared to determine functional differences in promoting T-cell migration.

To determine how FMNL1 and mDia1 each contribute to T-cell migration in different

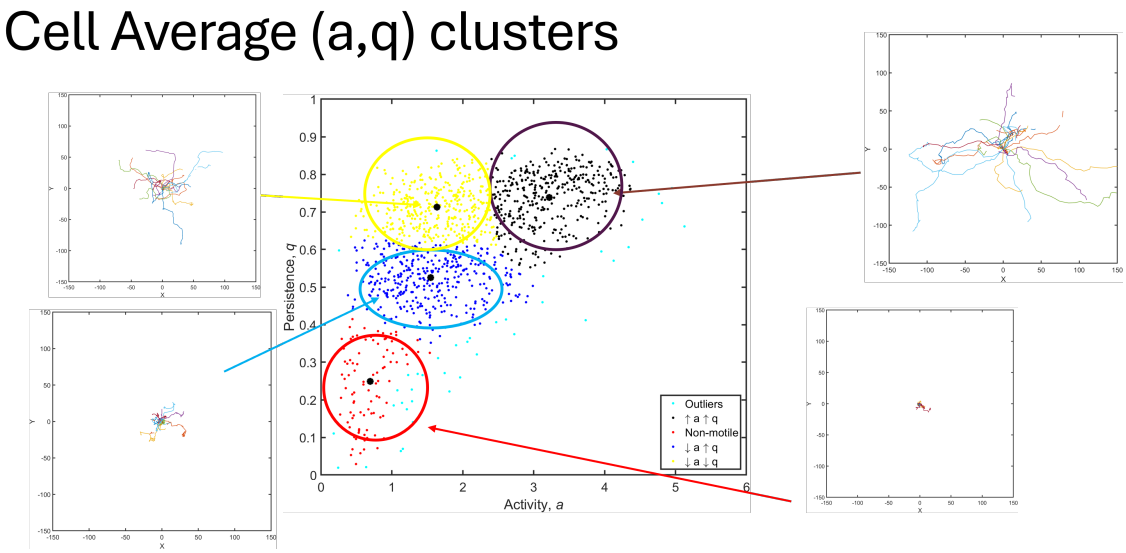

Fig 2.9. Example cell tracks from autonomously determined clusters. Cluster map in random motility parameter space with cell averaged 3D persistent random walk parameters (a, q). $K-$means clustering with $k = 4$ was performed as determined from silhouette analysis. The non-motile (red) and $(\downarrow a, \downarrow q)$ (blue) clusters are absorbed into a single cluster for further analysis of proportions. Representative trajectories from each cluster are displayed. X and Y axis have units of μm in the trajectory plots.

environments, we analyzed migration in 3D collagen matrices of varying densities. T-cells were embedded in collagen matrices of various densities (Fig 2.8 A-D, §2.3.1). Relative to WT T-cells, mDia1 KO T-cells had significant defects in all three population-level parameters analyzed (speed, arrest coefficient, and mean square displacement) regardless of the collagen density (Fig 2.8 E-G). Interestingly, however, the phenotype of FMNL1 KO T-cells was more dependent on the environment density. In low collagen density matrices, FMNL1 KO T-cells only had a small reduction in speed, but no significant defects in arrest and displacement. Conversely, in high density 3D environments, FMNL1 KO T cells had significant defects in both arrest coefficient and mean squared displacement (Fig 2.8 E-G). These data support that in 3D environments FMNL1 is needed for efficient T-cell migration through restrictive environments, whereas mDia1 is important for 3D motility in general.

To further quantify the motility phenotype in 3D environments, we analyzed T-cell activity (a) and persistence (q) by fitting the cell trajectories to a persistent random walk model (§2.2.3). We compared the activity and persistence of the T-cell populations in both the low- and high-density collagen (Fig 2.8 4H-I). We found that in the low-density collagen matrices, both FMNL1- and mDia1-deficiency led to significantly lower activity compared

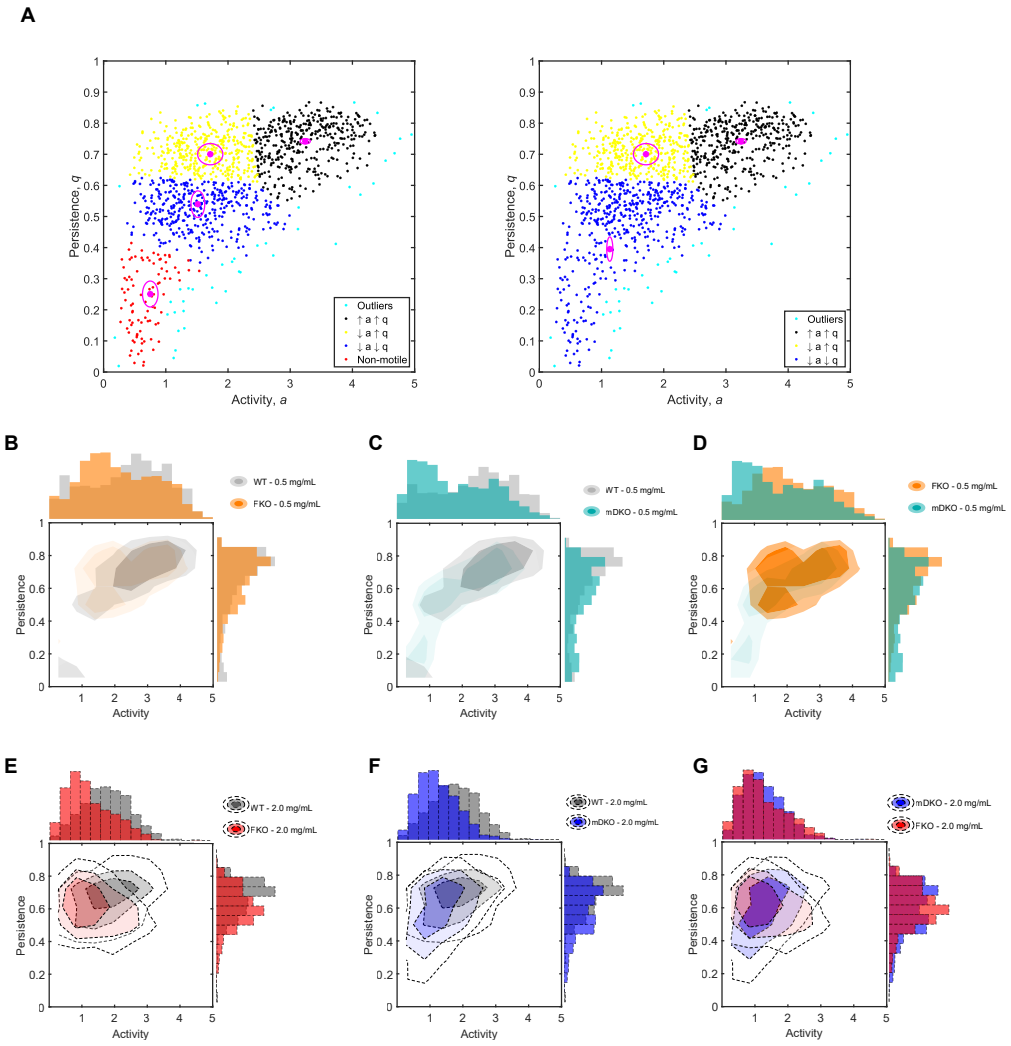

Fig 2.10. Persistent random walk clustering analysis of primary mouse T-cells. WT, FKO, and mDKO T cells trajectories from Fig 2.8 were fit to a persistent random walk model and activity and persistence values were calculated. (A) Cluster map with cell averaged 3D persistent random walk parameters $(\hat{a}, \hat{q})$. K-means clustering with $k = 4$ was performed (left) and non-motile cells were pooled with the $\downarrow a \downarrow q$ cluster for further analysis (right). (B-G) 2D contour maps representing probability distributions of cell averaged $(\hat{a}, \hat{q})$ values. Maps are overlaid to allow for visual comparison between WT, FKO, and mDKO cells within low- or high-density collagen.

to WT, with FMNL1-deficient cells having an intermediate activity (Fig 2.8 H). However, in high-density collagen, FMNL1- and mDia1-deficient cell activity is significantly lower than WT and nearly equivalent to each other. Interestingly, when comparing persistence,

FMNL1-deficiency was associated with a small, but significant increase in low-density environments, but a significant decrease in high-density environments relative to WT T-cells (Fig 2.8 I). In contrast, mDia1-deficient T cells had a significant decrease of migratory persistence in both low- and high-density collagen matrices. The improved persistence of FMNL1 KO T-cells in low-density collagen likely compensated these cells' reduced speed to prevent a significant drop of the mean squared displacements as compared with WT cells, explaining the phenotypic dependence of FMNL1-deficient cells on collagen density.

Next, we investigated the heterogeneity of the activity and persistence parameters within T-cell populations to identify novel phenotypes in sub-populations of cells that may be obscured by whole population averages of motility parameters. Thus, we performed K-means clustering based on each cell's activity and persistence values, identifying three sub-populations of T cells: high activity and persistence ($\uparrow a \uparrow q$), low activity and high persistence ($\downarrow a \uparrow q$), and low activity and persistence ($\downarrow a \downarrow q$) (Fig 2.10 A). We then compared the proportions of these three sub-populations in low- and high-density collagen for WT, FMNL1 KO, and mDia1 KO T-cells (Fig 2.8 J, Fig 2.10 B-G). In low-density collagen, deficiency of FMNL1 or mDia1 are both associated with significant reductions of the high motility ($\uparrow a \uparrow q$) sub-population. This reduction was partially balanced by an increase of the ($\downarrow a \uparrow q$) sub-population in FMNL1-deficient T cells, but mDia1-deficient cells had a large increase in the ($\downarrow a \downarrow q$) population (as shown by the shifts in probability contours of a and q in Fig 2.10 2B-D). In high-density collagen, deficiency of either formin led to the ($\uparrow a \uparrow q$) sub-population being virtually eliminated with significant increases to the size of the ($\downarrow a \downarrow q$) sub-population (Fig 2.8 J).

Taken together, these data indicate deficiency of either FMNL1 or mDia1 is associated with different phenotypes depending on environmental context. Furthermore, the difference in cluster proportions in low density collagen supports the hypothesis that FMNL1 and mDia1 have different mechanisms for promoting motility, specifically in modulating the persistence of migration in low density environments.

2.7 Discussion

The physical properties of different types of tissue, in which the ECM is a significant component, can vary greatly across different locations in the body [139]. However, during immune responses, this variation does not impede leukocytes from migrating toward sites that initiate inflammatory responses [105]. Therefore, the versatility in migration strategies that was observed *in vitro* has implications for understanding the ability of leukocytes to migrate across a range of environments during innate and adaptive immune responses.

The first study investigated the ability of neutrophils to migrate up a chemoattrac-

tant gradient with different degrees of ECM complexity. It was hypothesized that turning events would be a key factor for migration toward a chemoattractant source by allowing cells to circumvent obstacles in the matrix (e.g., narrow pores) and quickly resume their motion toward the chemoattractant. This hypothesis was tested using a custom-made 3D collagen matrix chemotaxis chamber, label-free automated cell tracking, statistical analyses and computational modeling to quantify the migratory trajectories of neutrophil-like HL-60 cells and the matrix deformation these cells exert during migration. A label-free automated cell tracking made it possible to analyze more than 20,000 migrating cells, yielding highly detailed, multiparametric statistics of the migratory process. Together with the 3D measurements of matrix deformation, these data have revealed mechanistic interplays between cell contractility and migratory parameters that had not been quantified before.

The measurements of 3D matrix deformations indicated that neutrophils could transiently deform low-[col] matrices using physical forces. In particular, the cell-generated collagen deformations were oriented preferentially toward the cell and along the chemoattractant gradient direction. However, the cells became unable to appreciably deform high-[col] matrices and the small deformations they generated in the collagen were more isotropic. The cells adapted to increased matrix rigidity in high-[col] matrices by turning more often, which caused a marked decrease in the spatial persistence of the direction of motion. A biased random walk model [26] with no adjustable parameters reproduced the evolution of cell motion orientation along the cell trajectories. Furthermore, the experimental data suggest that migrating neutrophils maintain their chemotactic efficiency as the matrix pore size is decreased by varying their bias distance in concert with their persistence so that $S_\theta \approx 3S_p$. This adaptability is crucial for effective chemotaxis because, unlike cancer cells, neutrophils do not heavily rely on proteolytic matrix degradation when facing restrictive 3D environments [104, 133]. This transition was triggered by the cells' inability to physically remodel their microenvironment, which was confirmed by pharmacological inhibition of contractile forces mediated by myosin-II, or protrusive forces exerted by Arp2/3-mediated dendritic actin polymerization. Overall, this work contributes to an enhanced mechanistic understanding of migration in restrictive collagen matrices which may provide crucial insights into molecules and processes to target for regulating pathological inflammatory responses.

While it is firmly believed that successful clearance of bacterial infection depends on the efficiency of leukocyte migration into infected tissues, average cell migration statistics may not serve as a viable indicator of leukocyte function. The discrepancy arises because the act of averaging those quantitative parameters over disimilar population masks natural the heterogeneity in cell phenotypes that affect motility behaviors. Transendothelial Migration (TEM) is a critical process for host defense to allow infiltration of immune cells, but ac-

cumulating these effector cells can exacerbate inflammation and tissue damage. To avoid uncontrolled leukocyte accumulation while still effectively combating infections, some leukocyte subsets are reportedly repelled from high chemoattractant concentrations, leading to their movement from the damage site back to the circulation [140]. However, the underlying molecular mechanisms of these processes are still under investigation. Here, the modulating effect of TEM was assessed on the subsequent migratory phenotype of the cells using an unsupervised migratory phenotyping method based on single cell trajectories and Bayesian sequential inference method. This method identified two distinct high and low motility migration phenotypes that are conserved and consistently present in dHL-60 cells, indicating that both phenotypes may play essential roles in different aspects of the immune response to clear bacterial infections effectively. A high motility cluster with faster, persistent cells undergoing fewer turns and a low motility cluster with lower speed, increased incidence of large turns were observed. We discovered that the cluster proportions are modified by the process of TEM by enriching the low motility population.

Furthermore, low motility cluster demonstrate a biphasic decay in VAF, characterized by a rapid loss of correlation for displacements less than about $10\,\mu$M and a shallow decay for longer displacements, with a transition between two distinct linear regimes. However, the high motility cluster doesn't exhibit decay in VAF. This raises questions about the underlying mechanisms contributing to these differential behaviors within the two motility subpopulations. Together, the second study revealed a critical role for TEM in the determination of subsequent leukocyte interstitial migration phenotype, strongly suggesting that the prevelance of the low motility cluster with tortous migration phenotype may promote efficient pathogen identification and clearance.

The ability of T-cells to efficiently migrate through a variety of tissues and directly interact with antigen-presenting cells and target cells is critical to their function. Similar to neutrophils, this requires a highly dynamic cytoskeletal network to rapidly adapt to these conditions. A family of proteins that elicit dynamic cytoskeletal remodeling is the formin family of actin effectors. Our analysis of T- cell migration in 3D collagen matrices demonstrated that FMNL1- and mDia1-deficiency have different impact dependent on the restrictiveness of the environment (i.e. [col]). This is emphasized by the significant fraction of FMNL1-deficient T cells that can move with high directional persistence through low-density collagen, albeit at a reduced speed. On the other hand, mDia1-deficient T cells experience a loss of both persistence and velocity in low-density collagen. Interestingly, in high density collagen both FMNL1- and mDia1-deficient T-cells showed an enrichment of the fraction of cells with reduced velocity and persistence. This data further reinforce the conclusion that FMNL1 is especially important for promoting migration through highly

restrictive environments.

2.8 Acknowledgements

The results presented in §2.4 is, in part, a published manuscript [1] : François, J., Kandasamy, A., Yeh, Y.-T., Schwartz, A., Ayala, C., Meili, R., Chien, S., Lasheras, J.C. and del Álamo, J. C. The interplay between matrix deformation and the coordination of turning events governs directed neutrophil migration in 3D matrices. *Science Advances* (2021). The dissertation author is a co-author in this paper.

The results presented in §2.5 is, in part, published as a pre-print [2] and is under revision : Schwartz, A. B., Kandasamy, A., del Álamo, J.C. and Yeh, Y.-T. Neutrophils exhibit distinct migration phenotypes that are modulated by transendothelial migration. *biorxiv*. 2024. The dissertation author is a co-author in this paper.

The results presented in §2.6 is, in part, a published manuscript [3] : Sigler, A. L., Scott T.B., Ellwood-Digel, L., Kandasamy, A., Michaels-Foster, M.J., Thumkeo D., Narumiya, S., del Álamo, J.C. and Jacobelli, J. FMNL1 and mDia1 promote efficient T cell migration through complex environments via distinct mechanisms. *Frontiers in Immunology* (2024). The dissertation author is a co-author in this paper.

Chapter 3

UNCERTAINTY-AWARE TFM

3.1 Introduction

Mechanical forces in the range of pico and nano Newtons have been implicated in fundamental cellular functions such as cell fate determination [141], cell positioning during embryonic development [14], individual and collective cell migration [7], and cardiac contractility [142]. Over the last half-century, biomechanical force measurement methods have enabled the discovery of cytoskeletal force generation and sensing mechanisms [41, 45, 61, 143]. Fluorescence microscopy-based methods such as traction force microscopy (TFM) [33, 37, 131, 144, 145], Förster resonance energy transfer (FRET) [146], and DNA-hairpin-based sensors [84, 147] provide spatial maps of traction stress and force fields with cellular and sub-cellular spatial resolution, and high temporal resolution.

Among these techniques, TFM has become a widely used tool to measure cell-exerted traction forces by tracking fiduciary markers (e.g., fluorescent beads) embedded in linearly elastic substrates of known mechanical properties. Typical TFM experiments do not require highly specialized laboratory equipment, and their preparation is relatively simple. In particular, two-dimensional (in-plane) and three-dimensional (out-of-plane) TFM experiments on flat surfaces can be performed with wide-field fluorescence microscopes [148], and image analysis software is widely available and runs in near real-time with off-the-shelf computers [49, 149–151]. There is a vast body of scientific literature using TFM in biomechanics and mechanobiology studies. In particular, TFM has been instrumental in investigating single cell locomotion in planar surfaces [144, 152], focal adhesion dynamics in adherent cells [47, 153], intercellular forces in collectively migrating epithelial monolayers [65, 91, 154, 155], human cardiomyocyte contractility [22, 156], platelet spreading [5, 157], leukocyte transmigration and interstitial migration [1, 70, 78, 82], and host-pathogen interaction [158].

TFM is a semi-computational method that solves the inverse elastostatic problem of finding the traction stress field which gives rise to the observed field of substrate displacements. This inverse problem is ill-posed because of the long-range decay of displacements, making the calculated traction stresses highly sensitive to experimental measurement noise of high spatial frequency [36, 41, 48]. The ill-posedness of TFM manifests itself in the numerical discretization of the elastostatic problem, leading to a linear system of equations with a high condition number [47, 144]. Even when this numerical issue is avoided by sparsely

block-diagonalizing the elastostatic system and inverting it exactly in Fourier space [33, 37], the slow decay of substrate deformation still causes noise amplification. Therefore, TFM algorithms have traditionally included regularization schemes in the form of implicit priors [36, 48–50, 144], explicit noise filters [47, 91], etc. Previous works have been instrumental to understand the differences among TFM methods [47, 49, 68]. However, there is no unified framework to comprehensively study the sensitivity and variability of TFM methods to the choice of elastostatic solution, numerical discretization, and the form of regularization scheme.

Most regularization methods in TFM involve optimizing a composite norm weighing model accuracy and complexity. This optimization determines the degree of spatial smoothing applied in the inversion process, affecting the dynamical range and the effective resolution of the recovered traction stress maps [35, 36, 48]. Several approaches have been introduced to balance these effects, e.g., χ^2-Criterion [48, 144], Morozov discrepancy principle [48, 63], the self-consistency principle[48], the L-curve criterion [47, 48], etc. Recent efforts have adopted Bayesian frameworks [49, 51, 159] following the seminal work of [144], proposing statistical metrics such as generalized cross-validation [46, 47, 68] to tailor the regularization level to each experimental deformation map. However, the optimal value of the regularization parameter estimated by the different criteria for the same experimental data has not always been consistent, leaving room for ambiguity in the balance between overfitting and smoothing [48].

Optimization metrics for TFM regularization are usually calculated over an entire microscopy image or region of interest, assuming that the noise is spatially uniform (i.e., homoskedastic). Therefore, the ensuing regularization is sensitive to localized anomalies (e.g., large bead aggregates and empty areas without beads). This sensitivity generates the need to introduce quality control steps in TFM analysis pipelines, which are usually binary (i.e., accept vs. reject) and seldom reported, thus limiting the yield and reproducibility of TFM experiments. More generally, fluorescence microscopy images for TFM can contain spatial gradients in bead focus or brightness, leading to spatially dependent noise in the measured substrate deformations. However, regularization of the inverse elastostatic problem rarely accounts for these spatial gradients. A recent work reformulating the optical flow method using the elastostatic equation as an optimization constraint is an important step towards effectively linking spatially-dependent image noise and the recovered traction stresses [63].

The vast majority of regularization schemes in TFM do not provide *a posteriori*, point-by-point estimates of experimental uncertainty. A usual approach to make up for this lack is to perform repeat experiments and report the statistics (e.g., mean and standard devia-

tion) of select readouts. However, this approach mixes the measurement uncertainty that is uniquely due to the experimental setup, imaging method, and mathematical model with the biological variability associated with the fact that two different cells do not exert the same traction stresses. The paucity of uncertainty quantification (UQ) tools in TFM is at odds with the considerable UQ efforts in particle image velocimetry (PIV) and other common methods to measure fluorescent bead displacements[160–164]. Consequently, the choice of crucial parameters affecting the resolution and noise in the measured displacements for TFM, e.g., the PIV interrogation window size, must be done without quantitative information about this choice's effect on the traction stresses. This factor adds to the ambiguity in regularization criteria, sensitivity to image artifacts, and impossibility to separate biological and experimental uncertainty, perpetuating the view that TFM is technically involved and challenging to interpret [35, 62], hindering its more widespread adoption.

This manuscript presents a traction force microscopy method with uncertainty quantification (TFM-UQ). The new TFM-UQ method adaptively regularizes the traction stresses in different regions of a measurement image to be self-consistent with the input deformation noise. Furthermore, it propagates the input noise forward to provide spatial uncertainty maps in the recovered traction stresses. The input noise in TFM-UQ is determined using a novel, non-parametric PIV uncertainty quantification (PIV-UQ) method suitable for fiduciary markers used in cell mechanics experiments. A computationally efficient PIV software with GPU acceleration is developed to make the PIV-UQ method tractable. To validate the TFM-UQ pipeline, we performed numerical TFM experiments that directly simulated the sources of image noise with synthetically generated fluorescent beads. In experimental microscopy images with different cell types (including images with visible imaging artifacts), the TFM-UQ method uncovered spatially heterogeneous PIV measurement noise, uncertainty associated with the choice of image processing procedure, and finally, provided confidence intervals to the traction stress output. Taken together, TFM-UQ improves the dynamic range of traction stresses and provides a tool to decouple biological heterogeneity from measurement (and procedural) variability. This framework is attractive for enabling reproducible TFM results and automating quality control and analysis of large datasets.

3.2 Methods

This section is organized as follows. First, we provide an overview of traditional traction force microscopy (TFM) and introduce the workflow used in TFM with uncertainty quantification (TFM-UQ, §3.2.1). Then, we describe a new PIV method to measure substrate deformation and estimate its uncertainty (§3.2.2), a crucial input to TFM-UQ. Next, we describe the elastostatic model used in this work (§3.2.3). Finally, we describe a hierarchi-

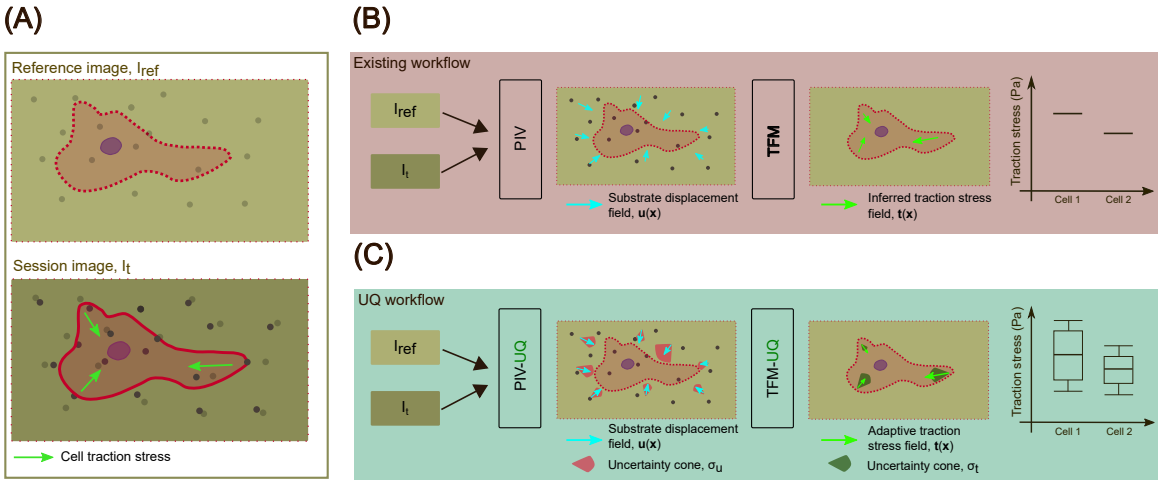

Fig 3.1. TFM-UQ method improves traction stress inference and provides uncertainty bounds. (A) Traction Force Microscopy experiment. Reference image ($\boldsymbol{I}_{ref}$) of the substrate markers is obtained at a stress-free state. Session image(s) ($\boldsymbol{I}_t$) of the substrate marker are obtained at the time point of interest. (B) Existing TFM workflow provides a point estimate of forces but does not consider the variability in the traction stress due to the microscopy images and TFM implementation. (C) The proposed TFM-UQ method considers the local image quality, ambiguity in regularization parameter selection, and the numerical implementation to provide locally adaptive smoothing and error bars.

cal Bayesian framework (§3.2.4) to propagate the uncertainty from deformation to traction stress and locally adjust regularization to account for spatially varying uncertainty levels.

3.2.1 Overview of TFM and TFM-UQ

Traction force Microscopy (TFM) requires a snapshot of fiduciary substrate deformation markers taken under stress, i.e., $\boldsymbol{I}_t$, to be compared with a stress-free reference image, $\boldsymbol{I}_{\mathrm{ref}}$. The stress-free state is achieved by lysing the cells, waiting for cells to move out of the region of interest, or using prior knowledge about fiduciary marker positions. The set of images $\boldsymbol{I} = \{\boldsymbol{I}_{\mathrm{ref}}, \boldsymbol{I}_{\mathrm{t}}\}$ form the experimental data for TFM analysis (Fig 3.1 A). Traditional TFM is implemented in two independent steps (Fig 3.1 B). The first step determines substrate deformation using, e.g., Particle Image Velocimetry (PIV), to obtain the point-wise most likely displacement field, $\boldsymbol{u}_{\mathrm{PIV}}$, between $\boldsymbol{I}_{\mathrm{t}}$ and $\boldsymbol{I}_{\mathrm{ref}}$. The second step solves the inverse elastostatic problem to recover the traction stresses $\boldsymbol{t}$. Traditional TFM methods output a point estimate of the $\boldsymbol{u}_{\mathrm{PIV}}$ and $\boldsymbol{t}$ fields as well as integrated quantities (Fig 3.1 B). These methods suffer from uncertainty propagation from the images to the traction stresses, but their analysis pipeline is not aware of the input data confidence level. Thus, the measurement uncertainty of the desired traction force reading is unavailable in traditional TFM.

Figure 3.1C summarizes the TFM-UQ analysis pipeline. Given a pair of experimental images, the first step in the pipeline is to estimate the substrate deformation and its uncertainty. To this end, we developed a non-parametric bootstrap PIV method (PIV-UQ, see §3.2.2) since PIV is the most common method to measure substrate deformation in TFM. In PIV-UQ, the input image pair is perturbed to find a model-free estimation of the empirical distribution of the deformation field conditional on the $\boldsymbol{I}$ pair. Nevertheless, the TFM-UQ pipeline is not critically dependent on the PIV method, and other registration techniques with UQ capabilities [164] could be adapted to work with TFM-UQ.

In the second step of the pipeline, the deformation vector ($\boldsymbol{u}_{\mathrm{PIV}}$) and its covariance matrix quantifying uncertainty ($\boldsymbol{\Sigma}_{\mathrm{PIV}}$) resulting from PIV-UQ are used as inputs to a Bayesian elastostatic inversion framework. We adopt a hierarchical Bayesian approach in which the model hyperparameters, such as the level of smoothing, are treated as random variables. This strategy allows us to regularize the inversion according to the noise in deformation measurements introduced by the spatially varying features of each $\boldsymbol{I}$ pair. In addition, the hierarchical Bayesian approach provides the confidence interval for traction stress output (Fig 3.1 C).

3.2.2 PIV Uncertainty Quantification (PIV-UQ) of Substrate Deformations

Particle image Velocimetry (PIV) is a commonly used method to measure substrate deformations from a pair of TFM images $\boldsymbol{I} = \{\boldsymbol{I}_{\mathrm{ref}}, \boldsymbol{I}_{\mathrm{t}}\}$. PIV identifies overlapping rectangular sub-domains $\mathbf{W}_{ij}$ (a.k.a. interrogation windows) in each member of $\boldsymbol{I}$, and registers them using cross-correlation as the similarity metric (Fig 3.2 A). This operation is performed for each $\mathbf{W}_{ij}$ resulting in a discrete deformation field $\boldsymbol{u}_{\mathrm{PIV}}$. Typically, PIV uses square interrogation windows of size W_L (pixels) separated by a constant distance of W_S pixels across the entire analyzed image. It is customary to set the window spacing as a fraction of window size, with $W_S = W_L/2$ providing the optimal trade-off between computational cost and the effective spatial resolution based on the Nyquist principle. Consequently, the error and resolution of PIV are usually dictated by one parameter, *i.e.*, W_L. Since, for a given image pair, both the PIV resolution and error increase with W_L, this parameter must be chosen carefully, but current PIV methods used for TFM do not provide information about the uncertainty in $\boldsymbol{u}_{\mathrm{PIV}}$. Below, we introduce a PIV-UQ method that estimates this measurement uncertainty that can be used independently of TFM-UQ to inform the choice of parameters for PIV analysis of experimental images or in conjunction with TFM-UQ to propagate measurement uncertainty to the recovered traction stresses.

PIV-UQ estimates the most likely substrate displacement $\hat{\mathbf{u}}$ and its uncertainty, $\sigma_{\hat{u}}$ by perturbing the input images to obtain a non-parametric, model-free approximation of

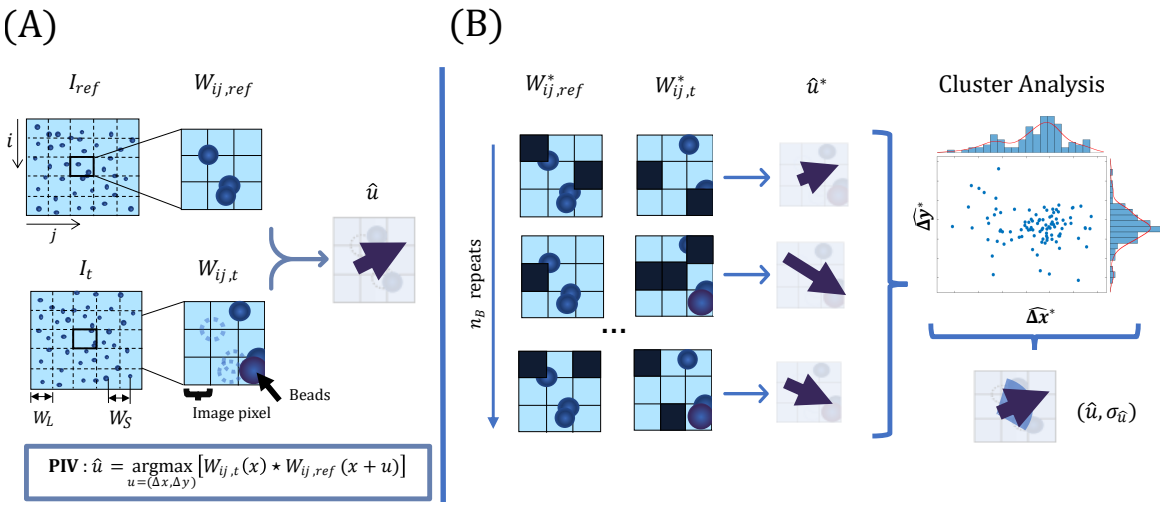

Data: Interrogation sub-windows, $\mathbf{W}_{ij} = \{\mathbf{W}_{ij,ref}, \mathbf{W}_{ij,t}\} \in \mathbb{R}^{n \times n}$
Result: $\hat{\mathbf{u}} \in \mathbb{R}^2, \sigma_{\hat{u}} \in \mathbb{R}^+$

$\hat{\mathbf{u}} \leftarrow \texttt{PIV}(\mathbf{W}_{ij,ref}, \mathbf{W}_{ij,t})$;
for $b = 1 : n_B$ **do**
  for $\mathbf{W}^*_{ij} = \{\mathbf{W}_{ij,ref}, \mathbf{W}_{ij,t}\}$ **do**
    Pixel indices, $i_p \leftarrow \texttt{U}(1, n^2, n^2/2)$;
    Deletion indices, $i_d \leftarrow [1 : n^2] \backslash i_p$;
    $\mathbf{W}^*_{ij}(i_d) \leftarrow 0$;
  end
  $\hat{\mathbf{u}}^*_b \leftarrow \texttt{PIV}(\mathbf{W}^*_{ij,ref}, \mathbf{W}^*_{ij,t})$;
end
$\sigma_{\hat{u}} \leftarrow \texttt{ClusterAnalysis}(\{\hat{\mathbf{u}}^*\})$;

Fig 3.2. Particle Image Velocimetry with Uncertainty Quantification (PIV-UQ) method. Top: Schematic of PIV and PIV-UQ. **(A)** The image data $\boldsymbol{I}$ is sectioned into overlapping square sub-windows $\mathbf{W}_{ij}$ of length W_L (n^2 pixels), their centers separated by W_S. PIV computes the most likely displacement for each sub-window $\mathbf{W}_{ij}$ that corresponds to the maximum of the cross-correlation metric. Each pixel of $\mathbf{W}_{ij}$ contributes to the correlation value, hence the maximization procedure. **(B)** PIV-UQ method bootstraps the contribution of individual pixels to the cross-correlation metric. Pixel indices are randomly sampled with replacement and the unsampled indices are set to 0 (Black pixels). Backslash denotes the set difference operation and $\texttt{U}(1, n^2, n^2/2)$ represents uniformly distributed $n^2/2$ samples in the interval $[1, n^2]$. The bootstrapped sample of size n_B is analyzed for multiple possible clusters and outliers, subsequently providing a metric of variability for each sub-window (i.e. for each discrete vector of the deformation field). **Bottom:** PIV-UQ bootstrap algorithm.

the empirical distribution of substrate displacements given the images $\boldsymbol{I}$. PIV-UQ applies the bootstrap procedure outlined in Fig 3.2 (panel B and algorithm). Bootstrapping is a computational method based on random resampling of limited empirical data to construct

measures of accuracy for sample estimates [55, 56]. As described in the figure, the bootstrap method uses square interrogation windows. However, this method is generally applicable to any PIV implementation, including more advanced algorithms using iterative window refinement or window deformation, and the various sub-pixel interpolation methods for finding the correlation peak [80] by replacing the `PIV` function accordingly. A first nominal PIV run is carried out for a given pair of interrogation windows to obtain the estimator $\hat{\mathbf{u}}$ for the $\boldsymbol{u}_{\mathrm{PIV}}$ field. Next, bootstrapped interrogation windows $\mathbf{W}^*_{ij}$ are built by randomly resampling pixels from $\mathbf{W}_{ij}$ with replacement, and unsampled pixels are left zero valued. The number of unsampled pixels is randomly drawn between 1 and the total number of pixels in the window using a uniform distribution. Then, PIV is performed to obtain the perturbed estimator $\hat{\mathbf{u}}^*$ from $\mathbf{W}^*_{ij}$. This process is repeated for n_B trials so that the set of bootstrap estimators $\{\hat{\mathbf{u}}^*\}$ represent each interrogation window's empirical distribution $p(\hat{\mathbf{u}}|\mathbf{W}_{ij})$.

The bootstrapped distributions $p(\hat{\mathbf{u}}|\mathbf{W}_{ij})$ are further processed using density-based `clusterAnalysis` (DBSCAN algorithm [117] with parameters $\epsilon = W_S/5$ and `minPts` $= n_B/10$) to identify outliers from the bootstrap procedure and verify their uni-modality. The parameter `minPts` denotes the minimum number of points required to form a cluster (scaled with the number of bootstrap iterations n_B), and ϵ is the minimum distance between two points within a cluster (scaled with the spacing between PIV windows W_S). Because the PIV cross-correlation optimization looks for pure translations of $\mathbf{W}_{ij}$ in $\boldsymbol{I}$, motion patterns that significantly depart from translation (e.g., rotation, shear) can lead to multi-modal distributions where more than one value of $\hat{\mathbf{u}}$ is plausible [80]. In `clusterAnalysis`, ϵ is important to identify multi-modality and, hence, PIV invalidation when the minimum distance from edges of clusters are separated by at least 20% of the PIV window spacing. In addition, image noise, lack of image features, and brightness gradients can bias $p(\hat{\mathbf{u}}|\mathbf{W}_{ij})$ towards a uniform or skewed distribution, producing erroneous estimates of $\hat{\mathbf{u}}$. PIV-UQ utilizes $p(\hat{\mathbf{u}}|\mathbf{W}_{ij})$ to validate $\hat{\mathbf{u}}$ instead of purely heuristic-based metrics such as ratio of correlation peaks [80, 165]. The 'bad' windows that fail the validation are deleted, and the standard deviation for each of the remaining sub-windows ($\sigma_{\hat{u}}$) is reported . For the purposes of TFM-UQ, the standard deviation of these windows are set to a high number (e.g. a factor of 5 to the maximum $\sigma_{\hat{u}}$). The number of 'bad' windows also serves as a diagnostic tool in selecting the parameter W_L and vaidating the PIV results for the image $\boldsymbol{I}$. For the rest of the manuscript, $\boldsymbol{u}_{\mathrm{PIV}}(\mathbf{x}) = \hat{\mathbf{u}}(\mathbf{x})$ and $\sigma_{u,\mathrm{PIV}}(\mathbf{x}) = \sigma_{\hat{u}}(\mathbf{x})$ for each interrogation window centered at $\mathbf{x} = (x, y)$. Coefficient of variation (CoV) $= \mathrm{Std}[\sigma_{\hat{u}}]/\,\mathrm{Mean}[\sigma_{\hat{u}}]$ is used as a metric to assess convergence of $\sigma_{\hat{u}}$ with number of bootstrap iterations n_B (see §3.3.3 and Fig 3.12).

3.2.3 Elastostatic model

We consider a flat inertia-less, linearly elastic substrate of Young's modulus E and Poisson's ratio ν, deformed under the action of traction stresses exerted at its free surface $z = h$. The substrate deformation field ($\boldsymbol{u}$) satisfies the elastostatic partial differential equation (PDE)

$$\nabla^2 \boldsymbol{u} + \frac{\nabla(\nabla \cdot \boldsymbol{u})}{1 - 2\nu} = 0, \tag{3.1}$$

with boundary conditions $\boldsymbol{u}(x, y, z = 0) = \mathbf{0}$ and $\boldsymbol{u}(x, y, z = h) = \boldsymbol{u}_{\mathrm{h}} \approx \boldsymbol{u}_{\mathrm{PIV}}$. Once this boundary value problem is solved, the constitutive relation for the stress tensor $\mathbf{T} = F(x, y, z; \boldsymbol{u}, E, \nu)$ allows for computing the traction stress vector at $z = h$ as $\boldsymbol{t}(x, y) = \mathbf{T}(x, y, z = h) \cdot \boldsymbol{n}$, where $\boldsymbol{n} \approx (0, 0, 1)$ is the vector normal to the substrate surface. Because the constitutive equation (i.e. F) and the elastostatic PDE are linear, we can denote the relationship between $\boldsymbol{t}$ and $\boldsymbol{u}_{\mathrm{h}}$ concisely using the linear transformation $\mathbf{M} : \boldsymbol{t} \rightarrow \boldsymbol{u}_{\mathrm{h}}$, where $\mathbf{M}$ is the elastic response operator. $\boldsymbol{u}_{\mathrm{h}}$ and $\boldsymbol{t}$ can be two- or three-component vector fields, and h can be finite or infinite.

Using this formulation, the forward problem of finding $\boldsymbol{u}_{\mathrm{h}}$ given a traction stress field $\boldsymbol{t}$ can be written as

$$\boldsymbol{u}_{\mathrm{h}} = \mathbf{M}\boldsymbol{t} + \boldsymbol{\varepsilon}_\beta + \boldsymbol{\varepsilon}_m, \tag{3.2}$$

$$\boldsymbol{\varepsilon}_\beta \sim N(0, \beta^{-1}\mathbf{U}), \tag{3.3}$$

$$\boldsymbol{\varepsilon}_m \sim N(0, \boldsymbol{\Sigma}_{\mathrm{PIV}}). \tag{3.4}$$

where $\boldsymbol{\varepsilon}_m$ is the measurement error arising from PIV and $\boldsymbol{\varepsilon}_\beta$ represents the other error sources from the elastostatic model, numerical discretization, etc. Both error terms are modeled as normally distributed, but $\boldsymbol{\varepsilon}_\beta$ is assumed to be global with precision parameter β, whereas $\boldsymbol{\varepsilon}_m$ is characterized by the spatially dependent variance $\boldsymbol{\Sigma}_{\mathrm{PIV}}$. Therefore, $\mathbf{U}$ is the identity matrix while $\boldsymbol{\Sigma}_{\mathrm{PIV}}$ is a diagonal matrix. The precision parameter β is unknown and is modeled as a hyperparameter in our hierarchical Bayesian approach (§3.2.4). On the other hand, $\boldsymbol{\Sigma}_{\mathrm{PIV}}$ is measured directly using the PIV-UQ method described in the previous section (§3.2.2), and therefore, it will be treated explicitly.

The form of $\mathbf{M}$ depends on each model's geometry (e.g., finite vs. infinite h, 2D vs. 3D deformation), solution method (Fourier transform, finite elements, etc), and substrate material properties. The particular form of $\mathbf{M}$ is inconsequential for the TFM-UQ algorithm, as seen below. For simplicity, this report considers the Fourier Transform Traction Cytometry (FTTC) response function, $\widetilde{\mathbf{M}}$, to build $\mathbf{M}$. In the Fourier domain, $\widetilde{\mathbf{M}}$ adopts a straightforward block-diagonal form that can be derived analytically for finite and infinite

h for various 2D and 3D boundary conditions at the substrate's surface [33, 34, 37, 38]. Without loss of generality, we used Lin *et al.*'s [38] concise derivation for the finite-h case with 2D boundary conditions:

$$\widetilde{M}(\mathbf{k}) = g_1(k) \begin{bmatrix} 1 & 0 \\ 0 & 1 \end{bmatrix} + g_2(k) \begin{bmatrix} k_x^2 & k_x k_y \\ k_x k_y & k_y^2 \end{bmatrix}, \tag{3.5}$$

where, $g_1 = 1/f_1$, $g_2 = -f_2/f_1(f_1 + k^2 f_2)$ and $k = |\mathbf{k}|$ is the absolute value of the wavenumber vector $\mathbf{k} = (k_x, k_y)$. The scalar functions are defined as

$$f_1 = E\frac{ck}{2(1+\nu)s}, \quad f_2 = E\frac{(3-4\nu)\nu sc^2 - (1-\nu)ckh + (1-2\nu)^2 s + 2(kh)^2}{(2(1-\nu^2)ks)((3-4\nu)sc + kh)},$$

with $c = \cosh kh$ and $s = \sinh kh$. Inverse Fourier transforming $\widetilde{\mathbf{M}}$, we obtain $\mathbf{M} = \mathbf{F}^H \widetilde{\mathbf{M}} \mathbf{F}$, where $\mathbf{F}$ is the discretized Fourier Transform (DFT) matrix and $\mathbf{F}^H$ its Hermitian transpose.

The finite-dimensional matrix $\mathbf{M}$ has a large condition number because the eigenvalues of $\widetilde{\mathbf{M}} \sim h$ for $kh \to 0$ (pure shear limit) while they vary as k^{-1} for $kh \gg 1$. Using the Nyquist criterion to determine the maximum wavenumber, $k_{max} = 2\pi/W_L$, we obtain $\kappa(\mathbf{M}) \sim h/W_L$, which worsens as the substrate becomes thicker and the spatial resolution becomes finer. Depending on the elastostatic model's geometry, the condition number of $\mathbf{M}$ can become even higher. For instance, under a more realistic assumption that the TFM fluorescent beads are located slightly under the substrate's surface, i.e., at $z = h - \Delta h$, the measured displacements are amplified by an additional factor $\exp(k\Delta h)$ [33] and, consequently, $\kappa(\mathbf{M}) \sim h/W_L \exp(2\pi\Delta h/W_L)$. Therefore, the noise terms $\boldsymbol{\varepsilon}_\beta$ and $\boldsymbol{\varepsilon}_m$ are susceptible to amplification when equation 3.2 is inverted, and the level of amplification may vary significantly among TFM methods.

3.2.4 Hierarchical Bayesian TFM formulation to propagate PIV uncertainty

This section presents a Bayesian framework to invert the elastostatic problem in the presence of local measurement noise and global model noise. A three-level hierarchical framework, summarized in Fig 3.3 is formulated. Consistent with the elastostatic model presented in equations (3.2)–(3.4), the likelihood of the observed displacement given a traction stress field, $p(\boldsymbol{u}_\mathrm{h}|\boldsymbol{t})$, is governed by the elastostatic matrix $\mathbf{M}$. The error due to PIV measurement of $\boldsymbol{u}_\mathrm{h}$ is modeled explicitly based on the variance $\boldsymbol{\Sigma}_\mathrm{PIV}$ maps obtained from bootstrap PIV-UQ, and the random global error is modeled as additive noise of variance β^{-1}, where β is a hyperparameter. The likelihood of measured displacements, $p(\boldsymbol{u}_\mathrm{h}|\boldsymbol{t}, \beta, \boldsymbol{\Sigma}_\mathrm{PIV})$, can be

expressed as a multivariate Gaussian distribution for the model residual,

$$p(\boldsymbol{u}_{\mathrm{h}}|\boldsymbol{t},\beta,\boldsymbol{\Sigma}_{\mathrm{PIV}}) = (2\pi)^{-N_w}|\Lambda|^{-1/2}\exp\left[-\frac{1}{2}(\boldsymbol{u}_{\mathrm{h}}-\mathbf{M}\boldsymbol{t})^T\Lambda^{-1}(\boldsymbol{u}_{\mathrm{h}}-\mathbf{M}\boldsymbol{t})\right], \tag{3.6}$$

Here, $\Lambda = \beta^{-1}\mathbf{U} + \boldsymbol{\Sigma}_{\mathrm{PIV}}$, and this matrix's determinant is expanded as the product of its diagonal elements, $|\Lambda| = \prod_{i=1}^{2n}\left[\beta^{-1} + \boldsymbol{\Sigma}_{\mathrm{PIV},ii}\right]$, where $\boldsymbol{\Sigma}_{\mathrm{PIV},ii}$ occupies the i-th position in the diagonal of $\boldsymbol{\Sigma}_{\mathrm{PIV}}$. The dimensions of the multivariate Gaussian, $2N_w$, is given by the total number of displacement measurements (i.e., the number of interrogation windows N_w multiplied by the number of displacement components).

The prior distribution of the traction stress $p(\boldsymbol{t})$ is based on a linear quadratic functional $\boldsymbol{t}^T\mathbf{L}\boldsymbol{t}$, leading to the zero-mean multivariate Gaussian distribution, *i.e.*,

$$p(\boldsymbol{t}|\boldsymbol{u}_{\mathrm{h}},\alpha,\mathbf{L}) \propto \alpha^{N_w}\exp\left[-\frac{\alpha}{2}\boldsymbol{t}^T\mathbf{L}\boldsymbol{t}\right], \tag{3.7}$$

where α is a hyper-parameter. The dimensions of $\boldsymbol{u}_{\mathrm{h}}$ and $\boldsymbol{t}$ need not be the same depending on the form of the solution matrix $\mathbf{M}$ (e.g. Boussinesq solution [48]). We used the discretized Laplacian operator for $\mathbf{L}$, establishing a Tikhonov low-pass filter of the traction stress field.

The hyperparameters α and β control the influence of the prior constraint and model misfit during the inversion process. The case of $\boldsymbol{\Sigma}_{\mathrm{PIV}} = 0$ and fixed hyperparameter values corresponds to the traditional (frequentist or Bayesian) approach, which is governed by the regularization parameter $\lambda = \alpha/\beta$ [47–49, 166]. In our formulation, setting $\boldsymbol{\Sigma}_{\mathrm{PIV}} = 0$ would be equivalent to neglecting the PIV measurement error or to assuming it is spatially uniform so it can be lumped into the model error β.

In the hierarchical framework, the hyperparameters α and β are modeled as random variables, using hyperpriors derived from the Gamma distribution, $p(x|\theta,\phi) = \phi^\theta x^{\theta-1}\exp\{-\phi x\}/\Gamma(\theta)$, where the term in the denominator is the Gamma function. To keep the hyperpriors non-informative, the shape and rate parameters were fixed to constant values ($\theta = 1, \phi = 10^{-5}$). This hierarchical approach (Fig 3.3) allows for including an acceptable level of variability of the hyperparameters given the observed $\boldsymbol{u}_{\mathrm{h}}$ distribution.

The conditional posterior distributions $p(\boldsymbol{t}|\boldsymbol{u}_{\mathrm{h}},\alpha,\beta)$, $p(\alpha|\boldsymbol{t},\boldsymbol{u}_{\mathrm{h}})$ and $p(\beta|\boldsymbol{t},\boldsymbol{u}_{\mathrm{h}})$ were obtained from the joint distribution of the traction stress, displacement and the hyperparameters,

$$\begin{aligned} &p(\boldsymbol{u}_{\mathrm{h}},\boldsymbol{t},\alpha,\beta|\boldsymbol{\Sigma}_{\mathrm{PIV}},\mathbf{L}) = p(\boldsymbol{u}_{\mathrm{h}}|\boldsymbol{t},\beta,\boldsymbol{\Sigma}_{\mathrm{PIV}})p(\boldsymbol{t}|\alpha,\mathbf{L})p(\alpha|\phi_\alpha,\theta_\alpha)p(\beta|\phi_\beta,\theta_\beta) \propto \\ &\propto |\Lambda|^{-1/2}\alpha^{N_w+\theta_\alpha-1}\beta^{\theta_\beta-1}\exp\Big\{-\frac{1}{2}\left[(\boldsymbol{u}_{\mathrm{h}}-\mathbf{M}\boldsymbol{t})^T\Lambda^{-1}(\boldsymbol{u}_{\mathrm{h}}-\mathbf{M}\boldsymbol{t})\right] - \frac{\alpha}{2}\boldsymbol{t}^T\mathbf{L}\boldsymbol{t} - \phi_\alpha\alpha - \phi_\beta\beta\Big\}. \end{aligned}$$

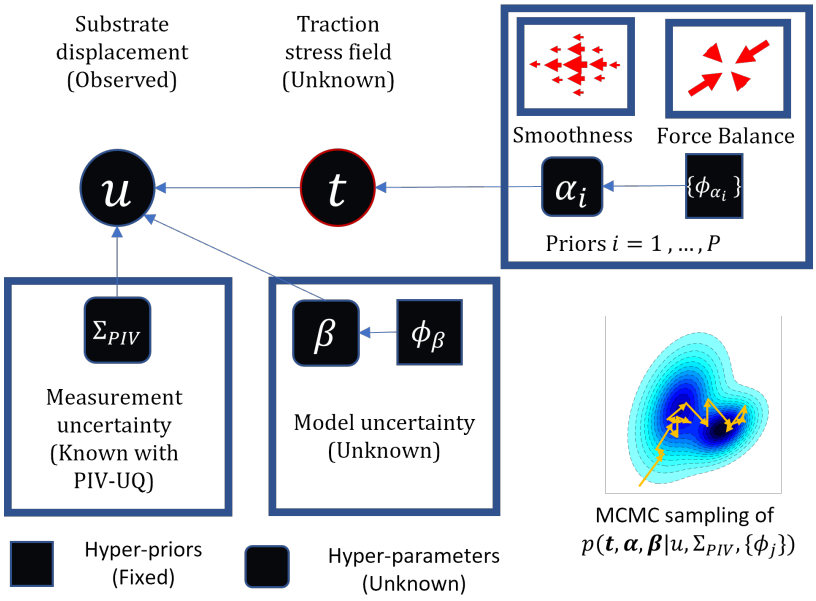

Fig 3.3. Hierarchical Bayesian TFM formulation for adaptive and self-consistent regularization. The problem of choosing a regularization parameter is treated in a Bayesian formulation. Substrate deformation ($\boldsymbol{u}_\mathrm{h}$) is the observed quantity, and it is modeled as the additive contribution of traction stresses ($\boldsymbol{t}$), locally resolved PIV measurement uncertainty $\boldsymbol{\Sigma}_\mathrm{PIV}$ and a global model error (β) that is unknown. The hierarchical formulation allows to express unknown hyper-parameters (α, β) for the prior on traction stress field and the model error term as random variables to be inferred. Therefore, a non-informative hyper-prior (ϕ_s) is specified to the hyper-parameters. The priors can encode reasonable assumptions such as smoothness and global force balance. Markov Chain Monte Carlo (MCMC), specifically an hybrid Gibbs sampling, is used for inference from the marginal posterior distribution, $p(\boldsymbol{t}|\boldsymbol{u}_\mathrm{h})$.

The posterior conditional distribution of traction stress is

$$p(\boldsymbol{t}|\boldsymbol{u}_\mathrm{h}, \alpha, \beta, \boldsymbol{\Sigma}_\mathrm{PIV}, \mathbf{L}) \propto \exp\left[-\frac{1}{2}(\boldsymbol{u}_\mathrm{h} - \mathbf{M}\boldsymbol{t})^T \Lambda^{-1}(\boldsymbol{u}_\mathrm{h} - \mathbf{M}\boldsymbol{t}) - \frac{\alpha}{2}\boldsymbol{t}^T\mathbf{L}\boldsymbol{t}\right]$$
$$\propto \exp\left[-\frac{1}{2}\left(\boldsymbol{t} - S_\mathrm{post}\mathbf{M}^T\Lambda^{-1}\boldsymbol{u}_\mathrm{h}^T\right]\mathbf{S}_\mathrm{post}^{-1}\left[\boldsymbol{t} - \mathbf{S}_\mathrm{post}\mathbf{M}^T\Lambda^{-1}\boldsymbol{u}_\mathrm{h}^T\right)\right], \quad (3.8)$$

with the covariance matrix $\mathbf{S}_\mathrm{post} = \left[\mathbf{M}^T\Lambda^{-1}\mathbf{M} + \alpha\mathbf{L}\right]^{-1}$. In turn, the conditional posterior distribution for the hyperparameter α is

$$p(\alpha|\boldsymbol{t}, \boldsymbol{u}_\mathrm{h}, \mathbf{L}) \propto \alpha^{N_w + \theta_\alpha - 1} \exp\left[-\frac{\alpha}{2}\left(2\phi_\alpha + \boldsymbol{t}^T\mathbf{L}\boldsymbol{t}\right)\right]. \quad (3.9)$$

These two probability density functions correspond to a Gaussian and a Gamma distribu-

Data: Displacement field, $\boldsymbol{u}_{\mathrm{h}} \in \mathbb{R}^{N_w}$; Displacement uncertainty, $\boldsymbol{\Sigma}_{\mathrm{PIV}}$; $\alpha_0, \beta_0 \in \mathbb{R}_{>0}$; Burn-in iterations, $\mathtt{it_b}$, max iterations, $\mathtt{it_m}$
Result: Posterior samples : $\{\boldsymbol{t}\} \in \mathbb{R}^{N_w}$; $\{\alpha\}, \{\beta\} \in \mathbb{R}_{>0}$

Initialization;
$\theta_\alpha \leftarrow 1$; $\theta_\beta \leftarrow 1$;
$\phi_\alpha \leftarrow 10^{-5}$; $\phi_\beta \leftarrow 10^{-5}$;
$\mathtt{it} \leftarrow 1$;
$\alpha \leftarrow \alpha_0; \beta \leftarrow \beta_0$
while $it < (it_b + it_m)$ **do**
  $\Lambda^{-1} \leftarrow [1/\beta \mathbf{U} + \boldsymbol{\Sigma}_{\mathrm{PIV}}]^{-1}$;
  $\mathbf{S}_{\mathrm{post}} \leftarrow [\mathbf{M}^T \Lambda^{-1} \mathbf{M} + \alpha \mathbf{L}]^{-1}$;
  $\mathbf{S}_{\mathrm{post}} \leftarrow \frac{1}{2}[\mathbf{S}_{\mathrm{post}} + \mathbf{S}_{\mathrm{post}}^T]$;
  $\boldsymbol{t} \sim N(\mathbf{S}_{\mathrm{post}} \mathbf{M}^T \Lambda^{-1} \boldsymbol{u}_{\mathrm{h}}, \mathbf{S}_{\mathrm{post}})$;
  $\alpha \sim \Gamma\left(\frac{n}{2} + \theta_\alpha, \frac{1}{2}(\boldsymbol{t}^T \mathbf{L} \boldsymbol{t}) + \phi_\alpha\right)$;
  `/* Simulate` β `by inverse transform sampling of discrete p.d.f */`
  $\hat{\beta} \leftarrow \arg\min \log(p(\beta | \boldsymbol{u}_{\mathrm{h}}, \boldsymbol{t}, \theta_\beta, \phi_\beta))$;
  Discrete β posterior domain, $\Omega_\beta \in [\hat{\beta} - 3\sigma_{\hat{\beta}}, \hat{\beta} - 3\sigma + \hat{\beta}]$;
  c.d.f, $F(x) = \int_{\Omega_{\hat{\beta}}} p(\beta | u, t, \theta_\beta, \phi_\beta)$;
  $\beta \sim F_x^{-1}(\mathtt{U(0,1)})$;
  if $it > it_b$ **then**
    Write $\{\boldsymbol{t}, \alpha, \beta\}$.
  end
end

Fig 3.4. Hybrid Gibbs sampler for TFM UQ inference.

tion, i.e.,

$$\boldsymbol{t} | \boldsymbol{u}_{\mathrm{h}}, \alpha, \beta, \boldsymbol{\Sigma}_{\mathrm{PIV}}, \mathbf{L} \sim N(\mathbf{S}_{\mathrm{post}} \mathbf{M}^T \Lambda^{-1} \boldsymbol{u}_{\mathrm{h}}^T, \mathbf{S}_{\mathrm{post}}), \tag{3.10}$$

$$\alpha | \boldsymbol{t}, \mathbf{L}, \theta_\alpha \sim \Gamma\left(N_w + \theta_\alpha, \frac{1}{2}|\mathbf{L}\boldsymbol{t}|^2 + \phi_\alpha\right), \tag{3.11}$$

and can be found in closed form. However, a similar derivation for the conditional posterior distribution for β,

$$p(\beta | \boldsymbol{t}, \boldsymbol{u}_{\mathrm{h}}) \propto |\Lambda|^{-1/2} \beta^{\theta_\beta - 1} \exp\left[-\frac{1}{2}(\boldsymbol{u}_{\mathrm{h}} - \mathbf{M}\boldsymbol{t})^T \Lambda^{-1} (\boldsymbol{u}_{\mathrm{h}} - \mathbf{M}\boldsymbol{t}) - \phi_\beta \beta\right], \tag{3.12}$$

did not produce an expression in closed form, since this expression also depended on $\boldsymbol{t}$. Consequently, we used the iterative Markov Chain Monte Carlo (MCMC) method [54, 167] to infer $p(\boldsymbol{t} | \boldsymbol{u}_{\mathrm{h}}, \alpha, \beta)$, $p(\alpha | \boldsymbol{t}, \boldsymbol{u}_{\mathrm{h}})$ and $p(\beta | \boldsymbol{t}, \boldsymbol{u}_{\mathrm{h}})$. The MCMC approach also provides

a straightforward way to calculate the quantity of interest, i.e., the marginal posterior distribution of the traction stress field, $p(\boldsymbol{t}|\boldsymbol{u}_{\mathrm{h}}) = \int p(\boldsymbol{t}|\boldsymbol{u}_{\mathrm{h}}, \alpha, \beta)\mathrm{d}\alpha\mathrm{d}\beta$ by summing over MCMC draws. The statistics of interest are approximated from the MCMC draws after a burn-in period ($\mathtt{it_b}$). Specifically, the expected (mean) marginal posterior traction stress field is given by $\hat{\mathbf{t}}(\mathbf{x}) = \mathbb{E}[\boldsymbol{t}(\mathbf{x})|\boldsymbol{u}_{\mathrm{h}}] \approx \frac{1}{N_d}\sum_i \boldsymbol{t}(\mathbf{x})_i$ and the marginal posterior standard deviation of the traction stress is $\mathrm{Std}[\boldsymbol{t}(\mathbf{x})|\boldsymbol{u}_{\mathrm{h}}] \approx \{\frac{1}{N_d}\sum_i(\boldsymbol{t}(\mathbf{x})_i - \mathbb{E}[\boldsymbol{t}(\mathbf{x})|\boldsymbol{u}_{\mathrm{h}}])^2\}^{1/2}$,where $\boldsymbol{t}_i$ represents the i^{th} draw of the vector of traction stress (out of N_d draws) from the Hybrid-Gibbs sampler. $\hat{\mathbf{t}}$ is the traction stress field output and the total, pointwise traction stress uncertainty $\sigma_t = \sqrt{\sigma_{tx}^2 + \sigma_{ty}^2}$, where σ_x is $\mathrm{Std}[t_x|\boldsymbol{u}_{\mathrm{h}}]$ and so on.

A hybrid-Gibbs sampler was adopted to sample these distributions using equations (3.10 - 3.12), as described in Fig 3.4. The hyperparameters were initialized to α_0 and β_0, which can be selected from reasonable maximum likelihood estimate values. In each sampling iteration, Gibbs sampling was performed by sequentially sampling the conditional posteriors, $p(\boldsymbol{t}|\boldsymbol{u}_{\mathrm{h}}, \alpha, \beta)$ and $p(\alpha|\boldsymbol{t}, \boldsymbol{u}_{\mathrm{h}})$. The posterior $p(\beta|\boldsymbol{u}_{\mathrm{h}}, \boldsymbol{t})$ was constructed numerically around the maximum *a posteriori* probability of $\beta|\boldsymbol{u}_{\mathrm{h}}, \boldsymbol{t}$ and an inverse transform sampling using the numerical cumulative distribution function was performed for $\beta|\boldsymbol{u}_{\mathrm{h}}, \boldsymbol{t}$. The burn-in was typically set to 20-50 iterations, and sampling was performed until convergence as assessed by trace plots and autocorrelation of the sampling chain. The convergence and, therefore, the computation time of Gibbs sampler depends on the size of the number of parameters (N_w) and the strength of spatial correlation in prior (i.e. $\mathbf{L}$) and $\boldsymbol{\varepsilon}_m$.

Using a laptop computer with Intel Core i7-10875H CPU and $< 10\,\mathrm{GB}$ RAM usage, PIV-UQ for a 2048×2048 px image analyzed with $W_L = 128$ ($N_w \approx 30$) and $n_B = 50$ took about 19 seconds (≈ 0.4 seconds per PIV run). The PIV-UQ compute time depends on the size of the image and W_L (e.g. with $W_L = 64$, 0.44 seconds per PIV run). For the typical resolution of the PIV field in TFM experiments, ($N_w \approx 30$ and $\mathtt{t_m} = 100$ iterations), it takes less than 3 minutes. For a higher resolution with $N_w \approx 60$, it takes approximately 1.5 hours. Since the matrix inversion is the computational bottleneck, workstations with more CPU cores can be used to speed up the computation.

3.2.5 Cell culture and imaging

Human vascular umbilical endothelial vein cells (HUVECs) (Cell Applications) were cultured in M199 (Gibco) supplemented with 10% (v/v) endothelial growth medium (Cell Applications), 10% (v/v) fetal bovine serum (Gibco), and 1% penicillin-streptomycin (Gibco). Mouse mesenchymal C3H/10T1/2 (ATCC) were cultured in low glucose Dulbecco's Modified Eagle's Medium (DMEM) supplemented with 10% v/v fetal bovine serum (Gibco) and 1% penicillin-streptomycin (Gibco). The cell plasma membranes were stained with CellMask

(5 μg/mL, Thermo Fisher Scientific) to visualize the HUVEC cells. Imaging is acquired with a live-cell, wide-field microscope (Leica DMI8 S inverted), 40 X NA 1.3 oil immersion objective and a sCMOS camera (Leica DFC9000) using LAS X software (Leica). Background subtraction (as indicated) is performed with Leica Thunder software (Instantaneous computational clearing).

3.2.6 Micropatterned polyacrylamide gel preparation

3.5 mm glass bottom dishes were pretreated in an ultraviolet ozone (UVO) box for 5 min, and the glass surface was then activated by using 2 M NaOH (Sigma) for 5 min. The whole dishes were washed with distilled water, dried, and treated with 3-aminopropyl-trimethoxysilane (Sigma) for 20 min. After removing silane, glass surfaces were rinsed with 100% EtOH (Decon), dried, and treated with 0.5% glutaraldehyde (Sigma) for 30 min. The activated surfaces were rinsed with distilled water and kept at room temperature for use within the same day.

Round 12 mm glass coverslips were pretreated in a UVO box for 5 min. The coverslips were then incubated with a 110 μL drop of 0.2 mg/mL PLL-PEG (poly[L-lysine] grafted with poly[ethylene glycol]) (Nanosoftpolymers) for 30 min at room temperature. After 30 minutes, PLL-PEG was removed from the coverslip surface by aspiration. The chrome face of the photomask (Advance Reproductions) was activated by UVO for 3 minutes. The PLL-PEG-coated coverslips were attached to the chrome side of the photomask by sandwiching a 2 μL drop of distilled water between both surfaces. The photomask and coverslips were then exposed to UVO light for 5 minutes. The photomask was detached from the coverslips by adding distilled water and then dried by aspirating excess water. A 110 μL drop of 50 μg/mL fibronectin (FN; Sigma-Aldrich) was placed on the PLL-PEG-coated surface of the coverslip and incubated for 1 hour. After 1 hour, the FN was removed, and the coverslip was washed once with distilled water. At this stage, the coverslip was ready to be printed with patterned FN on the PA gel surface. A thin film of FN was deposited on the areas of the coverslips that had been exposed to UVO light, whereas PLL-PEG prevented FN adhesion to the glass surface in the shadowed regions [168].

The polyacrylamide gels were fabricated with a mixture of acrylamide (Alfa Aesar) and bis-acrylamide (Fisher Bioreagent) following a well-established method [169]. For traction force microscopy, fluorescent 0.2 μm diameter beads were added to the mixture for later use as fiduciary markers of gel deformation. Phosphate-buffered saline (PBS, Gibco) was used instead of distilled water to promote bead distribution toward the surface of the gel. The Young's modulus was controlled via the amount ratio of acrylamide/bis-acrylamide, as previously described [169]. Once both coverslips were ready, freshly made 10% ammonium

sulfate (Sigma) and tetramethyl ethylenediamine (Sigma) were added to the polyacrylamide and bis-acrylamide mixture to initiate gel polymerization. Immediately after, a 2.5 μL drop of the mixture was pipetted on the treated glass bottom dish and sandwiched with the FN-patterned surface of the 12 mm round coverslip. The assembly was polymerized for 45 min before removing the round coverslip. The unpolymerized acrylamide was removed by rinsing twice with PBS. The resulting patterned gels were sterilized under 354 nm light for 5 min before adding the cells. The cells were seeded on top of the gels and allowed to adhere for 30 min. Unattached cells were washed off to avoid overgrowth of the patterns. The medium was reconstituted, and the cells were incubated overnight in the patterned regions.

3.3 Results

This section presents a computational verification and experimental demonstration of the proposed PIV-UQ and TFM-UQ techniques. PIV-UQ is verified using synthetic fluorescent bead images with prescribed displacement fields and noise sources in the image. PIV-UQ is shown to estimate substrate deformation uncertainty for each interrogation window. This information can be factored into the criteria to choose the critical PIV parameter, i.e., the interrogation window size, W_L. The synthetic simulations are then extended to the entire TFM pipeline to probe the influence of heteroskedasticity in PIV displacement data during the elastostatic inversion step. TFM-UQ applied to experimental data demonstrates the utility of the marginal posterior distribution in quantifying the variability due to hyperparameter selection and numerical implementation, and the automatic identification of high traction stress error areas associated with image artifacts.

3.3.1 PIV-UQ identifies local uncertainty arising from image features and substrate deformation

The bootstrap PIV-UQ method was verified on synthetically generated fluorescent bead images with spatially varying uncertainty. Fig 3.10 describes the computational pipeline to generate synthetic images for validation in detail. Briefly, 1024 $\times$ 1024 px images containing randomly placed synthetic beads with Gaussian intensity profiles (max. intensity 1000 a.u.) were generated. Each bead's centroid was displaced according to a prescribed substrate deformation field, and different fields including translation and shear were simulated. Gaussian pixel noise was added to the image with varying levels of signal-to-noise ratio (SNR), as shown in the left column of Fig 3.5A. SNR is defined as $20\log(1000/\sigma_{px})$, where σ_{px} is the std. dev. of the added pixel noise to the Gaussian bead image, saturated at an intensity of 1000 a.u. The process of random bead placement, displacement, and noise addition was repeated to generate ensembles of images. The baseline PIV and PIV-

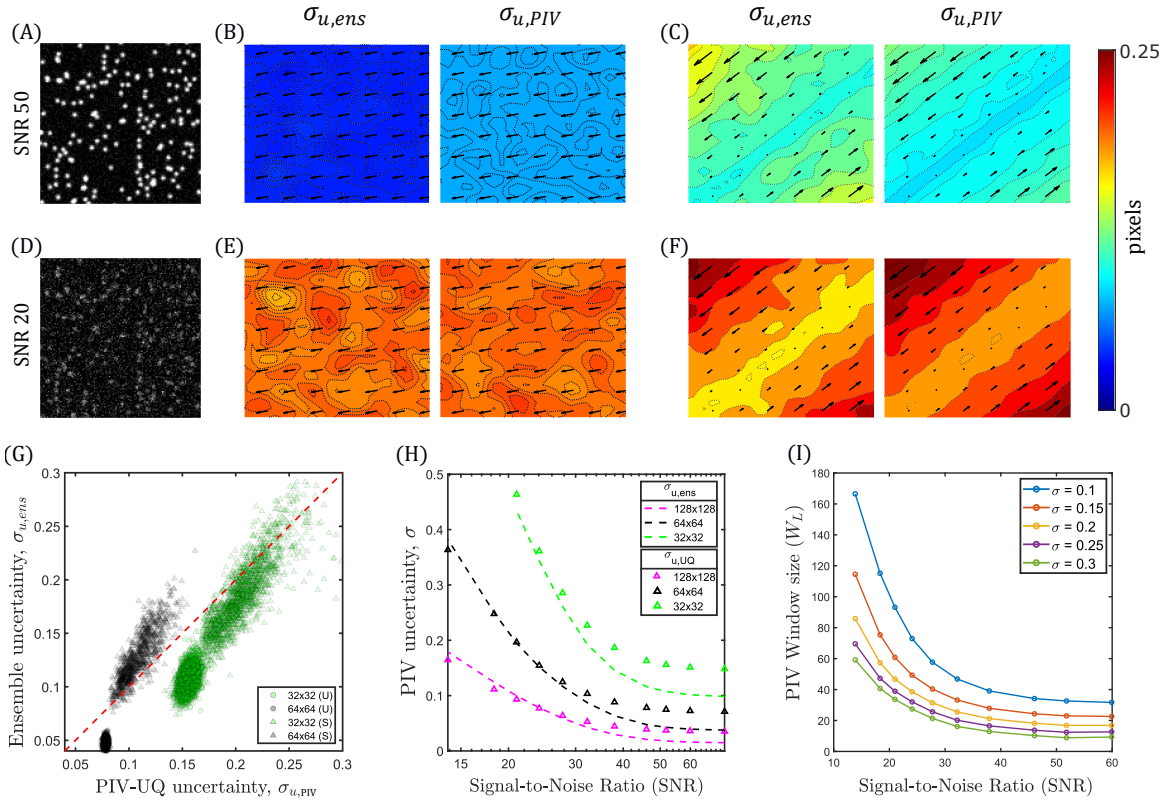

Fig 3.5. PIV-UQ synthetic validation. (A), (D) Gaussian profile synthetic beads are randomly generated at varying signal-to-noise ratio (SNR) of image pixel noise. A uniform (U) displacement field (B,E) or a shear (S) displacement field (C,F) is applied to the synthetic beads and PIV-UQ is performed as described in §3.2.2. In (B,C,E and F), left columns show ground-truth data consisting of applied displacement field vectors overlaid on contour maps of ensemble standard deviation ($\boldsymbol{u}_{ens}$ and $\sigma_{u,ens}$). The right columns represent the same data estimated from PIV-UQ, $\boldsymbol{u}_{PIV}$ and $\sigma_{u,PIV}$. (G) Joint distribution of $(\sigma_{u,ens}, \sigma_{u,PIV})$ for uniform (U) and shear (S) deformation fields for W_L of 32 and 64 pxs. Analysis procedure is described in Fig 3.10 (H) RMS of ensemble standard deviation and PIV UQ bootstrap estimates are compared for varying SNR values. (I) PIV Window size as a function of SNR with $\sigma_{u,\mathrm{PIV}}$ isolines derived from data presented in (H).

UQ algorithms were tested on all of the realizations and RMS values ($\sigma_{u,\mathrm{PIV}}$ and $\sigma_{u,ens}$ respectively. Total uncertainty, $\sigma = \sqrt{\sigma_{ux}^2 + \sigma_{uy}^2}$) were determined.

Two displacement fields were simulated (units in pixels):

$$\boldsymbol{u_1} = \begin{bmatrix} 2 \\ 0.6 \end{bmatrix}, \quad \boldsymbol{u_2} = \begin{bmatrix} \sin(\alpha) & g\cos^2(\alpha) \\ \cos(\alpha) & g\sin^2(\alpha) \end{bmatrix} \begin{bmatrix} x_0 \\ y_0 \end{bmatrix}. \tag{3.13}$$

Here, $\alpha = 45°$, $g = 20$ and $x_0, y_0 \in [-1, 1]$ px for the simulation domain. In line with literature [160, 164], a uniform displacement field $\boldsymbol{u_1}$ was simulated to understand the

statistical convergence of the PIV-UQ bootstrap method for varying levels of image noise, quantified by the signal-to-noise ratio SNR. In addition, a second displacement field, $\boldsymbol{u_2}$, representing shear was used as a benchmark to mimic the substrate deformation gradients typically seen in TFM experiments.

The left panels of Figs 3.5B,C display arrow plots of the ground-truth, ensemble-averaged displacement fields, $\boldsymbol{u}_{ens}$ overlaid on contour plots depicting the ensemble standard deviation, $\sigma_{u,ens}$. The right panels show the displacements and standard deviation obtained by the PIV-UQ bootstrap method, $\boldsymbol{u}_{\mathrm{PIV}}$ and $\sigma_{u,\mathrm{PIV}}$. For the uniform displacement field ($\boldsymbol{u}_1$), $\sigma_{u,ens}$ was spatially uniform (Fig 3.5B). On the other hand, the shear displacement field ($\boldsymbol{u}_2$) showed a clear spatial gradient and reached higher values in the upper left corner and lower right corner of the image. Visual comparison of the ground truth and PIV-UQ data suggests that the bootstrap method was able to estimate PIV uncertainty and its spatial variations, even if $\sigma_{u,\mathrm{PIV}}$ seemed to overestimate $\sigma_{u,ens}$.

The uncertainty estimation of PIV-UQ became more accurate when the image SNR decreased (Fig 3.5D–F). To analyze in more detail the ability of PIV-UQ to distinguish regions of varying deformation uncertainty, we plotted scatter plots of *true* standard deviation of each displacement vector vs. the corresponding PIV-UQ estimate in Fig 3.5G (and Fig 3.10). Uniform (U, circles) and shear (S, triangles) displacement fields are plotted using two different interrogation window lengths, $W_L = 32,\ 64$. The resulting point clouds approached the identity line $\sigma_{u,\mathrm{PIV}} = \sigma_{u,ens}$ as uncertainty increased, but there was a non-zero $\sigma_{u,\mathrm{PIV}}$ for zero true uncertainty, corresponding to the "floor" error level introduced by the bootstrap procedure.

Next, we analyzed the overall PIV uncertainty for the $\boldsymbol{u}_1$ field vs. SNR for different values of W_L (Fig 3.5H). As expected, $\sigma_{\boldsymbol{u},\mathrm{PIV}}$ decreased as SNR increased, and this dependence was steeper for smaller interrogation windows. In particular, $\sigma_{\boldsymbol{u},\mathrm{PIV}}$ followed the ground-truth values closely for $SNR \lesssim 30$, but it saturated for higher SNR values to the floor noise level described above. Of note, Fig 3.5H illustrates the common knowledge that PIV error decreases as the interrogation window is enlarged, setting a trade-off between spatial resolution and measurement error. Since PIV-UQ can quantify this dependence, it can be practical to plot W_L versus SNR for constant levels of σ, as in Fig 3.5I. The different curves in that plot indicate how the interrogation window size should be adjusted to keep a desired precision when performing PIV on images of varying quality. This approach offers an objective criterion for choosing W_L in TFM experiments.

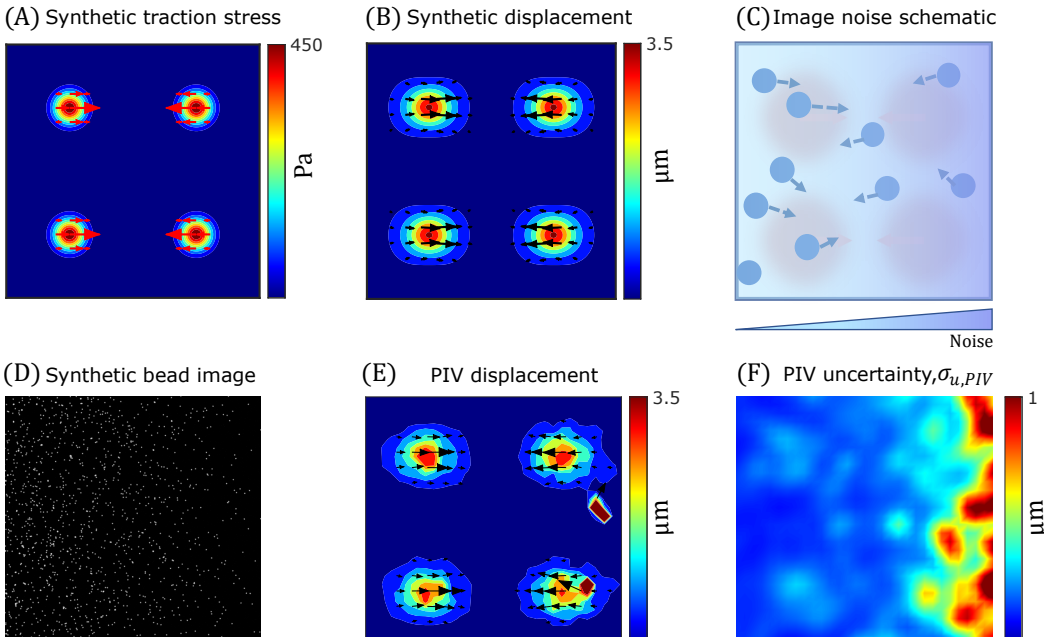

Fig 3.6. Synthetic pipeline to simulate experimentally relevant, spatially heterogeneous noise levels in TFM. (A) Synthetic traction stress generated from four traction islands of Gaussian profile, $\boldsymbol{t}_G$, one in each quadrant with a maximum stress of 500 Pa. (B) Synthetic displacement field resulting from the traction profile in (A). Substrate of $E = 5$ KPa and Poisson's ratio of 0.45 is used here. (C) Schematic depicting spatially heterogeneous noise addition directly to the synthetic image by varying fluorescent bead density in X-direction. The synthetic image also has image pixel noise equivalent to SNR = 50 (D) Synthetic fluorescent bead image encoding image pixel noise and bead density variations. (E) PIV-UQ deformation measurement $\boldsymbol{u}_{\text{PIV}}$ of the simulated bead images (D). (F) PIV-UQ estimation of uncertainty (standard deviation $\sigma_{u,\text{PIV}}$) showing higher uncertainty increasing with x-direction in agreement with noise addition process (C).

3.3.2 Heteroskedasticity of PIV measurement improves TFM regularization

Armed with the ability to estimate the spatially non-uniform (i.e., heteroskedastic) uncertainty in substrate deformation, we investigated how TFM-UQ propagated this uncertainty forward to the recovered traction stresses and how the regularization process was affected by heteroskedasticity. To establish ground-truth deformation data for this analysis, we used a synthetic traction stress field, $\boldsymbol{t}$, consisting of Gaussian traction islands ($\boldsymbol{t}_G$) i.e.,

$$\boldsymbol{t}_G = (t_{x,G}, t_{y,G}) = \left(t_p \exp\left\{-\left[(x-x_0)^2 + (y-y_0)^2\right] / \left(2s^2\right)\right\}, 0\right), \tag{3.14}$$

centered at (x_0, y_0) with a width equal to s^2 ($s = 15\,\mu$m) and peak traction stress $t_p = 500$ Pa. The stress field had four quadrants, each containing one traction island $\boldsymbol{t}_G$ pointing towards the vertical axis $x = 0$, as depicted in Fig 3.6A. The corresponding deformation

field, determined by solving equation (3.1) using Lin *et al*'s solution [38], is shown in Fig 3.6B. Synthetic fluorescent bead images were randomly generated and displaced according to the computed deformation field, as described in §3.3.1. To consider heteroskedasticity, a horizontal image noise gradient was generated by manipulating the bead density (Fig 3.6C–D) while keeping a spatially constant pixel noise (SNR = 50). The resulting images were used as inputs to PIV-UQ to determine the displacements and the corresponding standard deviation fields, $\boldsymbol{u}_{\mathrm{PIV}}(x,y)$ and $\sigma_{u,\mathrm{PIV}}(x,y)$, are represented in Fig 3.6E–F. Consistent with the results shown in §3.3.1, PIV-UQ captured the horizontal gradient of deformation uncertainty, as well localized increases in $\sigma_{\boldsymbol{u},\mathrm{PIV}}(x,y)$ at the four traction islands, where deformation gradients were more intense. The PIV-UQ outputs were used to build $\boldsymbol{u}_{\mathrm{h}} = \{u_{PIV}(x_1,y_1),\ldots,u_{PIV}(x_{Nw},y_{Nw}),v_{PIV}(x_1,y_1),\ldots,v_{PIV}(x_{Nw},y_{Nw})\}$ and the covariance matrix $\boldsymbol{\Sigma}_{\mathrm{PIV}} = \mathrm{diag}\left\{\sigma^2_{u,\mathrm{PIV}}(x_1,y_1),\ldots,\sigma^2_{u,\mathrm{PIV}}(x_{Nw},y_{Nw}),\sigma^2_{v,\mathrm{PIV}}(x_{Nw},y_{Nw}),\ldots,\sigma^2_{v,\mathrm{PIV}}(x_{Nw},y_{Nw})\right\}$, where N_w is the total number of interrogation windows. These variables were passed as inputs to the TFM-UQ framework described in §3.2.4.

The traction stress field recovered by TFM-UQ accurately approximated the prescribed ground truth $\boldsymbol{t}$ (Fig 3.7A). It is worth pointing out that TFM-UQ adapted its regularizer to the spatially varying noise of the displacement field, delivering a smooth traction stress map with spatial patterns resembling the ground-truth $\boldsymbol{t}$ field. Consistent with larger noise on the right-hand side of the image, regularization was stronger on that side. Moreover, TFM-UQ quantified the uncertainty of the recovered traction stresses at each point, defined as $\sigma_t = \sqrt{\sigma_{tx}^2 + \sigma_{ty}^2}$, (Fig 3.7B). This uncertainty increased from left to right, consistent with the noise gradient introduced in the image and the resulting $\boldsymbol{\Sigma}_{\mathrm{PIV}}$ distribution (Fig 3.6F). It also showed local maxima at the traction islands, where deformation gradients were highest.

Despite exhibiting a spatial gradient, the left-to-right growth of σ_t saturated quickly and its maximum value, $\sigma_{t,max} = 40$ Pa, was only 43% than its minimum value, $\sigma_{t,min} = 28$ Pa (Fig 3.7B). This uncertainty saturation was caused by the α-dependent noise reduction prior in eq. 3.7, as expected from the Bayesian theorem. To illustrate this phenomenon, here we provide an estimate for $\sigma_{t|\alpha,\beta}$ using the diagonal of the covariance matrix,

$$\mathbf{S}_{\mathrm{post}} = \left[\mathbf{M}^T\left(\beta^{-1}\mathbf{U} + \boldsymbol{\Sigma}_{\mathrm{PIV}}\right)^{-1}\mathbf{M} + \alpha\mathbf{L}\right]^{-1}.$$

This matrix has a heteroskedastic contribution from the PIV measurement variance, $\boldsymbol{\Sigma}_{\mathrm{PIV}}$ and a homoskedastic contribution from the β-proportional global error. Both contributions are affected by the elastostatic operator $\mathbf{M}$. In addition, $\mathbf{S}_{\mathrm{post}}$ has a homoskedastic contribution from the α-proportional noise reduction prior. Consider the homoskedastic model with identity prior (i.e. $\boldsymbol{\Sigma}_{\mathrm{PIV}} = \mathbf{0}$ and $\mathbf{L} = \mathbf{U}$ [49, 51]) equivalent to traditional Tikhonov

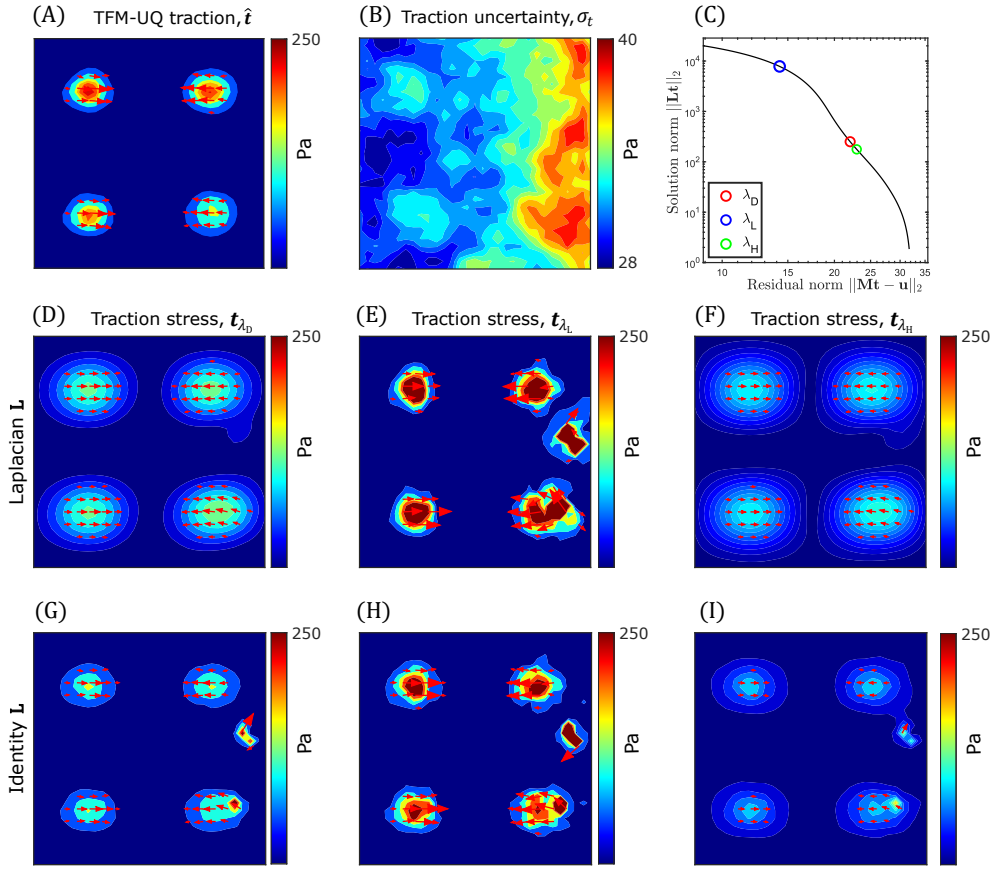

Fig 3.7. TFM-UQ adaptively regularizes based on the local displacement uncertainty. (A) Mean marginal posterior traction stress distribution ($\hat{\mathbf{t}} = \mathbb{E}[\boldsymbol{t}|\boldsymbol{u}_{\mathrm{h}}]$) approximated from Hybrid-Gibbs sampling. (B) Pointwise marginal posterior uncertainty (standard deviation σ_t) of posterior traction stress (C) L-curve to determine Tikhonov regularization parameter λ in traditional TFM methods. λ_D is obtained by finding the corner of the L-curve (maximum curvature) for differential noise simulation (Fig 3.6). λ_L and λ_H are regularization parameters obtained from L-curve corners of homoskedastic synthetic simulations with spatially uniform low noise (L) or high noise (H). (D,E,F) Tikhonov regularized traction stress field corresponding to L-curve corner λ_D, low noise λ_L and high noise λ_H respectively. $\mathbf{L}$ is the discretized Laplacian operator. (G,H,I) Tikhonov regularized traction stress field, with $\mathbf{L} = \mathbf{U}$ identity matrix. λ_D,λ_L and λ_H were determined to match 95^{th} percentile of traction stress magnitude with the respective fields in (D-F).

regularization ($\lambda = \alpha/\beta$). Considering the long wavelength limit $kh \ll 1$ for $\mathbf{M}$, the elastic interaction becomes local and spatially decoupled ($\mathbf{M} \to h/\mu\mathbf{U}$), where $\mu = E/2(1+\nu)$ is the shear modulus of the substrate [38]. In this case, each diagonal element of posterior traction,$\mathbf{S}_{\mathrm{post},ii} \to \beta^{-1}[h^2/\mu^2 + \lambda]^{-1}$. $\mathbf{S}_{\mathrm{post},ii}$ is bound between $\mu^2/h^2\beta^{-1}$ and α^{-1} for $h^2/\mu^2 \gg \lambda$ and $h^2/\mu^2 \ll \lambda$ respectively. The former limit is the maximum likelihood estimate when the prior contribution is minimum (less regularization) and vice versa. When

$\boldsymbol{\varepsilon}_m \neq 0$ (neglecting $\boldsymbol{\varepsilon}_\beta$), the corresponding bounds for $\mathbf{S}_{\text{post},ii}$ are $\mu^2/h^2\boldsymbol{\Sigma}_{\text{PIV},ii}$ and α^{-1} when $h^2/\mu^2 \gg \alpha\boldsymbol{\Sigma}_{\text{PIV},ii}$ and $h^2/\mu^2 \ll \alpha\boldsymbol{\Sigma}_{\text{PIV},ii}$ respectively. Analysis of $\mathbf{S}_{\text{post}}$ with $\boldsymbol{\Sigma}_{\text{PIV}}$ term illustrates that regularization in TFM-UQ is local corresponding to a spatially different regularization parameter $\lambda_i \sim \alpha\boldsymbol{\Sigma}_{\text{PIV},ii}$ compared to traditional regularization.

For finite-thickness substrates, the response of $\mathbf{M}$ depends on the frequency of the displacement field. Despite $\boldsymbol{\varepsilon}_m$ inducing heteroskedasticity in the posterior posterior traction stress distribution, the choice of a homoskedastic prior (i.e. global α) sets the global scale bringing the posterior variance in $\mathbf{S}_{\text{post}}$ close to α^{-1} (Fig 3.11 A). For Laplacian $\mathbf{L}$ matrix, a similar results are obtained with $\alpha\nabla^2(\boldsymbol{t}_i)\boldsymbol{\Sigma}_{\text{PIV},ii}$ depending on the local smoothness (Fig 3.6 A,B). This way, the Bayesian framework provides a systematic way to understand the effect of prior construction on both the scale of recovered traction stresses as well as the uncertainty propagation. To palliate this saturation, one could devise a heteroskedastic noise reduction priors such as replacing eq. 3.7 with

$$p(t|\alpha, \mathbf{L}) \propto \exp\left[-\frac{\alpha}{2}\boldsymbol{t}^T\boldsymbol{\Sigma}_{\text{PIV}}^{-1}\mathbf{L}\boldsymbol{t}\right],$$

which would make both the minimum and maximum values of the diagonal of $\mathbf{S}_{\text{post}}$ proportional to $\boldsymbol{\Sigma}_{\text{PIV}}$ under the assumptions outlined above. However, this prior would also provide weaker regularization in high-noise areas. Repeating the analysis in Fig 3.7A-B for this heteroskedastic noise reduction prior confirmed these predictions (see **??** B).

To further understand how TFM-UQ incorporated heteroskedasticity to regularize traction stresses, we compared this method's results with those obtained using a conventional, homoskedastic Tikhonov regularizer based on the same Laplacian kernel $\mathbf{L}$ and the elastostatic operator $\mathbf{M}$. The conventional regularizer depends on one hyperparameter, $\lambda = \alpha/\beta$, which was chosen by analyzing the L-curve, i.e., a log-log plot of $|\boldsymbol{t}^T\mathbf{L}\boldsymbol{t}|$ versus $|(\boldsymbol{u}_{\text{h}} - \mathbf{M}\boldsymbol{t})^T(\boldsymbol{u}_{\text{h}} - \mathbf{M}\boldsymbol{t})|$ (Fig 3.7C), to balance the solution's smoothness and its fit to the data as described previously [45, 46]. The value of λ at the point where the L-curve has the maximum curvature (the corner of the L-curve) is usually selected to regularize $\boldsymbol{t}$. Higher values of λ underfit the traction stresses and are located to the right of the L-curve corner. Conversely, lower λ values overfit and are located to the right of the corner. This standard approach attempts to find a one-fits-all value of λ for the whole image. This can lead to underfitting and overfitting in different regions of experiments with spatially dependent noise. Here, it is important to remark that the noise not only comes from the image, but also from the deformation imparted by the cells in the substrate, so local gradients of noise can arise even in high-quality images with uniform bead distributions.

In our validation dataset, we tested the conventional regularizer for three λ values: the optimal value λ_D corresponding to the L-curve corner, as well as a pair of values λ_H and

	True	TFM-UQ	λ_D	λ_L	λ_H
Weighted RMS error in $\boldsymbol{t}$ (Pa)	-	**26.44**	38.48	*64.46*	41.51
RMS σ_t (Pa)	-	**23.36**	N/A	N/A	N/A
Foreground mean $\boldsymbol{t}$ (Pa)	182.22	99.94	77.78	**170.13**	*63.53*
Foreground max $\boldsymbol{t}$ (Pa)	496	252.95	138.57	**477.31**	*110.17*
Background mean $\boldsymbol{t}$ (Pa)	8.65	**14.36**	23.67	*66.47*	22.38
Background max $\boldsymbol{t}$ (Pa)	76.79	**88.55**	119.20	*1428.77*	96.25
$SNR_{\boldsymbol{t}}$	21.05	**6.96**	3.28	*2.56*	2.84

Table 3.1. Performance comparison of locally regularized TFM-UQ with classical (global) Tikhonov regularization with discrete Laplacian Prior. The **best** and *worst* performing methods are highlighted in bold and italic respectively for each metric.

$\lambda_L < \lambda_H$ located on opposite sides of the corner. The λ_L and λ_H values were selected as the L-curve corner for synthetic simulations with low and high levels of spatially uniform noise. This corresponds to the left and right edges of the differential noise image (Fig 3.6 C,D). Compared with the ground-truth traction stresses shown in Fig 3.6A, the **L**-based Tikhonov regularizer underestimated and oversmoothed the traction stress field for $\lambda = \lambda_D$ (Fig 3.7D), showing significantly more spread patterns and lower traction stress values than TFM-UQ, without completely cancelling the noise (see the defect in the upper right quadrant). For $\lambda = \lambda_L$, **L**-based Tikhonov did not underestimate traction stresses values or spread their pattern (Fig 3.7E). However, this method produced significant noise and artifacts, including spurious concentrations of considerable traction stress in areas with zero ground-truth values. Finally, **L**-based Tikhonov severely underestimated and oversmoothed the traction stresses for $\lambda = \lambda_L$, producing non-zero values of $\boldsymbol{t}$ almost everywhere in the region of interest (Fig 3.7F).

For reference, we also recovered traction stress maps for λ_D, λ_L, and λ_H using a Tikhonov regularizer with the identity matrix (i.e., $\mathbf{L} = \mathbf{U}$) instead of the discretized Laplacian operator since this regularizer was preferred in several previous studies [47, 49]. The values of λs were selected so that the 95^{th} percentile of the traction stress field magnitude with $\mathbf{L} = \mathbf{U}$ matches with their counterparts using the Laplacian $\mathbf{L}$ precision matrix. These maps, displayed in Fig 3.7G–I, showed a similar trend as those obtained with the Laplacian smoother in their variation with λ. On the other hand, they had less spread stress contours but displayed more noise and spurious traction islands.

The behaviors visualized in Fig 3.7 manifested quantitatively in metrics of the recovered traction stress fields, summarized in Table 3.1. TFM-UQ provided the minimum root mean square (RMS) error with respect to the ground truth, and this error was well approximated by the TFM-UQ RMS σ_t estimate. To quantify how different regularizers balanced overfit-

ting and underfitting, we defined the foreground traction map as the region where the true stress magnitude $|\boldsymbol{t}| \geq \mathrm{RMS}(\boldsymbol{t})$ (i.e., 75 Pa for the synthetic field of 3.6 A). Likewise, the background traction map was defined as the region where $|\boldsymbol{t}| < \mathrm{RMS}(\boldsymbol{t})$. We then evaluated the mean and maximum traction stress magnitude of the foreground and background maps. A TFM method with a good overfitting-underfitting balance should yield both a large foreground traction magnitude and a low background traction magnitude. This analysis, also summarized in Table 3.1, showed that TFM-UQ outperformed the standard regularizers in all metrics except in mapping the foreground traction, where it ranked second best after the standard λ_L regularizer. However, λ_L performed worst among all methods in RMS error, keeping a low background traction and overall SNR of the traction map. Overall, TFM-UQ showed the best balance between overfitting and underfitting by considering the local deformation uncertainty from PIV-UQ. In addition, TFM-UQ was able to propagate PIV uncertainty to estimate the error of the recovered traction stresses.

3.3.3 Experimental Demonstration of PIV-UQ and TFM-UQ

This section describes two sets of live cell experiments demonstrating the practical application of PIV-UQ and TFM-UQ, and illustrate how these methods deal with spatially varying error in the measured substrate deformation. First, we performed experiments on C3H/10T1/2 fibroblasts seeded on substrates with micropatterned square fibronectin islands of width 75 μm (Fig 3.8 A). Micropatterning extracellular matrix proteins on cellular substrates is a common approach for guiding adherent cells to adopt predefined shapes [168]. In our study, we used patterned substrates as a benchmark for TFM-UQ, because these substrates can exhibit gradients of fluorescent bead brightness and background noise, as shown in Fig 3.8B. This feature allowed us to objectively assess PIV-UQ and TFM-UQ against different levels of image noise when observing the same cell at the same instant of time. To this end, we compared the traction stresses recovered from the "raw" images obtained by wide-field fluorescence microscopy as well as from a second dataset (Fig 3.8 C) obtained by applying a non-linear background subtraction ("BGS") method (Leica Instantaneous Image Clearing [170]) that improved the signal-to-noise of the image by a factor of 6.

Figs 3.8D,G show the in-plane substrate deformations measured by PIV-UQ for these two datasets using PIV interrogation windows of length $W_L = 128$ pixels, $\boldsymbol{u}_{\mathrm{PIV},128}(x, y)$. These vector maps were overlaid on their associated uncertainty maps, $\sigma_{\boldsymbol{u},\mathrm{PIV},128}(x, y)$. Consistent with the synthetic analyses presented in §3.3.1, the PIV uncertainty was markedly higher in the raw image. Also consistent with the synthetic analyses, regions with deformation gradients such as the edges and corners of the islands, also exhibited higher PIV uncertainty. Coefficient of variation (CoV) was used to determine convergence of the estimator $\sigma_{u,\mathrm{PIV}}$.

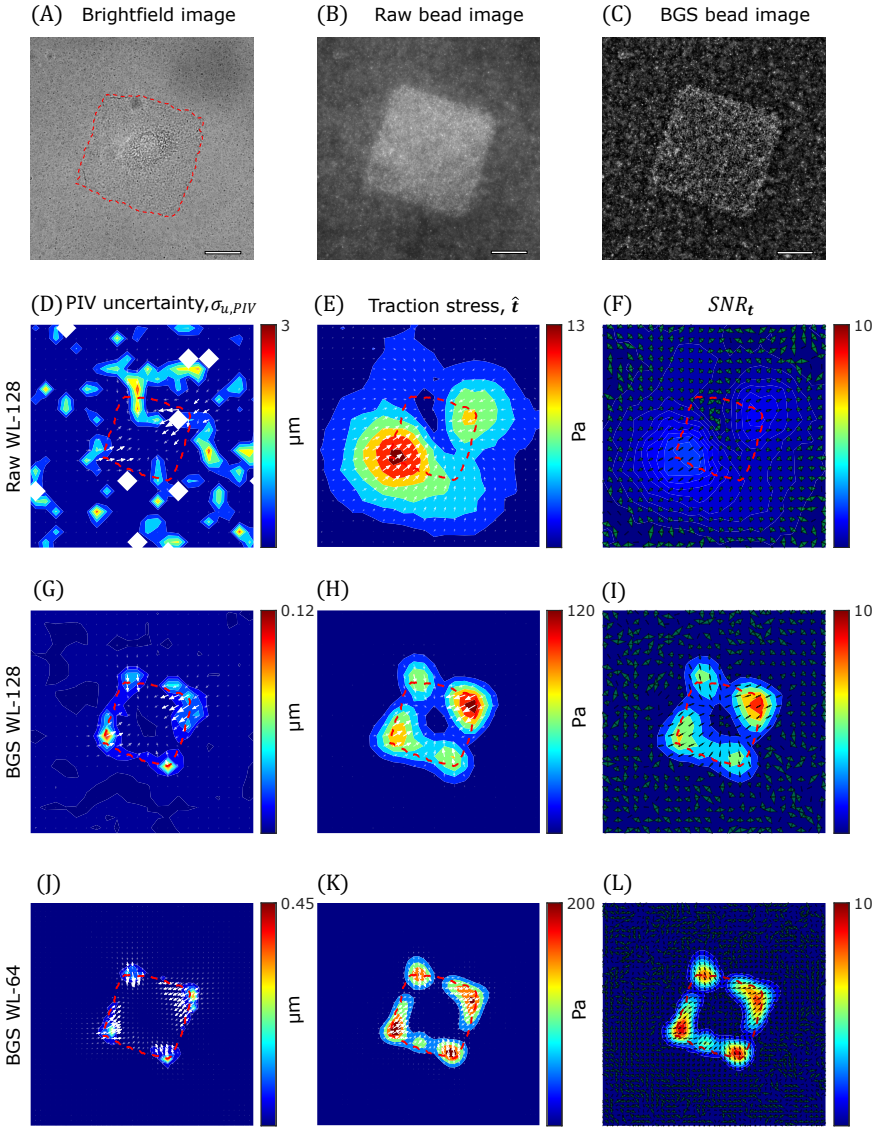

Fig 3.8. TFM-UQ captures variability associated with microscopy image quality. (A) Brightfield image of C3H/10T1/2 cell cultured on fibronectin micropatterned island of length 75 μm (Red dashed outline). (B) "Raw" wide-field fluorescent bead image (beads of size 0.2 μm). (C) "BGS" Background subtracted image processed from (B). (D,G,J) $\boldsymbol{u}_{\mathrm{PIV}}$ (arrows) overlaid on PIV-UQ uncertainty field ($\sigma_{u,\mathrm{PIV}}$) corresponding to raw WL-128, BGS WL-128 and BGS WL-64 respectively. Here, WL denotes the PIV interrogation window size W_L. (E,H,K) Mean marginal posterior traction stress field ($\hat{\mathbf{t}}$) corresponding to Raw WL-128, BGS WL-128 and BGS WL-64 respectively. (F,I,L) Traction stress signal-to-noise ratio ($SNR_{\boldsymbol{t}}$) plotted as a heatmap corresponding to Raw WL-128, BGS WL-128 and BGS WL-64 respectively. Overlaid uncertainty arrows denote the pointwise angular uncertainty corresponding to 1 circular std. dev. of marginal posterior $p(\boldsymbol{t}|\boldsymbol{u}_{\mathrm{h}})$. Scale bar : 25 μm.

Fig **??** shows that this convergence depends on the resolution as well as the image quality (e.g., to achieve 10% variability, raw images required $n_B \approx 48$ iterations, while BGS images only required $n_B \approx 7$ iterations). Figs 3.8E,H show the traction stress maps recovered from the raw and background subtracted (BGS) images for $W_L = 128$ pixels. The traction stresses recovered from the raw images were markedly weaker and their spatial patterns were more spread out than those obtained from the background subtracted images. The differences were due to the more aggressive regularization applied to the PIV vectors from the raw images, which had significantly more uncertainty.

These data illustrate that the effective spatial resolution of the traction stresses recovered by TFM-UQ is not uniquely determined by the PIV resolution. While this is a relatively well-known consequence of regularization shared with other TFM methods [35, 47], it is worth noting that TFM-UQ uses an objective criterion to select the level of regularization automatically. Moreover, the traction stress uncertainty, σ_t, can be used to quantify the signal-to-noise ratio in the recovered traction stresses, $SNR_{\boldsymbol{t},128} = |\hat{\mathbf{t}}_{128}|/\sigma_{t,128}$. Figs 3.8F,I display these $SNR_{\boldsymbol{t},128}$ for raw and BGS images together with vector fans whose width represents the angular uncertainty in the orientation of the $\boldsymbol{t}$ vector. The figures reveal that the largest variability in the direction of $\boldsymbol{t}$ was observed at locations of low traction stress magnitude. Moreover, and as expected, these data indicate that the $SNR_{\boldsymbol{t},128}$ obtained from the raw images was significantly worse than that obtained from the background subtracted ones with higher contrast.

The results presented above verify that the $SNR_{\boldsymbol{t}}$ maps obtained by TFM-UQ effectively capture how image quality affects traction stress recovery. A practical application of $SNR_{\boldsymbol{t}}$ is to evaluate how varying W_L affects this recovery. To illustrate this idea, we re-ran PIV-UQ and TFM-UQ for the BGS images at higher resolution, i.e., using $W_L = 64$ pixels, and asked if this change produced a more precise traction stress map. The answer to this question is not trivial and depends on whether the gain in PIV resolution (Fig 3.8J), which is accompanied by an increase in peak traction stresses at cell-substrate attachments (Fig 3.8K), compensates the increase in the PIV measurement error and its propagation to the traction stresses. In this case, comparing Figs 3.8I,L indicated that $SNR_{\boldsymbol{t},64} > SNR_{\boldsymbol{t},128}$ and, therefore, that refining the PIV window size led to a more precise representation of the traction stresses. Repeating the analysis for $W_L = 32$ pixels (Fig 3.13) did not yield a higher $SNR_{\boldsymbol{t},32}$ everywhere, compared to $SNR_{\boldsymbol{t},64}$, showing a notable decrease in the top-right corner. Likewise, the traction stresses recovered for $W_L = 32$ did not display a significantly higher spatial resolution than those obtained for $W_L = 32$ as the regularization was more aggressive for the $W_L = 32$ dataset. This example illustrates how TFM-UQ can be applied to objectively choose the optimal PIV window size that balances resolution with

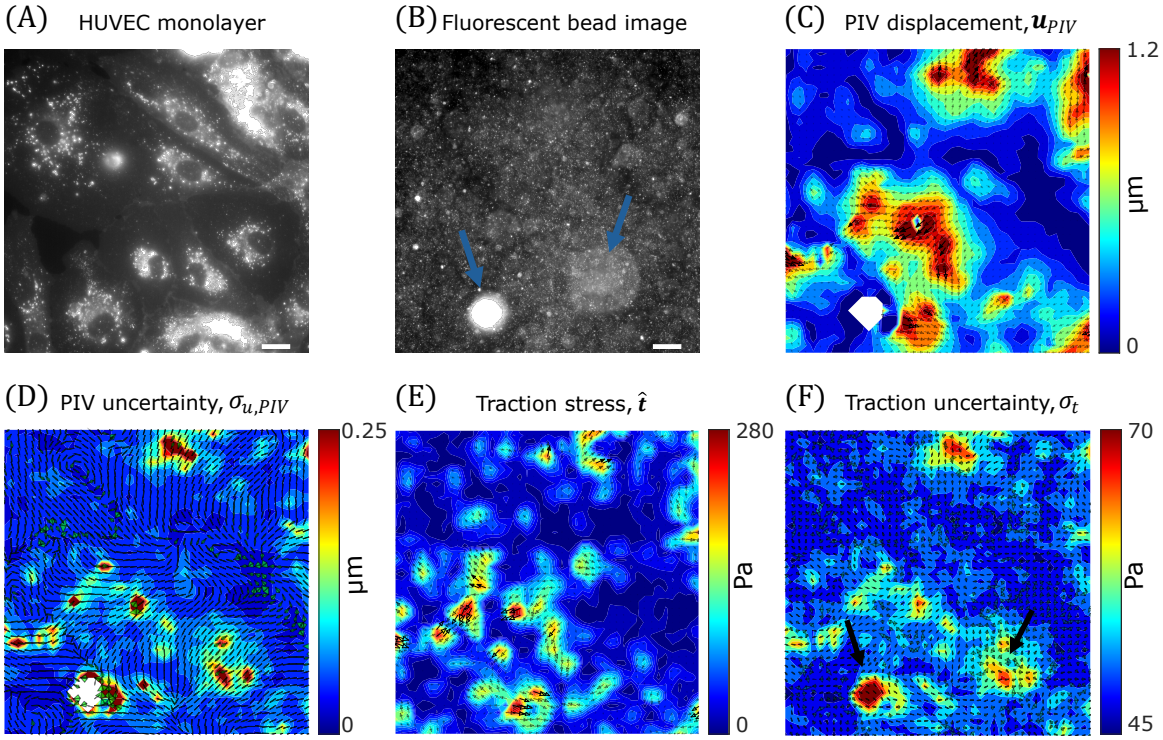

Fig 3.9. TFM-UQ applied to endothelial monolayer experiment demonstrates uncertainty propagation. (A) Membrane labelling of HUVEC monolayers with CellMask. (B) Corresponding fluorescent bead image (beads of size 0.2 μm). Arrows indicate bead-related image artifacts (C) PIV-UQ displacement field $\boldsymbol{u}_{\mathrm{PIV}}$ (D) PIV-UQ uncertainty map, $\sigma_{u,PIV}$. White regions indicate 'bad' PIV windows that were deleted and replaced as described in §3.2.2. Uncertainty arrows denote the pointwise angular uncertainty corresponding to 1 circular std. dev. of bootstrapped PIV-UQ distribution. (E) Inferred mean marginal posterior traction stress, $\hat{\mathbf{t}}$ (F) Marginal posterior traction stress uncertainty field (σ_t). Uncertainty arrows denote the pointwise angular uncertainty corresponding to 1 circular std. dev. of marginal posterior $p(\boldsymbol{t}|\boldsymbol{u}_{\mathrm{h}})$. Scale bar : 25 μm

error, which in this case would be $W_L = 64$ pixels.

A second set of experiments was performed with human umbilical vascular endothelial cells (HUVECs) seeded on fibronectin-coated PAA gels to form confluent monolayers (Fig 3.9A). To illustrate how TFM-UQ handles images with distinct areas of poor quality, we selected an example containing a large clump of fluorescent beads and an out-of-focus region, indicated by the arrows in Figure 3.9B. Figure 3.9C displays the substrate deformation map obtained by PIV-UQ for this experiment, showing significant spatial gradients consistent with previously reported data from HUVEC monolayers [78]. The associated PIV-UQ uncertainty maps in vector magnitude and direction, shown in Figure 3.9D, indicate that the PIV errors were mostly localized to regions of poor image quality and spatial gradients of $\boldsymbol{u}_{\mathrm{PIV}}$, in agreement with the results presented in §3.3.1. In the bead clump, PIV-UQ

failed to provide deformation vectors leading to the empty white areas in Figs 3.9C-D. To feed input to the TFM-UQ algorithm in this empty region, the displacement vectors were prescribed using a median filter, and $\boldsymbol{\Sigma}_{\mathrm{PIV}}$ was set to equal to the maximum value from the rest of the image. TFM-UQ used the $\boldsymbol{u}_{\mathrm{PIV}}$ and $\boldsymbol{\Sigma}_{\mathrm{PIV}}$ fields to recover and regularize the traction stresses (3.9E), and mapped the uncertainty in the magnitude and direction of the stress vectors (3.9F). It is worth noting that the areas of highest σ_t co-localized with the bead clump, the out-of-focus region in the fluorescent bead image and with the largest deformation gradients. These results illustrate how TFM-UQ integrates information from PIV measurements and image quality to map the confidence of the recovered traction stresses.

3.4 Discussion

Since the pioneering silicone membrane wrinkling assay [61] demonstrated the possibility of detecting cell-generated traction stresses, various strategies have been exploited to quantify these stresses. Currently, a common approach involves measuring substrate deformation by tracking fiduciary markers (e.g., fluorescent beads) embedded in elastic substrates of known mechanical properties. Then, the traction stresses corresponding to the measured deformation field are recovered by solving an inverse elastostatic problem. The shortage of tools to quantify how measurement uncertainty propagates to the recovered stresses hampers the objective evaluation of experimental protocols and elastostatic inversion methods. These limitations make it impossible to separate biological variability from measurement error and promote the view that TFM technique is susceptible to methodological arbitrariness [35, 52, 62].

3.4.1 Uncertainty Quantification in TFM

One of the most common methods to measure the cell-induced substrate deformations for TFM is particle image velocimetry (PIV), a technique originally developed to measure velocity vectors in fluid flows [79, 80]. PIV measurement errors are associated with the signal-to-noise ratio (SNR) of the image and spatial deformation gradients. In a typical TFM experiment, the image SNR can be optimized by choosing fluorescent beads of the appropriate size, and controlling their density and spatial distribution during substrate fabrication. Image quality can also be tuned by adjusting substrate thickness, the optics and operational settings of the microscope used for acquisition, and post-processing of the acquired images [22, 47, 52, 171]. Batch-to-batch variability in reagents and operator dependence in fabrication and imaging protocols can cause image quality variations (bead clumping, focus and bead density gradients, etc.) within and across experiments. In ad-

dition, differences in equipment, experimental, and analysis protocols among laboratories can create experimental uncertainty in TFM. Ultimately, PIV uncertainty is impossible to control *a priori* since it also depends on the deformation gradient generated by the cells on the substrate. Therefore, it is necessary to develop tools to estimate PIV uncertainty in individual TFM experiments and propagate this uncertainty to the recovered traction stresses.

The fluid mechanics community has devoted extensive research to quantifying PIV uncertainty [160–162], but significant differences between experimental images generated in elastic substrates and fluid flows impede the transfer of that knowledge to TFM. Typically, TFM images have limited bead brightness due to concerns over phototoxic effects. The substrate deformations are relatively small and experience gradients over micrometric lengthscales. Moreover, ensemble correlation approaches do not improve PIV resolution in TFM since the bead pattern does not vary over time, unlike in flowing fluids. In addition, TFM experiments can last hours and are more sensitive to drift and positioning errors along the optical axis. Consequently, image cross-correlation peaks are broader and more irregularly shaped in TFM than fluid flow experiments. This feature makes the parametric methods widely used to estimate uncertainty in fluid flow less well suited for TFM.

This work introduced a non-parametric bootstrap method to estimate PIV uncertainty in TFM experimental images (PIV-UQ). Bootstrap resampling is a powerful tool for constructing accuracy estimates without ground truth by randomly resampling limited data. Since the PIV estimate is exclusively based on the information contained within the interrogation windows ($\{\mathbf{W}_{ij}\}$), PIV-UQ teases out the possible displacement vectors by perturbing different pixel contributions to the final estimator. In PIV-UQ, the image pixels are bootstrapped multiple times to produce a distribution of measured substrate displacement vectors for each interrogation window, from which the most likely displacement and its standard deviation are calculated. Thus, the PIV-UQ estimates the variability or stability of PIV estimate due to the non-uniform motion of tracers, pixel noise due to experimental and imaging or post-processing employed. This approach generalizes Kybic's [164] bootstrap method by introducing perturbations directly in the image data instead of in the optimization that calculates the deformation. Therefore, the bootstrap method derived for PIV-UQ in this work could be extended to other deformation measurement techniques such as image registration. Apart from TFM experiments, PIV is routinely used in biomechanics and mechanobiology research to estimate *in vitro* and *in vivo* tissue flow [7, 14, 172], and cardiomyocyte contractility assays [22, 173]. The PIV-UQ tools developed here should be directly transferable to those applications.

Bayesian methods model the quantities of interest as random variables, assimilating in-

formation regarding physical models, input data, prior constraints, and their variability. Thus, these methods offer a natural framework to propagate substrate deformation uncertainty to the traction stresses recovered by TFM. Bayesian methods were proposed in Dembo and Wang's seminal TFM work [144], and the interest in adapting them to TFM is recently increasing [49, 63, 174]. Traditionally, Bayesian TFM workflows have focused on elastostatic inversion without explicitly considering the uncertainty in substrate deformation or propagating this uncertainty. Interestingly, Butler *et al*'s pioneering constrained FTTC method [37] considered the possibility of nonphysical displacement vectors and involved an iterative algorithm to correct these measurements so that the traction stresses satisfied a prior constraint. A more detailed Bayesian TFM model including cell area as a prior constraint has been developed recently [174]. However, both of these methods do not propagate measurement errors from the images or the displacement field. To the best of our knowledge, the only effort to propagate uncertainty from the images to traction stresses is Boquet-Pujadas *et al*'s optical flow method for substrate deformation [63], where traction stresses are modeled in the image registration process. This approach considers the traction stresses the only cause for deviations in pixel intensities in the image set $\boldsymbol{I}$. While the spatial variability of error is incorporated in the framework, the work was primarily theoretical and did not consider experimental data. In particular, it would be interesting to assess how the framework handles image error sources that are not explicitly modeled (e.g., fluorescent bead artifacts, camera focus variation, etc).

In this work, we developed TFM-UQ, a hierarchical Bayesian framework that propagates the PIV measurement variability estimated by PIV-UQ and provides point-by-point estimations of traction stress uncertainty. The resulting uncertainty maps, $\sigma_t(x, y)$, establish error bars for the traction stress recovered at each location, both in magnitude and direction of the stress vector. This information can help interpret and analyze TFM experiments for multiple reasons. Among these, it may help identify outliers automatically and objectively. It allows for separating biological and measurement uncertainties when pooling data from repeat experiments. It can also help pinpoint sources of measurement error and refine experimental protocols and image analysis methods.

Applying PIV-UQ to fluorescent bead images from TFM experiments, we demonstrated this method quantifies how the PIV error depends on the image quality and the size W_L of the interrogation window. The latter is a key PIV parameter affecting measurement error and resolution. TFM protocols often provide loose guidance suggesting W_L should be small enough to resolve the relevant spatial features of cell-generated deformations and large enough to minimize PIV error [22, 34]. The scarcity of UQ tools in TFM has hampered the development of more quantitative criteria. The PIV-UQ and TFM-UQ tools presented

in this manuscript can be used independently and/or together to objectively choose the optimal PIV window size for each experiment. Using PIV-UQ alone without TFM-UQ, one could analyze one or a few fluorescent bead images selected from a batch of frames (e.g., frame of maximum contraction) in a time-lapse experiment to adjust W_L, so that the PIV measurement error remains within expectations and is conserved across experiments. Using PIV-UQ and TFM-UQ together, it is possible to identify the value of W_L that maximizes the resolution and precision of the recovered traction stresses for each experiment.

3.4.2 Uncertainty-Aware Elastostatic Inversion and Regularization

A variety of mathematical models have been used to represent the elastostatic response of TFM substrates and an even wider variety of techniques has been proposed to invert the model equations, including boundary element methods [47, 49, 50, 144], Fourier expansions providing exact analytical solutions in frequency space [33, 34, 37, 38, 47], finite element methods [175], Bayesian methods [5, 49, 51, 63, 174], etc. Owing to the physics of elastostatics, this inversion amplifies the small-scale (high-frequency) features of the measured deformation field. Because measurement noise typically has a high content of small-scale features, TFM outputs can suffer from significant noise even when using exact analytical solutions for inversion. In addition, discretized numerical approximations of the elastostatic response can lead to singular or near-singular linear systems of equations, especially when the domain size and spatial resolution increase. Therefore, regularization is a crucial aspect of image analysis in TFM.

Regularization and data smoothing are routinely employed to enforce well-behaved traction stress fields and suppress the amplification of high-frequency noise during the inversion. The specifics of the regularization algorithm can vary among TFM formulations, but in general, all regularization schemes introduce a penalty term whose residual must be minimized together with the elastostatic residual. Regularization methods generally require specifying the values of the hyper-parameters controlling each residual's weight in the global minimization process. Heuristic approaches to hyperparameter selection, such as the L-curve criterion [45, 46], have enjoyed popularity, but they are susceptible to significant user bias and are often challenging to interpret objectively [35, 45, 52]. Self-consistency [48, 52, 63] is an appealing principle to find regularization parameters, but it requires *a priori* knowledge of $\boldsymbol{\Sigma}_{\mathrm{PIV}}$, which was not previously available. The PIV-UQ technique presented in this manuscript paves the way for a systematic application of this principle.

The interest in Bayesian methods to select hyperparameters has increased in the last decade [5, 49, 51, 63]. These methods formulate hyperparameter inference as the maximization of the posterior joint probability $p(\lambda, \boldsymbol{t}|\boldsymbol{u}_{\mathrm{h}})$ or the evidence $p(\lambda|\boldsymbol{u}_{\mathrm{h}})$, where λ is model

hyperparameter(s) and $\boldsymbol{u}_{\mathrm{h}}$ the measured substrate deformation. While this unified framework is attractive and has built-in self-consistency, the existing works pay little attention to the uncertainty in PIV-measured substrate deformation or the variability in hyperparameter selection. There is an abundance of methods (e.g., low-pass filtering, median filtering, etc) to "pre-regularize" the $\boldsymbol{u}_{\mathrm{h}}$ obtained from PIV or equivalent technique prior to traction stress recovery. However, once the measurements are pre-regularized, the information about which PIV vectors are less reliable than others is not passed on to the TFM algorithm. Consequently, existing Bayesian methods make strong assumptions about the nature of the noise distribution, i.e., that it is spatially uniform and independent of the effects of cellular forces [47, 49]. These assumptions have not been verified systematically.

To overcome the drawbacks of traditional TFM regularization schemes and the lack of posterior uncertainty quantification, we developed TFM-UQ – a hierarchical Bayesian framework with Markov Chain Monte Carlo (MCMC) sampling and non-informative hyperprior distributions for the hyperparameters. TFM-UQ accounts for the measured PIV uncertainty when enforcing prior constraints, such as the smoothness of the traction stress field, thereby adjusting the level of regularization to the spatial distribution of the measurement errors. We showed that this approach locally balances overfitting and smoothing, and can outperform traditional regularization methods, especially in experiments where the quality of the fluorescent bead images or the measured displacements exhibit appreciable gradients.

Uncertainty propagation in TFM-UQ considers the amplification of high-frequency noise in the substrate displacements and the effect of the regularizing prior(s) defined to suppress that noise. As a consequence of the interplay between these factors, the bounds of σ_t are determined by the PIV uncertainty and the strength of the regularizer respectively. This interdependence reflects the fact that regions with higher measurement uncertainty are regularized more heavily, so the prior information of the regularizer overrides the PIV contribution in those regions. The analysis also showed that the posterior traction precision is higher for softer gels in the long wavelength (pure shear) limit. Future studies should address the interactions between heteroskedastic measurements and Bayesian priors in the context of TFM and the effect of substrate material parameters on the uncertainty propagation. In particular, the possibility of introducing non-global smoothness priors (shrinkage or heteroskedastic priors) deserves further investigation. TFM-UQ can run on a personal computer in a few minutes depending on the resolution. Additional investigations using approximate inference methods are worthwhile to make the calculations near real-time for high throughput applications.

3.5 Acknowledgements

This chapter, in part, is published as a pre-print [4] and is under revision :

Kandasamy, A., Yeh, Y.-T., Serrano, R., Mercola, M. and del ´Alamo, J.C. Uncertainty-Aware Traction Force Microscopy. *bioRxiv* (2024). The dissertation author is the primary author of this work.

The authors thank Dr.Alejandro Gonzalo and Dr.Susanne Rafelski for providing critical feedback on the manuscript and Dr.Kelly Stevens for providing C3H/10T1/2 fibroblast cell line.

3.6 *Supplementary information*

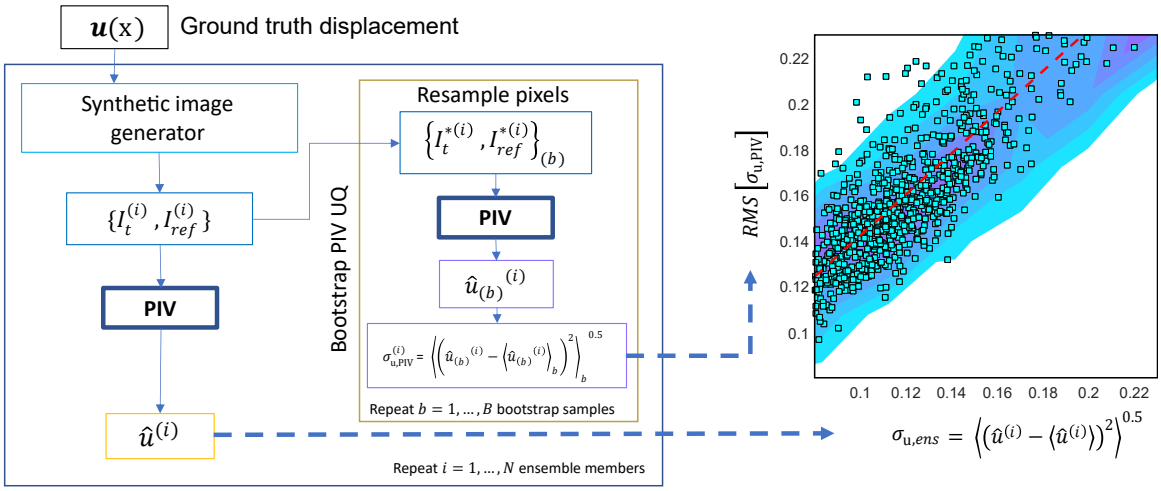

Fig 3.10. PIV-UQ synthetic validation workflow. A fixed, high-resolution ground truth displacement $\mathbf{u}(\mathbf{x})$ is generated. One realization of synthetic images corresponding to the ground truth displacement is obtained as follows : Synthetic beads are simulated by randomly placing Gaussian beads of prescribed density with a maximum brightness of 1000 a.u. ($\boldsymbol{I}_{ref}$). The centroid of the Gaussian beads are shifted according to $\mathbf{u}(\mathbf{x}_{bead})$ to generate $\boldsymbol{I}_t$. PIV is performed to generate a displacement vector for each interrogation window, $\hat{\mathbf{u}}$. This process is repeated N times to obtain an ensemble of synthetic image and $\hat{\mathbf{u}}$ realizations that provide the true ensemble standard deviation, $\sigma_{u,ens}$. For each of the i^{th} ensemble image set $\{\boldsymbol{I}_t^{(i)}, \boldsymbol{I}_{ref}^{(i)}\}$, PIV-UQ method is performed by bootstrapping n_B times generating an $\sigma_{u,\mathrm{PIV}}^{(i)}$ for each ensemble realization i. The root mean square (RMS) of $\sigma_{u,\mathrm{PIV}}$ is reported over N ensemble realizations for each interrogation window. The scatter plot depicts the point-wise uncertainty of true ensemble realizations with that of PIV-UQ estimate for a shear displacement field ($\mathbf{u}(\mathbf{x}) = \mathbf{u_2}$ (3.13)) showing the ability of PIV-UQ to predict spatial dependence of PIV uncertainty in non-uniform displacement. Overlaid heatmap shows the conditional distribution of $\sigma_{u,\mathrm{PIV}}$ given $\sigma_{u,ens}$. Black dotted line represents the best linear fit to the point cloud, showing correlation with a non-zero bias representing the floor error level.

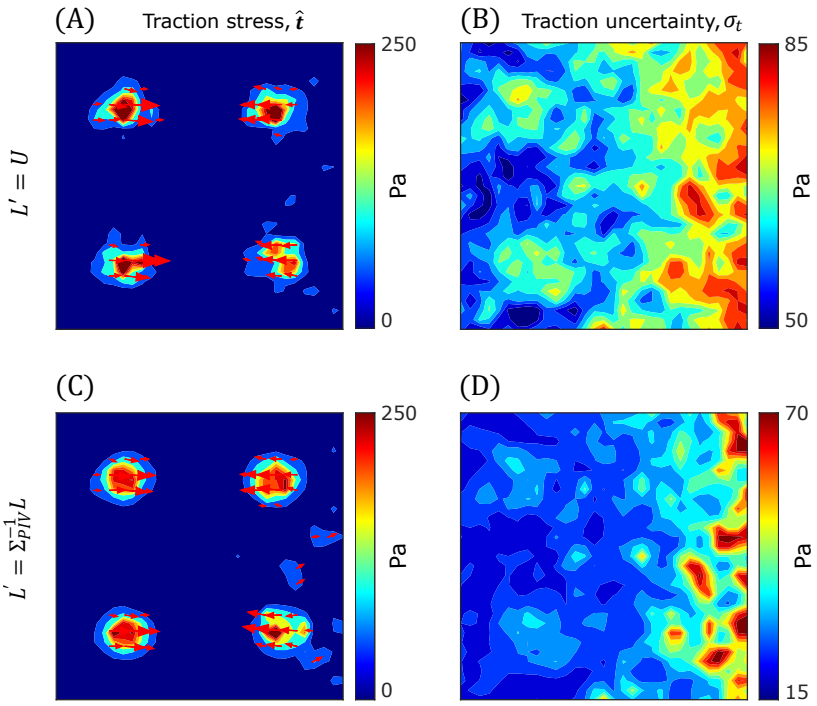

Fig 3.11. TFM-UQ uncertainty propagation is dependent on the choice of prior. TFM-UQ is applied to synthetic simulation described in Fig 3.6 with the choice of two different precision matrices : identity $\mathbf{L}' = \mathbf{U}$ (A-B) and heteroskedastic prior matrix $\mathbf{L}' = \mathbf{\Sigma}_{\mathrm{PIV}}^{-1}\mathbf{L}$ (C-D). Here, $\mathbf{L}$ is the discrete Laplacian operator with second-order finite differences. The prior is of the form $p(\boldsymbol{t}|\alpha) \propto \exp\left[\frac{\alpha}{2}\boldsymbol{t}^T\mathbf{L}'\boldsymbol{t}\right]$. (A,C) Mean marginal posterior traction stress magnitude $\hat{\mathbf{t}}$ and (B,D) Marginal posterior traction uncertainty (σ_t). The spatial range of traction stress uncertainty is increased with the heteroskedastic prior (D) as opposed to $\mathbf{\Sigma}_{\mathrm{PIV}}^{-1}\mathbf{L}$ as compared to $\mathbf{L}$ (Fig 3.7). However, this comes at the cost of under-regularization or over-fitting (C), because the regularization favours the elastostatic term (input measurement) even in the region of higher measurement uncertainty $\mathbf{\Sigma}_{\mathrm{PIV}}$.

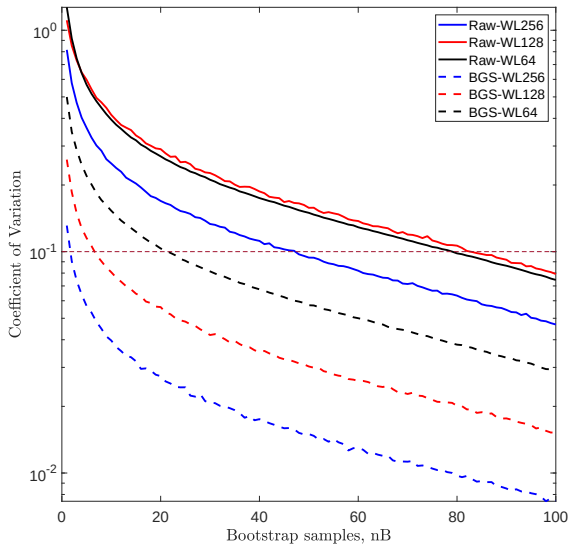

Fig 3.12. Coefficient of variation as a metric to assess PIV-UQ convergence and the variability of $\sigma_{u,\mathbf{PIV}}$ estimate. Coefficient of variation (CoV) = $\mathrm{Std}[\sigma_{u,\mathrm{PIV}}]/\,\mathrm{Mean}[\sigma_{u,\mathrm{PIV}}]$. "Raw" images tend to need higher iterations for the error in $\sigma_{u,\mathrm{PIV}}$ estimation to decay to 10% variation compared to "BGS" (Background subtracted) images in a resolution dependent manner.

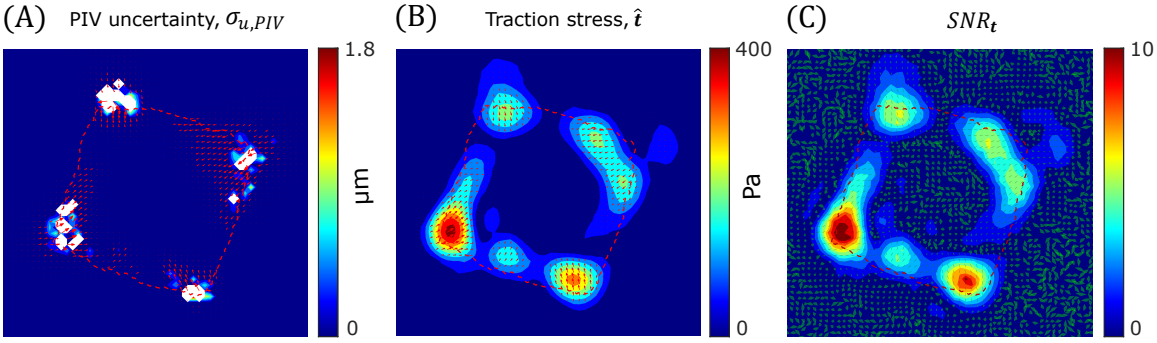

Fig 3.13. C3H/10T1/2 fibroblast spreading on fibronectin micropatterned island, analyzed with PIV window size $\mathbf{W_L} = \mathbf{32}$. (A) PIV measurement, $\boldsymbol{u}_{\mathrm{PIV}}$ (arrows) overlaid on PIV-UQ uncertainty field ($\sigma_{u,\mathrm{PIV}}$). White region indicates bad windows that are deleted during PIV-UQ validation (B) Mean marginal posterior traction stress field ($\hat{\mathbf{t}}$) showing smoothness prior in action in the place of bad PIV windows. (C) Traction stress signal-to-noise ratio ($SNR_{\boldsymbol{t}}$). Uncertainty arrows denote the pointwise angular uncertainty corresponding to 1 circular std. dev. of marginal posterior $p(\boldsymbol{t}|\boldsymbol{u}_{\mathrm{h}})$. Compared to WL-64 (Fig 3.8), a reduction in $SNR_{\boldsymbol{t}}$ was observed everywhere except the lower left traction corner of the micropatterened island (due to increase in the number of bad PIV windows in the corners). A higher traction stress magnitude is also observed only in the lower left corner where $SNR_{\boldsymbol{t}}$ is sustained from WL-64. Dashed outline indicate cell contour.

Chapter 4

SUB-CELLULAR TRACTION FORCE RESOLUTION IN PLATELETS

This chapter illustrates the application of Bayesian formulation developed in §3.2.4 to resolve sub-cellular forces when combined with reference-free TFM method independently of PIV-UQ.

4.1 Biological background

Platelets are circulating cells of discoid shape ($2 - 5\,\mu$m) that can respond to bleeding by binding to exposed collagen through the blood glycoprotein - von Willebrand factor (VWF) [176]. Platelet then aggregates to form a clot by bonding with other platelets via Fibrinogen and VWF, generating contractile force to stop bleeding [157, 177]. Disregulation of platelet force coordination is associated with excessive bleeding or thrombosis in case of excess contractility [178]. It has been observed that the actomyosin structure, responsible for platelet force generation, is different when platelets are spreading under different adhesive extra-cellular matrix coatings [179–181]. Early-bound platelets attaching to fibrinogen show punctate actin nodules while platelets spreading on VWF show centrally located actin fibers. It is noted that platelets spreading on VWF produce twice as much force compared to fibrinogen [182].

4.2 Methods

4.2.1 Reference-free TFM method

Reference-free TFM methods use prior knowledge about the fiduciary marker position to avoid imaging a reference state in traditional TFM methods (Fig 3.1). This strategy is advantageous when the cells are necessary for further analysis such as simultaneous immunofluorescence. 'Black dots' is such a reference-free method by micro-contact printing fluorescently labeled bovine serum albumin (BSA) onto a polydimethylsiloxane (PDMS) substrate in a way that generates circular non-fluorescent islands in a regular lattice [71]. The markers are identified with a peak finding algorithm and the centroid of each dot by segmentation is calculated. To estimate the reference state, dots near the edge (away from the platelet, assuming zero displacement) are fit through a rectangular grid by least squares. The estimated reference grid points closest to the dot centroids in the deformed configura-

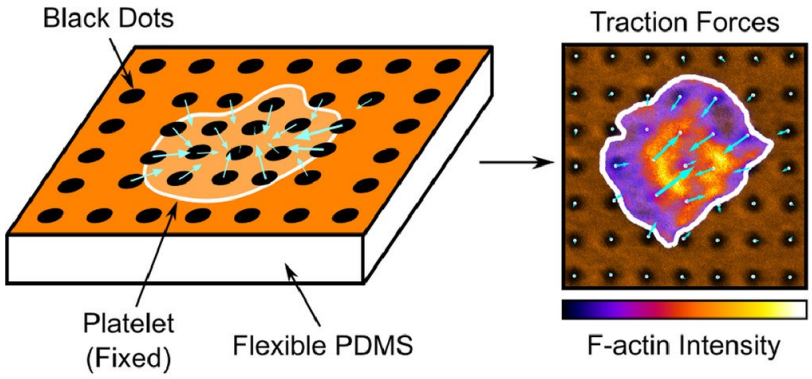

Fig 4.1. Microfabricated black dots as a reference free TFM method Microcontact printing is utilized to pattern fluorescent Bovine Serum Albumin (BSA) on a PDMS substrate. Spreading platelets deform the substrate which is imaged with fluorescence microscopy. The deformation is determined by computational analysis and traction forces are fitted using FTTC. Adapted from Buessman *et al* [71].

tion are assigned by the least Euclidean distance, and a displacement vector is constructed from the reference centroid to the deformed centroid. Force calculation was carried out by regularized-FTTC method [37, 47].

4.2.2 Increasing displacement measurement resolution by ellipse fitting

In addition to the centroid displacements, the shape of the deformed black dot was used to increase the resolution of the measured substrate deformation field. Before segmenting the black dot to measure the deformed black dot shape, the illumination intensity variation across the field of view was corrected by local image contrast normalization with a square structuring element (30 pixel width). The regions with significant substrate deformation were labelled as deformation region and the rest of the field of view was labeled as the reference region. To ensure consistency in segmentation over different images and experiments, the black dots in the reference region were first binarized with automated thresholding in ImageJ. Then, this reference intensity threshold is applied to segment the black dots in the deformed region. An ellipse was fitted to each of the black dots ('Analyze Particles' ImageJ plug-in) to obtain the reference and deformed shapes. The undeformed shape of the dots was modelled as a circle (i.e., average elliptical fit of the dots in the reference region) with centroids of the undeformed reference grid (Fig 4.2 A,B).

The displacement measurement was made as the vectorial difference between the vertices of the deformed ellipse and the corresponding angular position on the circumference of the

undeformed circle (Fig 4.2 quiver arrows). The affine transformation between a circle and an ellipse is not unique without the presence of discerning circumferential markers, thus there was an inherent, non-systematic uncertainty in the estimation of the displacement field which was taken into consideration using a Bayesian approach for force reconstruction.

4.2.3 Super-resolved Bayesian TFM formulation

The resolution of the force localization was improved by reconstructing the traction forces on a finer ($4X$ resolved), uniform grid ($\mathbf{x}' \in \Omega$) given the displacement measurement using the elliptical fit to the black dots on a non-uniform grid ($\mathbf{x} \in \Omega_{dots}$). Here, Ω_{dots} and Ω denote the displacement domain and the restricted solution domain within the cell contour of the single platelets respectively. As described in §3.2.3, the operator $\mathbf{M}$ relates the displacement field ($\boldsymbol{u}_\mathrm{h}$) to the in-plane traction stress field ($\boldsymbol{t}$. Here, the Boussinesq solution for an isotropic, elastic half-space is used to construct the $\mathbf{M}$ matrix in the real space [36, 47, 48, 183] by means of convolution with the Green's function :

$$\boldsymbol{u}_\mathrm{h} = \int_\Omega \mathbf{G}(\mathbf{x} - \mathbf{x}')\boldsymbol{t}(\mathbf{x}')\mathrm{d}\mathbf{x}' \approx \mathbf{M}\boldsymbol{t} \tag{4.1}$$

The following Green's function([47]) is used :

$$\mathbf{G}(\mathbf{x}) = \frac{1+\nu}{\pi E}\left[(1-\nu)\frac{\boldsymbol{I}}{r} + \nu\frac{\mathbf{x}\mathbf{x}^T}{r^3}\right], \tag{4.2}$$

where $\boldsymbol{I}$ is the identity matrix, ν the Poisson ratio and E the Young's modulus of the substrate. Boussinesq formulation has the advantage of prescribing the displacements and the traction stresses on different, non-uniform grids avoiding interpolation of displacement data from ellipse fitting and increasing the resolution of traction stress field. However, Boussinesq formulation has a singularity at origin as evidenced by the Green's function ((4.2)). The integration is performed using numerical quadrature and a cut-off in the $\mathbf{M}$ matrix is introduced to avoid the singularity as well as the use of non-collacted grid. This leads to underestimation of traction stresses which is compensated by $6X$ increase in the resolution of the traction stress field. Inverting (4.1) is highly ill-conditioned and the further increase in traction degree of freedom result in an under-determined problem.

A Bayesian approach (described in §3.2.4) was utilized to perform the traction stress inversion with $\boldsymbol{\Sigma}_\mathrm{PIV} = 0$. Briefly, the likelihood of the Boussinesq solution was taken to be distributed as a zero mean, multi-variate normal distribution with a precision parameter β,

$$p(\boldsymbol{u}_\mathrm{h}|\boldsymbol{t}, \beta) \propto \beta^{N_d} \exp\left\{\frac{-\beta}{2}\left\|\boldsymbol{u}_\mathrm{h} - \mathbf{M}\boldsymbol{t}\right\|\right\}.$$

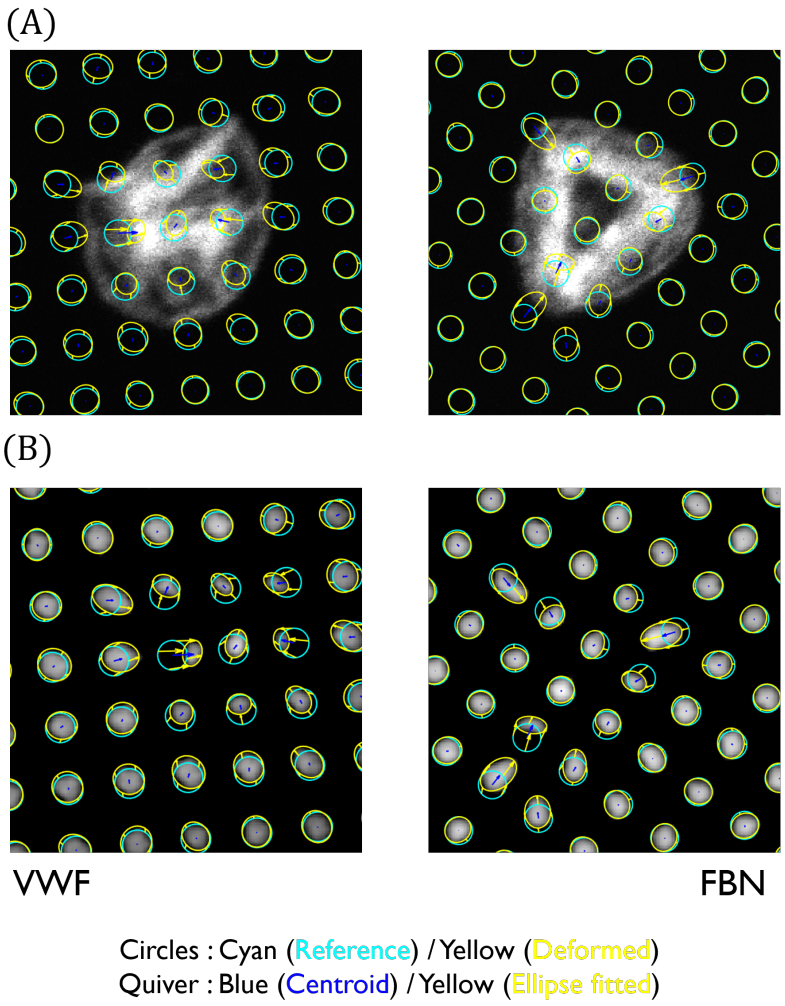

Fig 4.2. Illustration of ellipse fitting to increase displacement resolution. Reference circles (Cyan) and deformed ellipses (Yellow) are plotted over the actin images of a representative platelets spreading on VWF and FBN substrates (A) and inverted black dot image (B). Quiver arrows indicate the respective displacement fields.

N_d is the number of displacement grid points. The following priors are placed on the traction stresses: a) Regularization (R) b) Global force balance prior (B) and c) cell contour prior (C).The priors are modelled as zero-mean normal distributions of the form,

$$p(\boldsymbol{t}_i|\alpha_i) \propto \alpha^{N_i/2} \exp\left\{\frac{\alpha_i}{2} L_i(\boldsymbol{t})\right\}.$$

Here, $i \in R, C, B$ each corresponding to the respective priors, N_i is the number of positive eigenvalues of $L_i(\boldsymbol{t})$ and α_i are the respective precision hyper-parameters. N_i is generalized here to include rank deficient prior precision matrices (such as global force balance) with $L_i(\boldsymbol{t})$ a non-negative quadratic loss function encoding the respective constraint. $L_R = \int_\Omega \|\boldsymbol{t}(\mathbf{x})\|^2 \mathrm{d}\mathbf{x}$ constraints the $L-2$ norm of the traction stress field (Tikhonov regularization), $L_B = \left[\int_\Omega \boldsymbol{t}(\mathbf{x})\mathrm{d}\mathbf{x}\right]^2$ enforces the global force balance for isolated platelets, and $L_C = \int_\Omega \mathbb{1}(\mathbf{x} \notin \Omega) \|\boldsymbol{t}(\mathbf{x}\|^2 \mathrm{d}\mathbf{x}$ constrainst the traction stress field within the cell spread area. Denoting the hyper-parameter set by $\theta = \{\beta, \alpha_R, \alpha_B, \alpha_C\}$, the marginal conditional posterior distribution is given by Bayes' theorem (with uninformative hyper-priors, $p(\theta) \propto 1$),

$$p(\boldsymbol{t}|\boldsymbol{u}_\mathrm{h}) \propto \int p(\boldsymbol{u}_\mathrm{h}|\boldsymbol{t}, \theta) p(\boldsymbol{t}|\theta) p(\theta) \mathrm{d}\theta \approx p(\boldsymbol{u}_\mathrm{h}|\boldsymbol{t}, \hat{\theta}) p(\boldsymbol{t}|\hat{\theta}).$$

This approximation termed evidence analysis([49, 166]) assumes sharply peaked distribution for the evidence $p(\theta|\boldsymbol{u}_\mathrm{h})$ with mass concentrated around $\hat{\theta}$. The optimal hyper-parameter is found as $\hat{\theta} = \arg\max_{\{\theta\}} p(\theta|\boldsymbol{u}_\mathrm{h})$ by simultaneous optimization as part of the stress reconstruction process using MATLAB `fmincon` function. The posterior of the traction stress is available in closed-form under evidence approximation ($\Lambda = \boldsymbol{I}$ in (3.8)),

$$p(\boldsymbol{t}|\boldsymbol{u}_\mathrm{h}; \hat{\theta}) \sim \mathcal{N}(\bar{\boldsymbol{t}}, \mathbf{S}_\mathrm{post}). \tag{4.3}$$

The final traction stress is taken as the mean or mode of the posterior (4.3), $\bar{\boldsymbol{t}} = \beta \mathbf{S}_\mathrm{post} \mathbf{M}^T \boldsymbol{u}_\mathrm{h}$ and $\mathbf{S}_\mathrm{post} = [\beta \mathbf{M}^T \mathbf{M} + \Sigma_{i \in \{R,C,B\}} \alpha_i \mathbf{L}_i]^{-1}$. The ability to automatically select the hyper-parameters for individual cells is necessary to avoid over-smoothing or over-fitting as the spatial stress distribution, displacement measurement noise and the image segmentation quality varies over different cells as well as different experimental conditions.

4.3 Results

4.3.1 F-actin morphologies in fibrinogen and VWF-coated coverslips

After seeding human platelets isolated from whole blood onto fibrinogen-coated or VWF-coated coverslips and allowing them to spread, we observed distinct patterns in the F-actin morphology in individual platelets (Fig 4.3 A,B). On fibrinogen, the majority of platelets

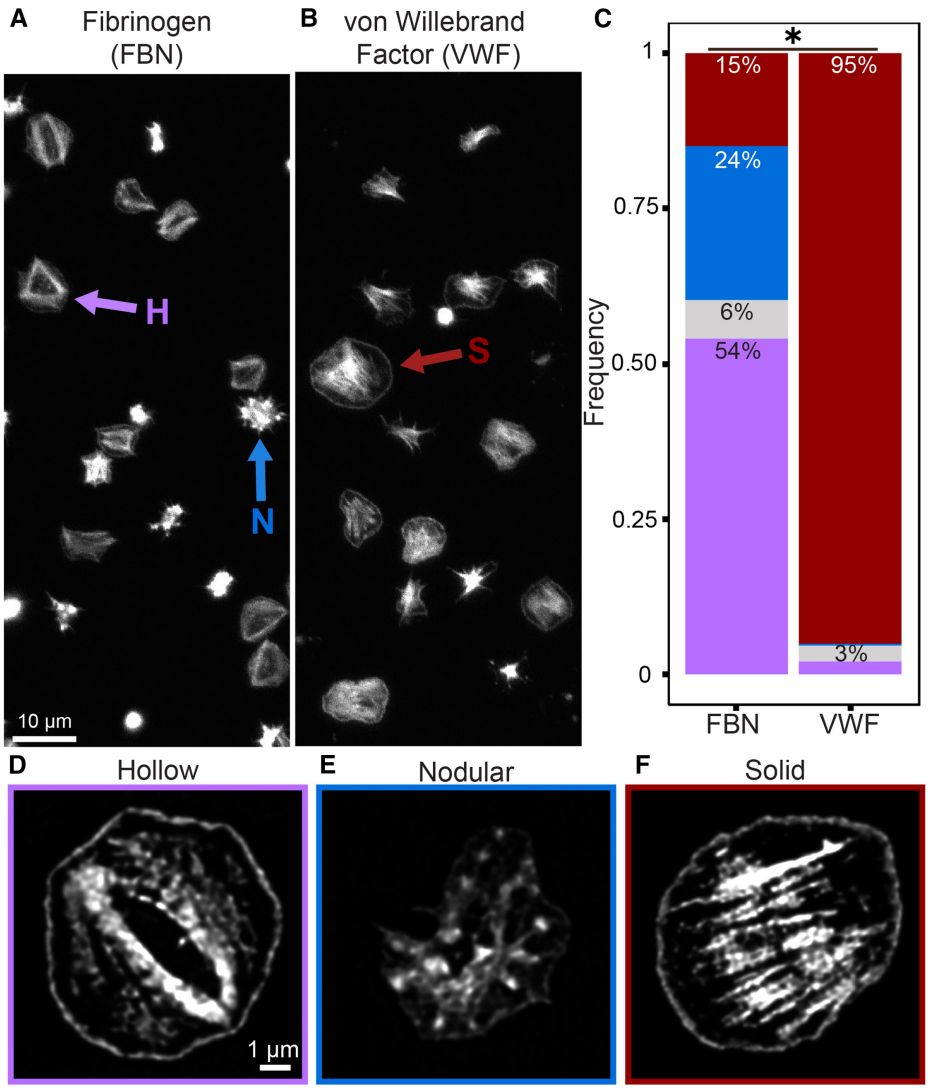

Fig 4.3. F-actin morphologies in platelets are distinct on FBN and VWF-treated coverslips. (A) After spreading on fibrinogen (FBN)-coated coverslips, platelet F-actin is commonly hollow (purple arrow) and nodular (blue arrow) while on (B) VWF-coated coverslips, these morphologies were rare and instead, platelets predominantly had solid (red arrow) F-actin patterns. (C) Manual quantification of n = 4,304 platelets (2,157 on fibrinogen and 2,147 on VWF) from ten experiments showed that on fibrinogen, 24% were nodular (blue), 54% were hollow (purple), 15% were solid (red), and 6% were indeterminate (gray). In contrast, 2% were hollow F-actin structure, 95% were solid, and 3% were indeterminate on VWF. When tested with a Pearson's Chi-squared test, these frequencies are significantly different ($p < 0.0001$). Between experiments, differences in morphology trended similarly (Table S1). (D-F) These hollow (D), nodular (E), and solid (F) F-actin patterns were further characterized in super-resolution using SIM. D, E, and F are on the same scale.

had F-actin arranged along the periphery of the cell and with a prominent absence of F-actin in the center, which we classified as hollow platelets (Fig 4.3 A purple arrow, D). In contrast, on VWF, hollow platelets were rare, and instead, most platelets had F-actin filaments that spanned the central region of their spread area, which we classified as solid platelets (Fig 4.3 B red arrow, F). Additionally, we observed that a portion of platelets on fibrinogen coatings had punctate nodules of F-actin, which we classified as nodular platelets (Fig 4.3 A blue arrow, E). Across ten distinct experiments, nodular platelets were rarely observed on VWF-coatings (Fig 4.3 C). Furthermore, we classified a platelet as indeterminate if its F-actin morphology displayed features of two or more other classifications or if it was unclear which pattern best represented it. By quantifying the distribution of these four classifications of platelets by their F-actin morphology, we found that the matrix coatings had distributions that were significantly different ($p < 0.0001$ by Pearson's Chi-squared) (Fig 4.3 C).

4.3.2 Validation of the super-resolution TFM method

To assess the sensitivity of the ellipse (§4.2.3) verses centroid method [71], we used a synthetic black dot simulation Fig 4.4. First, two distinct traction stress fields were constructed within a typical cell boundary: one with more centralized traction forces (i.e., as is observed on VWF, Fig 4.4 B (I)) and one with more peripheral traction forces (i.e., as is observed on FBN, Fig 4.4 C (I)). For these traction stress fields, Gaussian distributed traction spots were centered at $r/R = 0.7$ and 0.25 respectively where R is the maximum radial length of the synthetic cell contour and r represents the radial coordinate with cell centroid as origin. The width of the traction Gaussians were fixed to be 0.02 and 0.03 units normalized to R. The individual traction spots chosen contained 850 Pa, except the top peripheral traction spot that contained 1500 Pa. The displacement field to the synthetic traction field was generated using Fourier Series solution [37] (Fig 4.4 A middle). The true displacement field was then interpolated to the interrogation points on the fitted reference circles using a representative undeformed black dots frame without platelets. (Fig 4.4A right, green spots). The sensitivity analysis was carried out by varying the Gaussian noise added to the displacement field, then FTTC with centroid tracking as well as Bayesian evidence TFM with ellipse fitting were performed. The ability of these methods to resolve traction stress patterns is visualized by plotting quiver maps along with contours of regions containing traction stresses above 500 Pa (Black lines in Fig 4.4 B and C). The traction magnitude error is calculated as TME $= | \|\boldsymbol{t}_{inf}\| - \|\boldsymbol{t}_{true}\| | / \|\boldsymbol{t}_{true}\|$, where $\|\boldsymbol{t}\| = \int_\Omega (t_x^2 + t_y^2)^{0.5} \mathrm{d}A$, Ω is the traction stress domain. TME of 0 represents a perfect magnitude estimation.

We observe that the true traction stresses (Fig 4.4 B-C I, left) are qualitatively similar in localization to the traction stresses using ellipse fitting and Bayesian approach (Fig 4.4

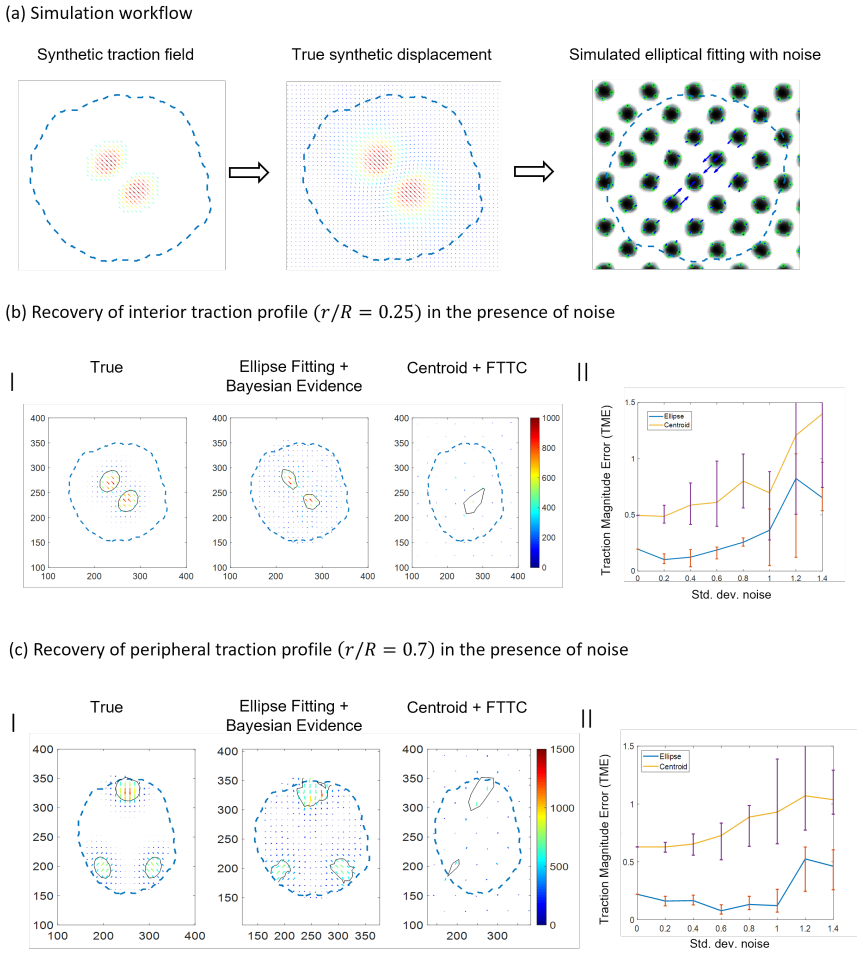

Fig 4.4. Synthetic simulation shows improved traction stress localization and magnitude recovery with high-resolution elliptical fitting and Bayesian evidence analysis. (A) The simulation workflow to assess the localization sensitivity of the centroid displacement/FTTC method versus the ellipse displacement/Bayesian approach. First, a synthetic traction field was generated within a typical cell boundary (left). For this synthetic traction field, true synthetic displacements were calculated (center). Noise was added to these true displacements and simulated experimental displacement measurements were plotted over a reference black dot image without platelets (right). (B-C) (I) Using Gaussian traction patterns typical of a VWF-bound platelet (i.e., forces are more centralized) (B) and of a FBN-bound platelet (i.e., forces are more peripheral) (C). Std. dev. noise have units of px. The blue and yellow lines in II represent the median and the error bars represent the 90% CI from n = 10 repeats. True traction field is undersampled for visual representation. Black lines in B and C I indicate regions with high contours of stresses ($> 500Pa$). Colorbar scale is Pa.

B-C I, middle). In contrast, the centroid and FTTC methodology does not qualitatively reproduce a traction pattern with a subcellular localization similar to the true traction profile (Fig 4.4 B-C I, right). (II) When examining traction magnitude error (TME) for

varying levels of noise, the traction magnitude error remains lower for the ellipse method (blue line) than the centroid method (yellow line). Ultimately, we observe that for a range of noise levels around experimental noise (RMS of 0.4380 px, indicated by the vertical, dashed black line) and traction spots of sizes comparable to that of the black dots, the ellipse method performs well in recovering both the traction localization and magnitudes.

4.3.3 Platelet sub-cellular forces correspond with F-actin patterns

As described the spatial resolution of the platelet forces were increased by fitting ellipsoids to the distorted image of each black dot (Fig 4.5A). Originally, we had identified the outline of each black dot in the array (Fig 4.5B, cyan shapes), determined its geometric centroid from those outlines (Fig 4.5B, red dots), and calculated its displacement vector (Fig 4.5B, white arrows). To enhance the resolution, we fitted ellipses to the fluorescent black dots (Figure 5C, cyan ellipses), identified the vertices of the ellipses (Fig 4.5C, red dots), and calculated four displacement vectors (Fig 4.5C, white arrows) per black dot. These higher resolution displacements combined with a Bayesian approach by maximizing model evidence with probabilistic priors for regularization, global force balance, and constraint of force exertion within the cell boundary result in high-resolution platelet traction forces with immunofluorescent stains (Fig 4.5 D, more examples in Figure S5A-B). As expected, platelet forces calculated with the ellipse method correlated with the centroid method (Figure S5C) without increasing noise (Figure S6-7). Qualitatively, the localization of these traction forces corresponded to the F-actin patterns, where the highest forces localized at the ends of F-actin fibers Fig 4.5D, more examples in Figure S5A-B).

4.3.4 Platelet subcellular forces are significantly more peripheral on fibrinogen and more central on VWF.

To analyze the forces spatially, we separated each platelet into four regions (Fig 4.7 A for regions of equal area, Figure S8 for regions of equal radius) based on proximity to the platelet centroid. We found that the fraction of force in the central areas (regions 1 and 2) was significantly higher on VWF than on fibrinogen ($p < 0.0001$ by ANOVA and Tukey's post hoc) (Fig 4.7B). In contrast, the fraction of force at the periphery (region 4) was significantly higher on fibrinogen than on VWF ($p < 0.0001$) (Fig 4.7 B). This difference corresponds to the F-actin patterns most prevalent on each protein. VWF-bound, solid platelets exerted a significantly higher fraction of force centrally (region 1) and a significantly lower fraction of force peripherally (region 4) than fibrinogen-bound hollow platelets ($p < 0.0001$, Fig 4.7 6C). These data indicate that localization of platelet forces was both protein- and F-actin pattern-dependent.

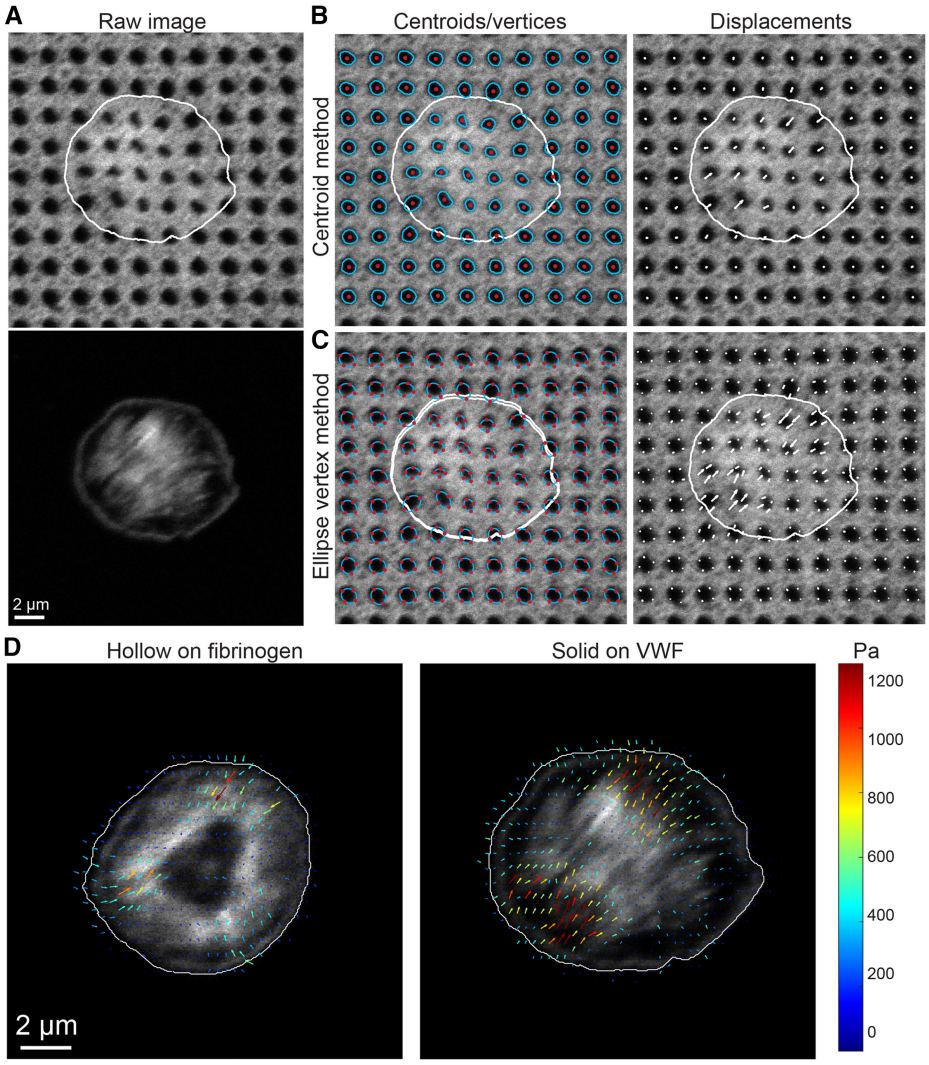

Fig 4.5. Platelet sub-cellular forces correspond with F-actin patterns. (A) For a representative fluorescently labeled platelet (F-actin, bottom) on black dots (top), (B) force per platelet was calculated by finding the outline of the fluorescent black dot pattern (cyan shapes, left image), determining the centroid of those outlines (red dots, left image), and calculating the centroid displacement (white arrows, right image) from the undeformed grid. (C) To enhance the resolution to better characterize subcellular localization of traction forces, ellipses were fit to the fluorescent black dot pattern (cyan ellipses, left image), finding the vertices of the ellipses (red dots, left image), and calculating the vertex displacement (white arrows, right image) from the undeformed grid. This results in four-fold higher resolution displacements. (D) These higher resolution displacements combined with a Bayesian approach result in high-resolution platelet traction forces with immunofluorescent stains. Qualitatively, the localization of these traction forces corresponded to the F-actin patterns, wherein the highest forces localized at the ends of F-actin fibers.

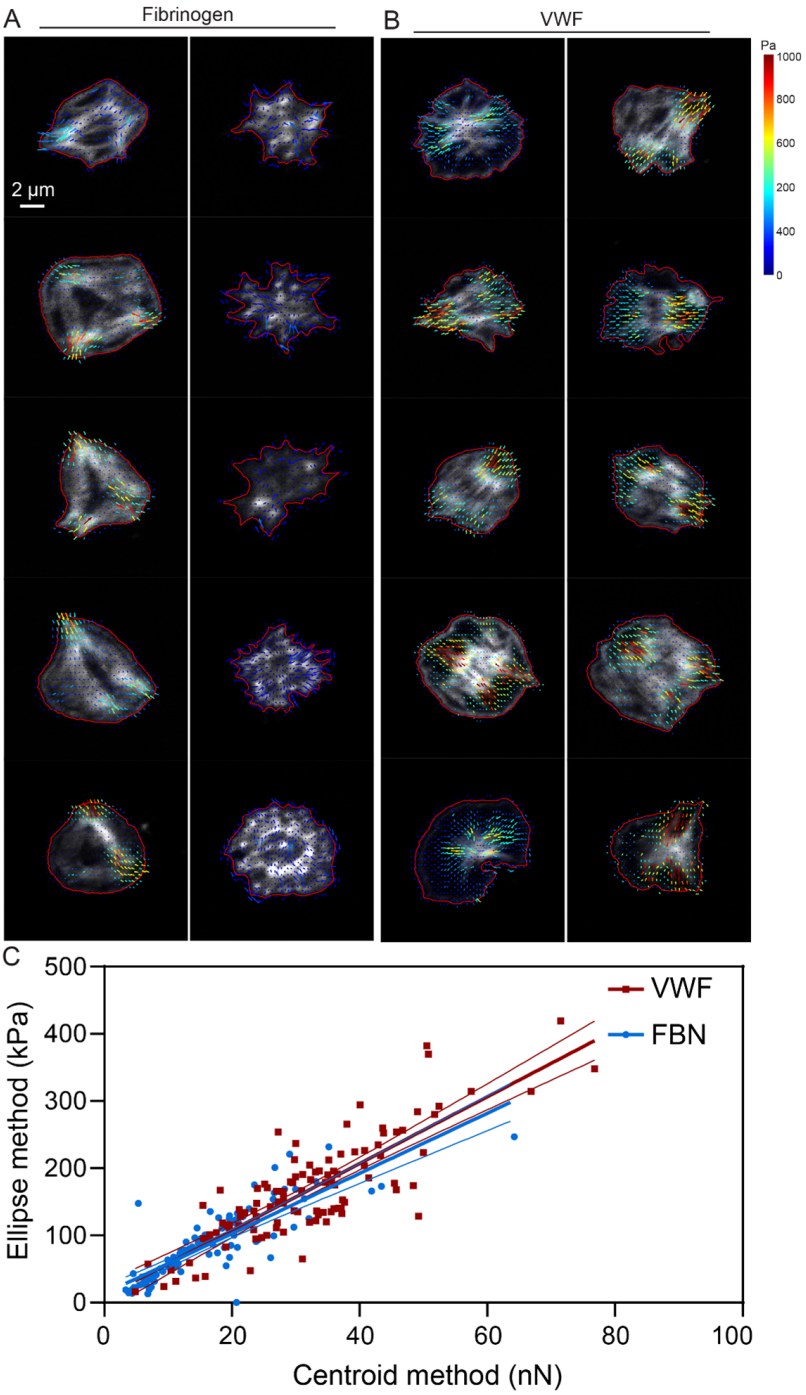

Fig 4.6. Examples of high-resolution platelet traction forces on fibrinogen and VWF. Representative platelets on fibrinogen (A) and VWF (B) with high-resolution traction forces. Cell boundaries are shown in red. Qualitatively, lower magnitude stresses were found on platelets with nodules than on platelets with filaments, which agrees with the quantitative assessment in Figure 3G. Additionally, higher magnitude forces tended to localize at the ends of filaments oriented parallel to the F-actin filaments. (C) Total stresses/forces calculated via the centroid method (x-axis) correlated with the ellipse method (y-axis). As expected, the relationship is not significantly different for VWF-bound (red dots and red line, thin line indicates 95% confidence intervals) versus FBN-bound platelets (blue dots and line) when tested with an analysis of covariance.

4.4 Discussion

We examined the sub-cellular traction forces and the corresponding F-actin patterns of platelets on fibrinogen and VWF in this study. Our data agree with previous studies that observed nodular and hollow platelet F-actin patterns on fibrinogen [179, 184], yet we found that these morphologies were almost completely absent on VWF. Instead, platelets on VWF had an inverse F-actin distribution, with F-actin localized in the platelet center. In addition to differences in F-actin structure on fibrinogen versus VWF, we observed differences in function, wherein platelets on VWF produced more force than platelets on fibrinogen, even when accounting for spread area. Additionally, hollow fibrinogen-bound platelets generated less force than hollow VWF-bound platelets but more force than nodular fibrinogen-bound platelets, indicating that platelet forces are both protein- and F-actin pattern-dependent. Nodular platelets' reduced forces align with the previous finding that treatment with inhibitors of contraction increases the fraction of nodular platelets on fibrinogen [179]. Because black dots enable simultaneous visualization of immunofluorescent stains and measurement of single-cell forces [71], we were able to co-visualize F-actin and force generation on the subcellular scale, finding that platelet F-actin structure corresponded with force localization. This builds on previous work that observed modest correlations between total platelet force and F-actin intensity [185] or F-actin dispersion [71], but could not measure the localization of subcellular forces. Additionally, we found that F-actin patterns induced by VWF resulted in forces localized significantly more centrally while patterns induced by fibrinogen resulted in forces localized significantly more peripherally.

Distinct F-actin patterns, contraction magnitudes, and subcellular localization of forces observed on fibrinogen versus VWF could have implications in hemostasis and thrombus architecture, due to the unique role of VWF in tethering platelets to the subendothelial matrix as the first step of platelet plug formation [186]. It is possible that toward cessation of bleeding, it is advantageous for the earliest bound platelets to be hypercontractile and that F-actin fibers formed through the center of the platelet enable maximal forces. Additionally, these F-actin structural and functional differences could be important in clots of different protein content and protein organization, such as the fibrin(ogen)-rich outer shell observed in acute ischemic stroke thrombi [187] and the distribution of VWF within a thrombi that is associated with stroke etiology and revascularization outcome [188].

Beyond the study of platelets, we see this study as a connection between advanced computational techniques (machine learning, fiber alignment quantifications), cellular structural characterizations (super-resolution microscopy of immunofluorescence-stained cellular components), and cellular functional measurements (single-cell and subcellular measurement of force generation). We anticipate that combination of these computational and experimen-

tal techniques will be complementary in the association of cellular structure and function, characterization of biological heterogeneity, and investigation of biological mechanisms.

4.5 Acknowledgements

Chapter 4 is in part a published manuscript [5] : Mollica, M. Y., Beussman, K.M., Kandasamy, A., Rodríguez, L.M., Morales, F.R., Chen, J., Manohar, K., del Álamo, J.C., López, J.A., Thomas, W.E. and Sniadecki, N.J. Distinct platelet F-actin patterns and traction forces on von Willebrand factor versus fibrinogen. *Biophysical Journal* (2023). The dissertation author is a co-author of this work.

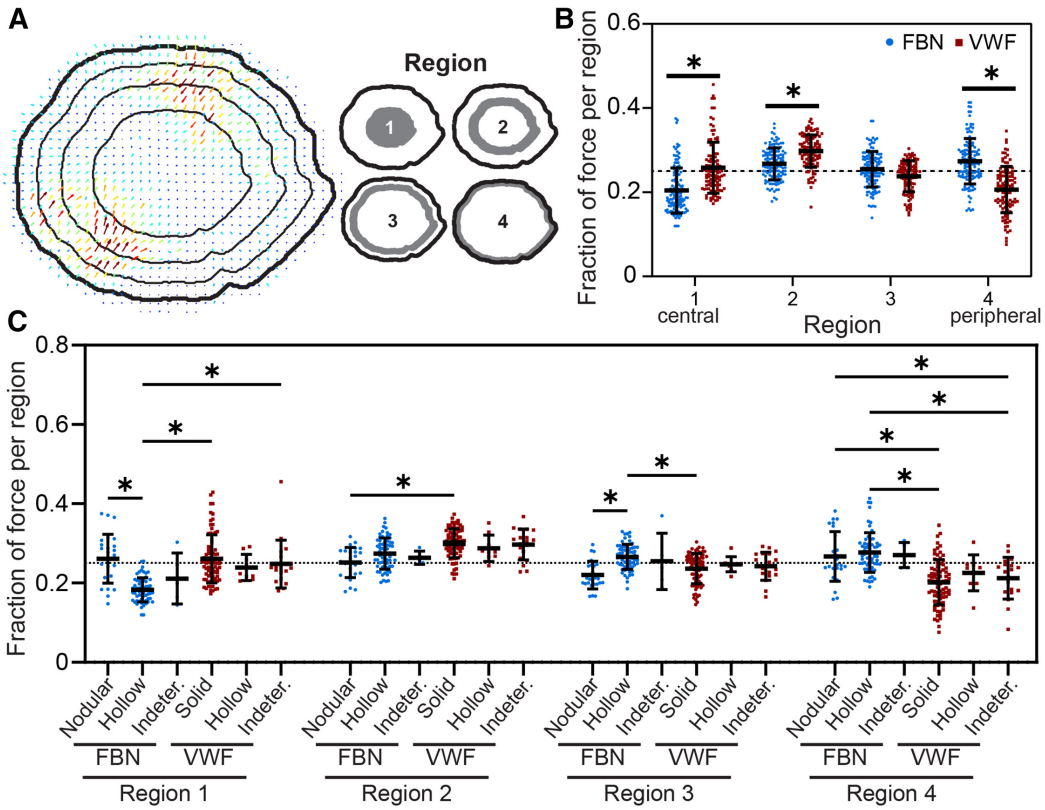

Fig 4.7. Platelet subcellular forces are significantly more peripheral on fibrinogen and more central on VWF. . (A-B) When separating the cell into four regions of equal area, we found that forces are significantly more peripheral on fibrinogen (FBN) ($p < 0.0001$ for region 4 when tested with an ANOVA and Tukey's post hoc) and significantly more central on VWF ($p < 0.0001$ for regions 1 and 2). The representative image in panel A is a VWF-bound platelet and its fraction of force in regions 1, 2, 3, and 4 is respectively 0.275, 0.300, 0.247, and 0.178. The horizontal dotted line at $y = 0.250$ indicates the expected fraction of force in each of the equal-area regions if forces were distributed randomly. (C) We next examined regional force localization by machine learning-assigned F-actin pattern. VWF-bound solid and indeterminate platelets had a significantly higher fraction of force than FBN-bound, hollow platelets in region 1 ($p < 0.0001$ and $p < 0.0001$, respectively, when tested with an ANOVA and Tukey's post hoc). FBN-bound nodular platelets also had a higher fraction of force than FBN-bound hollow platelets in region 1 ($p < 0.0001$). In region 2, VWF-bound solid platelets had a significantly higher fraction of force than FBN-bound nodular platelets ($p = 0.0007$). In region 3, FBN-bound, hollow platelets had a significantly higher fraction of force than VWF-bound solid ($p = 0.0295$) and FBN-bound nodular ($p = 0.0045$). In the most peripheral region (region 4), FBN-bound hollow platelet had a significantly higher fraction of force than VWF-bound solid platelets ($p < 0.0001$) and VWF-bound indeterminate platelets ($p < 0.0001$). Additionally, FBN-bound nodular platelets had a higher fraction of force than VWF-bound indeterminate platelets ($p = 0.0168$) and VWF-bound solid platelets ($p < 0.0001$) in region 4. The horizontal dotted line at $y = 0.250$ indicates the fraction of force expected if forces were randomly distributed. Therefore, compared to if randomly distributed, values above this dotted line indicate more force per region and values below indicate less force per region. Error bars represent standard deviation. Note that the sample platelet in panel A is VWF-bound solid pattern platelet in Fig 4.5 A-C and D (right).

Chapter 5

INFERENCE OF *IN VITRO* CARDIOMYOCYTE MONOLAYER ELASTICITY

5.1 Introduction

Advances in human induced pluripotent stem cell-derived cardiomyocytes (hiPSC-CMs) technology have enabled the production of cardiac cells at large-scale [189]. These in vitro cellular models have been used to evaluate the efficiency and safety of new treatments [190] in both models of healthy and disease-associated human genetic backgrounds. These studies focus on the quantification of one or more of the signals that determine cardiomyocyte function, namely: action potential, cytosolic calcium concentration, and mechanical force production [191, 192].

While assays that measure action potential and calcium signals are well-established [193, 194], quantifying mechanical contractility is still elusive. High-throughput contractility assays are, in general, based on optic measurements, typically high-framerate videos obtained with a High Content Screening system [22, 195]. Moreover, open-access contractility assays [196–199] are not well suited for their use in high-throughput applications.

There is also a lack of uniformity in the definition and physical meaning of the readout of these methodologies. Although the concept of contraction is intuitive, the way contractility is quantified in current methods is loosely defined. Some methods report indirect proxies for cell motion based on the change in light intensity [199] or correlation of image blocks [198]. More advanced methods use Particle Image Velocimetry (PIV) or optical flow algorithms to get a direct measurement of velocity fields during contraction [196, 197, 200, 201]. However, these methods directly estimate the cell motion as surrogate of contractility, but none of them outputs an actual force readout.

The conditions in which the cells are imaged are far from being standardized: some methods require images of a fluorescent label, whereas other methods work directly on transmitted light images. Remarkably, in all of the methods in current literature the cells are seeded directly on the bottom of a multiwell plate, made out of a rigid material such as glass or plastic. However, the stiffness of the substrate has been proven of key relevance in hiPSC-CMs maturity and function [156, 202].

Traction Force Microscopy (TFM) is considered the golden standard for optical microscopy-based accurate measurement of cell force. To perform TFM measurements, the cells must be

seeded on a compliant elastic gel of known mechanical properties. These gels are embedded with fluorescent beads that serve as tracers for the deformation caused by the cell-exerted forces. The measured deformations, together with the information about the substrate stiffness, is used to infer the resulting force field that caused such deformations. However, TFM is seldom used in high throughput applications [155].

Aside from contractility properties, the passive elasticity of cardiomyocytes affects the ability of cardiac tissue to relax. Changes in the stiffness of cardiomyocytes have been related to cardiac disease such as heart failure with preserved ejection fraction [203, 204]. Recent studies have uncovered proteins that contribute to the passive elasticity of cardiomyocytes as potential therapeutic targets for diastolic dysfunction [205–207]. Currently, the most common techniques to measure tissue stiffness are Atomic Force Microscopy [95] and cell stretchers [205], both of which requiring highly specialized tools and is time consuming. Today, even though both contractile forces and passive mechanical properties are known to be essential for the function of cardiac tissue, there are no methods to quantify cellular forces and cellular stiffness in high throughput.

In this work, we present a method to measure cardiomyocyte contractility and stiffness that is designed from the ground up to accommodate the specific challenges associated with high throughput experiments. The method incorporates automation in key steps that would otherwise require user interaction such as reference frame selection to compute cell deformations during a beating cycle, extraction of contractility parameters, and quality control metrics of the experimental data . Computing performance has been optimized with multi-threaded CPU and GPU routines if available in the workstation. We used this method in spontaneously beating monolayer of hiPSC-CMs of different cell-disease models , and benchmark drugs show the validity of our analysis as a tool for contractile phenotyping. Combining high-speed videos of the deformation of the cells with deformation of the substrate under cell contraction, we present a method to expand our cardiomyocyte contractility analysis to also measure the cells' passive stiffness.

5.2 Methods

5.2.1 High throughput, automatic quantification of contractility and stiffness of hiPSC-CM monolayers

A fully automated algorithm that retrieves cardiomyocyte motion, traction stresses, intercellular tension and stiffness information from high framerate timelapse images is illustrated in Figure 1. Human induced Pluripotent Stem Cell (hiPSC) from the target population is obtained from biopsy samples and are differentiated into cardiomyocytes (CM) (Fig 5.1 A). The contractility experiment is performed in high throughput on arrayed multi-well format

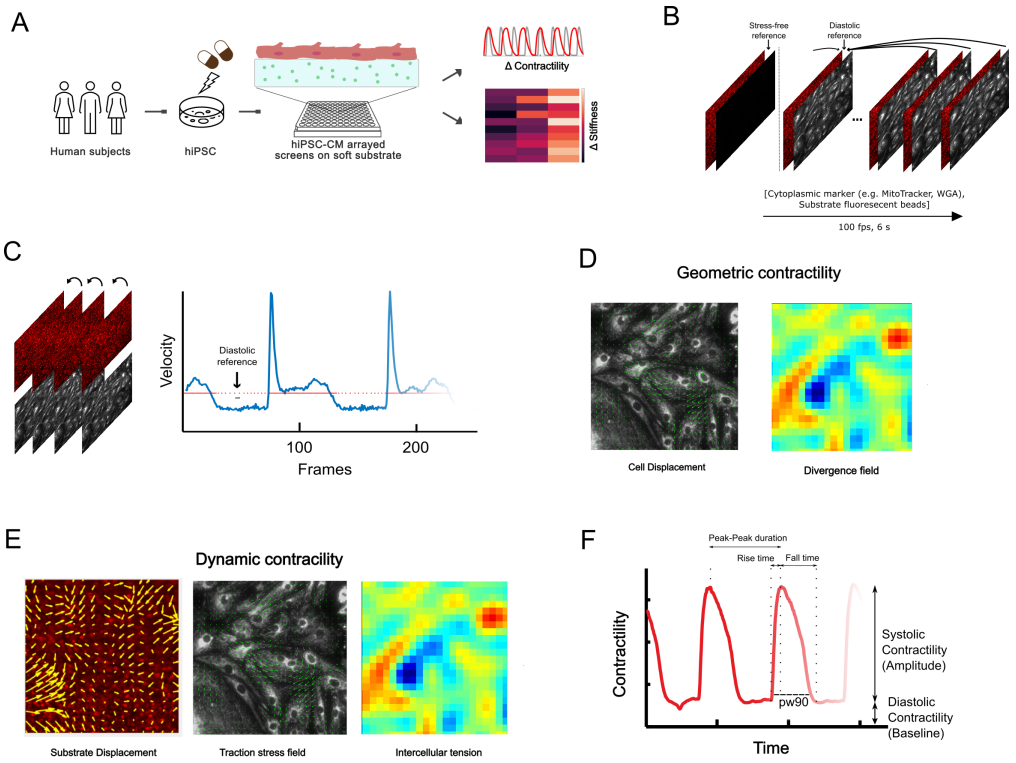

Fig 5.1. Overview of contractility and stiffness measurement method. (A) Human induced pluripotent stem cells (hiPSC) are derived from the target population. After differentiation to cardiomyocytes (CM), hiPSC-CM monolayers are cultured on soft compliant substrates in multiwell plate. From timelapse images of spontaneous contraction, contractility algorithm provides time traces and metrics of contraction and stiffness change in high throughput. (Inset) hiPSC-CM cultured on compliant substrates with embedded fluorescent beads (B) Contractility measurements are made with either cell-based images (e.g. cytoplasmic markers such as MitoTracker or Wheat Germ Agglutinin) or fluorescent tracers embedded in the substrate. Depending on the image channel, two types of reference images can be supplied. Cell-free reference of substrate beads is obtained after removal of hiPSC-CM cells by trypsin or treatment with cytoskeletal inhibitors such as cytochalasin-D. Dynamic reference refers to the relaxed phase of the contraction cycle, which is automatically calculated by the algorithm. Note that cell-free reference can only be applied to substrate fluorescent tracer images. Once identified, Particle Image Velocimetry (PIV) is used to measure the deformation relative to the appropriate reference frame. (C) Dynamic reference frame is automatically selected based on velocity measurement of timelapse movies. Low motion frames are skipped to reduce analysis time and save space. (D) Kinematic contractility obtained with cell-based image channel outputting cell motion and divergence of velocity field. (E) Dynamic contractility measurement made with substrate image channel outputting traction stresses and monolayer tension. (F) 1D contractility traces constructed from either dynamic (IT) or kinematic (DV) measurements. The following parameters fitted to 1D contractility curves to obtain contractility metrics for further analysis. Amplitude : Systolic amplitude, Peak-Peak : Time between contraction peaks, Baseline : Resting contractility at diastole, PW90 - Pulse width at 90% prominence, Rise time - Diastole to peak systole time, Fall time - Peak systole to diastole time.

by culturing confluent hiPSC-CMs on soft, elastic substrates (e.g. Polyacrylamide) embedded with fluorescent markers (Fig 5.1 A, inset). High content imaging of the spontaneous (or paced) contractions of the hiPSC-CM monolayer results in high frame rate timelapse images of one or more imaging channels (Fig 5.1 B). Atleast one channel imaging the substrate embedded fluorescent markers or cytoplasmic markers (e.g. MitoTracker) is sufficient for contractility analysis. For measuring stiffness, timelapse images of substrate markers is necessary (Table 5.1).

The starting point of contractility analysis is the measurement of motion in the high frame-rate timelapse images from high content screening system, which can be utilized to further analyze traction forces, intercellular stresses and the stiffness of the monolayer. Particle Image Velocimetry (PIV) is a quantitative image-correlation based technique, that estimates the flow or deformation between two images. PIV divides the set of images into overlapping rectangular sub-domains (windows) and finds the most probable displacement that registers each corresponding window between the two images. In order to accurately measure both the small and large deformations simultaneously, a multi-pass implementation of PIV is used. Multi-Pass PIV provides higher spatial resolution by employing progressively smaller windows, whose frame is shifted by an amount determined in the previous step (§1.4.2). A computationally efficient GPU-accelerated PIV method is developed, that is specifically tailored to analyze TBs of timelapse images generated by high content screening system in acceptable timeframe (§5.6.1). The software codebase is written in Matlab and will open-sourced in github at the time of publication, along with a Graphical User Interface (GUI).

Automated reference frame selection for high throughput contractility experiments

PIV requires comparing each frame of the acquisition to a reference frame. For contractility of hiPSC-Cardiomyocytes, the reference frame of interest is either where cells are at a relaxed state (dynamic reference) i.e. they are not contracting, or to a cell-free image (Table 5.1, Fig 5.1B). The cell-free image, only applicable to substrate marker images, is useful for decoupling the baseline isometric and the active contractile force exerted by hiPSC-CMs.

For cells undergoing spontaneous contractions, the information of a relaxed state (dynamic reference) is not known *a priori*. To automatically select the dynamic reference frame, instantaneous velocity field of cardiomyocytes at every time point is estimated by comparing consecutive frames (Fig 5.1C). Either the spatial average of pixel intensity differences or a lower resolution PIV deformation field is used to construct this velocity curve.

Typically, the velocity signal presents two distinct peaks (green arrow, Fig 5.1C) that correspond to maximum rates of contraction and relaxation, followed by periods of low

velocity corresponding to the beating frequency of the cells. In order to robustly identify the relaxation state versus the peak contracted state, the velocity signal is first window averaged in time. The reference frame is selected as that of minimum window-averaged signal (black arrow, Fig 5.1C). Optionally, more than one dynamic reference frame can be selected for phase-averaged PIV to improve signal-to-noise ratio of the PIV estimate. In addition, the velocity signal can be further utilized to reduce the computational expense of the next step by skipping low-motion frames in relaxed state (red dots, Fig 5.1C). The deformation field is then determined by PIV using all the high-motion frames of the video to the reference frame(s) (Fig 5.1B), yielding the corresponding instantaneous deformation fields (Fig 5.1D).

5.2.2 Quantification of contractility from traction force microscopy of spontaneously beating monolayers (Dynamic contractility)

Traction Force Microscopy (TFM) is a computational method for measuring cell-exerted traction forces and is starting to be accepted in the field of cardiac research (§1.4.1). hiPSC-CMs cultured on elastic substrates of physiologically relevant stiffness is measured computationally using optical microscopy observation of fluorescent marker displacement (Fig 5.1D) embedded in the substrate. Traction force field ($\boldsymbol{t}$) and additionally the monolayer stress tensor field ($\mathbf{P}$) of the hiPSC-CM monolayer is calculated by the analysis pipeline from the PIV analysis if the substrate fluorescent marker images are used.

The traction stresses are determined from the measured deformations by solving the partial differential equations of equilibrium for the polyacrylamide substratum (Linearly elastic substrate), as previously described [33, 34]. Dynamic analysis of the deformation allows for the traction stresses to be determined during several contraction cycles without removing the cells from the gels, upto an assumed constant isometric pre-stress. The cumulative intracellular tension transmitted through the cell sheet were determined by solving the Kirchhoff–Love equations of mechanical equilibrium for a thin elastic plate subject to the forcing created by the measured traction stresses, using previously described methods [65, 89, 91].

Since the quantity of interest is the contractile state of hiPSC cardiomyocytes over space and time, the most relevant quantity is the total principal normal stresses ($\mathrm{tr}(\mathbf{P}) = \mathbf{P}_{xx} + \mathbf{P}_{yy}$), which is a two-dimensional quantity over space with units of Pa (Fig 5.1E). A negative sign of $\mathrm{tr}(\mathbf{P})$ indicates a local contraction and positive sign indicates extensile behavior at that point. The total contractility trace over time is obtained by spatial averaging of the absolute value of $\mathrm{tr}(\mathbf{P})$ (Fig 5.1F).

The authors acknowledge that the time-resolved two dimensional deformation maps (Fig

5.1D) is provided as output, so that future users can expand and propose alternative ways to characterize cell contractility.

Quantification of contractility from cell motion of spontaneously beating monolayers (Geometrical contractility)

When the fluorescent substrate marker imaging is not available, the contractility analysis can be performed on cytoplasmic markers such as MitoTracker, Wheat Germ Agglutinin (WGA) or brightfield images (Fig 5.1B). It should be noted that the signal-to-noise ratio (SNR), in general, will be much lower than fluorescent marker images and the correct units should be reported for repeatability. A comparison of choosing PIV parameters between fluorescent beads (high SNR) with cell cytoplasmic markers is discussed in SI.

In the case of cell motion-based contractility (geometrical contractility), it is computed as local, relative changes in area –i.e. contraction / extension - by taking the divergence of the deformation fields (Fig 5.1D). The total contractility signal (Fig 5.1F) is then computed as the average value of the magnitude of the divergence field for each frame. The differentiation is done with third-order Pade's scheme

Contractility trace and parameter extraction

The time-dependent contractility signal (Fig 5.1F) can be computed from either div($\mathbf{u}$) or tr($\mathbf{P}$), calculated from the displacement field u or monolayer stress tensor $\mathbf{P}$. The former represents the relative change in area of the cardiomyocyte monolayer and the latter denotes the monolayer tension or compression. The 1D traces are calculated as the spatial average value of the magnitude of either of the quantities for each frame. The algorithm uses the monolayer stress tensor $\mathbf{P}$ if traction force microscopy option is enabled (i.e. using substrate fluorescent marker images). In case of cytoplasmic markers, the algorithm defaults to the deformation field.

5.2.3 Direct elastography model to measure cardiomyocyte stiffness in spontaneously contracting monolayers

The rheological properties (θ^c) of cell monolayers in a coarse-grained continuum framework is quantified by prescribing a constitutive model f such that,

$$\mathbf{P}^c = f(\mathbf{u}^c; \theta^c). \tag{5.1}$$

$\mathbf{P}^c$ is the first Piola-Kirchhoff stress tensor at reference configuration (diastolic reference, Fig 5.1) of the monolayer with material properties θ^c and $\mathbf{u}^c$ is the monolayer deformation

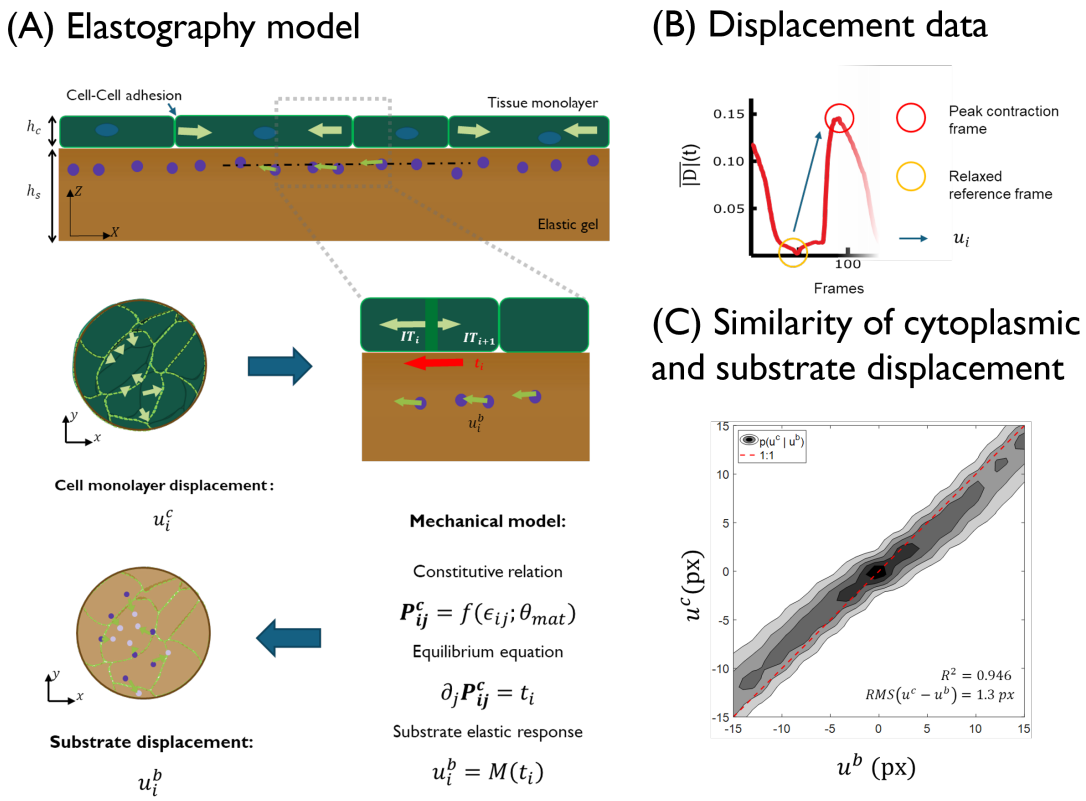

Fig 5.2. Biomechanical model for elasticity parameter inference. A) Elastography model. Cultured cardiomyocyte monolayer is assumed to be in mechanical equilibrium with the substrate and connected by cell-cell adhesions. Active contraction due to sarcomeric activity results in geometric contraction and cellular strain. Active contraction is also transmitted to the substrate via focal adhesions. Both the cellular strain and the substrate motion is observed with microscopy. The elastography model builds on TFM equations to link the cellular strain to substrate strain by mechanical equilibrium conditions at the interface and the elastostatic substrate response. (B) For elastography purposes, both cell and substrate deformation are considered only at peak contraction relative to the relaxed state (i.e. dynamic reference). (C) Empirical observation of pointwise cellular and substrate motion shows high correlation.

as measured by PIV. Combining contractility and TFM assays enables closed-loop continuum mechanical modeling of the experimental system (Fig 5.4A) as follows: Cell monolayer is modeled as a thin, continuous membrane of uniform thickness h^c and isotropic rheological parameters undergoing a deformation $\mathbf{u}^c$ in response to an internal stress tensor field $\mathbf{P}^c$. The monolayer is assumed to be in quasi-steady mechanical equilibrium with the elastic substrate underneath. The active stress exerted by the contractile machinery of the cardiomyocytes are not explicitly modeled in this system. Since the activity excites the

isotropic stress components [ref] , only the deviatoric component of the stress tensor is used for fitting. Neglecting inertia, the force balance at the cell-substrate interface is given by,

$$\nabla_{2D} \cdot \mathbf{P}^c = -\boldsymbol{t}/h^c. \tag{5.2}$$

$\boldsymbol{t} = (t_x, t_y)$ is the in-plane traction stress field at the planar substrate boundary ($z = h$). The thin-plate assumption implies stress-free boundary at $z = h^c$ and $\partial \mathbf{P}^c/\partial z = 0$ representing a $z-$averaged stress tensor. The elastic response of the underlying finite thickness substrate (h) with known elastic properties $\theta_s = E, nu$ to the applied planar traction field is mapped as,

$$\mathbf{u}^s = \mathbf{M}(\boldsymbol{t}; \theta^s). \tag{5.3}$$

E is the Young's modulus and ν the Poisson ratio, and the mapping $\mathbf{M} : \boldsymbol{t} \rightarrow \mathbf{u}^s$ comes from the solution to the elastostatic equation of the substrate [38]. Taken together, the measurements of the cellular deformation $\mathbf{u}^c$ and the elastic substrate deformation $\mathbf{u}^s$ allows combining eqns (5.1) - (5.3) to create a direct elastography kernel (DEK),

$$\mathbf{u}^s = \mathrm{DEK}(\mathbf{u}^c; \theta^c, \theta^s). \tag{5.4}$$

Cell monolayer material properties, θ^c, is inferred in this framework by Broyden-Fletcher-Goldfarb-Shannon (BFGS) unconstrained optimization with a L-2 cost function constructed on the residual of (5.4) . The direct method of rheology fitting avoids two regularization steps in the inverse problem of monolayer stress microscopy while dispensing of the constraint of linear elasticity for the cell monolayer [49].

High-throughput elastography inference framework

The particular theoretical and numerical details used in this studied are as follows. The cell monolayer is approximated as a thin, compressible Neo-Hookean hyperelastic solid with the strain energy density given by,

$$W = \frac{G}{2}(\boldsymbol{I}_F - 3) - G \ln J + \frac{1}{2} K (J-1)^2. \tag{5.5}$$

$\mathbf{P}^c$ is the first Piola-Kirchhoff stress tensor in the reference (diastolic reference) configuration [44] given by,

$$\mathbf{P}^c = f(\mathbf{u}^c; \theta^c) = 2G(\mathbf{F} - \mathbf{F}^{-T}) + 2KJ(J-1)\mathbf{F}^{-T} \tag{5.6}$$

where $\theta^c = G, k$, the shear and bulk modulus respectively. $\mathbf{F} = \boldsymbol{I} + \nabla \mathbf{u}^c$ is the deforma-

tion gradient tensor and the Jacobian determinant $J = \det(\mathbf{F})$. The active cardiomyocyte contraction implicitly modeled as additive isotropic volumetric compression to the stress tensor $\mathbf{P}^c$ [39] and the effective bulk modulus is denoted by K. Once the stress tensor is constructed, the traction stresses at the cell-substrate interface is readily available from (5.2). A third-order Pade's finite difference scheme is used for numerical derivatives and the mapping $\mathbf{M}$ is taken to be the Green's function solution for finite thickness elastic gel [38] to predict the substrate deformation. The elastic substrate in this manuscript has the properties of $E^s = 8\,\text{kPa}$ and $h \approx 150\,\mu\text{m}$.

For the inference of the shear modulus G, the displacement of both the cell monolayer and substrate is considered at the peak contraction relative to the dynamic reference (Fig 5.2 B). Experimentally, a strong linear correlation is observed between the cell monolayer deformation vector and the substrate deformation vector (Fig 5.2 C). This observation is used to further constrain the biomechanical model as $\mathbf{u}^c \approx \mathbf{u}^s$.

The unconstrained minimization to infer the rheological properties θ^c is performed using BFGS routine in matlab optimization toolbox using quasi-steady algorithm and finite difference Hessian approximation. For all of the benchmark data presented, the optimization was stable and resulted in a local minimum.

5.3 Experimental methods

5.3.1 Differentiation and culture of hiPSc-CM

The hiPSC clones were cultured in E8 cell culture media (Thermo Fisher Scientific, A1517001) in plates coated with growth factor-reduced Matrigel (Corning, 356231). The hiPSC were differentiated into CMs utilizing a chemically defined cardiomyocyte differentiation protocol [208] with modifications. Briefly, hiPSCs were treated with CHIR99021 (Tocris, 4423) for 3 days in RPMI 1640 (Thermo Fisher Scientific, 11875119) with B27-insulin (Thermo Fisher Scientific, A1895601). Subsequently, the cells were treated with the Wnt inhibitor C59 (Tocris, 5148) in RPMI supplemented with B27-insulin (RPMI/B27-) for another 2 days. Between 5–11 days of differentiation, RPMI/B27- media refreshed every other day and switched to RPMI supplemented with 1X B27(RPMI/B27+) after beating was observed. On day 11, cells were cultured in RPMI/B27+ without glucose, supplemented with 5 mM sodium L-lactate (Sigma Aldrich, 71718) for 3 days, to improve the CMs purity. On day 14, the cells were cultured on RPMI/B27+. On day 15, the hiPSC-CMs were dissociated with TrypLE 10x (Thermo Fisher Scientific, A1217703) and seeded in 6-well Matrigel-coated plates at a density of 3×10^6 per well in RPMI/B27+ containing 10% KOSR and ROCK inhibitor Y-27632 (Tocris, 1253) (replating media). After 2 days, cells were cultured in RPMI/B27+ without glucose for 3 days and then switched to maturation media [209] and

cultured for an additional 4-5 weeks prior to replating on matrigel in 96-well plates (Matrigen 96 glass) for high throughput analysis. All experiments were performed day 49 post differentiation.

5.3.2 High throughput automated multi-channel timelapse acquisition

At day 42, cells were dissociated using 10X TrypLE (ThermoFisher Scientific) and plated onto Matrigel-coated Softwell 96 Glass with Easy Coat,8 kPa stiffness, and 1 μM yellow-green Soft Trac beads at a density of 150,000 cells/well in 100 μL of maturation media supplemented with 10% KOSR and 2 μM Thiazovivin (Selleck Chemicals). The next day, 100 μL of warm maturation media were added to each well. 100 μL of media were removed from each well and replaced with 100 μL of fresh, pre-warmed maturation every other day. All experiments were performed day 49 post differentiation.

hiPSC-CMs were removed from a 37 ^{o}C and 5% CO_2 incubator and placed immediately into in a tissue culture cabinet on a dry heat block set to 37 ^{o}C to prevent temperature fluctuation during the subsequent washing and dye loading steps. All subsequent manipulations were conducted on a 37 ^{o}C dry heat block. 2X dye solution containing Hoechst 33258 4 mug/mL and MitoTracker Deep Red FM 100 nM, was prepared in maturation media and warmed to 37 ^{o}C in a water bath. 100 μLof media were removed and replaced with 2X dye solution. The plate was placed back in a 37 ^{o}C and 5% CO_2 incubator for 15 minutes. After the 15-minute incubation, the cells were washed 4X by removing and replacing 100 μL of pre-warm fresh maturation media. After washing, the cells were placed back in an IC200 KIC instrument (Vala Sciences, California, USA) at 37 ^{o}C and 5% CO_2 incubator for 10 minutes to recover. High-resolution, high-framerate timelapse videos (2048x2048 pixels) were acquired automatically using the IC200 KIC instrument at an acquisition frequency of 60 Hz for a duration of 6 seconds, with interleaved acquisition of excitation/emission wavelengths of 488/530 nm (beads channel) and 633/660 nm (MitoTracker channel) using a 0.75 NA 20X Nikon Apo VC objective.

5.3.3 Dose-response experiments using benchmark compounds

Force dose-response and stiffness dose-response curves were obtained for Istaroxime (IST), Omecamtiv mecarbil (OM), Mavacamten (MYK) and Sotalol (SOT). Reference compound isoproterenol (Tocris) was diluted in water and Omecamtiv Mecarbil (Selleck Chemicals) and Digoxin (Tocris) were diluted in DMSO. Each compound was diluted in maturation media solution to a 2X concentrated stock and was warmed to 37 ^{o}C using a dry heat block prior to application to hiPSC-CMs.

For each well in the microtiter plate, image sequences of substrate beads and cytoplasmic

marker (MitoTracker) were recorded simultaneously using two-channel interleaved acquisition at 5 regions of interest (ROIs). To obtain a cell-free reference for calculating diastolic tension, the substrate fluorescent markers were imaged prior to culturing hiPSC-CMs at the same 5 ROIs. Imaging of beating cells was performed before and 30 minutes after treatment of the 5 dose titers to obtain matched controls at zero dose.

5.4 Results

5.4.1 Measurement of drug response against benchmark compounds

To illustrate the ability to capture the effect of drugs and application of the method, hiPSC-CM monolayers were cultured in 96 well plates. The cells were spontaneously beating at the time of recording. The analysis platform was evaluated for the capacity of obtaining dose response curves from the above-mentioned contractility data against four compounds : Istaroxime, Omecamtiv Mecarbil (OM), Mavacamten (MYK) ad Sotalol. The plate was imaged twice: before the cells were subject to any treatment, and after the corresponding dose of compound was added. In addition, if measurement of diastolic tension is required, a cell-free reference state of the substrate fluorescent markers should be imaged in addition, either before culturing or after cell removal.

For each well in the microtiter plate, 5 positions were recorded, before and 30 minutes after treatment of 5 dose titers, of substrate marker and cell membrane channels. This small benchmark compound dataset resulted in about 1 TB approximately. By imaging before a treatment, the same set of cells can be used as internal control after the compound was added.

Istaroxime is a first-in-class agent which acts through inhibition of the sarcolemmal Na+/K+ pump and activation of the SERCA2 pump [210]. We observe that Fig 5.3 A shows that Istaroxime treatment increases the amplitude and peak-peak duration of the contraction for higher doses with a decrease in diastolic tension (baseline). This is evidenced by the traces for 0.1 μM (Fig 5.3 B). This is accompanied by increases in rise and fall time as well and a significant increase of pw90 at 0.1 μM.

Omecamtiv Mecabril (OM) is known to stabilize thick filament myosin cross-bridge kinetics, leading to increased passive stiffness [211]. OM shows a significant decrease in systolic amplitude with increase in diastolic tension (baseline), pw90, rise time and fall time for all doses. The overall effect is a decrease in systolic contraction with increased diastolic tension and pw90 implying increased work.

MYK is a myosin inhibitor currently in clinical trials for the treatment of hypertrophic cardiomyopathy, by decreasing the ATP activity of the cardiac myosin heavy chain. Due to this mechanism, the effect of this drug can't be studied using action potential or calcium

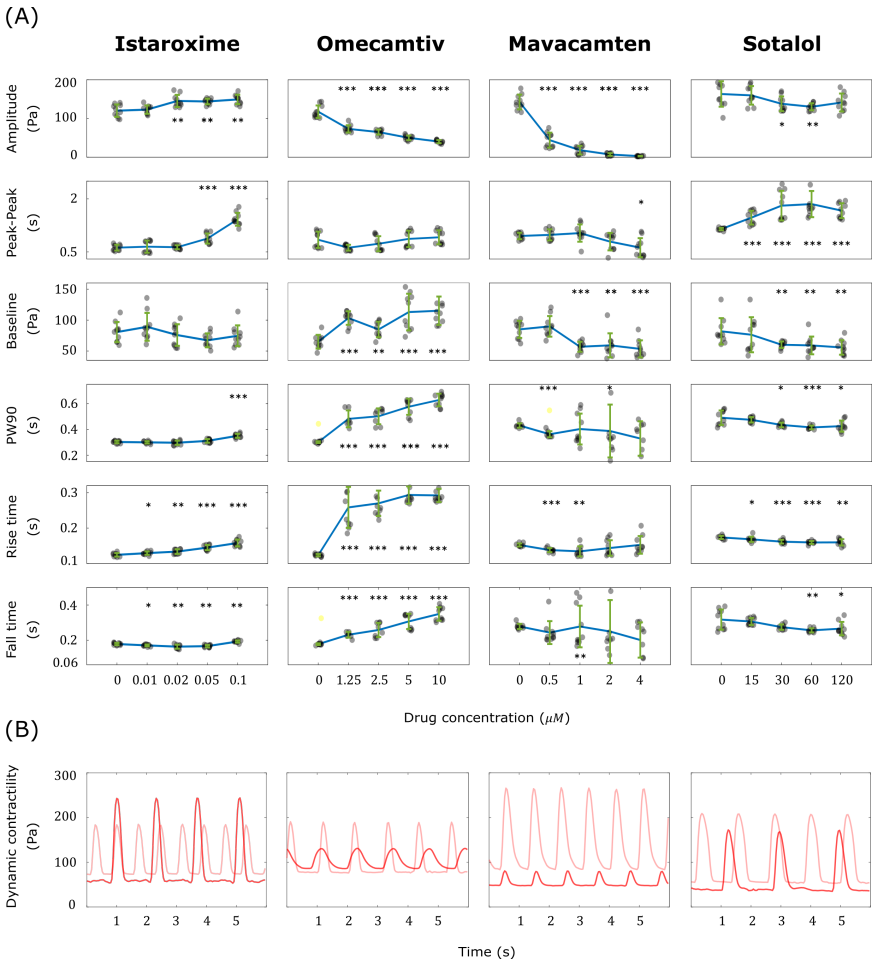

Fig 5.3. Measurement of drug response in hiPSc cardiac disease models. Dose response to benchmark compounds at 30 min after treatment (left to right : Istaroxime, Omecamtiv, Mavacamten, Sotalol). Concentration of 0 μM denote the vehicular control after media change. Dynamic contractility metrics from traction force microscopy ($\boldsymbol{t}$ in units of Pa) : Amplitude of the peak (diastolic reference), Peak-Peak duration, baseline stress (Cell-free reference), Average peak width at 90% prominence, peak rise time and peak fall time. Yellow scatter dots indicate points treated as outliers ($< 10^{th}$ and $> 90^{th}$ percentile) and are omitted from calculations. Data for each concentration of the compound has n=10 videos before outlier removal. (B) Representative dynamic contractility traces ($\mathrm{tr}(\boldsymbol{\sigma})$) for Istaroxime (0.1 μM), Omecamtiv (10 μM), Mavacamten (1 μM) and Sotalol (60 μM) respectively from left to right (Bold red). Light red lines are representative vehicular control traces. P-values are reported based on Mann-Whitney U test ($*-p \leq 0.05$, $**-p \leq 0.01$, $***-p \leq 0.001$)

kinetics assays. The effect in cardiomyocyte contractility is a decrease in overall contractile force. Sotalol is a beta blocker is used as an anti-arrhythmic drug [212]. Sotalol displays a prolongation of peak-peak duration for all doses as expected with a decrease in other metrics.

5.4.2 Elastography method captures cardiomyocyte stiffness change with Omecamtiv and Mavacamten

As a proof-of-concept, two benchmark compounds known to modulate the myocardial stiffness, Omecamtiv Mecarbil (OM) and mavacamten (MYK) are used. The shear modulus of the spontaneously beating hIPSc monolayer treated is quantified before and after 30 minutes of treatment. Fig 5.4 briefly summarizes the contractile dynamics of the two compunds. Visually, the quiver displacement maps (diastole to systolic peak, Fig 5.2 B) shows a drastic reduction in magnitude after treating with high dose of both drugs. $|D_{\text{peaks}}|$ represent the contractilty div($\mathbf{u}$) at peak systole, which quantifies the observed decrease. However a significant increase in shear modulus is observed upon treatment of Omecamtiv and a decrease in shear modulus after treatment with Mavacamten (Fig 5.4 B), both dose- and time-dependent. Typical values of inferred shear modulus for control is shown as a box plot. This illustrates the ability of the minimal Direct Elastography Model (DEK) to decouple changes in force generation with the material properties of cardiomyocytes in a high-throughput manner.

5.5 Discussion

Improvements to the techniques for producing hiPSC-CMs in large quantities and with better maturity pose great appeal for the use in drug screening, toxicity, and the study of disease *in vitro*. Existing high-throughput assays for cardiac contractility rely on the measurement of surrogate variables such as the changes in the intensity of the image. Moreover, most of these assays have been realized on a stiff surface such as glass or plastic. In contrast, substrate stiffness is a feature that has proven to be of relevance, especially for hiPSC maturity. Traction Force Microscopy has been established as the golden standard for force measurement, however there is a lack of both hardware and software that allows for the implementation of high-throughput TFM experiments.

In this paper, we have presented a pipeline for analyzing the mechanical contractility and the stiffness of spontaneously beating hiPSC-CM monolayer images generated by the high content screening experiments. TFM is implemented in the proposed software for the accurate measurement of cellular forces. The presented combination of hardware and software is a full solution for a high-throughput platform for the study of cardiac contrac-

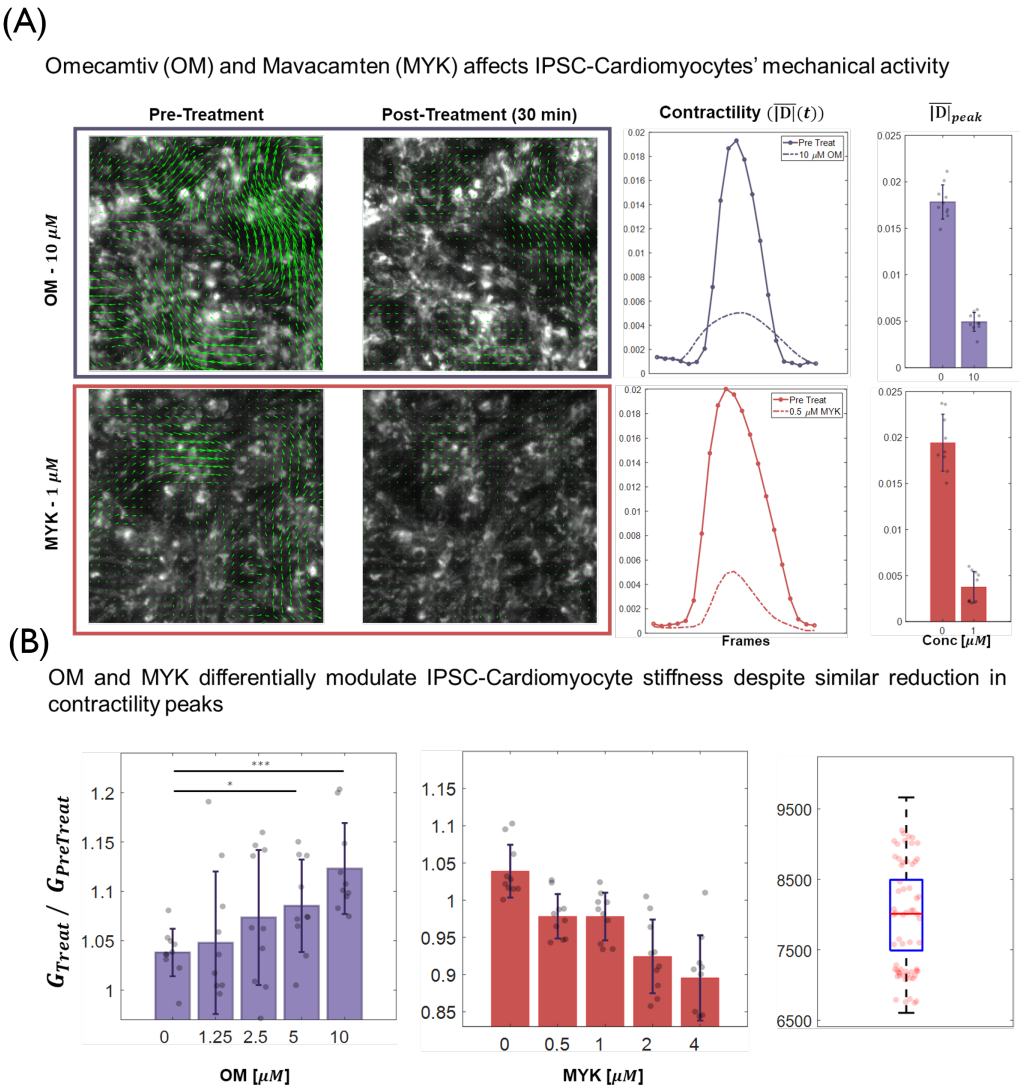

Fig 5.4. OM and MYK differentially modulates stiffness and contractile amplitude. (A) OM and MYK shows a decrease in systolic amplitude. Overlaid diastole-peak systole displacement field on top of MitoTracker images visually show the change in amplitude. Trace and bar plots quantifies the reduction in the peak amplitude. (B) Elastography results indicate that OM increases shear modulus and MYK decreases shear modulus relative to control. Box plot depicts nominal value of shear modulus inferred for control wells.

tility and mechanical properties. We have performed experiments of spontaneously beating hiPSC-CM seeded on a 96 well plate with PA gels and employed to retrieve changes in force against benchmark compounds.

Alterations to myocardial mechanical properties are implicated in diseases like heart failure with preserved ejection fraction and restrictive cardiomyopathy affecting the end diastolic volume without apparent systolic contractility dysfunction [203, 204]. Cardiomyocyte elastic property contributes to ventricular stiffness, which emerges as a result of sarcomere organization, accessory protein structure (titin isoforms), actomyosin kinetics or microtubules. Measuring cardiomyocyte tissue stiffness provides a valuable mechanical phenotype readout of cytosolic structural organization in relation to cardiac function, genetic screening and drug testing.

However, existing technologies to probe mechanical properties remains extremely low throughput and hinders assessment of passive stiffness as a biomarker in large scale genetic or drug screens. A striking clinical case study for the need of stiffness readout of the drug Omecamtiv Mecarbil (OM). It was orignially developed as a cardiac myosin ATPase activator stabilizing ON state of thick filament (myosin heads with bound ADP) and showing benefit for increasing cardiac stroke volume [211]. Recent studies using hiPSC and rat samples [59, 213] noticed increase in passive stiffness as a result of myosin cross-bridge number increase, with a potential to alter diastolic function .

Taking advantage of high throughput contractility assay described in the paper, a minimal biomechanical model is developed to computationally infer the passive elastic properties of hiPSC cardiomyocyte monolayer. The monolayer is modeled as a planar, 2D Neo-Hookean hyper-elastic continuum material characterized by isotropic material parameters effective bulk modulus K and shear modulus G. The inference is performed at each of the peak contraction of the contractility cycle.

Experimentally, a high correlation and linearity is observed between the cell deformation vector and the substrate deformation vector at the peak contraction and at the resolution of the imaging. The RMS of the error between the two deformation fields is of order of the optimization residual. Using this empirical observation, additional constraint of displacement continuity at the interface between the cell monolayer and the substrate is placed in addition to the traction stress continuity. This overdetermined system allows estimation of the material properties from high signal-to-noise substrate displacement field only.

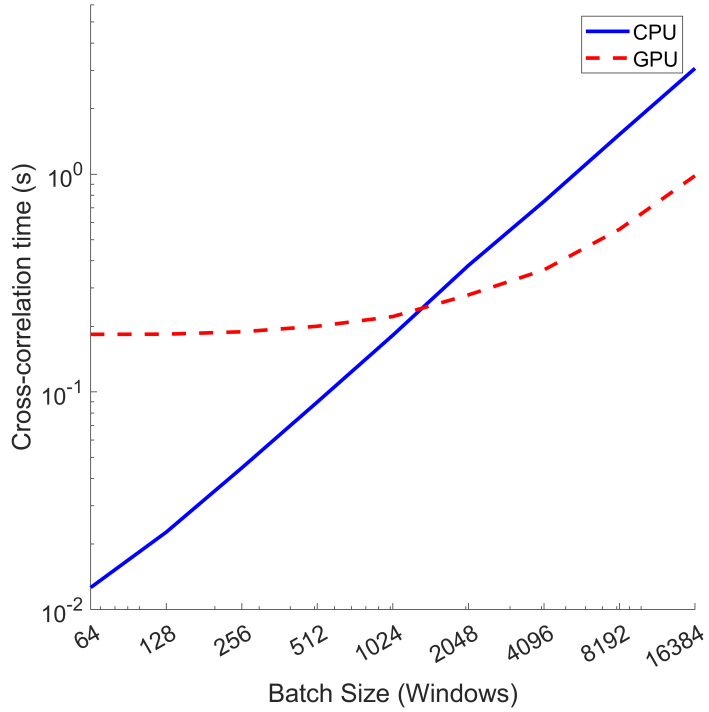

Fig 5.5. PIV cross-correlation time as a function of batch size. The bottle-neck in PIV computation, the cross-correlation step, is timed for different sizes of batches (i.e. the number of sub-windows run at a single time) for $W_L = 128$ px. GPU compute time is dominated by the memory transfer between RAM and GRAM, but is faster for large datasets. 16,384 (214) batch of 128x128 sub-windows corresponds to 16 images of 2048x2048 px in size ($\sim$ 8.5 GB). A typical timelapse consists of 150 images, resulting in an approximate speedup of 28.

5.6 Supplementary Information

5.6.1 High efficiency GPU-accelerated multi-Pass PIV software

The single threaded, sequential execution of PIV operation over all interrogation windows is not conducive to the large amount of data generated in a typical high frame-rate, high throughput contractility experiments (TBs). The efficiency of timelapse contractility PIV algorithm is improved as follows. First, the maximum usable RAM or GPU memory (GRAM) is identified, then all the interrogation windows are pre-allocated in memory and imported into the RAM in parallel. If the total memory available is less than what is needed for a given dataset, the computation occurs in batches. Secondly, the core of the computations, involving Fast Fourier Transform (FFT), is multi-threaded and vector optimized for each batch. GPU acceleration in MATLAB is used to further improve performance. Fig 5.5 shows the computation time for the cross-correlation step which is the rate-limiting

step (after RAM transfer) using Intel Xeon W-2123 CPU and Nvidia Quadro RTX 5000 GPU (16 GB GRAM). The memory transfer time to GRAM slows GPU computations in smaller batches, however GPU implementation shows an order of magnitude improvement over CPU calculation time. The maximum batch size tested (2^14) corresponds to about 8.5 GB of memory that can hold 16 images (2048x2048 px size of single float datatype) when using the sub-window size $W_L = 128\,\text{px}$. This results in about a speedup of 3 and a total speedup of 28 considering 150 images in a timelapse. By automatically skipping low-motion frames (Fig 5.1 C), the analysis is made faster.

Microscopy image	Geometric contractility	Elastography	Systolic tension	Diastolic tension
Brightfield	Y	N	N	N
+ Cell marker (Cytoplasmic / Membrane)	Y	N	N	N
+ Substrate marker (Diastolic ref)	Y	Y	Y	N
+ Substrate marker (Systolic ref)	Y	Y	Y	Y

Table 5.1. Requirements of available contractility measurements. Intercellular stress and elastography measurements require substrate fluorescent trace image. This table illustrates the additional measurements possible as more modalities are added starting from brightfield images.

5.7 Acknowledgements

This chapter is being prepared for publication : Serrano, R*., Kandasamy, A*., Staudt, D.W., Mercola, M. and del Álamo, J.C. Multi-modality high-throughput contractility and stiffness measurement of hiPSC-derived cardiomyocytes. *In preparation.* The dissertation author is the co-primary author of this work.

Chapter 6

CONCLUDING REMARKS

This thesis focuses on improving biomechanical tools to phenotype random walk characteristics, traction stress with uncertainty maps and cardiomyoycte monolayer elasticity by combining physical models, microscopy data and computational optimization. Motion tracking, a critical component of microscopy-based phenotyping forms the foundation for further analysis. The work presented here advances motion measurement techniques and uses statistical modeling to enhance mechanical parameter inference. These developments hold promise for basic mechanobiology applications, high throughput screening and precision medicine, particularly in the context of limited data and inherent biological variability. Specific applications to immunology and heart failure drug development demonstrate the utility of these methods leveraging various phenotyping methods presented in this thesis. The main conclusions of this thesis are summarized below, with a more detailed discussion provided at the end of each chapter.

In chapter 2, the relevance of matrix deformation and frequent turning to achieve chemotaxis as well as the heterogeneity of migrating leukocytes were discussed. The physical properties of the ECM space are a significant component which can vary greatly across different locations within an organism. However, during an immune response, this variation does not impede neutrophils from migrating towards sites of inflammation. In the present study, label-free automated cell tracking made it possible to analyze more than 20,000 migrating cells, yielding highly detailed multiparametric statistics of the migratory process. The measurements of 3D matrix deformations indicated that neutrophils could transiently deform low collagen concentration matrices using physical forces. In particular, the cell-generated collagen deformations were oriented preferentially toward the cell and along the chemoattractant gradient direction. However, the cells became unable to appreciably deform high collagen concentration matrices and the small deformations they generated in the collagen were more isotropic. The cells adapted to increased matrix rigidity in high collagen concentration matrices by turning more often, which caused a marked decrease in the spatial persistence of the direction of motion. This transition was triggered by the cells' inability to physically remodel their microenvironment, which was confirmed by pharmacological inhibition of contractile forces mediated by myosin-II, or protrusive forces exerted by Arp2/3-mediated dendritic actin polymerization. A biased random walk model with no

adjustable parameters reproduced the evolution of cell motion orientation along the cell trajectories. This experimental data and analysis suggest that 3D migrating neutrophils maintain their chemotactic efficiency as the matrix pore size is decreased by varying their bias distance in concert with their persistence so that $S_\theta \approx 3S_p$.Overall, this work contributes to an enhanced mechanistic understanding of the role that the Arp 2/3 complex, myosin-II, and surrounding collagen density play in 3D neutrophil chemotaxis, which, in turn, may provide crucial insights into molecules and processes to target for regulating pathological inflammatory responses.

Measuring traction stresses in 3D interstitial and fibrous collagen gel is confounded by non-linear material properties. Phenomena such as fiber realignment with force and local modification of the matrix are biologically relevant but remain difficult to be modeled. Improvements in this avenue will allow direct measurement of traction stresses and potentially provide a granular understanding of mechanical forces in directed migration. (e.g. how the cells sense impenetrable obstructions and determine the path of least resistance in fibrous matrices). Biological variability is ubiquitous for their function but is not readily quantifiable with current methods. While trajectories with high spatial and temporal resolutions are available, systematic analysis of single-cell motion using Bayesian statistics holds promise to correlate single-cell biochemical activity to biophysical phenotype. Methods to identify heterogeneous sub-populations in this thesis make a turn in this direction.

A computational pipeline to autonomously cluster cells exhibiting different random walk characteristics identified two naturally occurring migratory phenotypes : a high motility cluster with faster, persistent cells undergoing fewer turns and a low motility cluster with lower speed, increased incidence of large turns. It was discovered these cluster proportions are modified by transendothelial migration which preferentially enriched the low motility population. As extravasation is a necessary step in the inflammation response, these observations provide insights into the biophysical impacts of mechanically priming neutrophils to conduct sentinel functions in a subpopulation of cells. Such migratory heterogeneity is also demonstrated in mouse primary T-cells showing that proteins of the same Formin family, Formin-like 1 and mammalian diaphanous-relation formin 1, despite having similar mechanisms of actin polymerization differentially regulate T-cell motility based on the collagen density.

Many biophysical measurements rely on image-based deformation measurements. In chapter 3, Traction Force Microscopy Uncertainty Quantification (TFM-UQ) method was developed to estimate the uncertainty in image-based deformation measurement and utilize the information to adaptively regularize the ill-conditioned equations involved in the TFM procedure. To quantify uncertainty in the image-to-deformation procedure of Particle

Image Velocimetry (PIV), a technique based on bootstrapping of image pixels is adapted. PIV and, hence, TFM error, is shown to be dependent on local image quality, deformation gradient and the size W_L of the sub-windows. The latter is a key PIV parameter affecting measurement error and resolution. Methodologically, TFM-UQ employs a hierarchical Bayesian framework for propagating PIV error and incorporating the hyperparameter (regularization parameter) variability as random variables. The resulting uncertainty maps from Markov Chain Monte Carlo sampling establish error bars for the traction stress recovered at each location, both in magnitude and the direction of the stress vector. This information can help interpret and analyze TFM experiments for multiple reasons. Among these, it may help identify outliers automatically and objectively. It allows for separating biological and measurement uncertainties when pooling data from repeat experiments. It can also help pinpoint sources of measurement error and refine experimental protocols. TFM-UQ can run on a personal computer in a few minutes depending on the resolution. Additional investigations using approximate Bayesian inference methods are worthwhile to make the calculations near real-time for high throughput applications. The Bayesian framework also provides a way to incorporate other physically meaningful prior information such as cell contour segmentation.

In chapter 5, we have presented a pipeline for analyzing the mechanical contractility and the stiffness of spontaneously beating hiPSC-CM monolayer images generated by high-content screening experiments. Existing technologies to probe mechanical properties remain extremely low throughput and hinder the assessment of elasticity as a biomarker in large-scale genetic or drug screens. TFM is implemented in the proposed software for the accurate measurement of cellular forces. The presented software is a full solution for a high-throughput platform in the study of cardiac contractility and mechanical properties. Benchmark experiments of spontaneously beating hiPSC-CM seeded on a 96 well plate with a drug panel retrieved key metrics of changes in force and stiffness. While both Omecamtiv and Mavacamten show a decrease in systolic amplitude, Omecamtiv was seen to increase the shear modulus while Mavacamten showed a decrease in shear modulus, highlighting the utility of the new stiffness module.

Viscosity, arising from microtubules, is known to modulate the relaxation kinematics of cardiomyocytes during diastole. While this study quantifies the passive stiffness affecting the end-diastole volume, modeling viscoelasticity of the time-dependent behavior during a contraction cycle holds promise to differentiate the phenotypic modifications by pharmacological compounds. It is worthwhile to note that the stiffness measurement in this thesis does not consider the bulk modulus, which determines the resistance to compression. Since the active contractile stresses excite the volumetric contraction, without an explicit model

for activity, it is not possible to differentiate the active volumetric contraction from passive resistance. Using fluorescence calcium sensors can provide a way to incorporate the active contraction in the inference model potentially revealing bulk modulus contribution in addition to the shear modulus described in this thesis. Furthermore, there is appreciable variability in the ratio of shear modulus which possibly stems from the assumption of isotropic material properties. Using single cell segmentation or sarcomere protein labelling such as α - actinin provides anisotropic information that can be included in the modeling. Finally, adapting TFM-UQ and a Bayesian framework used in other chapters of this thesis to the stiffness measurement method can potentially improve the sensitivity and precision of the elasticity measurements.

BIBLIOGRAPHY

1. François, J. *et al.* The interplay between matrix deformation and the coordination of turning events governs directed neutrophil migration in 3D matrices. *Science Advances* **7,** 3882–3896. ISSN: 23752548 (2021) (cit. on pp. x, 28, 44, 49, 56, 57).
2. Schwartz, A. B., Kandasamy, A., del Álamo, J. C. & Yeh, Y.-T. Neutrophils exhibit distinct migration phenotypes that are modulated by transendothelial migration. *bioRxiv* (2024) (cit. on pp. x, 56).
3. Sigler, A. L. *et al.* FMNL1 and mDia1 promote efficient T cell migration through complex environments via distinct mechanisms. *Frontiers in Immunology* **15.** ISSN: 1664-3224 (2024) (cit. on pp. x, 56).
4. Kandasamy, A., Yeh, Y.-T., Serrano, R., Mercola, M. & del Álamo, J. C. Uncertainty-Aware Traction Force Microscopy. *bioRxiv* (2024) (cit. on pp. x, 88).
5. Mollica, M. Y. *et al.* Distinct platelet F-actin patterns and traction forces on von Willebrand factor versus fibrinogen. *Biophysical Journal* **122,** 3738–3748. ISSN: 15420086 (2023) (cit. on pp. x, 57, 86, 105).
6. Huse, M. Mechanical forces in the immune system. *Nature Reviews Immunology* **17,** 679–690 (2017) (cit. on pp. 1, 12, 16).
7. Ladoux, B. & Mège, R. M. Mechanobiology of collective cell behaviours. *Nature Reviews Molecular Cell Biology* **18,** 743–757. ISSN: 14710080 (2017) (cit. on pp. 1, 57, 84).
8. Fadul, J. & Rosenblatt, J. The forces and fates of extruding cells. *Current opinion in cell biology* **54,** 66–71 (2018) (cit. on p. 1).
9. Godard, B. G. & Heisenberg, C.-P. Cell division and tissue mechanics. *Current opinion in cell biology* **60,** 114–120 (2019) (cit. on p. 1).
10. Wang, N., Butler, J. P. & Ingber, D. E. Mechanotransduction across the cell surface and through the cytoskeleton. *Science* **260,** 1124–1127 (1993) (cit. on p. 1).
11. Ladoux, B. *et al.* Strength dependence of cadherin-mediated adhesions. *Biophysical journal* **98,** 534–542 (2010) (cit. on p. 1).
12. Engler, A. J., Sen, S., Sweeney, H. L. & Discher, D. E. Matrix elasticity directs stem cell lineage specification. *Cell* **126,** 677–689 (2006) (cit. on p. 1).

13. Alberts, B. *et al. Molecular Biology of the Cell (6th ed.)* (W.W. Norton Company., 2015) (cit. on pp. 1, 5).

14. Smutny, M. *et al.* Friction forces position the neural anlage. *Nature Cell Biology* **19,** 306–317. ISSN: 1465-7392 (2017) (cit. on pp. 1, 57, 84).

15. Guillot, C. & Lecuit, T. Mechanics of epithelial tissue homeostasis and morphogenesis. *Science* **340,** 1185–1189 (2013) (cit. on p. 1).

16. Krndija, D. *et al.* Active cell migration is critical for steady-state epithelial turnover in the gut. *Science* **365,** 705–710 (2019) (cit. on p. 1).

17. Northey, J. J., Przybyla, L. & Weaver, V. M. Tissue force programs cell fate and tumor aggression. *Cancer discovery* **7,** 1224–1237 (2017) (cit. on p. 1).

18. Lawson, D. A., Kessenbrock, K., Davis, R. T., Pervolarakis, N. & Werb, Z. Tumour heterogeneity and metastasis at single-cell resolution. *Nature cell biology* **20,** 1349–1360 (2018) (cit. on p. 1).

19. Papalexi, E. & Satija, R. Single-cell RNA sequencing to explore immune cell heterogeneity. *Nature Reviews Immunology* **18,** 35–45 (2018) (cit. on p. 1).

20. Goolam, M. *et al.* Heterogeneity in Oct4 and Sox2 targets biases cell fate in 4-cell mouse embryos. *Cell* **165,** 61–74 (2016) (cit. on p. 1).

21. Asp, M. E. *et al.* Mechanobiology as a tool for addressing the genotype-to-phenotype problem in microbiology. *Biophysics Reviews* **4,** 021304. ISSN: 2688-4089 (2023) (cit. on p. 1).

22. Sharma, A. *et al.* High-throughput screening of tyrosine kinase inhibitor cardiotoxicity with human induced pluripotent stem cells. *Science Translational Medicine* **9.** ISSN: 1946-6234 (2017) (cit. on pp. 1, 13, 57, 83–85, 107).

23. Vincent, F. *et al.* Phenotypic drug discovery: recent successes, lessons learned and new directions. *Nature Reviews Drug Discovery* **21,** 899–914 (2022) (cit. on p. 1).

24. Thompson, D. W. *On Growth and Form* (ed Bonner, J. T.) (Cambridge University Press, 1992) (cit. on p. 2).

25. Phillips, R., Kondev, J., Theriot, J. & Garcia, H. *Physical biology of the cell* (Garland Science, 2012) (cit. on p. 3).

26. Schienbein, M. & Gruler, H. Langevin equation, Fokker-Planck equation and cell migration. *Bulletin of Mathematical Biology* **55,** 585–608 (1993) (cit. on pp. 3, 4, 19, 21, 22, 42, 54).

27. Langevin, P. On the theory of brownian motion. *CR Acad Sci (Paris)* **146,** 530 (1908) (cit. on p. 3).

28. Einstein, A. *et al.* On the motion of small particles suspended in liquids at rest required by the molecular-kinetic theory of heat. *Annalen der physik* **17,** 208 (1905) (cit. on p. 4).

29. Wu, P.-H., Giri, A., Sun, S. X. & Wirtz, D. Three-dimensional cell migration does not follow a random walk. *Proceedings of the National Academy of Sciences* **111,** 3949–3954 (2014) (cit. on pp. 4, 19, 20, 38, 49, 50).

30. Metzner, C. *et al.* Superstatistical analysis and modelling of heterogeneous random walks. *Nature communications* **6,** 7516 (2015) (cit. on pp. 4, 24, 46).

31. Codling, E. A., Plank, M. J. & Benhamou, S. Random walk models in biology. *Journal of the Royal society interface* **5,** 813–834 (2008) (cit. on p. 4).

32. Tranquillo, R. T., Lauffenburger, D. A. & Zigmond, S. A stochastic model for leukocyte random motility and chemotaxis based on receptor binding fluctuations. *The Journal of cell biology* **106,** 303–309 (1988) (cit. on p. 4).

33. Del Álamo, J. C. *et al.* Spatio-temporal analysis of eukaryotic cell motility by improved force cytometry. *Proceedings of the National Academy of Sciences* **104,** 13343–13348 (2007) (cit. on pp. 5, 9, 13, 57, 58, 65, 86, 111).

34. Del Álamo, J. C. *et al.* Three-Dimensional Quantification of Cellular Traction Forces and Mechanosensing of Thin Substrata by Fourier Traction Force Microscopy. *PLoS ONE* **8,** e69850. ISSN: 1932-6203 (2013) (cit. on pp. 5, 23, 65, 85, 86, 111).

35. Zancla, A., Mozetic, P., Orsini, M., Forte, G. & Rainer, A. A primer to traction force microscopy. *Journal of Biological Chemistry* **298** (2022) (cit. on pp. 5, 9, 13, 58, 59, 81, 83, 86).

36. Dembo, M., Oliver, T., Ishihara, A. & Jacobson, K. Imaging the traction stresses exerted by locomoting cells with the elastic substratum method. *Biophysical Journal* **70,** 2008–2022. ISSN: 00063495 (1996) (cit. on pp. 5, 9, 13, 57, 58, 95).

37. Butler, J. P., Toli-Nørrelykke, I. M., Fabry, B. & Fredberg, J. J. Traction fields, moments, and strain energy that cells exert on their surroundings. *American Journal of Physiology - Cell Physiology* **282,** 595–605. ISSN: 03636143 (2002) (cit. on pp. 5, 9, 13, 23, 34, 57, 58, 65, 85, 86, 94, 99).

38. Lin, Y. C. *et al.* Mechanosensing of substrate thickness. *Physical review. E, Statistical, nonlinear, and soft matter physics* **82.** ISSN: 1550-2376 (2010) (cit. on pp. 5, 9, 65, 75, 76, 86, 114, 115).

39. Banerjee, S. & Marchetti, M. C. Contractile stresses in cohesive cell layers on finite-thickness substrates. *Physical review letters* **109,** 108101 (2012) (cit. on pp. 5, 17, 115).

40. Edwards, C. M. & Schwarz, U. S. Force localization in contracting cell layers. *Physical review letters* **107,** 128101 (2011) (cit. on pp. 5, 8).

41. Gómez-González, M., Latorre, E., Arroyo, M. & Trepat, X. Measuring mechanical stress in living tissues. *Nature Reviews Physics 2020 2:6* **2,** 300–317. ISSN: 2522-5820 (2020) (cit. on pp. 5, 17, 57).

42. Forgacs, G., Foty, R. A., Shafrir, Y. & Steinberg, M. S. Viscoelastic properties of living embryonic tissues: a quantitative study. *Biophysical journal* **74,** 2227–2234 (1998) (cit. on p. 6).

43. Andersen, T. *et al.* Cell size and actin architecture determine force generation in optogenetically activated cells. *Biophysical Journal* **122,** 684–696 (2023) (cit. on pp. 6, 8).

44. Ogden, R. Non-linear elastic deformations. *Engineering Analysis* **1,** 119. ISSN: 0264-682X (1984) (cit. on pp. 7, 114).

45. Hansen, P. C. & O'Leary, D. P. The use of the L-curve in the regularization of discrete ill-posed problems. *SIAM journal on scientific computing* **14,** 1487–1503 (1993) (cit. on pp. 8, 9, 57, 77, 86).

46. Hansen, P. C. Regularization tools version 4.0 for Matlab 7.3. *Numerical algorithms* **46,** 189–194 (2007) (cit. on pp. 8, 9, 58, 77, 86).

47. Sabass, B., Gardel, M. L., Waterman, C. M. & Schwarz, U. S. High Resolution Traction Force Microscopy Based on Experimental and Computational Advances. *Biophysical Journal* **94,** 207–220. ISSN: 0006-3495 (2008) (cit. on pp. 9, 13, 57, 58, 66, 78, 81, 83, 86, 87, 94, 95).

48. Schwarz, U. S. *et al.* Calculation of Forces at Focal Adhesions from Elastic Substrate Data: The Effect of Localized Force and the Need for Regularization. *Biophysical Journal* **83,** 1380–1394. ISSN: 0006-3495 (2002) (cit. on pp. 9, 10, 57, 58, 66, 86, 95).

49. Huang, Y. *et al.* Traction force microscopy with optimized regularization and automated Bayesian parameter selection for comparing cells. *Scientific Reports 2019 9:1* **9,** 1–16. ISSN: 2045-2322 (2019) (cit. on pp. 9, 13, 57, 58, 66, 75, 78, 85–87, 97, 114).

50. Han, S. J., Oak, Y., Groisman, A. & Danuser, G. Traction microscopy to identify force modulation in subresolution adhesions. *Nature Methods 2015 12:7* **12,** 653–656. ISSN: 1548-7105 (2015) (cit. on pp. 9, 58, 86).

51. Nier, V. *et al.* Inference of Internal Stress in a Cell Monolayer. *Biophysical Journal* **110,** 1625–1635. ISSN: 0006-3495 (2016) (cit. on pp. 9, 17, 58, 75, 86).

52. Denisin, A. K., Kim, H., Riedel-Kruse, I. H. & Pruitt, B. L. Field Guide to Traction Force Microscopy. *Cellular and Molecular Bioengineering 2024,* 1–20. ISSN: 1865-5033 (2024) (cit. on pp. 9, 13, 83, 86).

53. Hansen, P. C. *Rank-deficient and discrete ill-posed problems: numerical aspects of linear inversion* (SIAM, 1998) (cit. on p. 10).

54. Gelman, A., Carlin, J. B., Stern, H. S. & Rubin, D. B. Bayesian Data Analysis. *Bayesian Data Analysis* (1995) (cit. on pp. 10, 11, 68).

55. Efron, B. in *Breakthroughs in statistics: Methodology and distribution* 569–593 (Springer, 1992) (cit. on pp. 12, 63).

56. Hastie, T., Tibshirani, R., Friedman, J. H. & Friedman, J. H. *The elements of statistical learning: data mining, inference, and prediction* (Springer, 2009) (cit. on pp. 12, 63).

57. Teerlink, J. R. *et al.* Cardiac myosin activation with omecamtiv mecarbil in systolic heart failure. *New England Journal of Medicine* **384,** 105–116 (2021) (cit. on p. 12).

58. Hochmuth, R. M. Micropipette aspiration of living cells. *Journal of biomechanics* **33,** 15–22 (2000) (cit. on p. 12).

59. Ballan, N., Shaheen, N., Keller, G. M. & Gepstein, L. Single-cell mechanical analysis of human pluripotent stem cell-derived cardiomyocytes for drug testing and pathophysiological studies. *Stem Cell Reports* **15,** 587–596 (2020) (cit. on pp. 12, 121).

60. Stamenović, D. *et al.* Rheological behavior of living cells is timescale-dependent. *Biophysical journal* **93,** L39–L41 (2007) (cit. on p. 12).

61. Harris, A. K., Wild, P. & Stopak, D. Silicone rubber substrata: a new wrinkle in the study of cell locomotion. *Science* **208,** 177–179 (1980) (cit. on pp. 13, 57, 83).

62. Polacheck, W. J. & Chen, C. S. Measuring cell-generated forces: a guide to the available tools. *Nature Methods 2016 13:5* **13.** review forces in cells, 415–423. ISSN: 1548-7105 (2016) (cit. on pp. 13, 59, 83).

63. Boquet-Pujadas, A. & Olivo-Marin, J. C. Reformulating Optical Flow to Solve Image-Based Inverse Problems and Quantify Uncertainty. *IEEE Transactions on Pattern Analysis and Machine Intelligence* **45,** 6125–6141. ISSN: 19393539 (2023) (cit. on pp. 13, 58, 85, 86).

64. Alvarez-Gonzalez, B. *et al.* Cytoskeletal mechanics regulating amoeboid cell locomotion. *Applied Mechanics Reviews* **66.** ISSN: 00036900 (2014) (cit. on p. 13).

65. Trepat, X. *et al.* Physical forces during collective cell migration. *Nature Physics 2009 5:6* **5,** 426–430. ISSN: 1745-2481 (2009) (cit. on pp. 13, 17, 57, 111).

66. Landau, L. D., Pitaevskii, L., Kosevich, A. M. & Lifshitz, E. M. *Theory of elasticity: volume 7* (Elsevier, 2012) (cit. on p. 13).

67. Colin-York, H., Eggeling, C. & Fritzsche, M. Dissection of mechanical force in living cells by super-resolved traction force microscopy. *nature protocols* **12,** 783–796 (2017) (cit. on p. 13).

68. Blumberg, J. W. & Schwarz, U. S. Comparison of direct and inverse methods for 2.5 D traction force microscopy. *PLoS ONE* **17,** e0262773 (2022) (cit. on pp. 13, 58).

69. Wang, Y.-l. & Lin, Y.-C. Traction force microscopy by deep learning. *Biophysical Journal* **120,** 3079–3090 (2021) (cit. on p. 13).

70. Rabodzey, A., Alcaide, P., Luscinskas, F. W. & Ladoux, B. Mechanical Forces Induced by the Transendothelial Migration of Human Neutrophils. *Biophysical Journal* **95,** 1428–1438. ISSN: 0006-3495 (2008) (cit. on pp. 13, 57).

71. Beussman, K. M. *et al.* Black dots: High-yield traction force microscopy reveals structural factors contributing to platelet forces. *Acta biomaterialia* **163,** 302–311 (2023) (cit. on pp. 13, 93, 94, 99, 104).

72. Bergert, M. *et al.* Confocal reference free traction force microscopy. *Nature communications* **7,** 12814 (2016) (cit. on p. 13).

73. Lendenmann, T. *et al.* Cellogram: on-the-fly traction force microscopy. *Nano letters* **19,** 6742–6750 (2019) (cit. on p. 13).

74. Yamaguchi, N. *et al.* Rear traction forces drive adherent tissue migration in vivo. *Nature cell biology* **24,** 194–204 (2022) (cit. on p. 13).

75. Vorselen, D. *et al.* Microparticle traction force microscopy reveals subcellular force exertion patterns in immune cell–target interactions. *Nature communications* **11,** 20 (2020) (cit. on p. 14).

76. Garcia-Herreros, A. *et al.* Tunable photoinitiated hydrogel microspheres for direct quantification of cell-generated forces in complex three-dimensional environments. *bioRxiv,* 2023–03 (2023) (cit. on p. 14).

77. Ingremeau, F. *et al.* Optical sensing of mechanical pressure based on diffusion measurement in polyacrylamide cell-like barometers. *Soft Matter* **13,** 4210–4213 (2017) (cit. on p. 14).

78. Yeh, Y. T. *et al.* Three-dimensional forces exerted by leukocytes and vascular endothelial cells dynamically facilitate diapedesis. *Proceedings of the National Academy of Sciences of the United States of America* **115,** 133–138. ISSN: 10916490 (2018) (cit. on pp. 14, 19, 57, 82).

79. Willert, C. E. & Gharib, M. Digital particle image velocimetry. *Experiments in Fluids* **10,** 181–193. ISSN: 07234864 (1991) (cit. on pp. 14, 83).

80. Adrian, R. J. & Westerweel, J. *Particle image velocimetry* **30** (Cambridge university press, 2011) (cit. on pp. 14, 63, 83).

81. Scarano, F. & Riethmuller, M. L. Iterative multigrid approach in PIV image processing with discrete window offset. *Experiments in Fluids* **26,** 513–523. ISSN: 1432-1114 (1999) (cit. on p. 16).

82. Schwartz, A. B. *et al.* Elucidating the Biomechanics of Leukocyte Transendothelial Migration by Quantitative Imaging. *Frontiers in Cell and Developmental Biology* **9,** 704. ISSN: 2296634X (2021) (cit. on pp. 16, 17, 19, 20, 57).

83. Lagendijk, A. K. *et al.* Live imaging molecular changes in junctional tension upon VE-cadherin in zebrafish. *Nature Communications* **8.** ISSN: 2041-1723 (2017) (cit. on p. 16).

84. Brockman, J. M. *et al.* Mapping the 3D orientation of piconewton integrin traction forces. *Nature Methods* **15,** 115–118. ISSN: 1548-7105 (2017) (cit. on pp. 16, 57).

85. Neubauer, J. W. *et al.* Mechanoresponsive Hydrogel Particles as a Platform for Three-Dimensional Force Sensing. *ACS Applied Materials amp; Interfaces* **11,** 26307–26313. ISSN: 1944-8252 (2019) (cit. on p. 16).

86. Zhang, J., Chada, N. C. & Reinhart-King, C. A. Microscale Interrogation of 3D Tissue Mechanics. *Frontiers in Bioengineering and Biotechnology* **7.** ISSN: 2296-4185 (2019) (cit. on p. 16).

87. Cost, A.-L., Ringer, P., Chrostek-Grashoff, A. & Grashoff, C. How to Measure Molecular Forces in Cells: A Guide to Evaluating Genetically-Encoded FRET-Based Tension Sensors. *Cellular and Molecular Bioengineering* **8,** 96–105. ISSN: 1865-5033 (2014) (cit. on p. 16).

88. Sarangi, B. R. *et al.* Coordination between Intra- and Extracellular Forces Regulates Focal Adhesion Dynamics. *Nano Letters* **17,** 399–406. ISSN: 1530-6992 (2016) (cit. on p. 17).

89. Tambe, D. T. *et al.* Monolayer Stress Microscopy: Limitations, Artifacts, and Accuracy of Recovered Intercellular Stresses. *PLoS ONE* **8** (ed Kumar, S.) e55172. ISSN: 1932-6203 (2013) (cit. on pp. 17, 111).

90. Zimmermann, J. *et al.* Intercellular Stress Reconstitution from Traction Force Data. *Biophysical Journal* **107,** 548–554. ISSN: 0006-3495 (2014) (cit. on p. 17).

91. Serrano, R. *et al.* Three-Dimensional Monolayer Stress Microscopy. *Biophysical journal* (2019) (cit. on pp. 17, 23, 57, 58, 111).

92. Harris, A. R. *et al.* Characterizing the mechanics of cultured cell monolayers. *Proceedings of the National Academy of Sciences* **109,** 16449–16454. ISSN: 1091-6490 (2012) (cit. on p. 17).

93. Mazuel, F. *et al.* Magnetic Flattening of Stem-Cell Spheroids Indicates a Size-Dependent Elastocapillary Transition. *Physical Review Letters* **114.** ISSN: 1079-7114 (2015) (cit. on p. 17).

94. Rodriguez, M. L. *et al.* Measuring the Contractile Forces of Human Induced Pluripotent Stem Cell-Derived Cardiomyocytes With Arrays of Microposts. *Journal of Biomechanical Engineering* **136.** ISSN: 1528-8951 (2014) (cit. on p. 17).

95. Borin, D., Pecorari, I., Pena, B. & Sbaizero, O. Novel insights into cardiomyocytes provided by atomic force microscopy. *Seminars in Cell amp; Developmental Biology* **73,** 4–12. ISSN: 1084-9521 (2018) (cit. on pp. 17, 108).

96. Escribano, J. *et al.* Balance of mechanical forces drives endothelial gap formation and may facilitate cancer and immune-cell extravasation. *PLoS computational biology* **15,** e1006395 (2019) (cit. on p. 19).

97. Martinelli, R. *et al.* Probing the biomechanical contribution of the endothelium to lymphocyte migration: diapedesis by the path of least resistance. *Journal of cell science* **127,** 3720–3734 (2014) (cit. on p. 19).

98. Ley, K., Laudanna, C., Cybulsky, M. I. & Nourshargh, S. Getting to the site of inflammation: the leukocyte adhesion cascade updated. *Nature reviews immunology* **7,** 678–689 (2007) (cit. on p. 19).

99. Sarris, M. *et al.* Inflammatory chemokines direct and restrict leukocyte migration within live tissues as glycan-bound gradients. *Current Biology* **22,** 2375–2382 (2012) (cit. on p. 19).

100. Niethammer, P., Grabher, C., Look, A. T. & Mitchison, T. J. A tissue-scale gradient of hydrogen peroxide mediates rapid wound detection in zebrafish. *Nature* **459,** 996–999 (2009) (cit. on p. 19).

101. Deng, Q., Harvie, E. A. & Huttenlocher, A. Distinct signalling mechanisms mediate neutrophil attraction to bacterial infection and tissue injury. *Cellular microbiology* **14,** 517–528 (2012) (cit. on p. 19).

102. McDonald, B. *et al.* Intravascular danger signals guide neutrophils to sites of sterile inflammation. *Science* **330,** 362–366 (2010) (cit. on p. 19).

103. Gruler, H. Directed cell movement: A biophysical analysis. *Blood cells* **19,** 91–91 (1993) (cit. on p. 19).

104. Lerchenberger, M. *et al.* Matrix metalloproteinases modulate ameboid-like migration of neutrophils through inflamed interstitial tissue. *Blood* **122,** 770–780. ISSN: 0006-4971 (2013) (cit. on pp. 19, 54).

105. Weninger, W., Biro, M. & Jain, R. Leukocyte migration in the interstitial space of non-lymphoid organs. *Nature Reviews Immunology* **14,** 232–246 (2014) (cit. on pp. 20, 53).

106. Krummel, M. F., Bartumeus, F. & Gérard, A. T cell migration, search strategies and mechanisms. *Nature Reviews Immunology* **16,** 193–201 (2016) (cit. on p. 20).

107. Sun, L., Su, Y., Jiao, A., Wang, X. & Zhang, B. T cells in health and disease. *Signal transduction and targeted therapy* **8,** 235 (2023) (cit. on p. 20).

108. Sixt, M. & Lämmermann, T. In vitro analysis of chemotactic leukocyte migration in 3D environments. *Cell Migration: Developmental Methods and Protocols,* 149–165 (2011) (cit. on pp. 20, 27, 31).

109. Yamada, K. M. & Sixt, M. Mechanisms of 3D cell migration. *Nature Reviews Molecular Cell Biology* **20,** 738–752. ISSN: 1471-0080 (2019) (cit. on p. 20).

110. Lämmermann, T. & Sixt, M. Mechanical modes of 'amoeboid' cell migration. *Current Opinion in Cell Biology* **21,** 636–644. ISSN: 0955-0674 (2009) (cit. on p. 20).

111. Krause, M. & Gautreau, A. Steering cell migration: lamellipodium dynamics and the regulation of directional persistence. *Nature Reviews Molecular Cell Biology* **15,** 577–590. ISSN: 1471-0080 (2014) (cit. on p. 20).

112. Barbier, L. *et al.* Myosin II Activity Is Selectively Needed for Migration in Highly Confined Microenvironments in Mature Dendritic Cells. *Frontiers in Immunology* **10.** ISSN: 1664-3224 (2019) (cit. on p. 20).

113. Thompson, S. B. *et al.* Formin-like 1 mediates effector T cell trafficking to inflammatory sites to enable T cell-mediated autoimmunity. *elife* **9,** e58046 (2020) (cit. on pp. 20, 29).

114. Dong, B. *et al.* Mammalian Diaphanous-Related Formin 1 Regulates GSK3-Dependent Microtubule Dynamics Required for T Cell Migratory Polarization. *PLoS ONE* **8** (ed Parsons, M.) e80500. ISSN: 1932-6203 (2013) (cit. on p. 20).

115. Raffel, M. *et al. Particle image velocimetry: a practical guide* (springer, 2018) (cit. on p. 23).

116. Ayachit, U. *The paraview guide: a parallel visualization application* (Kitware, Inc., 2015) (cit. on p. 23).

117. Ester, M., Kriegel, H.-P., Sander, J., Xu, X., *et al. A density-based algorithm for discovering clusters in large spatial databases with noise* in *kdd* **96** (1996), 226–231 (cit. on pp. 25, 63).

118. Rousseeuw, P. J. Silhouettes: a graphical aid to the interpretation and validation of cluster analysis. *Journal of computational and applied mathematics* **20,** 53–65 (1987) (cit. on p. 25).

119. Hennig, C. Cluster-wise assessment of cluster stability. *Computational Statistics & Data Analysis* **52,** 258–271 (2007) (cit. on p. 25).

120. Bishop, C. M. & Nasrabadi, N. M. *Pattern recognition and machine learning* **4** (Springer, 2006) (cit. on p. 26).

121. Afonso, P. V., McCann, C. P., Kapnick, S. M. & Parent, C. A. Discoidin domain receptor 2 regulates neutrophil chemotaxis in 3D collagen matrices. *Blood, The Journal of the American Society of Hematology* **121,** 1644–1650 (2013) (cit. on p. 27).

122. Geraldo, S., Simon, A. & Vignjevic, D. M. Revealing the cytoskeletal organization of invasive cancer cells in 3D. *JoVE (Journal of Visualized Experiments),* e50763 (2013) (cit. on p. 28).

123. Millius, A. & Weiner, O. D. Chemotaxis in neutrophil-like HL-60 cells. *Chemotaxis: Methods and Protocols,* 167–177 (2009) (cit. on p. 28).

124. Sakata, D. *et al.* Impaired T lymphocyte trafficking in mice deficient in an actin-nucleating protein, mDia1. *The Journal of experimental medicine* **204,** 2031–2038 (2007) (cit. on p. 29).

125. Ershov, D. *et al.* TrackMate 7: integrating state-of-the-art segmentation algorithms into tracking pipelines. *Nature methods* **19,** 829–832 (2022) (cit. on p. 30).

126. Tinevez, J.-Y. *et al.* TrackMate: An open and extensible platform for single-particle tracking. *Methods* **115,** 80–90 (2017) (cit. on pp. 30, 44).

127. Schindelin, J. *et al.* Fiji: an open-source platform for biological-image analysis. *Nature methods* **9,** 676–682 (2012) (cit. on p. 31).

128. Lodish, H. F. *Molecular cell biology* (Macmillan, 2008) (cit. on p. 31).

129. Fratzl, P. in *Collagen: structure and mechanics* 1–13 (Springer, 2008) (cit. on p. 31).

130. Marasco, W. *et al.* Purification and identification of formyl-methionyl-leucyl-phenylalanine as the major peptide neutrophil chemotactic factor produced by Escherichia coli. *Journal of Biological Chemistry* **259,** 5430–5439 (1984) (cit. on p. 33).

131. Steinwachs, J. *et al.* Three-dimensional force microscopy of cells in biopolymer networks. *Nature Methods* **13,** 171–176. ISSN: 1548-7105 (2015) (cit. on pp. 33, 34, 57).

132. Hall, M. S. *et al.* Fibrous nonlinear elasticity enables positive mechanical feedback between cells and ECMs. *Proceedings of the National Academy of Sciences* **113,** 14043–14048 (2016) (cit. on p. 33).

133. Wolf, K. *et al.* Physical limits of cell migration: control by ECM space and nuclear deformation and tuning by proteolysis and traction force. *Journal of Cell Biology* **201,** 1069–1084 (2013) (cit. on pp. 33, 54).

134. Nyberg, K. D. *et al.* Quantitative deformability cytometry: rapid, calibrated measurements of cell mechanical properties. *Biophysical journal* **113,** 1574–1584 (2017) (cit. on p. 33).

135. Kuntz, R. M. & Saltzman, W. M. Neutrophil motility in extracellular matrix gels: mesh size and adhesion affect speed of migration. *Biophysical journal* **72,** 1472–1480 (1997) (cit. on p. 38).

136. Petrie, R. J., Doyle, A. D. & Yamada, K. M. Random versus directionally persistent cell migration. *Nature reviews Molecular cell biology* **10,** 538–549 (2009) (cit. on p. 38).

137. Boal, D. H. *Mechanics of the Cell* (Cambridge University Press, 2012) (cit. on p. 39).

138. Nossal, R. & Zigmond, S. H. Chemotropism indices for polymorphonuclear leukocytes. *Biophysical Journal* **16,** 1171–1182 (1976) (cit. on p. 39).

139. Handorf, A. M., Zhou, Y., Halanski, M. A. & Li, W.-J. Tissue Stiffness Dictates Development, Homeostasis, and Disease Progression. *Organogenesis* **11,** 1–15. ISSN: 1555-8592 (2015) (cit. on p. 53).

140. Burn, T. & Alvarez, J. I. Reverse transendothelial cell migration in inflammation: to help or to hinder? *Cellular and Molecular Life Sciences* **74,** 1871–1881. ISSN: 1420-9071 (2016) (cit. on p. 55).

141. Kumar, A., Placone, J. K. & Engler, A. J. Understanding the extracellular forces that determine cell fate and maintenance. *Development* **144,** 4261–4270 (2017) (cit. on p. 57).

142. Ehler, E. & Perriard, J. C. Cardiomyocyte Cytoskeleton and Myofibrillogenesis in Healthy and Diseased Heart. *Heart Failure Reviews 2000 5:3* **5.** Review paper talking about force generation and force transmission mechanics aspect of DCM, 259–269. ISSN: 1573-7322 (2000) (cit. on p. 57).

143. Eyckmans, J., Boudou, T., Yu, X. & Chen, C. S. A hitchhiker's guide to mechanobiology. *Developmental cell* **21,** 35–47 (2011) (cit. on p. 57).

144. Dembo, M. & Wang, Y. L. Stresses at the cell-to-substrate interface during locomotion of fibroblasts. *Biophysical Journal* **76,** 2307. ISSN: 00063495 (1999) (cit. on pp. 57, 58, 85, 86).

145. Koch, T. M., Münster, S., Bonakdar, N., Butler, J. P. & Fabry, B. 3D traction forces in cancer cell invasion. *PLoS ONE* **7,** e33476–e33476 (2012) (cit. on p. 57).

146. Grashoff, C. *et al.* Measuring mechanical tension across vinculin reveals regulation of focal adhesion dynamics. *Nature 2010 466:7303* **466,** 263–266. ISSN: 1476-4687 (2010) (cit. on p. 57).

147. Blakely, B. L. *et al.* A DNA-based molecular probe for optically reporting cellular traction forces. *Nature Methods 2014 11:12* **11,** 1229–1232. ISSN: 1548-7105 (2014) (cit. on p. 57).

148. Hazlett, L. *et al.* Epifluorescence-based three-dimensional traction force microscopy. *Scientific Reports 2021 10:1* **10,** 1–12. ISSN: 2045-2322 (2020) (cit. on p. 57).

149. Barrasa-Fano, J. *et al.* TFMLAB: A MATLAB toolbox for 4D traction force microscopy. *SoftwareX* **15,** 100723. ISSN: 2352-7110 (2021) (cit. on p. 57).

150. Martiel, J. L. *et al.* Measurement of cell traction forces with ImageJ. *Methods in Cell Biology* **125,** 269–287. ISSN: 0091-679X (2015) (cit. on p. 57).

151. Bauer, A. *et al.* pyTFM: A tool for traction force and monolayer stress microscopy. *PLOS Computational Biology* **17,** e1008364. ISSN: 1553-7358 (2021) (cit. on p. 57).

152. Smith, L. A., Aranda-Espinoza, H., Haun, J. B., Dembo, M. & Hammer, D. A. Neutrophil traction stresses are concentrated in the uropod during migration. *Biophysical Journal* **92.** ISSN: 00063495 (2007) (cit. on p. 57).

153. Elosegui-Artola, A. *et al.* Mechanical regulation of a molecular clutch defines force transmission and transduction in response to matrix rigidity. *Nature Cell Biology 2016 18:5* **18,** 540–548. ISSN: 1476-4679 (2016) (cit. on p. 57).

154. Brugués, A. *et al.* Forces driving epithelial wound healing. *Nature Physics 2014 10:9* **10,** 683–690. ISSN: 1745-2481 (2014) (cit. on p. 57).

155. Park, J. A. *et al.* Unjamming and cell shape in the asthmatic airway epithelium. *Nature Materials 2014 14:10* **14,** 1040–1048. ISSN: 1476-4660 (2015) (cit. on pp. 57, 108).

156. Ribeiro, A. J. *et al.* Contractility of single cardiomyocytes differentiated from pluripotent stem cells depends on physiological shape and substrate stiffness. *Proceedings of the National Academy of Sciences* **112,** 12705–12710 (2015) (cit. on pp. 57, 107).

157. Hanke, J., Probst, D., Zemel, A., Schwarz, U. S. & Köster, S. Dynamics of force generation by spreading platelets. *Soft Matter* **14,** 6571–6581. ISSN: 17446848 (2018) (cit. on pp. 57, 93).

158. Bastounis, E. E., Yeh, Y. T. & Theriot, J. A. Matrix stiffness modulates infection of endothelial cells by Listeria monocytogenes via expression of cell surface vimentin. *Molecular Biology of the Cell* **29,** 1571–1589. ISSN: 19394586 (2018) (cit. on p. 57).

159. Plotnikov, S. V., Sabass, B., Schwarz, U. S. & Waterman, C. M. High-Resolution Traction Force Microscopy. *Methods in Cell Biology* **123,** 367–394. ISSN: 0091-679X (2014) (cit. on p. 58).

160. Wieneke, B. PIV uncertainty quantification from correlation statistics. *Measurement Science and Technology* **26,** 074002. ISSN: 0957-0233 (2015) (cit. on pp. 59, 72, 84).

161. Sciacchitano, A. Uncertainty quantification in particle image velocimetry. *Measurement Science and Technology* **30,** 092001. ISSN: 0957-0233 (2019) (cit. on pp. 59, 84).

162. Bhattacharya, S., Charonko, J. J. & Vlachos, P. P. Particle image velocimetry (PIV) uncertainty quantification using moment of correlation (MC) plane. *Measurement Science and Technology* **29,** 115301. ISSN: 0957-0233 (2018) (cit. on pp. 59, 84).

163. Kybic, J. Fast no ground truth image registration accuracy evaluation: Comparison of bootstrap and Hessian approaches. *2008 5th IEEE International Symposium on Biomedical Imaging: From Nano to Macro, Proceedings, ISBI,* 792–795 (2008) (cit. on p. 59).

164. Kybic, J. Bootstrap resampling for image registration uncertainty estimation without ground truth. *IEEE Transactions on Image Processing* **19,** 64–73. ISSN: 10577149 (2010) (cit. on pp. 59, 61, 72, 84).

165. Xue, Z., Charonko, J. J. & Vlachos, P. P. Particle image velocimetry correlation signal-to-noise ratio metrics and measurement uncertainty quantification. *Measurement Science and Technology* **25,** 115301 (2014) (cit. on p. 63).

166. Molina, R., Katsaggelos, A. K. & Mateos, J. Bayesian and regularization methods for hyperparameter estimation in image restoration. *IEEE Transactions on Image Processing* **8,** 231–246. ISSN: 10577149 (1999) (cit. on pp. 66, 97).

167. Howard, M., Luttman, A. & Fowler, M. Sampling-based uncertainty quantification in deconvolution of X-ray radiographs. *Journal of Computational and Applied Mathematics* **270,** 43–51. ISSN: 0377-0427 (2014) (cit. on p. 68).

168. Vignaud, T., Ennomani, H. & Théry, M. in *Methods in cell biology* 93–116 (Elsevier, 2014) (cit. on pp. 70, 79).

169. Tse, J. R. & Engler, A. J. Preparation of hydrogel substrates with tunable mechanical properties. *Current protocols in cell biology* **47,** 10–16 (2010) (cit. on p. 70).

170. Felts, L., Kohli, V., Marr, J., Schumacher, J. & Schlicker, O. *An Introduction to Computational Clearing* `https://www.leica-microsystems.com/science-lab/life-science/an-introduction-to-computational-clearing`. Retrieved : July 27, 2024. 2020 (cit. on p. 79).

171. Zündel, M., Ehret, A. E. & Mazza, E. Factors influencing the determination of cell traction forces. *PLoS ONE* **12,** e0172927. ISSN: 1932-6203 (2017) (cit. on p. 83).

172. Sun, Y. *et al.* Electric field–guided collective motility initiation of large epidermal cell groups. *Molecular biology of the cell* **34,** ar48 (2023) (cit. on p. 84).

173. Sharma, A. *et al.* Use of human induced pluripotent stem cell–derived cardiomyocytes to assess drug cardiotoxicity. *Nature protocols* **13,** 3018–3041 (2018) (cit. on p. 84).

174. Fujikawa, R. *et al.* Bayesian traction force estimation using cell boundary-dependent force priors. *Biophysical Journal* **122,** 4542–4554. ISSN: 0006-3495 (2023) (cit. on pp. 85, 86).

175. Colin-York, H. *et al.* Spatiotemporally super-resolved volumetric traction force microscopy. *Nano letters* **19,** 4427–4434 (2019) (cit. on p. 86).

176. White, J. G. Platelet structure. *Platelets* **2,** 45–71 (2007) (cit. on p. 93).

177. Feghhi, S. & Sniadecki, N. J. Mechanobiology of platelets: techniques to study the role of fluid flow and platelet retraction forces at the micro-and nano-scale. *International journal of molecular sciences* **12,** 9009–9030 (2011) (cit. on p. 93).

178. Williams, E. K., Oshinowo, O., Ravindran, A., Lam, W. A. & Myers, D. R. *Feeling the force: measurements of platelet contraction and their diagnostic implications* in *Seminars in thrombosis and hemostasis* **45** (2019), 285–296 (cit. on p. 93).

179. Calaminus, S. D., Thomas, S., McCarty, O., Machesky, L. & Watson, S. Identification of a novel, actin-rich structure, the actin nodule, in the early stages of platelet spreading. *Journal of Thrombosis and Haemostasis* **6,** 1944–1952 (2008) (cit. on pp. 93, 104).

180. Yuan, Y. *et al.* The von Willebrand factor-glycoprotein Ib/V/IX interaction induces actin polymerization and cytoskeletal reorganization in rolling platelets and glycoprotein Ib/V/IX-transfected cells. *Journal of Biological Chemistry* **274,** 36241–36251 (1999) (cit. on p. 93).

181. Feghhi, S. *et al.* Glycoprotein Ib-IX-V complex transmits cytoskeletal forces that enhance platelet adhesion. *Biophysical journal* **111,** 601–608 (2016) (cit. on p. 93).

182. Miles, J. *et al.* Storage temperature determines platelet GPVI levels and function in mice and humans. *Blood advances* **5,** 3839–3849 (2021) (cit. on p. 93).

183. Brask, J. B., Singla-Buxarrais, G., Uroz, M., Vincent, R. & Trepat, X. Compressed sensing traction force microscopy. *Acta biomaterialia* **26,** 286–294 (2015) (cit. on p. 95).

184. Hagmann, J. Pattern formation and handedness in the cytoskeleton of human platelets. *Proceedings of the National Academy of Sciences* **90,** 3280–3283 (1993) (cit. on p. 104).

185. Myers, D. R. *et al.* Single-platelet nanomechanics measured by high-throughput cytometry. *Nature materials* **16,** 230–235 (2017) (cit. on p. 104).

186. Springer, T. A. von Willebrand factor, Jedi knight of the bloodstream. *Blood, The Journal of the American Society of Hematology* **124,** 1412–1425 (2014) (cit. on p. 104).

187. Di Meglio, L. *et al.* Acute ischemic stroke thrombi have an outer shell that impairs fibrinolysis. *Neurology* **93,** e1686–e1698 (2019) (cit. on p. 104).

188. Mereuta, O. M. *et al.* Correlation of von Willebrand factor and platelets with acute ischemic stroke etiology and revascularization outcome: an immunohistochemical study. *Journal of neurointerventional surgery* **15,** 488–494 (2023) (cit. on p. 104).

189. Yoshida, Y. & Yamanaka, S. Induced Pluripotent Stem Cells 10 Years Later: For Cardiac Applications. *Circulation Research* **120,** 1958–1968. ISSN: 1524-4571 (2017) (cit. on p. 107).

190. Ebert, A. D., Liang, P. & Wu, J. C. Induced Pluripotent Stem Cells as a Disease Modeling and Drug Screening Platform. *Journal of Cardiovascular Pharmacology* **60,** 408–416. ISSN: 0160-2446 (2012) (cit. on p. 107).

191. Del Álamo, J. C. *et al.* High throughput physiological screening of iPSC-derived cardiomyocytes for drug development. *Biochimica et Biophysica Acta (BBA) - Molecular Cell Research* **1863,** 1717–1727. ISSN: 0167-4889 (2016) (cit. on p. 107).

192. Van Meer, B. J., Tertoolen, L. G. & Mummery, C. L. Concise Review: Measuring Physiological Responses of Human Pluripotent Stem Cell Derived Cardiomyocytes to Drugs and Disease. *Stem Cells* **34,** 2008–2015. ISSN: 1549-4918 (2016) (cit. on p. 107).

193. Daily, N. J., Santos, R., Vecchi, J., Kemanli, P. & Wakatsuki, T. Calcium Transient Assays for Compound Screening with Human iPSC-derived Cardiomyocytes: Evaluating New Tools. *Journal of Evolving Stem Cell Research* **1** (ed Wang, C.) 1–11. ISSN: 2574-4372 (2017) (cit. on p. 107).

194. Li, X., Zhang, R., Zhao, B., Lossin, C. & Cao, Z. Cardiotoxicity screening: a review of rapid-throughput in vitro approaches. *Archives of Toxicology* **90,** 1803–1816. ISSN: 1432-0738 (2015) (cit. on p. 107).

195. McKeithan, W. L. *et al.* Reengineering an Antiarrhythmic Drug Using Patient hiPSC Cardiomyocytes to Improve Therapeutic Potential and Reduce Toxicity. *Cell Stem Cell* **27,** 813–821.e6. ISSN: 1934-5909 (2020) (cit. on p. 107).

196. Hayakawa, T. *et al.* Image-based evaluation of contraction–relaxation kinetics of human-induced pluripotent stem cell-derived cardiomyocytes: Correlation and complementarity with extracellular electrophysiology. *Journal of Molecular and Cellular Cardiology* **77,** 178–191. ISSN: 0022-2828 (2014) (cit. on p. 107).

197. Huebsch, N. *et al.* Automated Video-Based Analysis of Contractility and Calcium Flux in Human-Induced Pluripotent Stem Cell-Derived Cardiomyocytes Cultured over Different Spatial Scales. *Tissue Engineering Part C: Methods* **21,** 467–479. ISSN: 1937-3392 (2015) (cit. on p. 107).

198. Maddah, M. *et al.* A Non-invasive Platform for Functional Characterization of Stem-Cell-Derived Cardiomyocytes with Applications in Cardiotoxicity Testing. *Stem Cell Reports* **4,** 621–631. ISSN: 2213-6711 (2015) (cit. on p. 107).

199. Sala, L. *et al.* MUSCLEMOTION: a versatile open software tool to quantify cardiomyocyte and cardiac muscle contraction in vitro and in vivo. *Circulation research* **122,** e5–e16 (2018) (cit. on p. 107).

200. Ahola, A., Pölönen, R.-P., Aalto-Setälä, K. & Hyttinen, J. Simultaneous measurement of contraction and calcium transients in stem cell derived cardiomyocytes. *Annals of biomedical engineering* **46,** 148–158 (2018) (cit. on p. 107).

201. Czirok, A. *et al.* Optical-flow based non-invasive analysis of cardiomyocyte contractility. *Scientific Reports* **7.** ISSN: 2045-2322 (2017) (cit. on p. 107).

202. Boothe, S. D. *et al.* The effect of substrate stiffness on cardiomyocyte action potentials. *Cell biochemistry and biophysics* **74,** 527–535 (2016) (cit. on p. 107).

203. Westermann, D. *et al.* Role of Left Ventricular Stiffness in Heart Failure With Normal Ejection Fraction. *Circulation* **117,** 2051–2060. ISSN: 1524-4539 (2008) (cit. on pp. 108, 121).

204. Zile, M. R., Baicu, C. F. & Gaasch, W. H. Diastolic Heart Failure — Abnormalities in Active Relaxation and Passive Stiffness of the Left Ventricle. *New England Journal of Medicine* **350,** 1953–1959. ISSN: 1533-4406 (2004) (cit. on pp. 108, 121).

205. Chen, C. Y. *et al.* Suppression of detyrosinated microtubules improves cardiomyocyte function in human heart failure. *Nature Medicine* **24,** 1225–1233. ISSN: 1546-170X (2018) (cit. on p. 108).

206. LeWinter, M. M. & Granzier, H. Cardiac Titin: A Multifunctional Giant. *Circulation* **121,** 2137–2145. ISSN: 1524-4539 (2010) (cit. on p. 108).

207. Linke, W. A. & Hamdani, N. Gigantic Business: Titin Properties and Function Through Thick and Thin. *Circulation Research* **114,** 1052–1068. ISSN: 1524-4571 (2014) (cit. on p. 108).

208. Lian, X. *et al.* Robust cardiomyocyte differentiation from human pluripotent stem cells via temporal modulation of canonical Wnt signaling. *Proceedings of the National Academy of Sciences* **109.** ISSN: 1091-6490 (2012) (cit. on p. 115).

209. Feyen, D. A. *et al.* Metabolic Maturation Media Improve Physiological Function of Human iPSC-Derived Cardiomyocytes. *Cell Reports* **32,** 107925. ISSN: 2211-1247 (2020) (cit. on p. 115).

210. Carubelli, V. *et al.* Treatment with 24hour istaroxime infusion in patients hospitalised for acute heart failure: a randomised, placebo-controlled trial. *European Journal of Heart Failure* **22,** 1684–1693. ISSN: 1879-0844 (2020) (cit. on p. 117).

211. Planelles-Herrero, V. J., Hartman, J. J., Robert-Paganin, J., Malik, F. I. & Houdusse, A. Mechanistic and structural basis for activation of cardiac myosin force production by omecamtiv mecarbil. *Nature Communications* **8.** ISSN: 2041-1723 (2017) (cit. on pp. 117, 121).

212. Anderson, J. L. & Prystowsky, E. N. Sotalol: An important new antiarrhythmic. *American Heart Journal* **137,** 388–409. ISSN: 0002-8703 (1999) (cit. on p. 119).

213. Nagy, L. *et al.* The novel cardiac myosin activator omecamtiv mecarbil increases the calcium sensitivity of force production in isolated cardiomyocytes and skeletal muscle fibres of the rat. *British Journal of Pharmacology* **172,** 4506–4518. ISSN: 1476-5381 (2015) (cit. on p. 121).